The Dissertation Committee for Sean Evan Sullivan
certifies that this is the approved version of the following dissertation:

Nonequilibrium Heat and Spin Transport in Materials with Long Carrier Relaxation Lengths

Committee:

Li Shi, Supervisor

Jianshi Zhou, Co-Supervisor

Jung-Fu Lin

Raymond Orbach

Yaguo Wang

Nonequilibrium Heat and Spin Transport in Materials with Long Carrier Relaxation Lengths

by

Sean Evan Sullivan

Dissertation

Presented to the Faculty of the Graduate School of

The University of Texas at Austin

in Partial Fulfillment

of the Requirements

for the Degree of

Doctor of Philosophy

The University of Texas at Austin

December 2018

For my family.

Acknowledgments

I am grateful to my advisor, Prof. Li Shi, and co-advisor, Prof. Jianshi Zhou, for providing me with the opportunity to work on many interesting and distinct areas of research − their guidance and patience have helped me grow immensely during my time at UT. I am grateful for our many fruitful discussions and for their dedication, passion for science, and desire for understanding, which they have further engendered in me.

My time at UT has been defined by the people I've had the pleasure of getting to know and work with − I'm very grateful for the support, friendship and camaraderie of other members of the Li Shi group. In particular, I'd like to thank Dr. Annie Weathers for her immense amount of help with the spin-heat coupling measurements, Dr. Xi Chen for his guidance in materials synthesis and thermal conductivity measurements, and Dr. Jaehyun Kim for his help with micro-bridge thermometry. In addition, I'd like to thank Dr. Iskandar Kholmanov for sharing his expertise on graphene growth, Eric Ou and Dr. David Choi for their help with microfabrication, and Dr. Evan Fleming for his help in developing the modulated techniques.

And lastly, I am grateful for my friends and family whose love and unwavering support in so many ways has been invaluable to my success. My friends in Austin have been a bastion of support and refuge. My parents have shared with me their intellectual curiosity, work ethic, sense of humor, and patience; they have enabled me to achieve all that I have today. Finally, I thank Dr. Ernest Wisniewski and Dr. Tom Savin who have have been a personal inspiration to me in walking this path.

Abstract

Nonequilibrium Heat and Spin Transport in Materials with Long Carrier Relaxation Lengths

Sean Evan Sullivan, Ph.D.
The University of Texas at Austin, 2018

Supervisors: Li Shi
and
Jianshi Zhou

Many modern technologies rely on the ability to shuttle energy and information from one point to another, which is accomplished through the fine control of the various microscopic energy, charge, and spin carriers that exist as quantized excitations in materials. The continued advancement of devices for computation and energy conversion and storage, however, is stymied by the lack of material systems that can effectively and efficiently transport these microscopic carriers without dissipating their energy or encoded information en route.

This work seeks to advance the understanding of how materials can be engineered to maximize energy carrier transport by studying three different classes of

materials that achieve their properties in different ways. In particular, heat or spin transport are studied in suspended two-dimensional graphene far from equilibrium, semiconducting boron arsenide (BAs), and heterostructures consisting of Pt and the magnetic insulator yttrium iron garnet (YIG). Transport in these materials is investigated using a variety of experimental approaches, including inelastic light scattering spectroscopies, thermal conductance, and lock-in magnetotransport measurements. In addition, signal modulation coupled with frequency domain analysis are utilized to create new sensitive non-contact thermometers and magnetometer microprobes based on Raman and Brillouin light scattering (BLS) spectroscopies.

Micro-Raman measurements of high thermal conductivity (κ) suspended graphene show that focused optical excitation can drive different phonon polarizations out of local thermal equilibrium, with the low-frequency flexural acoustic (ZA) phonons being underpopulated inside the submicron laser spot, complicating the determination of diffusive κ from the Raman thermometry measurements. Furthermore, numerical lock-in based Raman thermometry is developed to provide noncontact thermal transport measurements and validate BAs as the only known semiconductor with ultrahigh bulk κ, approaching 1000 $\mathrm{Wm^{-1}K^{-1}}$ at room temperature. Lastly, lock-in magnetotransport and electrothermal measurements of Pt/YIG heterostructures show that spin caloritronic effects such as the spin Peltier effect can modulate the Pt resistance, although the influence of the spin Seebeck effect needs to be evaluated in future experiments. An analytical multitemperature model for coupled spin and heat transport in the heterostructure is used to compute the temperature profiles and evaluate the spin-mediated heat flux at the Pt/YIG interface. Meanwhile, modulated BLS measurements are explored as a sensitive magnetometer to probe magnon injection due to the spin Hall effect in the Pt.

Table of Contents

List of Tables

List of Figures

Chapter 1

Introduction

One of the hallmarks of the last century was the development of the microprocessor, a technology that opened the doors for massive new industries and revolutionized the way people lead their lives. Such developments were enabled by advances in condensed matter physics and materials science, which teased out the requisite transport phenomena residing in clumps of atoms and established the scalable processing required to turn these atomic clumps into affordable consumer devices. Unfortunately, as one shapes these materials into devices and biases them into a state of driven activity, entropy rears its head causing these cold groupings of atoms to heat up. The beautifully clear and controllable signals observed at low temperatures become noisy as things jiggle about, scatter and diffuse. Switches become less switchable, pristine order melts into disorder, and the flow of energy, previously free and unimpeded, is stymied. The second law of thermodynamics imposes itself on this and all other forms of human activity and industry: relegating our endeavors to diminished simulacra of their theoretical greatness. One hopes, however, that there exist materials − certain configurations of atoms − that, with a little human intervention, can mitigate the second law and allow our creations to approach their telos. In particular, this means finding materials that enable the management of the heat that we generate in the activities of everyday life.

The study of energy transport in materials is applicable not only to microelectronics, where heat dissipation has been cited as one of the greatest barriers to continued advancement in the industry,[1,2] but also spans to the extremes of scale. From grid-scale power generation and transmission grappling with quads of rejected

energy[3] to qubits in quantum computers fighting decoherence at millikelvin temperatures,[4] transmission of energy in condensed matter holds the key.

Developing materials that can effectively transport energy requires a fundamental understanding of microscopic processes at play that contribute to transport. Classically, heat transfer in materials is described by Fourier's law of heat conduction, which relates the temperature gradient developed across a material in response to an applied heat flux by the phenomenological thermal conductivity (κ). For a given heat flux, a material with a higher κ develops a proportionally smaller temperature gradient as compared with a material with lower κ. On the macroscale, one can readily extract a value for κ via experiment, and that value neatly packages the requisite information on a material's thermal performance. However, as electronic devices are now routinely produced with characteristic length scales on the order of the relaxation lengths and wavelengths of the energy carriers − namely, lattice vibrations, magnetic excitations, and charge carriers − the importance of the microscopic energy transport picture becomes clear from an engineering perspective. Fortunately, the theoretical tools and experimental methods necessary to understand energy transport at the nanoscale have been growing to meet the shrinking size of our specimens for study.

Over the past several decades, great emphasis has been placed on reducing κ in order to develop superior direct energy conversion materials like thermoelectrics.[5,6] In contrast, this work seeks to advance the understanding of how energy can be efficiently transported inside materials by focusing on several examples of materials and material systems that achieve efficient and long-distance energy or spin transport in their own unique ways, studying the local nonequilibrium behavior that can arise in these materials, and developing sensitive techniques to probe the transport by the energy carriers.

In semiconductors and insulators, heat is predominately transmitted by vibrations in the atomic lattice, or phonons. In the early 1970s, Glenn Slack outlined a list of criteria necessary for achieving a high thermal conductivity by phonons.[7] Namely, such materials should have relatively simple crystal structure, have strong, stiff atomic bonding, low-mass atomic nuclei, and low anharmonicity. This pointed out diamond and other insulators with low-mass elements like cubic boron nitride (cBN), as well as some conductors like graphitic carbon. Chapter 2 describes what happens when energy carriers in a high thermal conductivity material, graphene, are

weakly coupled to one another. In a graphene sheet, an appreciable contribution to the thermal conductivity comes from the acoustic phonons that propagate in the plane of the sheet, with an out-of-plane polarization. These ZA phonons have long energy relaxation lengths because they are weakly involved in resistive scattering processes.[8] In Chapter 2, micro-Raman spectroscopy experiments are used to drive different phonon polarizations in suspended graphene out of local thermal equilibrium and measure their equivalent temperatures. The results are coupled with a first principles-based multitemperature model to show that graphene's ZA phonons are underpopulated in the focused laser heating experiments. Such nonequilibirum would reduce the contribution of the ZA modes to the thermal conductivity, and reduce overall heat spreading, which is of fundamental importance in graphene-based devices.

While Slack's criteria have pointed primarily to light-element compounds for realizing high phonon thermal conductivity, within the last decade, theoretical calculations have predicted the semiconductor boron arsenide (BAs), that contains light boron and heavy arsenic atoms, to achieve ultrahigh thermal conductivity at room temperature due to its unique phonon band structure. In Chapter 3, a new non-contact modulated Raman thermometry technique is developed to measure the ultrahigh thermal conductivity of BAs crystals, and validate BAs as the only semiconductor with ultrahigh thermal conductivity, having room temperature bulk values approaching 1000 $\mathrm{Wm^{-1}K^{-1}}$. Furthermore, a BAs microstructure is studied using a combination of microfabricated resistance heater/thermometers and the modulated Raman technique.

And lastly, the spin Hall effect (SHE) in heavy normal metals like platinum (Pt) has become an essential ingredient for the detection and interconversion of charge and spin-based currents. Coupled with the magnetic insulator yttrium iron garnet (YIG), which is capable of transporting pure spin currents over long distances without the capacitive effects of charge transport, SHE-based spin current transduction and the interfacial transport of spin and energy between the YIG and the metal is central to potential devices that are dependent upon spin-heat coupling. In addition, separation of spin Hall effects from other effects is necessary for the correct interpretation of measurements of the spin Seebeck effect (SSE) and reciprocal spin Peltier effect (SPE). Chapter 4 presents an analysis of spin and spin-mediated energy transfer

at the interface of Pt films and YIG crystals. First, an analytical model for coupled spin and heat transport in the heterostructure is developed. Using a sensitive Wheatstone circuit approach, lock-in electrothermal measurements then provide information about the phonon temperature in the Pt while amplitude-modulated micro-Brillouin light scattering (BLS) measurements directly probe the population distribution of magnons at the Pt/YIG interface. Harmonic analysis of the electro- and optothermal measurements, along with magnetic field dependence, allow separation of other spurious thermoelectric and magnetotransport effects, isolating the measured temperature and magnon frequency modulation at the first harmonic to either the SPE or Oersted fields. The amplitude-modulated approach developed here demonstrates BLS as a sensitive local and multifunctional magnetometer.

Materials that can effectively transport energy in the form of heat have important applications in heat spreading for thermal management. Meanwhile, those materials that can play host to magnetic excitations over long distances are applicable to devices that encode information in spin, such as computer memories, as well as classical and quantum logic architectures. The synthesis between these seemingly disparate fields lies in the burgeoning domain of spin caloritronics, which studies the relationship between heat, spin, and charge transport in materials. The remaining sections in this chapter are intended to provide a relevant introduction into heat, spin, and charge transport by phonons, magnons, and electrons in materials and at interfaces, with a focus on spin caloritronics.

1.1 Transport by Phonons, Magnons, and Electrons in Materials and Interfaces

Traditionally, devices have been restricted to the control of one or two energy carriers. Classical transistors manipulate electronic transport, producing heat as a byproduct. Meanwhile, thermoelectric materials utilize the coupling between heat and charge carriers to actuate the interconversion between heat and electricity. In effect, these excited energy carriers are the "working fluid" of the device. By leveraging the interactions between charge, spin, and thermal transport, spin caloritronics obtains an additional working fluid, and seeks new routes for functional devices. Mo-

tivated by several discoveries, including the spin Seebeck effect (SSE)[9] and the spin Peltier effect (SPE),[10] spin, charge, and heat coupling has yielded the generation and control of spin currents for spintronic applications in functional logic and memory devices, including thermally driven spin transfer torque[11,12], all magnon-based transistors and spin valves,[13–15] as well as potential new methodologies for direct energy conversion.[16–18] Because it involves charge, heat, and spin transfer, a spin caloritronic device is an ideal place to introduce transport by phonons, magnons, and electrons. Utilizing a material structure that is important in spin caloritronic experiments − the interface between a magnetic insulator and a heavy metal − as a framework, we will introduce the transport behavior of these various energy carriers, as well as some experimental techniques that are used to characterize them.

1.1.1 Heat and Spin Transport in a Magnetic Insulator

The classic depiction is that adding heat to a material causes its atoms to jiggle about. The energies levels of thermal vibrations of the atoms in a crystal lattice are discrete, and just as photons are the quanta of the electromagnetic field, we can describe phonons as quantized excitations of the atomic "elastic field" of the material. Phonons are generally the dominant heat carriers in semiconductors and insulators, and the thermophysical properties of these systems, like the thermal conductivity and specific heat can often be well-described by considering phonons alone. Magnetic materials, on the other hand, have an additional degree of ordering in their individual magnetic moments. Collective excitations in the magnetic ordering that lead to a change in net magnetization are called spin waves, and these spin waves can be quantized into quasiparticles called magnons. While phonons are perturbations that are restored by the strength of the bonds between atoms, magnons are perturbations that are restored by dipolar and exchange interactions between spins. Whereas phonons only carry heat, magnons can carry both heat and spin, i.e. the quanta of angular momentum. Coupling between phonons and magnons − that is, the interaction between the moving atomic lattice and the magnetic lattice plays an important role in spin caloritronics.

Lattice Dynamics: Prediction of Normal Modes

An important concept for understanding transport by elastic waves is the dispersion relation, which can be conveniently introduced with classical harmonic forces and Newton's equations of motion. Consider a model atomic lattice that consists of a one-dimensional (1D) chain of atoms. If atom number l in the chain is displaced from its equilibrium position by r_l, under the harmonic approximation, its potential energy is[19–21]

$$U_l = \frac{1}{2} C r_l^2 \tag{1.1}$$

The force on atom l is the derivative of the potential energy with respect to the displacement:

$$F_l = -\frac{dU_l}{dr_l} = -Cr_l \tag{1.2}$$

where C is the "spring constant" that represents the stiffness of the interaction between adjacent atoms. To make the model slightly more general, consider a 1D chain of alternating heavy and light atoms with masses M and m, respectively, as illustrated in Fig. 1.1. The equilibrium spacing between adjacent M atoms or adjacent m atoms is called the lattice parameter, a, and each adjacent M and m atom pair can be grouped together in a unit cell, which can be translated by integers of a to generate the crystal lattice.

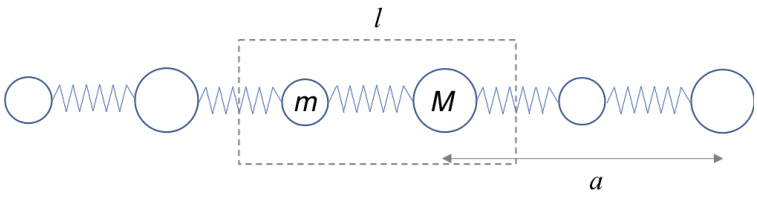

Figure 1.1: Schematic of a one-dimensional diatomic chain.

For heavy atoms with displacements r and light atoms with displacements u, relating Newton's second law to equation 1.2 yields two equations of motion (EOM):

$$\begin{aligned} M\frac{d^2 r_l}{dt^2} &= -C\left(u_{l-1} - r_l\right) - C\left(u_l - r_l\right) = -C\left(u_{l-1} - 2r_l + u_l\right) \\ m\frac{d^2 u_l}{dt^2} &= -C\left(r_{l-1} - u_l\right) - C\left(r_l - u_l\right) = -C\left(r_{l-1} - 2u_l + r_l\right) \end{aligned} \tag{1.3}$$

noting that only interactions between the nearest neighboring atoms are considered. To simulate a real (effectively infinite) crystal, we can apply periodic boundary conditions that wrap the 1D chain into a circle with circumference L. The solutions are of the form

$$\begin{aligned} r_l(x,t) &= re^{-i(\omega t - \boldsymbol{q}la)} \\ u_l(x,t) &= ue^{-i(\omega t - \boldsymbol{q}la)} \end{aligned} \tag{1.4}$$

where ω is the angular frequency of the oscillation, la defines the position, and the wavevector $\boldsymbol{q} = 2\pi n/L$ in which n takes a positive integer value up to the number of unit cells that fit within the length L. Plugging (1.4) into (1.3) yields the system of equations

$$\begin{bmatrix} M\omega^2 - 2C & C\left(1 + e^{-i\boldsymbol{q}a}\right) \\ C\left(1 + e^{i\boldsymbol{q}a}\right) & m\omega^2 - 2C \end{bmatrix} \begin{bmatrix} r \\ u \end{bmatrix} = 0 \tag{1.5}$$

Setting the determinant of the first matrix to zero, the solutions are

$$\omega^2(\boldsymbol{q}) = C\left(\frac{1}{M} + \frac{1}{m}\right) \pm C\left[\left(\frac{1}{M} + \frac{1}{m}\right)^2 - \frac{4\sin^2\frac{\boldsymbol{q}a}{2}}{mM}\right]^{\frac{1}{2}} \tag{1.6}$$

The result is that there are two real solutions for the frequency ω at each particular wavevector $\boldsymbol{q}$. These two frequencies are the normal modes of the system and are so-called because they are completely independent of one another. Plotted as a function of $\boldsymbol{q}$, the dispersion of the two normal modes for our 1D chain appear as two separate branches in Fig. 1.2. Because the second term in Eqn. (1.6) indicates that the frequency varies sinusoidally with $\boldsymbol{q}$, it is common practice to plot only $\boldsymbol{q}$ values that result in one full period of oscillation, usually $-\pi/2 < \boldsymbol{q} < \pi/2$, which is referred to as the first Brillouin zone.

The higher frequency branch shows the normal mode corresponding to out-of-phase vibrations between m and M atoms within a single unit cell and is often referred to as the optical branch because, in many materials, these vibrations are similar in frequency to and couple strongly with light. If one were to model a 1D chain that had more than two types of atoms in a single unit cell, the number of optical branches would increase with the number of unique atom types since there

is a proportional increase in the number of normal modes. Similarly, a crystal with only one unique atom in its basis, like elemental metals, has no optical branches in its dispersion.

Meanwhile, the lower frequency branch, or acoustic branch, represents the coherent motion of atoms in a unit cell. As the name implies, low-momentum acoustic phonons are responsible for carrying sound in materials. As the ratio m/M between the masses of the two constituent atoms decreases, the two normal modes move further apart in frequency. Thus, materials that have a large difference in the masses of their constituent atoms can be expected to have a large separation between their optical and acoustic normal modes. The slope of the different branches, the frequency change per wavevector change, has units of velocity. This is the so-called phonon group velocity and is much higher for the dispersive acoustic branch than for the flatter optical branch.

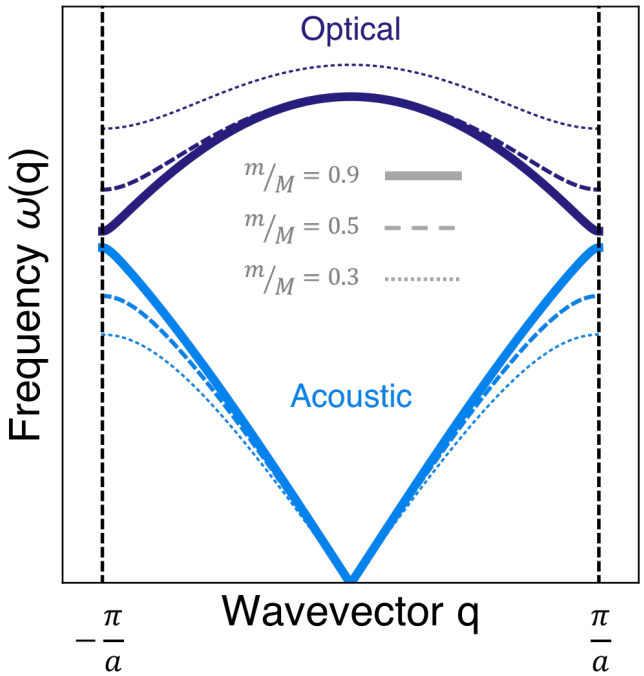

Figure 1.2: Dispersion of normal mode vibrations in a 1D diatomic chain for different atomic mass ratios, m/M.

The process detailed above is commonly used to predict the phonon dispersions in materials and is referred to as lattice dynamics (LD).[22] In LD, a parametrized

function − harmonic or otherwise − that approximates the potential energy of atoms in the lattice is used to calculate the forces on the atoms, and Newtonian mechanics with periodic boundary conditions is used to calculate the dispersion.

Molecular Dynamics and a Demonstration of Anharmonicity

In real materials, the potential that characterizes the atomic interaction is not harmonic. Intuitively, one would expect the interaction between two bonded atoms to diminish as they are pulled farther apart. This is indeed the case: the potential is no longer the perfect parabola of the harmonic case, but rather flattens out as the interatomic spacing is increased. This anharmonicity has implications for determining material properties and the normal modes, as is illustrated below using molecular dynamics.

While LD is particularly useful for calculating phonon dispersions in materials, it does not inherently capture the dynamical behavior of atoms in time, which is especially applicable for describing transport. An extension of LD, where the equations of motion are updated temporally, is called molecular dynamics (MD). MD solves the equations of motion for each atom l:

$$\begin{aligned} \dot{r_l} &= v_l \\ \dot{v_l} &= \frac{F_l}{m_l} \end{aligned} \tag{1.7}$$

where the time differentiation is done by a finite difference method over discrete time steps, Δt. Using a simple Verlet-type algorithm, the atomic velocities are calculated as[23]

$$\dot{r_l} = \frac{r\left(t+\Delta t\right) - r\left(t-\Delta t\right)}{2\Delta t} \tag{1.8}$$

To demonstrate this in practice, consider a 1D chain of three atoms, A, B, and C all with mass m. The potential characterizing the interactions between the atoms is either harmonic like Eqn. (1.2) or has been parametrized to be anharmonic like atoms in a real material. The harmonic potential case is illustrated in Fig. 1.3. When the atoms are at equilibrium, $r_{AB} = r_{BC} = r_0$. Starting from the equilibrium configuration, dynamics are initiated by perturbing atom C slightly and using the Verlet algorithm to integrate the equations of motion to obtain the updated atomic

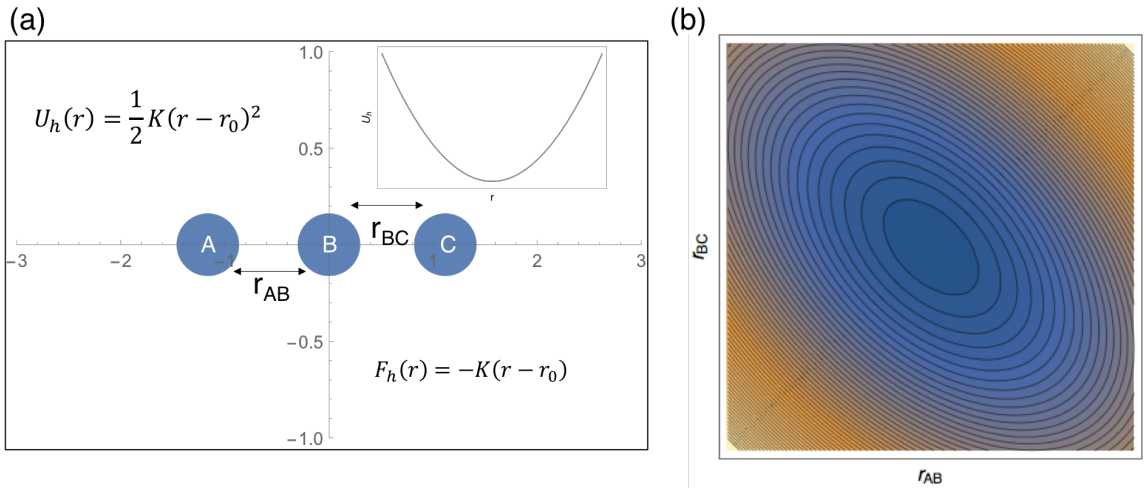

Figure 1.3: Harmonic potential for three-particle system. (a) Equilibrium positions of three atoms with spacings r_{AB} and r_{BC} and a plot of the harmonic potential (inset). (b) Contour plot of the potential energy surface for the three-particle system as a function of r_{AB} and r_{BC}.

positions and velocities in time. The interatomic spacings r_{AB}, r_{BC} during the MD simulation are shown by the black line in Fig. 1.4(a) overlaid on the potential energy surface contour plot. For this case, perturbing the position of atom C results only in a periodic change in r_{BC}. Meanwhile, Fig. 1.4(b) shows the resulting velocity of atom A in time. The linear reaction causes atom A to move in a perfect sinusoid, as evidenced by the single peak in the Fourier transform (FFT) of its velocity (Fig. 1.4(c)). To summarize, the perturbation of atom C causes only the distance r_{BC} to change, while atoms A and B move rigidly together, with distance r_{AB} remaining at equilibrium. The perturbation has excited a normal mode of the system, and there is no coupling between changes in r_{BC} to r_{AB}.

Let us now consider a more realistic potential by including anharmonicity. The Lennard-Jones (LJ) potential is an anharmonic potential that has been used to model non-covalently bonded systems and is frequently used as a didactic example[24]. It is given by

$$U_{LJ}(r) = 4\epsilon\left(\frac{\sigma^{12}}{r^{12}} - \frac{\sigma^6}{r^6}\right) \tag{1.9}$$

where ϵ and σ are constants. The three-particle system with the LJ potential is illustrated in Fig. 1.5.

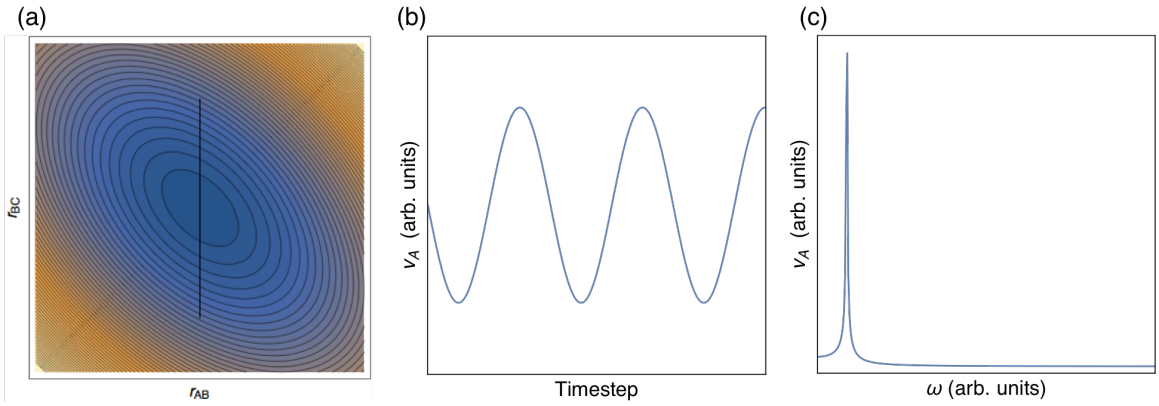

Figure 1.4: Harmonic positions and velocities. (a) The changes in r_{AB} and r_{BC} during the MD simulation (traced out by the black line) overlaid on the potential energy surface for the system. The collinear reaction caused by a perturbation of atom C from its equilibrium position causes only a periodic change in the separation r_{BC} while r_{AB} remains at equilibrium. (b) The velocity of atom A changes sinusoidally, indicated by the single fundamental frequency in the FFT (c).

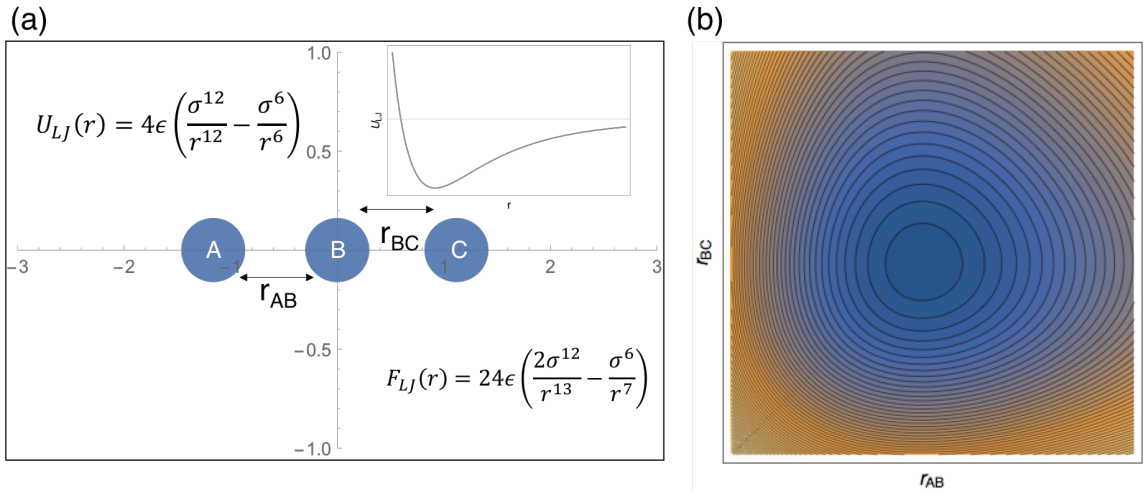

Figure 1.5: Lennard-Jones potential for three-particle system. (a) Equilibrium positions of three atoms with spacings r_{AB} and r_{BC} and a plot of the LJ potential (inset). (b) Contour plot of the LJ potential energy surface for the three-particle system as a function of r_{AB} and r_{BC}.

When dynamics are performed as with the harmonic potential case, a perturbation to atom C initiates a reaction that now causes both the spacings r_{AB} and r_{BC} to change in time (Fig. 1.6(a)). Additionally, the velocity of atom A is no longer a per-

fect sinusoid, but contains multiple frequency components as shown in Fig. 1.6(b,c). Instead of just exciting the single normal mode as in the harmonic potential, multiple vibrational modes are excited at different frequencies. Intuitively, one can say that the power input to initiate the collinear reaction must now be subdivided among multiple frequencies that result from anharmonic coupling that is inherent in the potential. On the other hand, all of the power goes into exciting one normal mode in the harmonically bonded system. Notice, too, that the system spends a larger fraction of its time the region where both r_{AB} and r_{BC} are larger than the equilibrium value, r_0. This result is equivalent to an expansion of the lattice, where anharmonically bonded atoms tend to spend more time farther apart when they are excited to an energy level so that they sweep out a larger portion of their interatomic potential. This is an illustrative example of the effects of anharmonicity, which plays a vital role in limiting energy transport and causing thermal expansion in real materials.

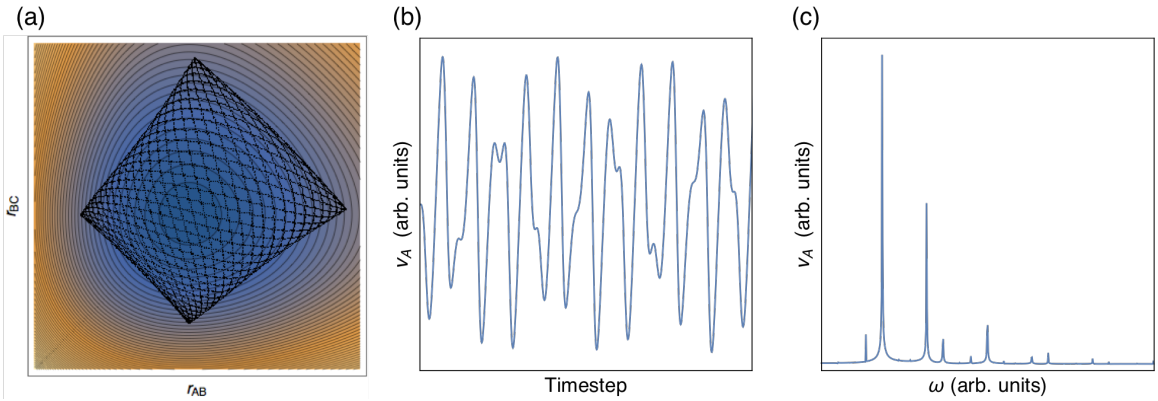

Figure 1.6: Lennard-Jones positions and velocities. (a) The changes in r_{AB} and r_{BC} during the MD simulation (traced out by the black dots) overlaid on the potential energy surface for the system.The collinear reaction caused by a perturbation of atom C from its equilibrium position causes a coupled change in both r_{AB} and r_{BC}. (b) The velocity of atom A changes periodically, but with higher higher-order frequency components indicated by the multiple harmonics in the FFT (c).

Magnetic Excitations

When atoms or ions have electronic configurations with a net, permanent magnetic moment, their magnetic moments can also order on a magnetic lattice. Materials

whose adjacent magnetic lattice sites have parallel magnetic moments are considered to be ferromagnetic. Meanwhile, materials with ordering of antiparallel magnetic moments of the same magnitude are antiferromagnetic, and those with antiparallel magnetic moments with different magnitude are ferrimagnetic. The magnetic insulator yttrium iron garnet (YIG) is a ferrimagnet; however, it is often modeled as a ferromagnet, with its ferrimagnetic character only becoming evident at elevated temperatures.[25] In equilibrium at zero temperature, the magnetic moments in ferromagnets all point exactly in the same direction, which is the direction of magnetization for the entire crystal and may be set by the application of an external field. However, as the temperature is increased, thermal fluctuations cause the magnetic moment vectors to deviate from their perfectly aligned configuration, reducing the net magnetization. Instead of spins completely flipping over one-by-one, a lower energy configuration is to distribute the melting of magnetic order via spin precession, where the individual magnetic moments each sweep out a conical solid angle that is centered around the net magnetization vector, $\vec{M}$. Shown schematically in Fig. 1.7, the mechanism by which the gyroscope-like motion of the individual magnetic moments reduce the total magnetization can be understood intuitively in the following way. As the temperature is increased, the magnetic moments sweep out a larger and larger cone. As the magnetic moments now have larger vector components that point away from the direction where they would all be perfectly aligned, their components along $\vec{M}$ are diminished, and the net magnetization of the crystal is reduced. As each magnetic moment $\boldsymbol{\mu}$ precesses about $\vec{M}$, an external magnetic field $\boldsymbol{H}$ will exert a torque $\boldsymbol{\tau} = \boldsymbol{\mu} \times \boldsymbol{H}$. This can be re-written in terms of the change of the net magnetic moment per volume, $\boldsymbol{M}$, in time as

$$\frac{d\boldsymbol{M}}{dt} = \gamma(\boldsymbol{M} \times \boldsymbol{H}) \tag{1.10}$$

where γ is the gyromagnetic ratio. Strong, short-range exchange interactions and weaker, but longer-range dipolar interactions between spins cause this behavior to be distributed through the magnetic lattice as a wave of precessing spins. Considering nearest-neighbor exchange interactions, the EOM for a spin $\vec{S} = \frac{\boldsymbol{M}}{|\boldsymbol{M}|}$ on ferromagnetic lattice site l is

$$\frac{d\vec{S}_l}{dt} = \left(\frac{2J}{\hbar}\right)\left(\vec{S}_l \times \vec{S}_{l-1} + \vec{S}_l \times \vec{S}_{l+1}\right) \tag{1.11}$$

where $\hbar$ is the reduced Planck's constant, and J is a measure of the strength of the interaction (in units of energy) between adjacent spins, called the exchange constant. This EOM forms the basis for spin waves. In real materials, however, spin precession does not continue indefinitely, but rather is dissipates over time, which limits the lifetime for spin waves. This was handled in a phenomenological fashion when Gilbert added a viscous damping-like parameter $0 < \alpha_G < 1$ to the Eqn. (1.10) as[26]

$$\frac{d\vec{S}}{dt} = \gamma(\vec{S} \times \boldsymbol{H}) + \alpha_G(\vec{S} \times \frac{d\vec{S}}{dt}) \tag{1.12}$$

which is commonly referred to as the Landau-Lifshitz-Gilbert (LLG) equation.

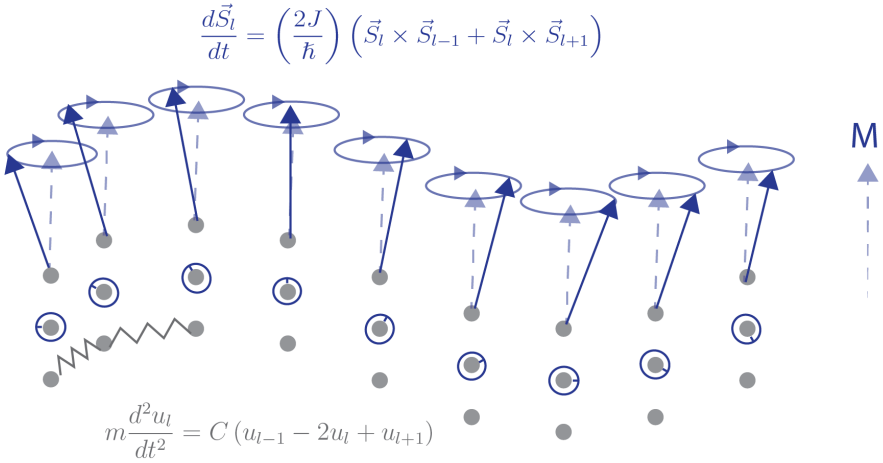

Figure 1.7: Schematic illustration of vibrational waves in an atomic lattice (gray) and spin waves in a ferromagnetic lattice (blue) that is coupled to the atomic lattice. The vibrational motion of atoms sitting on the atomic lattice are restored by the elastic strength of the interatomic bonds, whereas the precessional (gyroscope-like) motion of a spin on the magnetic lattice is influenced by torques applied by neighboring magnetic moments with an exchange constant, J, that mediates the interaction. The phase of the precessional motion marches forward by a set amount from one magnetic lattice site to the next, forming a spin wave that is distributed in space.

The EOM for spin precession in ferromagnets has wavelike solutions of the

form $a(r,t) = ae^{i(\boldsymbol{q}r-\omega t)}$ with frequency

$$\omega = \sqrt{\omega_H(\omega_H + \gamma\mu_0 M_0 \sin^2\theta)} \tag{1.13}$$

where ω_H is the spin wave frequency in response to a field $\boldsymbol{H}_0$, and $\sin^2\theta = (q_x^2+q_y^2)/q^2$ for a magnetic field along $\hat{z}$. Equation (1.13) describes the dispersion relation for magnetostatic, or dipolar spin waves in a ferromagnet. Meanwhile, spins are subject to interactions with their nearest neighbors by the exchange interaction, which applies an effective exchange field $\boldsymbol{H}_{ex}$ and modifies the spin wave frequency with an additional term that depends on the wavevector as $\omega_H + A\boldsymbol{q}^2$, where A is referred to as the exchange stiffness. The dispersion is then modified to

$$\omega(\boldsymbol{q}) = \sqrt{(\omega_H + \gamma A\boldsymbol{q}^2)(\omega_H + \gamma A\boldsymbol{q}^2 + \gamma\mu_0 M_0 \sin^2\theta)} \tag{1.14}$$

which includes both exchange and dipolar interactions. While the dispersion of lattice and spin waves can be described well with classical Newtonian EOMs, in crystals, these waves have discrete energy levels. The quanta of elastic waves are called phonons, while the quanta of spin waves are called magnons. Quantization implies that their frequency (ω) versus wavevector ($\boldsymbol{q}$) dispersion relation is equivalent to a dispersion of quasiparticles with discrete units of energy $\hbar\omega$ and pseudomomentum $\hbar\boldsymbol{q}$. Unlike phonons, however, magnons also carry quanta of angular momentum, $\hbar S$. The number of quasiparticles can be characterized by a population distribution, f, given by the Bose-Einstein distribution

$$f_{m,p} = \frac{1}{\exp\left[\left(\hbar\omega_{m,p} - \mu_{m,p}\right)/k_B T_{m,p}\right] - 1} \tag{1.15}$$

where μ is the chemical potential, k_B is the Boltzmann constant, T is the temperature, and the subscripts m, p refer to magnon or phonon, respectively. In equilibrium, $\mu_{m,p} = 0$ and (1.15) becomes the equilibrium Bose-Einstein distribution, n_0. A zero chemical potential implies that there is no energy penalty for creating or annihilating a quasiparticle and so the total particle number is not a conserved quantity. As the temperature T is increased, the number of magnons or phonons with energy $\hbar\omega$ and at particular wavevector $\boldsymbol{q}$ increases as well. In particular, an increase in T causes that quasiparticle mode to become more populated, and this effect plays a large role

in determining the temperature-dependent behavior of materials. The energy of a particular phonon or magnon mode is characterized by its population as

$$\epsilon_{m,p} = \hbar\omega_{m,p}\left(n_{m,p} + \frac{1}{2}\right) \tag{1.16}$$

where $\hbar\omega/2$ is the zero-point energy that arises out of the quantum harmonic oscillator solution for elastic and spin waves, which invokes the uncertainty principle. The term "mode" is used to denote a population of phonons or magnons at a particular $\boldsymbol{q}$ in the dispersion with a particular polarization.

Quantizing these excitations also helps to simplify the description of energy transport through the Boltzmann transport equation (BTE). In essence, the BTE provides bookkeeping for the changes to a population distribution in time and at a particular location by keeping track of mechanisms that can add to or subtract from the population distribution in real space ($\boldsymbol{r}$), momentum space ($\boldsymbol{q}$), and time (t). Since the individual particles carry energy and momentum, the BTE nicely encapsulates energy and mass transport due to changes in particle number. The BTE reads

$$\frac{\partial f}{\partial t} + \frac{d\boldsymbol{r}}{dt}\cdot\nabla_{\boldsymbol{r}} f + \frac{d\boldsymbol{q}}{dt}\cdot\nabla_{\boldsymbol{q}} f = \frac{\Delta f}{\Delta t} \approx \frac{f - f_0}{\tau} \tag{1.17}$$

where $\frac{\Delta f}{\Delta t}$ is the rate of change in particle population at point $\boldsymbol{r}$, $\boldsymbol{q}$ and is often considerably simplified by the relaxation time approximation (RTA) as $(f - f_0)/\tau$.[27] The RTA introduces a time τ that describes how long it takes a nonequilibrium particle distribution to relax back to the equilibrium distribution f_0. Various scattering mechanisms contribute in varying degrees to the relaxation rate $1/\tau$. During scattering events, magnons and phonons must obey energy and momentum conservation, for N number of states scattering into M number of states:

$$\begin{aligned} \hbar\sum_i^N \omega_i &= \hbar\sum_j^M \omega_j \\ \hbar\sum_i^N \boldsymbol{q}_i &= \hbar\sum_j^M \boldsymbol{q}_j \pm \boldsymbol{G} \end{aligned} \tag{1.18}$$

where $\boldsymbol{G}$ is a reciprocal lattice vector that can be equal to zero and $N + M = 2$, 3, or 4-particle scattering. In this way, magnons and phonons can exchange energy

and momentum during scattering events with one other, while also creating and annihilating new magnons and phonons. While the number of phonons is not a conserved quantity ($\mu_p = 0$), magnons may have a finite chemical potential under quasi-equilibrium conditions, meaning that the number of magnons is a conserved quantity and the magnon chemical potential is not necessarily equal to zero. In this case, it is useful to separate the types of scattering mechanisms that conserve particle number from those non-conserving scattering processes. Figure 1.8 and Table 1.1 summarize some of the number-conserving and non-conserving scattering mechanisms for magnons and phonons. Because magnons carry spin angular momentum in

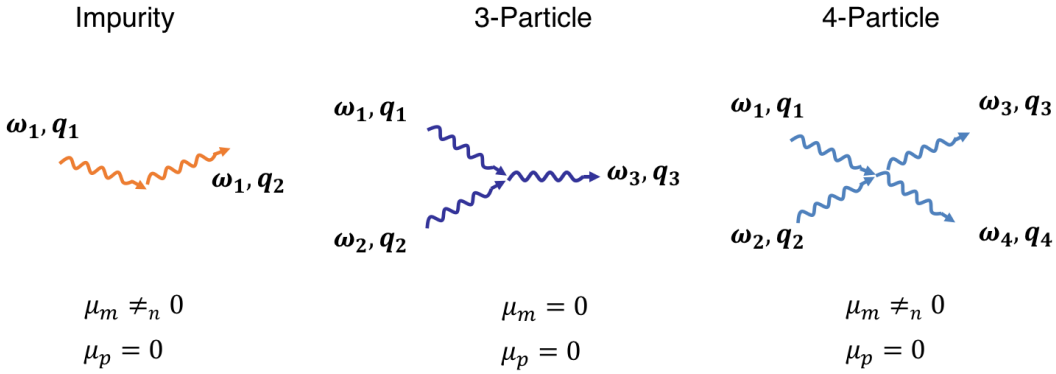

Figure 1.8: Illustration of different scattering mechanisms for magnons and phonons in a magnetic insulator. Impurity (2-particle) scattering can conserve particle number and energy, but results in a change in wavevector. Three-particle scattering does not conserve particle number, whereas four-particle scattering does, yet both types of scattering result in energy relaxation.

addition to energy and pseudomomentum, magnon number density is directly linked to the crystal's net magnetization. In particular, the net saturation magnetization per unit volume (V) of a ferromagnet as a function of temperature is

$$\boldsymbol{M}(T) = \boldsymbol{M}(0) - \frac{g\mu_B}{V}\sum_{\boldsymbol{q}} f_m(T,\ \boldsymbol{q}) \tag{1.19}$$

where $\boldsymbol{M}(0)$ is the saturation magnetization at zero temperature, g is the Landé g-factor, μ_B is the Bohr magneton, and the number of magnons n_m is summed over

Table 1.1: Magnon and Phonon Scattering Processes

Scattering Mechanism	**Conserve number?**	**Relax spin?**	**Remarks**
Impurity	Y	N	2-particle scattering
3-phonon	N	n/a	
3-magnon	N	Y	Only allowed for small $\boldsymbol{q}$ dipolar magnons
4-phonon	Y	n/a	
4-magnon	Y	N	Dominated by large $\boldsymbol{q}$ exchange magnons
Phonon-magnon	Y, N	N, Y	Can be number-conserving or non-conserving

$\boldsymbol{q}$. The quantity $g\mu_B$ describes how much each spin in a particular magnetic material contributes to the magnetization, and so as the number of magnons increases with increasing temperature, the net saturation magnetization of the crystal decreases. Thus, scattering processes that do not change the number of magnons preserve the net magnetization, while those processes that create (annihilate) magnons reduce (increase) the net saturation magnetization.

As discussed before, there are both dipolar and exchange interactions between spins in a ferromagnet. Strong exchange interactions occur over very short length scales on the order of the interatomic spacing, whereas dipolar interactions can act over longer distances, but are in general weaker. Therefore, in the long wavelength (small $\boldsymbol{q}$) regime, it is dipole interactions that dominate magnon transport, while exchange interactions dominate magnon transport in the short wavelength (large $\boldsymbol{q}$) limit.[25] Because three-magnon scattering is only allowed for dipolar magnons, scattering events that do not conserve magnon number, and therefore spin, are dominant for small $\boldsymbol{q}$ magnons. In contrast, and especially in YIG, four-magnon scattering dominates the exchange magnons at larger $\boldsymbol{q}$ values. These higher-energy magnons are populated only at elevated temperatures, and so spin-conserving four-magnon scattering may dominate over the three-magnon scattering that is limited to small-$\boldsymbol{q}$ magnons.[28] Both three-magnon and four-magnon scattering can relax energy, and so they both contribute to the energy relaxation rate $1/\tau_{m,\epsilon}$; however, only three-magnon scattering results in a relaxation of spin. Therefore, in ferromagnetic insulators such as YIG, there are two different timescales for energy relaxation ($\tau_{m,\epsilon}$) and for spin

relaxation ($\tau_{m,S}$). These can be recast into length scales as

$$\begin{aligned} l_{m,\epsilon}(\boldsymbol{q}) &= v_m(\boldsymbol{q})\tau_{m,\epsilon}(\boldsymbol{q}) \\ l_{m,S}(\boldsymbol{q}) &= v_m(\boldsymbol{q})\tau_{m,S}(\boldsymbol{q}) \end{aligned} \tag{1.20}$$

where v_m is the magnon group velocity. Because $\tau_{m,\epsilon}$ is shorter than $\tau_{m,S}$, the magnon spin relaxation length, $l_{m,S}$, can be significantly longer than the energy relaxation length at elevated temperatures.[29]

Phonons, in comparison, do not ordinarily carry spin angular momentum,[30] and so are parametrized only by the length scale over which they relax energy. Additionally, three-phonon scattering is not as restricted as three-magnon scattering, and it, in fact, occurs with a much higher probability than four-phonon scattering. Thus, the thermal energy transport in most materials can be described well by considering only three-phonon processes at room temperature and below. However, four-phonon scattering can play an important role in materials with large anharmonicity or uniquely engineered phonon band structures, such as high thermal conductivity BAs.[31–36]

Magnon and Phonon Thermal Conductivity

Both magnons and phonons can make contributions to the thermal conductivity of a material. A temperature gradient dT/dx applied across a material will cause a difference in the magnon and phonon number densities from one region of the material to the next. This gradient in particle number density naturally results in diffusion down the gradient. Since both phonons and magnons carry energy, i.e. they make some contribution to the material's specific heat, the diffusive flux of magnons or phonons results in a heat flux. In this particle picture, consider a distribution of particles in a material in with each carrying energy $\hbar\omega$ and traveling with velocity v_x in one dimension. Under the relaxation time approximation, each particle will carry its energy over distance $l_{\epsilon,x} = v_x\tau$ before relaxing its energy in a scattering event. Therefore the energy flux is given by the product of the particle velocity, the energy, and the number of particles per unit volume as

$$Q_x(x, \boldsymbol{q}) = \frac{1}{V} v_x \hbar\omega(\boldsymbol{q}) f(t, x, \boldsymbol{q}) \tag{1.21}$$

The distribution function $f(t, x, \boldsymbol{q})$ for magnons and phonons is given by the Bose-Einstein distribution. Under steady state conditions, both the temperature gradient dT/dx and the particle distribution function not vary in time. Since the Bose-Einstein distribution just depends on temperature, the distribution function in Eqn. (1.21) can be written in terms of the temperature gradient based on the Boltzmann transport equation as

$$f(x, \boldsymbol{q}) = f_0(x, \boldsymbol{q}) - \tau v_x \frac{df_0}{dT}\frac{dT}{dx} \tag{1.22}$$

where $f_0(x, \boldsymbol{q})$ is the equilibrium Bose-Einstein distribution. Inserting into Eqn. (1.21) yields

$$Q_x(x, \boldsymbol{q}) = \frac{1}{V} v_x \hbar\omega(\boldsymbol{q}) \left[f_0(x, \boldsymbol{q}) - \tau v_x \frac{df_0}{dT}\frac{dT}{dx} \right] \tag{1.23}$$

which describes the particular heat flux contribution by a particular phonon or magnon mode. By adding together contributions from all modes (all polarizations p and points along $\boldsymbol{q}$ in the dispersion), the total phonon or magnon heat flux can be obtained. When this is done, the heat flux Q_x is related to the temperature gradient dT/dx by a collection of terms

$$Q_x = -\frac{1}{V} \sum_{p,\boldsymbol{q}} \left[\hbar\omega(\boldsymbol{q}) v_x^2 \tau \frac{df_0}{dT} \right] \frac{dT}{dx} \tag{1.24}$$

and

$$\kappa_x = \frac{1}{V} \sum_{p,\boldsymbol{q}} \left[\hbar\omega(\boldsymbol{q}) v_x^2 \tau \frac{df_0}{dT} \right] = \frac{1}{V} \sum_{p,\boldsymbol{q}} \left[\hbar\omega(\boldsymbol{q}) v_x l_{\epsilon,x} \frac{df_0}{dT} \right] \tag{1.25}$$

is the thermal conductivity along the x direction for either magnons or phonons. Thus those modes that make an appreciable contribution in terms of (1) group velocity v_x, (2) specific heat $C(\boldsymbol{q}) = \frac{d}{dT}(\hbar\omega D(\omega) f(T, \omega))$, or (3) have a long relaxation time τ or length $l_{\epsilon,x}$ will make the dominate contribution to the thermal conductivity. For most insulators, κ is dominated by acoustic phonons with their high group velocities. In YIG, magnons neither have very high group velocities nor make a large contribution to the specific heat, and so their contribution to the thermal conductivity is almost negligible.[37] However, ultrahigh group velocity magnons have been shown to make the dominant contribution to thermal conductivity in some quasi-low dimensional antiferromagnets.[38–40]

1.1.2 Heat, Charge, and Spin Transport in a Normal Metal

Nonmagnetic heavy metals, e.g. platinum (Pt), are used extensively in spin-heat coupling experiments. In metals, charge- and spin-carrying electrons take the predominate role as energy carriers. By virtue of their lack of a band gap, metals have a large number of electrons above the Fermi energy that are available to transport heat, charge, or spin. That is to say, there is a large density of states (DOS) in the metal's conduction band. This DOS can be so high that the electrons can behave as "gas" of charged particles, or plasma, that interact over large distances by the Coulomb interaction, resulting in long-range behavior. Similar to magnons and phonons in the MI, this gas of electronic excitations in the metal can be driven to transport by diffusion, which is a statistical phenomenon where particles in a region with greater particle density tend toward regions with lower density. The non-uniform particle density can be driven by thermal gradients, where one region is at an elevated temperature and has a proportionally higher population, relative to the colder region. The electron population distribution is given by the Fermi-Dirac distribution

$$f_e = \frac{1}{\exp\left[\left(\epsilon_e - \epsilon_F\right)/k_B T\right] + 1} \tag{1.26}$$

where ϵ_F is the Fermi energy.

The Boltzmann transport equation under the linearized relaxation time approximation for electrons is

$$\frac{\partial f}{\partial t} + \underbrace{\frac{d\boldsymbol{r}}{dt} \cdot \nabla_{\boldsymbol{r}} f}_{\text{diffusion}} + \underbrace{\frac{\boldsymbol{F}}{m_e} \cdot \nabla_{\boldsymbol{v}} f}_{\text{forced}} = \underbrace{\frac{f - f_0}{\tau}}_{\text{collision}} \tag{1.27}$$

Given that each electron carries the elementary charge $-e$, they are subject to forces $\boldsymbol{F}$ mediated by the Coulomb interaction. As before, contributions to τ are added in parallel and can come from a variety of sources, including electron-electron scattering, electron-phonon scattering, and scattering by impurities. In addition, a spatial gradient in electron distribution generates a gradient in the electrochemical potential $\nabla\Phi$, that includes contributions from the electrostatic and chemical potential. When the chemical potential gradient is zero, the gradient in the electrochemical potential yields the electric field $-\nabla\Phi = \boldsymbol{E}$When the gradient in the electron popula-

tion distribution is caused by diffusion down a temperature gradient, this is referred to as the Seebeck effect, and physically represents the entropy carried per conduction electron. The Seebeck effect and other coupled charge-heat transport phenomena are referred to broadly as thermoelectric effects. The charge and energy currents that develop in response to gradients are often written as relating to phenomenological thermoelectric transport coefficients. These charge and heat current densities, J_c and J_Q are expressed as[19,41]

$$\begin{aligned} J_c &= L_{11}\nabla\Phi - L_{12}\nabla T \\ J_Q &= L_{21}\nabla\Phi - L_{22}\nabla T \end{aligned} \tag{1.28}$$

where L_{ij} are phenomenological coefficients. In the 1930s, Onsager showed that these transport coefficients obey the reciprocity relation $L_{ij}T = L_{ji}$.[42,43] The experimentally relevant transport coefficients like electrical conductivity (σ), Seebeck coefficient (α), and electronic thermal conductivity (κ_e) can be determined from various measurements where J_c, J_Q, $\nabla\Phi$, and ∇T are controlled parameters as

$$\begin{aligned} \sigma &= L_{11} \\ \alpha &= L_{12}/L_{11} \\ \kappa_e &= L_{22} - L_{21}\alpha \end{aligned} \tag{1.29}$$

and so (1.28) becomes

$$\begin{aligned} J_c &= \sigma(\nabla\Phi - \alpha\nabla T) \\ J_Q &= \Pi J_e - \kappa\nabla T \end{aligned} \tag{1.30}$$

where the $\Pi = \alpha T$ is the Peltier coefficient and is obtained from Onsager reciprocity of the Seebeck coefficient. The Peltier effect is the generation or absorption of heat that is proportional to a charge current flowing through a material. In addition, currents flowing through a conductor will generate irreversible heating due to the interaction of the charge carriers with the atomic lattice. This is referred to as Joule heating and is proportional to J_c^2. The total combination of reversible and irreversible heat production caused by charge current flow in a conductor was originally written by Domenicali as[44]

$$\frac{J_c^2}{\sigma} + \nabla\cdot(\kappa\nabla T) - TJ_c\cdot\nabla\alpha = 0 \tag{1.31}$$

in which the first term is the irreversible Joule heating, the second term is the irreversible flow of heat down the temperature gradient (Fourier's law), and the last term is the production or absorption of heat due to Peltier/Seebeck effect. An additional term due to the Thomson effect − irreversible heat flow down a temperature gradient − should be added to (1.31) for completeness: $\beta J_c \nabla T$, where β is the Thomson coefficient. The electrical conductivity $L_{11} = \sigma$ can be phenomenologically related to the electronic thermal conductivity as

$$\frac{\kappa_e}{\sigma} = \frac{k_B^2}{e^2} LT \tag{1.32}$$

in which k_B is the Boltzmann constant, and L is a dimensionless value called the Lorenz number. Wiedemann and Franz showed that L is roughly constant for a variety of common metals. Therefore, at a given temperature, a metal with high σ (low resistivity), can be expected to have a proportionally higher electronic thermal conductivity.

Magnetic Field-Dependent and Spin-Dependent Transport

In addition to carrying charge and energy, electrons carry quantized angular momentum that is comprised of both orbital and intrinsic contributions. The latter of which is referred to as spin. This spin has two possible states, $\pm\hbar/2$, often referred to as spin-up and spin-down. Ordinary paramagnetic metals have the same density of states for up-spins as for down-spins and so the average net spin of the conduction electrons is zero. In spite of this, paramagnetic metals can still transport spin-polarized currents over a limited distance, called the spin diffusion length, before the spin polarization is averaged out. In the presence of a magnetic field, the transport behavior of a metal's electron gas can be altered. The Lorentz force results in transverse acceleration on moving charges. For negatively charged carriers traveling with a velocity v_x along the x-direction, a magnetic field applied along the y-direction, B_y, will apply a force along $-z$: $\boldsymbol{F}_z = -ev_x \times B_y$. In a current-carrying conductor, this means that a transverse magnetic field deflects the charge carriers to one side, creating a potential difference perpendicular to the current flow, as shown in Fig. 1.9(a). This is known as the Hall effect, and it can be probed by measuring the transverse voltage that develops in the presence of a magnetic field.

In a ferromagnetic conductor, an electron current feels additional transverse forces that depend on the electron spin, with opposite spin polarizations feeling oppositely-directed forces. Since the charge current in a ferromagnetic conductor is spin-polarized and dependent on the magnetization direction, these forces cause an unequal distribution of the spin-polarized electrons to be sent to one side, also causing a transverse voltage to develop (Fig. 1.9(b)). This is referred to as the anomalous Hall effect (AHE) and arises predominately from the interaction between electrons' orbital and spin angular momentum, both intrinsically between and during scattering events.[45,46] A variety of phenomena have been identified as possible sources for the transverse spin-dependent interactions, including extrinsic side-jump scattering [47] and spin-skew scattering,[48] as well as intrinsic mechanisms such as the spin-orbit interaction yielding a non-zero Berry curvature in the band structure.[49,50]

This effect may be present in normal metals, too, but since they do not sustain spin-polarized currents, the spin-dependent transverse forces do not result in a voltage. Instead, it results in a segregation of electrons purely by their spin polarization, resulting in a transverse spin current with no net charge (Fig. 1.9(c)). This mechanism was identified by D'yakanov in the 1970s[51] and eventually referred to as the spin Hall effect (SHE) by Hirsch in the 1990s.[52] The SHE has been found to be strongest in metals that exhibit strong interactions between their electrons' orbital and angular momenta, or spin-orbit coupling. In general, these tend to be heavier metals like Pt, Ta, or W. The strength of the SHE is measured by the fraction of an ordinary charge current that the SHE can transduce into a pure spin current. Often called the "spin Hall angle", it is defined as $\Theta_{SH} = \frac{e}{\hbar}\frac{\sigma^c_{xx}}{\sigma^s_{xz}}$, where σ^c_{xx} is the longitudinal charge current conductivity and σ^s_{xz} is the transverse spin current conductivity, or spin Hall conductivity.[53]

1.1.3 Coupled Transport at a Metal/MI Interface

When a spin current-carrying conductor is placed in close proximity to a magnetic insulator, the carriers in the two different materials become free to exchange energy and spin angular momentum. Predominately, the flux of energy between the metal and MI is carried by acoustic phonons that are transmitted across the interface. Given that the two materials may have different phonon spectral properties, there is

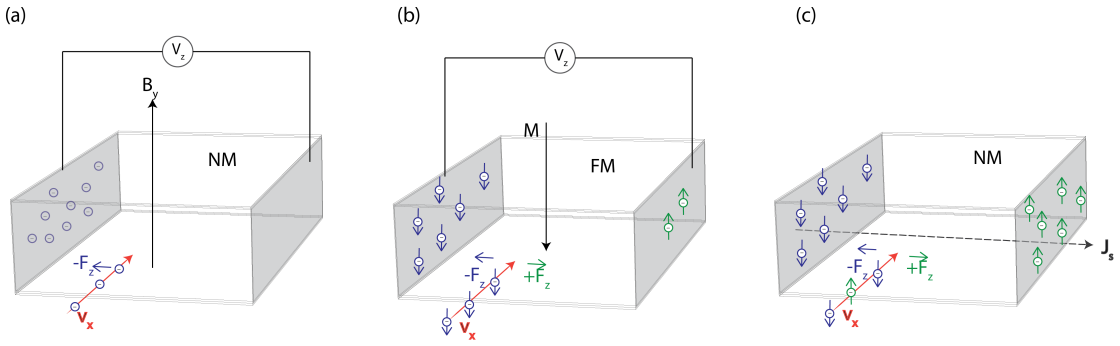

Figure 1.9: Schematic illustration of (a) the Hall effect in a normal metal (NM), (b) the anomalous Hall effect in a ferromagnetic metal (FM) with magnetization M along $-y$, and (c) the spin Hall effect in a NM.

an thermal resistance associated with the interface called the Kaptiza resistance that results in a temperature drop between the two materials. Referring back to Eqn. (1.31), in the Pt, the phonons can be appreciably heated through electron-phonon interactions by irreversible Joule heating by the electron current and electron diffusion down the thermal gradient. In addition, the Pt phonons can be heated or cooled by the Peltier effect. A phonon heat flux across the interface from the Pt will result in a temperature rise of the phonons in the MI.[54–56]

In addition, the presence of the spin degree of freedom in both the metal and the MI facilitates the exchange of spin angular momentum between the two. Since angular momentum is a vector quantity, the exchange is highly dependent on orientation. When a transverse spin current J_s is generated in a metal (M1) that is adjacent to another conductor (M2), the spin-polarized conduction electrons that make up J_s are free to enter the conduction band of M2. In the case where there is no net transfer of charge, the outflow of an electron from M1→M2 must be balanced by an inflow of an electron from M2→M1. While no net charge is transferred, there is still the possibility for the net transfer of spin angular momentum given by the difference in spin polarization between the outflowing and inflowing electrons. The resulting transfer of angular momentum exerts a torque on the magnetization, $\vec{\tau} = -\boldsymbol{M} \times I_s \times \boldsymbol{M}$, from one set of spins to another that is proportional to the spin current.[57] This spin transfer torque (STT) modifies the magnetization dynamics and adds a source term to the LLG equation: $\left(\frac{\partial \boldsymbol{M}}{\partial t}\right)_{torque} = \frac{\gamma}{\boldsymbol{M}_s}\boldsymbol{M} \times I_s \times \boldsymbol{M}$.[57,58]

Now consider the case for a heavy NM film (e.g. Pt) on a MI (e.g. YIG). Shown

schematically in Fig. 1.10, the spin Hall effect generates a transverse spin current and a "spin accumulation" at the MI interface. Because the insulating YIG cannot accept the transfer of electrons from the Pt, they are scattered at the interface. Some of these scattering events result in Pt electrons flipping their spin polarization direction (Fig. 1.10(b)). Conservation of angular momentum during spin-flip scattering is maintained by the transfer of spin to the magnons in the YIG, resulting in change in the magnon population and thus the local magnetization. The changing magnon population is equivalent to heating or cooling depending on the orientation of the YIG magnetization relative to the orientation of the Pt electron spin polarization vectors. The spin-flip mediated interaction between the Pt electrons and the YIG magnons can facilitate the exchange of energy between the two materials. When the two vectors are orthogonal, the spin current applies a torque on the YIG magnetization direction, but does not affect the magnetization magnitude or the magnon population. When the electron spin polarization vectors in the Pt and the magnetization direction in the YIG are parallel or antiparallel, the transfer of energy with the magnons is maximized with the heat current exchanged following the relation $J_q \propto J_c \times \boldsymbol{M}$. This spin-mediated transfer of energy has been termed the spin Peltier effect (SPE).[10,59,60]

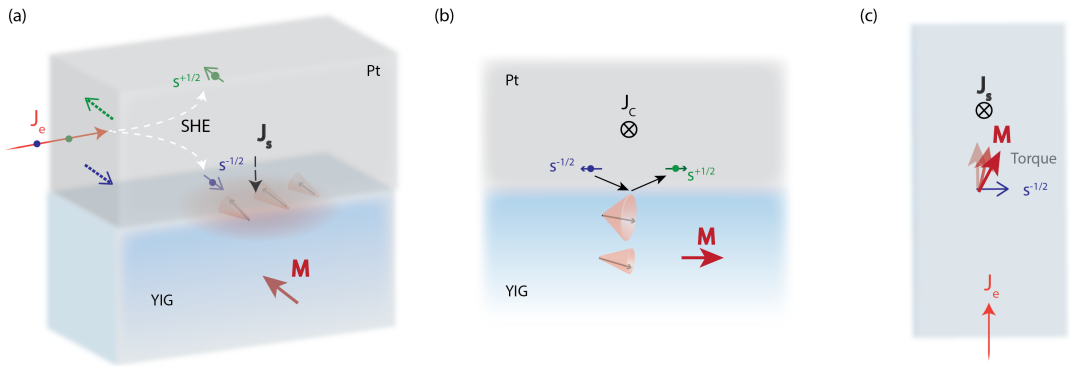

Figure 1.10: Schematic illustration of (a) the spin Hall effect injecting spin angular momentum from Pt into YIG. (b) A cross-cut view that shows the spin-flip scattering mechanism and the resulting change in the YIG magnetization. (c) Top-down view showing the torque applied to the YIG magnetization when the spin polarization vector and is orthogonal to $\boldsymbol{M}$.

The reciprocal of the SPE, the spin Seebeck effect (SSE), has enjoyed greater

study over a longer time compared to the SPE. The SSE is the generation of a spin current in response to a temperature gradient (∇T) and was first thought to have been observed a decade ago by Uchida in a $Pt/Ni_{81}Fe_{19}$ structure with an in-plane collinear ∇T and magnetic field.[61] The expectation was that in-plane ∇T was driving an in-plane diffusional spin current in the ferromagnetic metal film that was then able to be detected by the inverse spin Hall effect (ISHE) in the Pt electrodes; however, the measurements were complicated by temperature gradients between the $Pt/Ni_{81}Fe_{19}$ and the possibility of additional thermoelectric effects. Uchida subsequently confirmed the SSE a couple years later in Pt/YIG structures where the applied ∇T was applied across the interface between the Pt and the magnetic material, and orthogonal to the magnetization in the YIG.[9] The discovery of both the SSE and of the utility of the SHE/ISHE have driven forward the field of spin caloritronics, as well as spin current manipulation in magnetic insulators.

1.1.4 Experimental Techniques

As outlined in the above discussion, there are a limited number of experimentally observable quantities that can be measured to quantify spin caloritronic effects; namely, temperature, voltage, and magnetization. The purpose of this section is to briefly outline some of the experimental techniques used to observe these quantities as applied to spin caloritronics.

Electrical Detection

Perhaps the first major confirmation of a coupled spin, heat, and charge phenomenon was offered by the detection of the spin Seebeck effect (SSE) in Pt/YIG.[9] Here, a temperature gradient across the Pt/YIG interface drove a diffusive spin current from the YIG into the Pt film. The transverse spin current J_s with spin polarization vector $\vec{s}$ parallel to the YIG magnetization was then partially converted into longitudinal electric field by the inverse spin Hall effect (ISHE) in the Pt as $\boldsymbol{E}_{ISHE} = (\Theta_{SH}\rho_{Pt})J_s \times \vec{s}$, where ρ_{Pt} is the platinum electrical resistivity.[62] The detected voltage signal in a SSE measurement is given by[37,63]

$$V_{SSE} = C_{MI}\Delta T_{m-e} G_r \Theta_{SH} \rho \Delta x \eta \frac{\lambda}{l} \tanh \frac{l}{2\lambda} \tag{1.33}$$

where C_{NM} contains the physical properties of the MI and ΔT_{m-e} is the temperature difference between electrons in the NM and magnons in the MI. Additionally, G_r is the real component of the spin-mixing conductance of the interface, λ is the spin-flip diffusion length, l is the film thickness, and Δx is the distance between the voltage probes. The term η is called the backflow correction factor, given as $\eta = \left[1 + G_r \rho \lambda \coth \frac{l}{\lambda}\right]^{-1}$. Since its discovery, the ISHE has been an essential mechanism for allowing the electronic detection of spin currents. SSE/ISHE-based measurements have been extended to nonlocal geometries where a spin current injected into a magnetic insulator by the spin Hall effect[64] or by laser heating[65] and the resulting laterally diffusing spin current in the YIG is detected some distance away using the ISHE in a separate NM transducer line. The sensitivity of these measurements is improved using lock-in detection.

Measurement of the modest temperature changes caused by the reciprocal SPE, however, has fundamentally been more difficult than SSE measurements. The first report of the SPE in Pt/YIG by Flipse utilized a thermopile device consisting of a series of microfabricated thermocouples.[10] Measurements of the changing electrical resistance in the metal films can also provide a considerable amount of information on both temperature and magnetization. Resistance thermometry is a particularly sensitive technique that is able to distinguish small temperature changes. In the high temperature limit, the resistivity of a nonmagnetic metal is sensitive to the temperature of acoustic phonons as described by the Bloch-Grüneisen relation[19]

$$\rho(T) = g_{ep} \frac{T^5}{\Theta^5} \int_0^{\Theta_D/T} \frac{x^5}{(e^x - 1)(1 - e^{-x})} dx \tag{1.34}$$

where g_{ep} is the electron-phonon coupling parameter and Θ_D is the Debye temperature.

In magnetic conductors, the resistivity is dependent on the orientation of the magnetization, an effect which is generally referred to as magnetoresistance (MR). A variety of MR effects have been observed that show unique dependence on the angle of an applied magnetic field and can be used to characterize the magnetotransport behavior.[66–68] In NM/MI structures, meanwhile, there is a nonlocal MR effect in the NM that results from the spin Hall effect and spin angular momentum transfer between the two, called spin Hall magnetoresistance (SMR).[63,69,70] SMR arises arises

when the SHE generates a spin current in a NM film that travels normal to the film thickness with spin polarization vectors parallel to the film surface. As the spin current attempts to enter a neighboring MI, it is reflected back from the surface into the NM film, which results in the spin accumulation near the surface. The reflected current, however, can also generate a resistance modulation in the NM caused by the ISHE. The reflection of the spin current back into the NM and the subsequent voltage modulation by the ISHE is dependent on the magnetization direction of the MI and has been termed the spin Hall magnetoresistance. When the magnetization of the adjacent MI is perpendicular to the spin polarization of the spin current, the spin current may be absorbed at the interface of the metal and the MI by the transfer of angular momentum, which applies a torque on the magnetization of the MI, minimizing the reflected spin current. On the other hand, when the magnetization and spin polarization are parallel, a small fraction of the spin current is absorbed at the interface and so the reflected spin current is larger. The ISHE then converts this reflected spin current into a voltage that reduces the resistance. SMR can thus be summarized as a coexistence of the SHE/ISHE in the NM film, whose signal is dependent on the magnetization direction of an adjacent ferromagnet.

Lock-in Infrared Thermography (LIT)

For measurements close to room temperature where infrared thermal emission is appreciable, temperature modulations in NM/MI heterostructures resulting from spin caloritronic effects have been observed by means of lock-in infrared detection. In these measurements, a sensitive calibrated infrared camera monitors the emission change of a device that is coated with a highly emissive substance to homogenize the emissivity as a modulated charge current is passed through it. By collecting infrared emission maps at the harmonics of the modulated current frequency over many measurement cycles, the temperature sensitivity can be improved into the mK range. This technique has recently been used to characterize the SPE in Pt/YIG, [59] W/YIG, Au/YIG, and Pt/Al_2O_3/YIG[71], as well as to separate the SPE from the anomalous Ettingshausen/Nernst effect (AEE/ANE) in Pt/YIG and FePt/Si based on the magnetic field dependence of the two effects.[72] These will be discussed in greater detail in Chapter 4, but the Nernst and Ettingshausen effects are reciprocal effects that develop in conductors when a flowing charge current, temperature gradient

∇T and magnetic field $\boldsymbol{B}$ or magnetization $\boldsymbol{M}$ are all orthogonal to one another. In particular, the Ettinsghausen effect generates a heat flux $Q_E = NT\boldsymbol{B} \times \boldsymbol{J}_c$, where N is the Nernst coefficient. In addition, LIT has recently been employed to observe the anisotropic magneto-Peltier effect (AMPE) in nickel.[73] The AMPE is the dependence of the local Peltier coefficient in a ferromagnetic metal on the angle between a charge current and the metal's magnetization and can result in Peltier cooling in the absence of a junction with another conductor with a different Peltier coefficient.

Ferromagnetic Resonance (FMR)

Ferromagnetic resonance (FMR) is a spectroscopic technique that is extremely important in characterizing the aforementioned Gilbert damping, and thus spin wave transport, in ferromagnetic materials. Its principle of operation relies on the asymptotic nature of the frequency-dependent magnetic susceptibility $\chi = \boldsymbol{M}/\boldsymbol{H}$. The susceptibility for a ferromagnet is

$$\chi = \frac{\chi_0}{1 - (\omega/\omega_0)^2} \tag{1.35}$$

where $\omega_0 = \omega_0(\boldsymbol{H}_{ext})$ is the resonance frequency that depends on the applied external field.[74] Ferromagnetic resonance occurs when $\omega \to \omega_0(\boldsymbol{H}_{ext})$, causing Eqn. (1.35) to diverge. Experimentally, this is realized by applying an excitation source with frequency $\omega/2\pi$ usually in the microwave (GHz) range to a ferromagnetic specimen by means of an antenna. By sweeping an external applied magnetic field, the field-dependent resonant frequency can be tuned so that $\omega \to \omega_0(\boldsymbol{H}_{ext})$. This is because the FMR frequency is field-dependent as described by the Kittel equation $\omega_0(\boldsymbol{H}_{ext}) = \gamma\sqrt{\boldsymbol{H}_{ext}(\boldsymbol{H}_{ext} + \boldsymbol{M}_s)}$, where $\boldsymbol{M}_s$ is the saturation magnetization. When the resonance condition is met, the material absorbs a great deal of electromagnetic radiation from the excitation source, creating a lot of magnons, and resulting in a large dip in the transmitted microwave spectrum. This results in the driven generation of a large population of spin waves with frequency ω in the material. Using a microwave spectrum analyzer, the line width of the peak (in units of magnetic field) can be measured. Generically, the field-swept line width is related to the damping

parameter α_G as[75]

$$\Delta \boldsymbol{H} = \Delta \boldsymbol{H}_0 + \frac{2\alpha_G \omega}{\mid \gamma \mid} \tag{1.36}$$

FMR measurements have revealed the low damping parameters in bulk and thin film YIG crystals[76,77], and have additionally been used to investigate the spin-flip diffusion length and spin Hall angle in Pt on magnetic cobalt[78] and spin pumping from the spin Hall effect at NM/YIG interfaces.[79]

Nitrogen Vacancy (NV) Center Magnetometry and Thermometry

Naturally occurring in carbon diamond, nitrogen-vacancy (NV) centers are a pair of adjacent point defects in the diamond crystal structure. NV centers consist of a nitrogen atom sitting on one of the carbon atom sites which is next to a vacant site, as shown in Fig. 1.11. NV centers can be found in natural diamond, as-grown in synthetic diamond, or artificially introduced by ion implantation.[80]

This coupled NV center in the C diamond environment acts like a molecule with discrete energy levels that are dependent on the NV center's spin state. NV centers exist in a charge neutral (NV^0) and negative (NV^-) configuration, which have different electronic structures. Figure 1.11(b) shows the electronic structure for a NV^- center. Upon excitation by a 532 nm laser, the excited states can decay by emitting photons, which can be measured by photoluminescence (PL) microscopy. In the PL spectra, there is a so-called zero phonon line (ZPL) that corresponds primary transition energy between the ground and excited state. In the the NV^- case, the ZPL corresponds to a wavelength of 638 nm. Other PL features may be observed relating to the ground and excited spin triplet states. The ground spin triplet state is split into three spin sublevels with a splitting between the lower one and the degenerate upper two of 2.87 GHz, which is called the zero-field splitting energy. The lower sublevel corresponds to an electron spin quantum number of $m_s = 0$, while the upper two are degenerate and correspond to $m_s = \pm 1$. In the presence of a magnetic field B, however, Zeeman splitting causes these upper two states to split in energy by $2\gamma B$, where γ is the electron gyromagnetic ratio. This magnetic field-dependent splitting can be observed in optically detected magnetic resonance (ODMR) experiments, which are functionally similar to FMR measurements.[81] In ODMR, the PL spectra from a NV center are measured while an external microwave

field is swept in frequency. When the microwave frequency reaches resonance with the zero field splitting transition (2.87 GHz for NV^-), there is a dip in the fluorescence intensity. By applying an external field, two dips at different microwave frequencies can be seen that correspond to the $m_s = 0 \rightarrow -1$ and the $m_s = 0 \rightarrow +1$ transitions. The splitting between the two observed dips in the ODMR spectra resulting from the ± 1 spin state splitting is extremely sensitive to the local magnetic field, temperature, and strain.

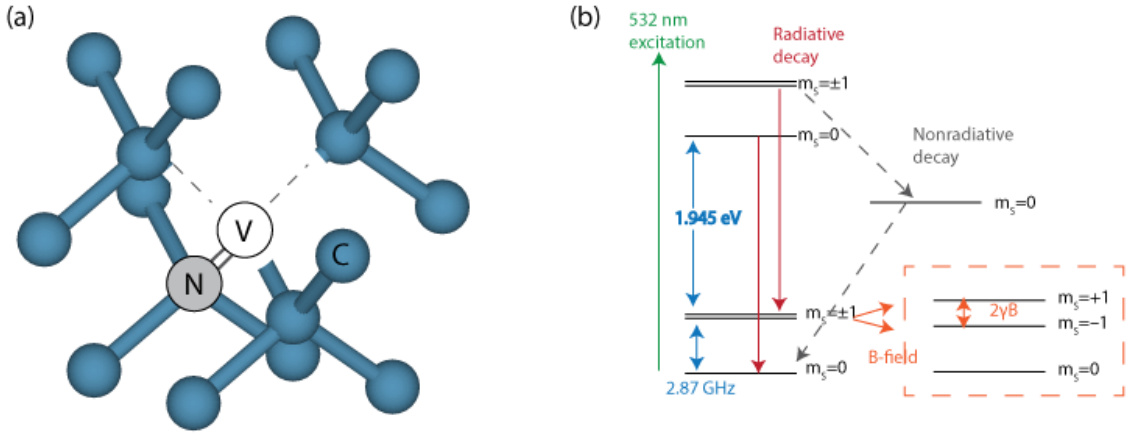

Figure 1.11: (a) Nitrogen-vacancy center defect in the crystal structure of diamond. (b) Electronic structure for a NV^- center showing the optical transitions, zero phonon line (ZPL) at 1.945 eV (638 nm), as well as the zero-field splitting of the ground state (2.87 GHz) and the field-dependent Zeeman splitting, $2\gamma B$, in the ground state triplet.

Fiducial NV centers have also been used as sensitive nanoscale magnetometers[82] and temperature sensors.[83] NV centers placed in close proximity to magnetic materials such as YIG have been used to directly detect spin waves, citing potential applications in quantum information buses[84]. In addition, NV centers have been used to quantify the magnon chemical potential in microwave YIG devices, finding that it can be tuned by driving the system's FMR.[85]

Brillouin Light Scattering Spectroscopy (BLS)

While FMR spectroscopy probes the interaction between microwave photons and spin waves in a ferromagnetic material, both magnons and phonons can interact strongly with visible light as well. Inelastic light scattering spectroscopies including

Raman spectroscopy and Brillouin light scattering spectroscopy (BLS) have become a popular method for directly characterizing the energy and populations of equilibrium and nonequilibrium phonons and magnons in materials. In particular, BLS has proven to be a powerful technique for investigating spin waves. Quasiparticle excitations like magnons and phonons make small perturbations to a material's dielectric susceptibility tensor that vary both in time and in space. These time- and space-varying perturbations in the material can then mediate interactions with the electric field and magnetic field components of incoming photons. Through this process, incoming light can exchange energy and momentum with the material by creating or annihilating quasiparticles, referred to as a Stokes process and anti-Stokes process, respectively. The exchange of energy and momentum can be written as

$$\begin{aligned} \hbar\omega_{out} &= \hbar(\omega_{in} - \omega_e) \text{ (Stokes)} \\ \hbar\omega_{out} &= \hbar(\omega_{in} + \omega_e) \text{ (anti-Stokes)} \\ \hbar\boldsymbol{k}_{out} &= \hbar(\boldsymbol{k}_{in} \pm \boldsymbol{q}_e) \end{aligned} \tag{1.37}$$

where e refers to the material excitation. Both Raman and BLS measure the energy shift of outgoing photons from from Stokes or anti-Stokes scattering events relative to the energies of incident photons from a coherent light source. Raman experiments typically probe excitations with frequencies in the 300 GHz to 10s of THz range, usually corresponding to higher energy optical phonons in materials. Meanwhile the Brillouin scattering process involves much lower energy acoustic phonons and magnons with frequencies in the GHz range.[86] To achieve an adequate spectral resolution with energy shifts so near to the laser frequency, a standard diffraction grating-based spectrometer approach is insufficient to measure Brillouin-scattered light. Instead, an interferometric approach is often taken, whereby a scanning Fabry-Pérot interferometer cavity is used to select for different frequencies of light around the laser frequency and the intensity is measured by a colorblind photon counter when the cavity allows a certain frequency of light to pass. A Fabry-Pérot (FP) interferometer consists of an optical cavity made up by two parallel mirrors with spacing L. In an ideal FP cavity, light of wavelength λ will only be transmitted through the cavity when the constructive interference condition $L = n\lambda/2$ is met, where n is an integer. That is, light is transmitted when an integer number of half wavelengths can fit within dis-

tance L. By scanning the spacing L, different wavelengths of light can be let through. Fig. 1.12 shows a typical micro-BLS experimental setup and the operating principle of the BLS interferometer. Perhaps the most standard design is that by Sandercock and colleagues,[87] which utilizes two FP cavities with slightly different mirror spacings and a total of six optical passes through the cavities (three through FP1 and three through FP2) to improve contrast and free spectral range without sacrificing spectral resolution.

The inelastic scattering mechanism for magnons and phonons is subtly different. Alterations in the dielectric susceptibility due to changes in the local magnetization can facilitate interactions with light through magneto-optic effects. Light scattered in this manner by magnons has its polarization rotated 90° relative to the incoming light polarization due to scattering selection rules (Appendix A). Meanwhile, light scattered by phonons preserves its original polarization. The micro-BLS system schematized in the left portion of Fig. 1.12 is set up for the measurement of magnons. Here, vertically polarized light from the laser is transmitted through a Glan-Laser calcite polarizer, which acts like a polarizing beam splitter. The light is then focused onto the sample by an objective lens where it scatters with the magnons, emitting inelastically scattered light with shifted frequency and polarization rotated by 90°. The scattered light collected by the objective lens then passes back through the Glan-Laser polarizer, which separates the vertical and horizontal polarization components. The horizontally polarized light scattered by magnons is then rejected by the Glan-Laser polarizer and sent to the tandem scanning Fabry-Pérot interferometer. Detection of phonons can be performed by inserting a quarter-wave ($1/4\lambda$) plate immediately before the microscope objective lens to convert the linearly polarized light into circular polarization, equivalent to a 45° rotation in polarization.

The magnon spectrum can then be directly measured by the interferometer. For the confocal geometry shown in Fig. 1.12, the in-plane wavevector of the magnon probed by BLS is set by the angle of incidence of the incoming photons, θ as[88,89]

$$\boldsymbol{q}_{m,||} = \frac{4\pi}{\lambda} \sin\theta \tag{1.38}$$

As a result, in the complete backscattering configuration ($\theta = 0°$), the probed magnon wave vector is zero, corresponding to the $\boldsymbol{\Gamma}$ point. Meanwhile, the magnon frequency

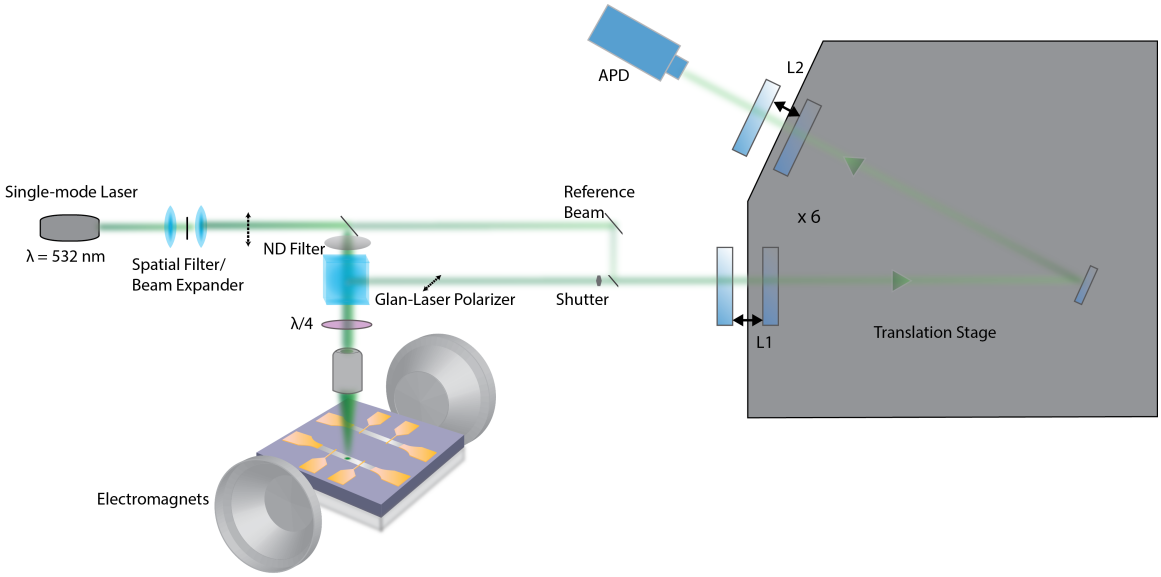

Figure 1.12: Schematic of a typical micro-BLS measurement setup for probing spin waves.

f_m, given as the center of the magnon peak when it is fit by a Lorentzian function, can be related to the change in magnon population, thus making BLS a local magnetometer.

BLS measurements have played an important role in probing spin wave phenomena in magnetic materials. By changing the angle of incidence, one can select for different wavevectors of magnons probed in-plane. Using this approach, angle-resolved BLS measurements have been used to probe magnon dispersions near the $\mathbf{\Gamma}$-point.[88,90] In addition, spatially resolved measurements have been able to visualize spin wave transport,[91,92] while time-resolved measurements have allowed measurement of fast-propagating spin waves[93] and pointed toward the formation of Bose-Einstein condensates by magnons in YIG during microwave pumping.[94] In addition, steady-state micro-BLS measurements have been demonstrated as phonon and magnon temperature sensors in a variety of materials,[95–97] and simultaneous measurement of magnons and phonons has been used to probe the magnon spin-flip relaxation length in YIG.[98]

1.2 Summary

The intent of the beginning of this chapter was to provide an introduction to the fundamental questions that this work seeks to investigate regarding materials with effective energy and spin carrier transport. In particular, this work investigates (1) whether focused laser excitation can drive phonons out of local equilibrium in long mean free path graphene, (2) if the semiconductor BAs does indeed have ultrahigh room temperature thermal conductivity, (3) new methodologies to improve the sensitivity of inelastic light scattering thermometry, and (4) how much energy is transferred across Pt/YIG interfaces due to the spin Peltier effect.

An additional purpose of this chapter was to introduce some of the requisite transport phenomena necessary to understand the coupling between heat, spin, and charge that is leveraged in the field of spin caloritronics. Using a normal metal/magnetic insulator heterostructure as a pedagogical framework, it explored the different the transport of heat and spin by phonons and magnons in the magnetic insulator, charge and spin transport by electrons in the normal metal, and the coupling of all three at the interface between the two. Finally, several experimental methodologies important to probing and driving spin-heat-charge coupling phenomena were outlined.

Chapter 2

Nonequilibrium Phonons in Suspended Graphene[1]

2.1 Background

2.1.1 Energy Transport in sp^2 Carbons

Elemental carbon forms strong covalent bonds with itself that arise out of different hybridizations − or mixing of valence states − of the carbon atoms' electrons. Specifically, the $2s$ and $2p$ orbitals mix giving rise to sp^n (n =1, 2, 3) hybridized orbitals. The result is that carbon atoms can form several different crystal configurations or allotropes. When one $2s$ and three $2p$ orbitals mix, they produce four hybridized sp^3 orbitals that form covalent bonds in a tetrahedral arrangement. This is the basis for the diamond structure. On the other hand, when one $2s$ and two $2p$ orbitals mix, they form three hybridized sp^2 bonds that all lie in the same plane but spaced 120° apart plus one additional p orbital. This strong directional sp^2 bonding results in hexagonal sheetlike carbon structures, forming the basis for layered graphite. All carbon allotropes consist of simple unit cells with light atoms that form

[1]The content of this chapter was published in S. Sullivan, A. Vallabhaneni, I. Kholmanov, X. Ruan, J. Murthy, and L. Shi, Nano Lett. 17, 2049 (2017). L.S., J.M., and X.R. designed research. S.S. and I.K. grew and transferred graphene. S.S. fabricated the substrates and performed measurements. A.V. performed ab initio calculations. S.S. and L.S. wrote the manuscript and all other authors commented on and edited the manuscript.

very stiff covalent bonds with one another. These characteristics meet the criteria outlined by Slack in the 1970s for materials with high thermal conductivity, which is why diamond and basal plane graphite have some of the highest room temperature thermal conductivity values of any material.[7]

By isolating, in particular, the sp^2 carbon allotropes, one can obtain structures with reduced dimensionality, including 2D graphene, as well as rolled-up versions like carbon nanotubes (1D) and fullerenes (0D). As a result of quantum confinement and the uncovering of new symmetries, the transport behavior in low-D structures differs somewhat from that in 3D.[27,99,100] A celebrated example is that of graphene.

2.1.2 Graphene

Graphene has been of great interest for use in next-generation electronic and optoelectronic devices due to its superior electronic and thermal transport characteristics. In particular, it has been found to have an exceedingly high electronic mobility,[101,102] large[8,103,104] and debated length-divergent[105] phonon thermal conductivity, as well as unique hydrodynamic electronic transport[106] and predicted hydrodynamic phonon transport at elevated temperatures.[107,108] The reasons for these phenomena lie in graphene's unique structure.

The valence and conduction bands in monolayer graphene approach each other with linear dispersion near the **K** high-symmetry points at the corners of the Brillouin zone and intersect directly at each of the six **K**-points. The sp^2 hybridized states leave one additional p orbital that can form a π bond that overlaps with one of the three σ bonds, yielding two delocalized electrons and and thus two double-bonds per aromatic ring in graphene. This means that one particular **K**-point is not equivalent to its neighbors, dividing the six **K**-points into two sets of three inequivalent, but degenerate **K** and **K'** points. Furthermore, the atomic nuclei themselves in the graphene sheet can readily vibrate with a polarization that is out of the plane of the sheet. Acoustic phonons in graphene with out-of-plane polarization, or flexural acoustic (ZA) phonons have a quadratic dispersion near the $\mathbf{\Gamma}$ symmetry point and have long umklapp scattering mean free paths.[8] Meanwhile, the optical phonons (vibrations between the two inequivalent C atoms in the graphene unit cell) have much higher energies than the ZA and in-plane acoustic phonons. Calculations of

the graphene phonon dispersion and temperature-dependent phonon density of states can be found in Appendix B. The performance of graphene-based devices is directly linked to the scattering processes between electrons and phonons, as well as scattering between these different phonon modes.

Energy Relaxation in Graphene

On short enough time or length scales, energetic excitation of a material can result in considerable nonequilibrium among its energy carriers. To make functional devices out of these materials, it is important to understand the cascade of scattering and thermalization mechanisms that can eventually lead to equilibrium, or to investigate if significant nonequilibrium will be maintained within the device. In graphene, optical or electrical excitation generates hot charge carriers with energies on the order of several hundred meV. These hot carriers scatter with one another to reach local thermal equilibrium on a time scale on the order of 0.1 ps and over a length scale of 100 nm.[109–112] The charge carriers then relax their energy by scattering with optical and acoustic phonons over different time and length scales that depend on the charge carrier energy, the phonon modes that are involved, as well as defects and extrinsic scattering pathways from the environment. For hot carriers with energies above the large, $\sim$ 196 meV, optical phonon energy, optical phonon emission is the dominant cooling mechanism.[113] In the absence of defects, meanwhile, hot carriers with energies below 196 meV must relax their energy by scattering with acoustic phonons.[113] However, the intrinsic scattering rates between charge carriers and acoustic phonons in undoped graphene are highly restricted at room temperature and above because the small Fermi surface of graphene restricts the maximum allowable scattering phonon wavevector to $\boldsymbol{q}_{max} = 2k_F$, where k_F is the Fermi wavevector. This restricted scattering means that these lower energy charge carriers are slower to cool[113–115], and the weak charge carrier-acoustic phonon coupling has been used to explain the enhanced optical response due to carrier multiplication in graphene photodetectors and bolometers.[116,117] The temperature at which phonons with wavevector $\boldsymbol{q} = 2k_F$ are populated is called the Bloch-Grüneisen temperature, T_{BG}.[118] The presence of defects, however, enables "supercollision" cooling of carriers by making the entire thermal distribution of phonons accessible via two-phonon scattering, even when the phonon temperature is greater than T_{BG}.[115,119,120] For supported graphene, hot charge carriers can have

additional extrinsic scattering pathways due to surface polar optical phonons and charged impurity scattering in the substrate.[121]

Despite disorder and substrate effects, several ultrafast optical measurements of both suspended and supported graphene have revealed rapid thermalization between hot carriers and optical phonons on the order of 50 to 150 fs[111,122–125] and subsequent cooling of the optical phonons with acoustic phonons on a slower timescale of 2 to 3 ps.[111,124] These measurements obtain the time scales for hot charge carriers and optical phonons to cool down to the ambient temperature, while assuming that the acoustic phonons are not significantly heated. In contrast, several measurements have indicated that the acoustic phonons in highly biased graphene devices are appreciably heated.[126–128] If the acoustic phonons in the ultrafast measurements were appreciably heated, one might expect the measured cooling times to be longer than the observed relaxation time because the acoustic phonons would also take some time to cool. While the dispersive acoustic phonons typically dominate the contribution to the thermal conductivity, they must be appreciably populated to contribute to heat spreading. The complex interplay between a unique electronic band structure

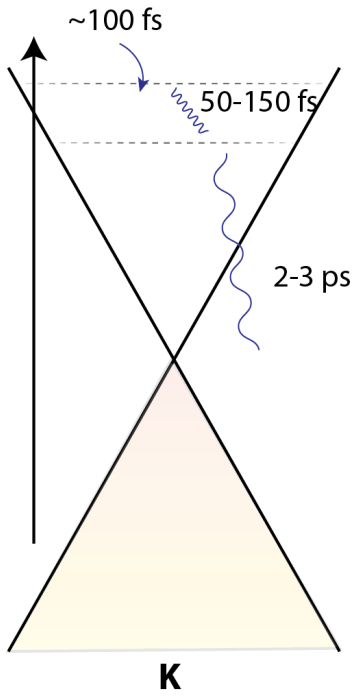

Figure 2.1: Schematic of hot carrier decay around the Dirac point in graphene.

and phonon dispersion leads to graphene's unique nature that can be probed with electrical and optical characterization. As outlined above and uncovered in many prior measurements, graphene's transport characteristics leave it prone to a variety of nonequilibrium phenomena. Past studies are focused primarily on hot charge carriers and their cooling pathways with the acoustic phonon "bath". However, little attention has be paid to whether or not the various acoustic phonon populations are in thermal equilibrium with one another. Such a consideration is important not only for heat spreading in and performance of graphene optoelectronic devices, but also in Raman opto-thermal measurements, which, as a non-contact technique, has become an increasingly popular method for measuring thermal transport in graphene and other 2D materials.[103,104,126,127,129–134] These Raman measurements rely on optical heating directly from the laser probe, and the heating power is obtained based on the optical absorption. Even for graphene alone, different measurements have obtained a large range of thermal conductivity values. The variation in these measurements has been partly attributed to the different optical absorption values used in the data analysis [103,104,129]. However, given the propensity for nonequilbrium behavior in graphene, it is possible that the Raman measurement itself could drive the energy carriers out of equilibrium.

In one Raman measurement of graphene,[130] the authors assume a thermalization length of 1 μm between hot electrons and phonons and use this length scale in their numerical solutions to the heat diffusion equation instead of the ~ 0.5 μm laser spot; they base this off of prior results.[113,122] Moreover, Cai et al.[104] found evidence to suggest that the lower-frequency acoustic phonons were in the quasi-ballistic regime and were at a lower temperature than the higher frequency optical phonons in their Raman-based thermal conductivity measurements of suspended graphene using different laser spot sizes. In addition, recent first-princples-based multitemperature calculations by Vallabhaneni et al.[135] have indicated that hot charge carriers and different phonon polarizations can be driven out of local thermal equilibrium under laser heating in Raman experiments. Such nonequilibrium between different phonon polarizations would not only affect the interpretation of Raman measurements but would also affect the contribution to the thermal conductivity made by the lower frequency acoustic phonons, which ordinarily dominate heat spreading in suspended graphene under equilibrium conditions.[136,137] Nonequilibrium that is sustained over

moderately long length scales could have deleterious effects on the performance of graphene-based devices. The Raman-based experiments described below have been designed to both drive and probe phonon nonequilibrium in graphene.

2.1.3 Raman Spectroscopy

The Raman process involves inelastic scattering between the incident photons and a population of Raman-active vibrational modes, either directly or mediated by electronic transitions. In first-order Raman scattering experiments, the wavevectors of the probe photons are often quite small, thereby restricting measurements to excitations very near the Brillouin zone (BZ) center. Additionally, visible light has relatively high energy in the range of a couple eV and tends to polarize dipoles in materials that oscillate at frequencies comparable to optical phonon frequencies, thus the strongest interactions for incoming light in Raman experiments typically involve high-energy electronic states and optical phonons. As an inelastic scattering process, the probe photons exchange energy and momentum with excitations in the material. Conservation of energy and momentum requires

$$\begin{aligned} \hbar\omega_s &= \hbar(\omega_i - \omega_e) \text{ (Stokes)} \\ \hbar\omega_s &= \hbar(\omega_i + \omega_e) \text{ (anti-Stokes)} \\ \hbar k_s &= \hbar(k_i \pm \boldsymbol{q}_e) \end{aligned} \tag{2.1}$$

where s, i, and e refer to the frequency (ω) or wavevector (k or $\boldsymbol{q}$) of the scattered photon, incident photon, and material excitation, respectively. The frequency of the scattered photon will differ from the incident photons by an amount that is equal to the frequency of the material excitation. When $\omega_s < \omega_i$, the quasiparticles in the material have gained energy, which is referred to as a Stokes process. In the anti-Stokes process, $\omega_s > \omega_i$, and represents a transfer of energy from the quasiparticles in the material to the scattered photon. In the Raman experiment, these processes appear in the spectra as peaks centered about the particular energy of the phonons that are interacting with the light, $\hbar\omega_e = \hbar(\omega_i \pm \omega_s)$. Meanwhile, the relative intensities of these peaks are proportional to the population of quasiparticles with which the photons exchange energy. In semiconductors or Dirac metals such as graphene, both first and second order processes are mediated by optically-induced electronic transi-

tions.[138] Further details and theory behind inelastic light scattering can be found in Appendix A.

Graphene Raman Spectrum

The Raman spectrum of graphene is rich in information. Figure 2.2 shows a representative Raman spectrum for suspended single layer graphene (SLG) in the range of 1000 to 4000 wavenumbers (cm^{-1}) on the Stokes side, while the inset shows the temperature dependence of the Stokes and anti-Stokes signal for the Raman band centered near 1580 cm^{-1}, which is about 196 meV. Before discussing the Raman measurements of phonon temperature and graphene thermal conductivity, it is helpful to discuss the origins of these various peaks in the Raman spectrum. The peak centered near 1580 cm^{-1} is often referred to as the G-band and results from a one-phonon inelastic scattering process involving an in-plane polarized longitudinal optical (LO) phonon at the Brillouin zone center ($\mathbf{\Gamma}$). One-phonon processes are only Raman-active if their wavevector is zero and their symmetry results in a change in polarizability, which can be determined from group theory. The G-band arises when incident light excites electronic transitions between the filled valence (π^*) band and empty conduction (π) band in the graphene Dirac cone. An intraband transition then results in the emission of a phonon with zero wavevector and relatively high energy, which is the zone-center LO phonon (Fig. 2.3(a)).[139]

In addition, some graphitic samples may have a strong D-peak that arises from the breathing mode of the six-membered C rings in graphene and requires a defect (i.e. missing C atom) to be activated.[139] Thus graphitic samples with few defects do not have a clearly defined D-peak. The D-peak involves in-plane transverse optical (TO) phonons near the Brillouin zone corner **K**-points (Fig. 2.3(b)). In defect-assisted Raman processes, phonons with non-zero wavevectors can be elastically scattered by defects, relaxing the zero-momentum Raman selection requirement. Additionally, the D-band is dispersive with the laser excitation energy due to the Kohn anomaly at **K**.[140,141]

The large 2D-band centered at roughly twice the D-band frequency near 2670 cm^{-1}, on the other hand, involves the absorption or emission of two in-plane transverse optical (iTO) phonons near the **K** points with relatively large and opposite wavevectors. Because the 2D-band involves two phonons, it does not require defects

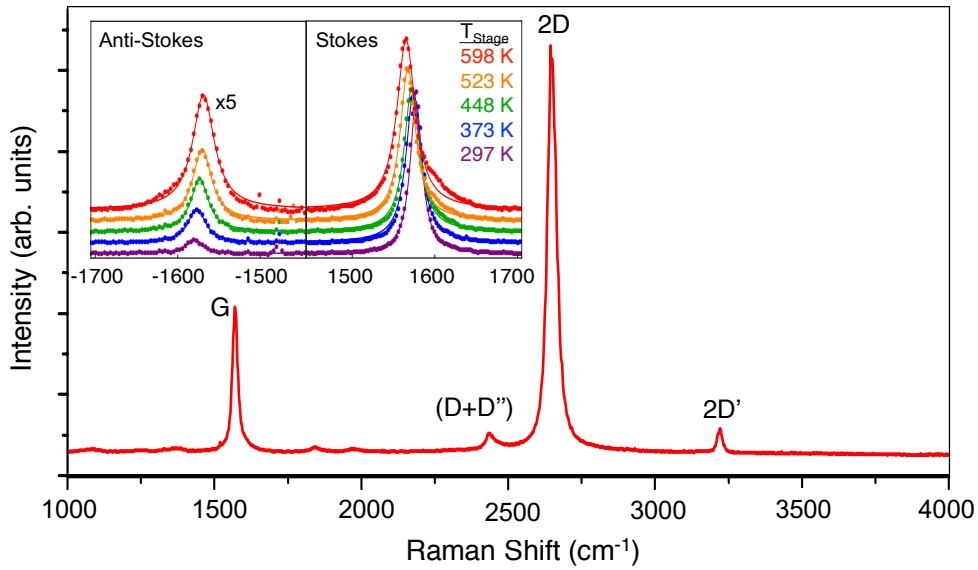

Figure 2.2: Stokes Raman spectrum of suspended monolayer graphene. Inset: temperature dependence of the Stokes and anti-Stokes G-band.

Table 2.1: Origin of Raman-Active Bands in SLG

Designation	**Frequency (cm^{-1})**	**Symmetry-Point**	**Phonons Involved**
D	1350	$\mathbf{\Gamma}$	TO
G	1580	$\mathbf{\Gamma}$	LO
(D+D")	2450	$\mathbf{\Gamma}$-$\mathbf{K}$	iTO + LA
2D	2670	$\mathbf{K}$	2×iTO
2D'	3240	$\mathbf{\Gamma}$	2×LO

to be activated (Fig. 2.3(d)). There are two other peaks visible on either side of the 2D-band in Fig. 2.2: the (D+D") band near 2450 cm^{-1} and the 2D'-band near 3240 cm^{-1}. The (D+D") peak arises from electronic-transition mediated scattering by a combination of two phonons, the aforementioned TO phonon and a longitudinal acoustic (LA) phonon along the $\mathbf{\Gamma}-\mathbf{K}$ direction.[139,142] The 2D'-band, meanwhile, is an overtone peak of two LO (D') phonons with small, opposite wavevectors near the zone-center (Fig. 2.3(e)).[139] Several first-and second-order Raman peaks are summarized in Table 2.1.

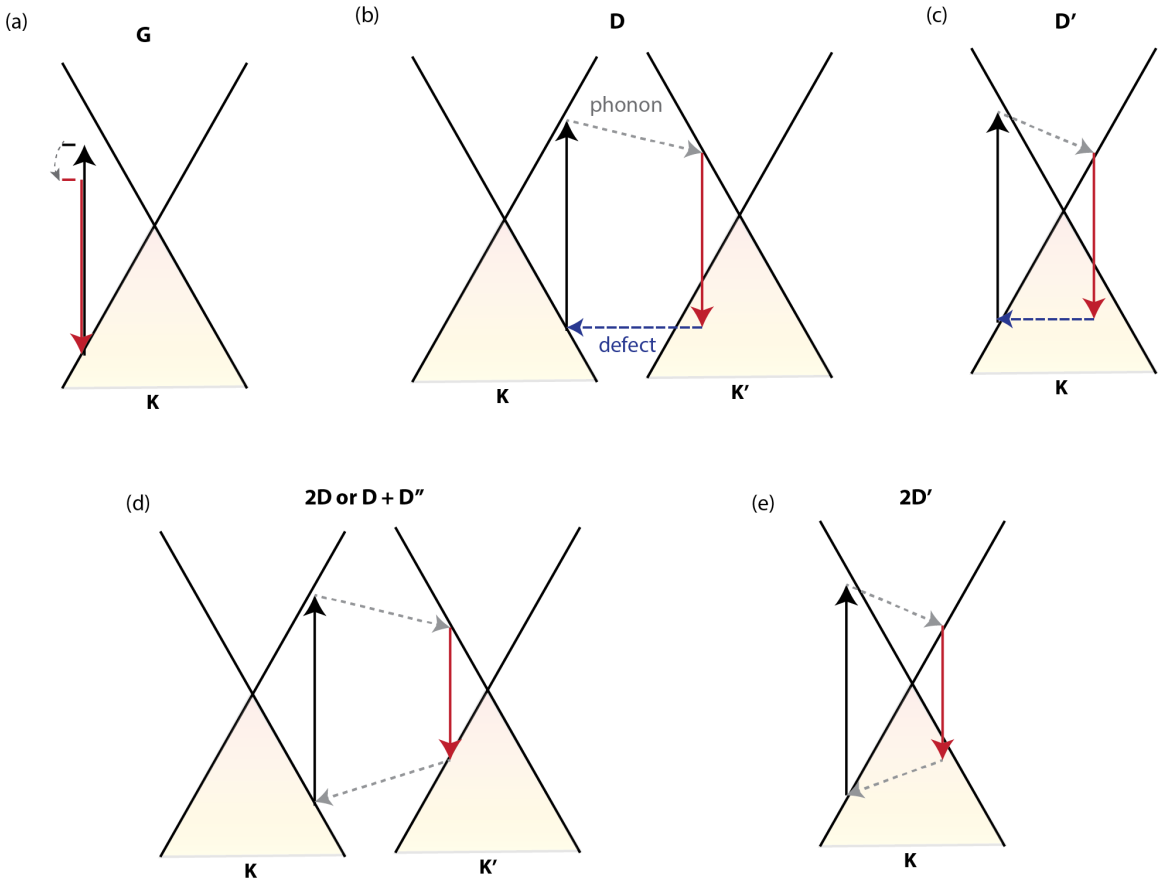

Figure 2.3: Schematics for electronic excitation-mediated Raman processes in graphene. The black arrow corresponds to an photon absorption, gray dashed arrows correspond to phonons, red arrows correspond to photon emission, and blue dashed arrows correspond to defect-mediated processes. (a) The single-phonon G-band in graphene arises from photon absorption and emission with no change in wavevector, corresponding to the $\mathbf{\Gamma}$-point. (b) Intervalley defect-mediated process producing the D-band and (c) intravalley defect-mediated process yielding the D' band. (d) Intervalley two-phonon processes corresponding to the 2D overtone peak (two D phonons with opposite wavevectors) or the combination D + D" band. (e) Intravalley 2D' process.

2.2 Experimental Design

2.2.1 Substrate Fabrication, Graphene Growth, and Assembly

Opto-thermal measurements were performed on monolayer graphene suspended over holes etched in a substrate, providing a circular membrane geometry for the

measurements, as in previous studies.[104,129,131] The substrates used here consisted of nominally 400 nm-thick low-stress silicon nitride (SiN_x) deposited on 500 μm-thick silicon wafers. Square suspended membranes of SiN_x were formed on one side of the wafers by patterning the backside silicon nitride with CF_4 reactive ion etching (RIE) and subsequently etching the underlying silicon in a 4% vol/vol solution of tetramethylammonium hydroxide (TMAH) in H_2O heated at 90 °C. The backside of the suspended nitride membranes was then coated with several nanometers of chromium by electron beam evaporation. Arrays of holes ranging in diameter from 2 to 20 μm were then cut in the nitride membranes using focused ion beam (FIB) milling. Following milling, the holey membranes were cleaned in piranha solution (2:1 H_2SO_4:H_2O_2) to remove any organic contaminants on the surface.

Monolayer graphene was grown via low pressure chemical vapor deposition (LPCVD) on copper foils.[143,144] Prior to growth, 25 μm-thick Alfa Aesar 99.8% metal basis Cu foils (stock number 13382) were etched overnight in glacial acetic acid. Immediately following acetic acid etching, they were rinsed with DI water and placed in 10% hydrochloric acid (HCl) for 20 minutes. The foils were then rinsed with DI water, acetone, isopropyl alcohol (IPA), and dried with dry nitrogen gas. The cleaned foils were loaded in a clean quartz tube, which was then evacuated to the base pressure of the vacuum system (approximately 0.1 mTorr). Hydrogen gas was flowed (5 sccm) while the tube furnace was heated to 1035 °C in 30 minutes. The foils were annealed at 1035 °C under 5 sccm H_2 flow for one hour. After annealing, 5 sccm of methane (CH_4) was flowed in addition to the H_2 for 10 minutes. The vacuum was throttled until the pressure was approximately 400 mTorr and the furnace was turned off and allowed to cool while the gases continued to flow. Graphene grown on Cu foils was characterized using scanning electron microscopy and Raman spectroscopy using a 488 nm laser to minimize Cu fluorescence.

The as-grown graphene on copper foil was then cut into $\sim$1 cm^2 squares that were flattened between two clean glass slides. These squares were placed on a clean microscope cover slip and the edges of the foil taped down. A solution of 4% 496k g/mol molecular weight polymethyl methacrylate (PMMA) in chlorobenzene was spin coated on the graphene/copper at 3500 rpm for one minute. The PMMA-coated squares were then removed from the cover slips and the tape-covered edges were cut off. The PMMA was then cured at 120 °C for five minutes. The squares were

then floated uncoated side-down in 10% nitric acid for two minutes and then rinsed with DI water to remove graphene on the backside of the Cu foil. These squares were then transferred to an aqueous solution of 0.15 M ammonium persulfate (APS) in H_2O where they were allowed to float until the copper foil completely etched away. Following copper etching, the floating PMMA/graphene was then transferred to a bath of clean DI water using a spoon and allowed to float for several minutes. This was then repeated with another bath of DI water, where the PMMA/graphene was allowed to float for one hour. The floating PMMA/graphene was then scooped up with the holey membrane substrate and allowed to dry in air. After drying, the PMMA/graphene/substrate was dipped carefully in warm acetone and slowly removed at a 45° angle and then placed in a tube furnace, which was evacuated to ∼1 mTorr. The sample was then heated following the profile shown in Fig. 2.4 under a flow of H_2 and Ar gas at a pressure of 2 Torr to soften, decompose, and remove much of the remaining PMMA on the graphene surface without tearing the suspended graphene.

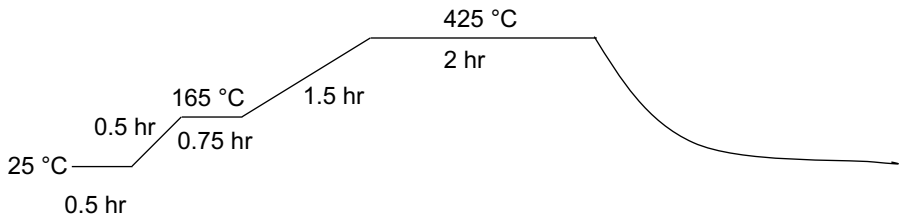

Figure 2.4: Heating profile used to remove PMMA residue from the suspended and supported graphene on holey silicon nitride membranes under hydrogen and argon flow at a pressure of 2 Torr.

Following graphene transfer and removal of the PMMA, the samples were mounted inside a small homebuilt vacuum chamber and a thin (150 μm) microscope coverslip was placed above and sealed with epoxy. Inside the chamber, the samples were mounted to a flat resistive ceramic heater with a built-in K-type thermocouple using a small amount of silver paint. This heater was capable of temperatures up to 400 °C. The sample chamber was evacuated and the whole assembly placed on a confocal Raman microscope system. Using a 50× objective lens, a 532 nm laser was focused through the coverslip and on the center of graphene suspended over the holes for Raman measurements.

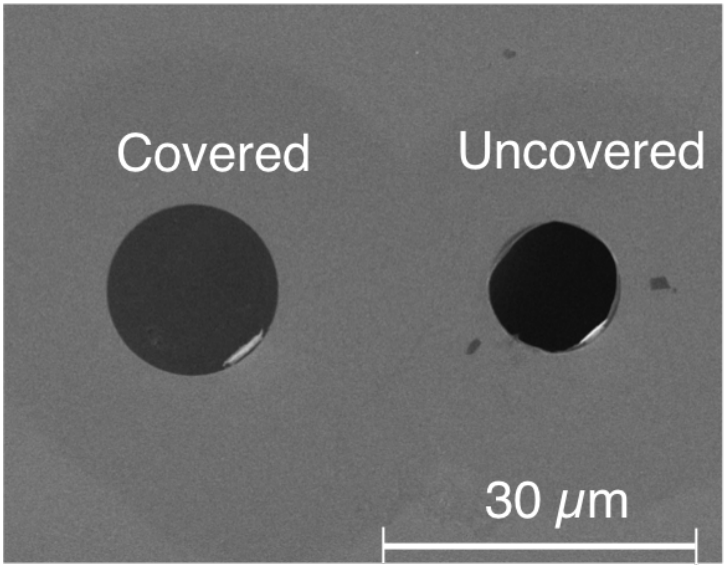

Figure 2.5: Scanning electron micrograph of a holey silicon nitride membrane with one hole covered by monolayer graphene and one hole uncovered.

2.2.2 Characterization of Laser Spot Size and Absorption

Characterization of the focused Gaussian beam radius and the laser absorption by the graphene is critical to extract the graphene thermal conductivity. The laser spot size was measured using a modified knife edge method.[104] A clean silicon wafer was cleaved and approximately 100 nm of gold was deposited on the sharp cleaved edge using an electron beam evaporator. Using the piezoelectric nanopositioning stage on the Raman microscope (WITec Alpha 300), the edge was scanned in 20 nm increments across the probe laser, taking a Raman spectrum at each point. This measurement was repeated 20 times. The same type of coverslip used in the vacuum chamber was placed over the silicon sample to simulate the conditions of the graphene measurements. The integrated intensity (I) of the silicon 520 cm^{-1} Raman peak was then plotted as a function of position and fit using a cubic spline. The derivative of this fit yielded a Gaussian peak that could be fit with the function $\frac{dI}{dx}(x) = Ae^{-(x-x_0)^2/r^2}$ with the fitting parameter r being the Gaussian beam radius of the laser spot. This procedure yielded a Gaussian beam radius of 360 $\pm$ 3 nm, which is comparable to previous measurements performed on the same Raman microscope system.

To measure the absorption of the 532 nm laser by the graphene, the graphene/holey

SiN_x substrate was placed on top of a laser power meter. The laser power was measured through a graphene covered 10 μm-diameter hole, as well as through an uncovered 10 μm-diameter hole. The difference in the two measured laser power values yielded an absorption of 3.1 $\pm$ 1.4% for monolayer graphene.

2.3 Raman Measurements of Suspended Graphene

Following characterization of the laser spot profile and absorption, Raman measurements were carried out on graphene suspended over a 10 μm-diameter hole. Five different ambient stage temperatures ranging between 297 K and 598 K and four different incident laser powers between 0.77 mW and 4.71 mW were used, taking between 6 and 27 measurements at each condition. For these measurements, a 600 line/mm grating was used to obtain two different spectra: one that includes four different Stokes peaks in the range from 1000 to 4000 cm^{-1}, and one that includes both the anti-Stokes and Stokes G-band ($\sim$1580 cm^{-1}) in the same measurement. The positions of the four Stokes peaks, and the intensity of the anti-Stokes and Stokes G-band peaks were then taken by fitting each peak to a Lorentzian function $Y(x) = \frac{2}{\pi}\frac{\Gamma}{(x-x_0)^2+\Gamma^2}$ where Γ is the full width at half-maximum (FWHM), and x_0 is the peak position. The background was subtracted prior to fitting by assuming it followed a linear profile in a window 100 to 200 cm^{-1} window centered around the first guess for x_0. Fig. 2.2 shows a representative Stokes Raman spectrum of high-quality monolayer suspended graphene.

2.3.1 Raman-Based Temperature Measurements

Intuitively, the intensity of the Raman signal is proportional to the population, and thus equivalent temperature, of phonons involved in the Raman process. However, the intensity is also dependent on the specifics of the optical measurement setup, including focusing, as well as variations in the Raman cross-section for different phonon modes.[138] In order to limit these effects, the ratio ($\rho = I_{aS}/I_S$) of the integrated intensity of the anti-Stokes peak relative to that of the Stokes peak is often taken to cancel out mode-dependent and experimental setup-specific contributions. The Stokes and anti-Stokes intensities of the G-band in graphene, which arises

from a first-order Raman process, are proportional to $C_S(\omega_L - \omega_G)^4(n_G + 1)$ and $C_{aS}(\omega_L + \omega_G)^4 n_G$, respectively, where n_G is the occupation of the zone-center optical phonon mode described by the Bose-Einstein distribution, $n_G = \left[e^{\frac{-\hbar\omega_G}{k_B T}} - 1\right]^{-1}$, C_x is a calibration factor that, among other things, accounts for the spectral sensitivity of the spectrometer at either the anti-Stokes or Stokes frequency, and ω_L is the laser frequency.[126,145,146] Thus, taking the ratio yields

$$\rho = C\left(\frac{\omega_L + \omega_G}{\omega_L - \omega_G}\right)^4 e^{\frac{-\hbar\omega_G}{k_B T_O}} \tag{2.2}$$

in which $C = C_{aS}/C_S$ and T_O is the phonon temperature of the population of longitudinal optical (LO) phonons that contribute to the Raman G-band in graphene. The anti-Stokes/Stokes intensity ratio has previously been employed as a temperature sensor in graphitic materials including graphene[126,127,129] and CNTs.[147]

In addition to the intensity ratio, the positions of the 2D- and G-bands in graphene have been demonstrated as temperature sensors and used in prior studies to measure the thermal conductivity of supported and suspended graphene.[103,104,126,127,131] The Raman peak position (ω) is related to the phonon energy $E = \hbar\omega$. As the temperature increases, bond softening and anharmonic coupling with additional phonons (recall the discussion on normal modes in Chapter 1) lead to a decrease in the phonon energy, meaning the Raman-measured peak position is also redshifted. The shift in the Raman peak frequencies contain information on the populations, and thus temperatures, of the intermediate frequency phonon (IFP) and acoustic phonon polarizations that are involved in the anharmonic decay process of the Raman-active modes, in addition to thermal expansion.[148] In particular, the Raman frequency shift can be described by the real portion of the phonon self-energy, $\Delta(\omega)$, which describes the renormalization of the phonon frequency when anharmonic interactions are included. For a phonon mode with wavevector $\boldsymbol{q}$ on branch j, the real portion of the self-energy consists of three parts:[149,150]

$$\Delta(\boldsymbol{q}j,\omega) = \Delta_0 + \Delta^{(3)}(\boldsymbol{q}j,\omega) + \Delta^{(4)}(\boldsymbol{q}j,\omega) \tag{2.3}$$

in which the first term Δ_0 is the thermal expansion and the last term $\Delta^{(4)}$ corresponds to a quartic anharmonic correction resulting from four-phonon scattering and gives

rise to a constant frequency shift similar to the thermal expansion. The third-order term $\Delta^{(3)}$, meanwhile, can be written in terms of the imaginary portion of the phonon self-energy $\Gamma(\omega)$ using the Kramers-Kronig relation

$$\Delta^{(3)}(\boldsymbol{q}j,\omega) = -\frac{2}{\pi} PV \int_0^\infty \frac{\omega'}{\omega'^2 - \omega^2} \Gamma(\omega') d\omega' \tag{2.4}$$

where PV denotes the Cauchy principle value, and the imaginary component of the phonon-self energy is given as

$$\Gamma(\omega) = \mid V_3^+ \mid^2 (1 + n_1 + n_2)\, D^+(\omega) + \mid V_3^- \mid^2 (n_2 - n_1)\, D^-(\omega) \tag{2.5}$$

which considers the interaction of phonon modes with Bose-Einstein occupation factors $n_1 = n(\boldsymbol{q}_1, j_1)$ and $n_2 = n(\boldsymbol{q}_2, j_2)$. Here, $V_3(\boldsymbol{q}_1 j_1, \boldsymbol{q}_2 j_2)$ is the cubic coefficient in the expansion of the anharmonic potential energy, $D(\omega)$ is the two-phonon density of states, and the superscripts $\pm$ represent sum and difference scattering events. Graphene's negative coefficient of thermal expansion contributes to an increase of the Raman frequency with increasing temperature; however, this effect is small compared with the downshift caused by anharmonic phonon-phonon scattering. As such, the frequency redshift during laser heating is a reflection of the increasing population of the various interacting phonon modes, which can not necessarily be described by the equilibrium Bose-Einstein distribution at a single temperature. This peak shift based temperature measurement is in contrast to using intensity ratio as a temperature sensor, which is directly sensitive to that particular phonon population.

2.4 Raman-Measured Temperatures and Thermal Conductivity in Suspended Graphene

To use the anti-Stokes/Stokes intensity ratio, Eqn. (2.2), as a temperature sensor, the coefficient C needed to first be calibrated. In these measurements, the calibration was performed by measuring the ratio ρ as a function on incident laser power, ranging from 0.77 mW to 4.7 mW. The laser power-dependent and temperature dependent G-band anti-Stokes/Stokes intensity ratio for the suspended graphene are shown in Fig. 2.6. The calibration factor was obtained at the highest stage tem-

perature (T_{stage} = 598 K) so that an anti-Stokes signal could be resolved even at the lowest laser power. Owing to graphene's large optical phonon energies, the anti-Stokes intensity was too weak to be clearly measured at low laser powers and stage temperatures. The ρ versus P_{laser} data were then fit with a second order polynomial and the value $\rho_0 = \rho(P_{laser} = 0)$ was extrapolated, as shown by the red dashed curve in Fig. 2.6(a). With the extrapolated intensity ratio, Eqn. (2.2) was solved to obtain the calibration factor $C = 0.68 \pm 0.06$. Once calibrated, the range of C values was used to obtain the corresponding optical phonon temperature T_O at each laser power and stage temperature using Eqn. (2.2).

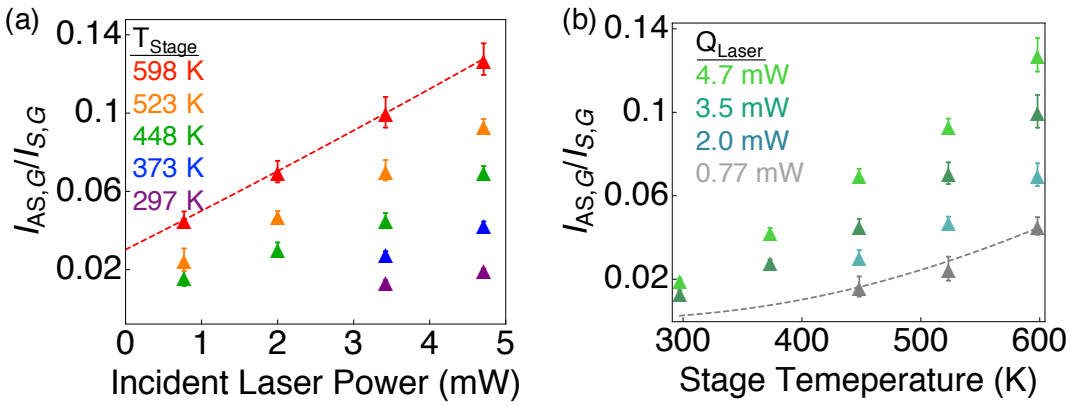

Figure 2.6: The G-band anti-Stokes/Stokes intensity ratio as a function of laser power (a) and stage temperature (b) for the suspended graphene. The red dashed curve in (a) is a fit to the data at the 598 K and is used to extrapolate the intensity ratio at zero incident laser heating, allowing the coefficient C to be obtained from Equation (2.2).

The Stokes peak shifts for all the Raman bands as a function of laser power and stage temperature are shown in Fig. 2.7. For the (D+D")-band in particular, which consists of contributions from a TO and a LA phonon, the LA (D") phonon contribution can be obtained from $\omega_{D''} = \omega_{(D+D'')} - \omega_{2D}/2$ as in prior works.[139,145,151] In the measurements discussed here, a linear fitting of the data obtained at the lowest laser power was used to obtain the temperature coefficient of the peak position, $\chi = d\omega/dT$, for each peak (gray dashed lines). Even at the lowest power used (0.77 mW), laser heating can be expected in the monolayer graphene. However, by extrapolating the laser power-dependent data to the case of zero laser heating for the

lowest stage temperature (297 K) by fitting with a second-order polynomial (purple dashed lines), the Raman shift (ω_0) was found in the case of no laser heating at room temperature (T_∞) where the graphene phonons would be at equilibrium. Thus, the temperature measured from the Raman peak shift is $T^{eq} = (\omega - \omega_0)\chi^{-1} + T_{stage}$, which yields a temperature where all the phonon modes are presumed to be in equilibrium.

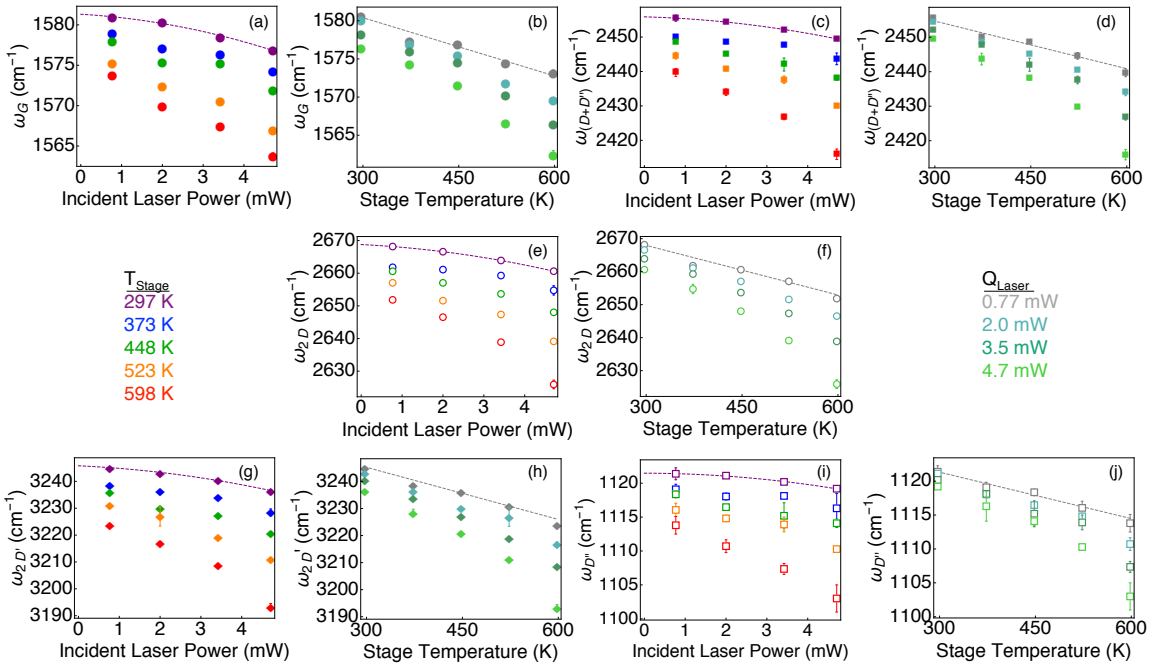

Figure 2.7: Stokes Raman shift as function of laser power and ambient temperature for the G-band (a, b), D+D"-band (c, d), 2D-band (e, f), 2D'-band (g, h), and the D"-band (i, j). The dashed purple lines at the lowest stage temperature are quadratic fits to the peak shift vs. laser power data. The dashed gray lines at the smallest laser power are linear fits to the peak shift vs. ambient temperature.

2.4.1 Nonequilibrium Phonon Temperatures

Figure 2.8 shows the measured phonon temperatures based on the G-band anti-Stokes/Stokes intensity ratio and positions of the different peaks. Especially at low stage temperatures, there is an evident difference between the temperatures obtained by different spectral features, with those temperatures obtained by the intensity ratio being the highest and the temperatures obtained from the D" peak shift the lowest.

Such nonequilibrium can be observed up to incident laser powers of 2 mW and ambient temperatures of $T_{stage} = 523$ K. Because the calibration procedure for the peak shift data relies on the fitting of the second-order polynomial fit to the data obtained at the lowest stage temperature, those data points that fall considerably outside of the peak shift range covered by the fitting were not included in the temperature conversion, i.e. those data points in Fig. 2.7 that fall outside of the y-axis range covered by the dashed purple lines.

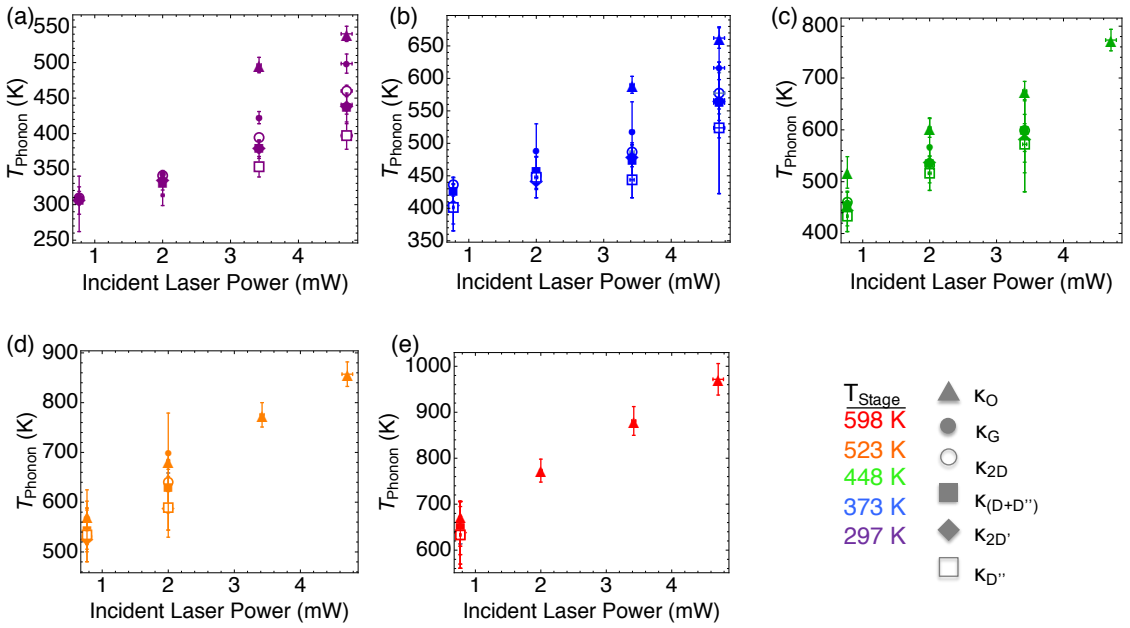

Figure 2.8: Measured temperatures of the suspended graphene based on different Raman spectral features. Filled triangles represent optical phonon temperatures (T_O) obtained from the intensity ratio, while the filled and open circles, filled diamonds, and filled and open squares are the equivalent temperatures measured by the shift of the G-band, 2D-band, 2D'-band, (D+D")-band, and the D" frequencies, respectively.

Multitemperature Model

To better understand the observed nonequilibrium, first-principles calculations and a multitemperature model were employed by Xiulin Ruan's group (Purdue). As in their previous work, density functional perturbation theory (DFPT) was used to directly calculate the electron-phonon and phonon-phonon scattering rates.[135] Un-

der conditions simulated to be equivalent to the experiment, the DFPT-calculated scattering rates were then fed into a multitemperature model to compute the temperatures of the hot electrons and six phonon polarizations in graphene as energy was transferred from the incident photons to the electrons and optical phonons and to the acoustic phonons at different rates. These calculations were performed on a 5×5 μm^2 Cartesian domain with quarter-symmetry to simulate the experimental measurements of graphene suspended over a 10 μm-diameter hole. The two can be considered equivalent because the calculated temperature rise 5 μm from the center is found to be negligible. The calculation results are dependent on the contribution of electrons to the thermal conductivity, κ_e. Past measurements have indicated much lower κ_e than the intrinsic first-principles calculated value as attributed to defects in measured samples.[135] As such, different values of κ_e were trialed in the calculations. Figure 2.9 shows the calculated electronic, iTO, LO, and ZA temperature distributions at the lowest stage temperature and laser power for an electronic thermal conductivity of the form $\kappa_e = (20\text{Wm}^{-1}\text{K}^{-1})T_e/(300\text{ K})$.

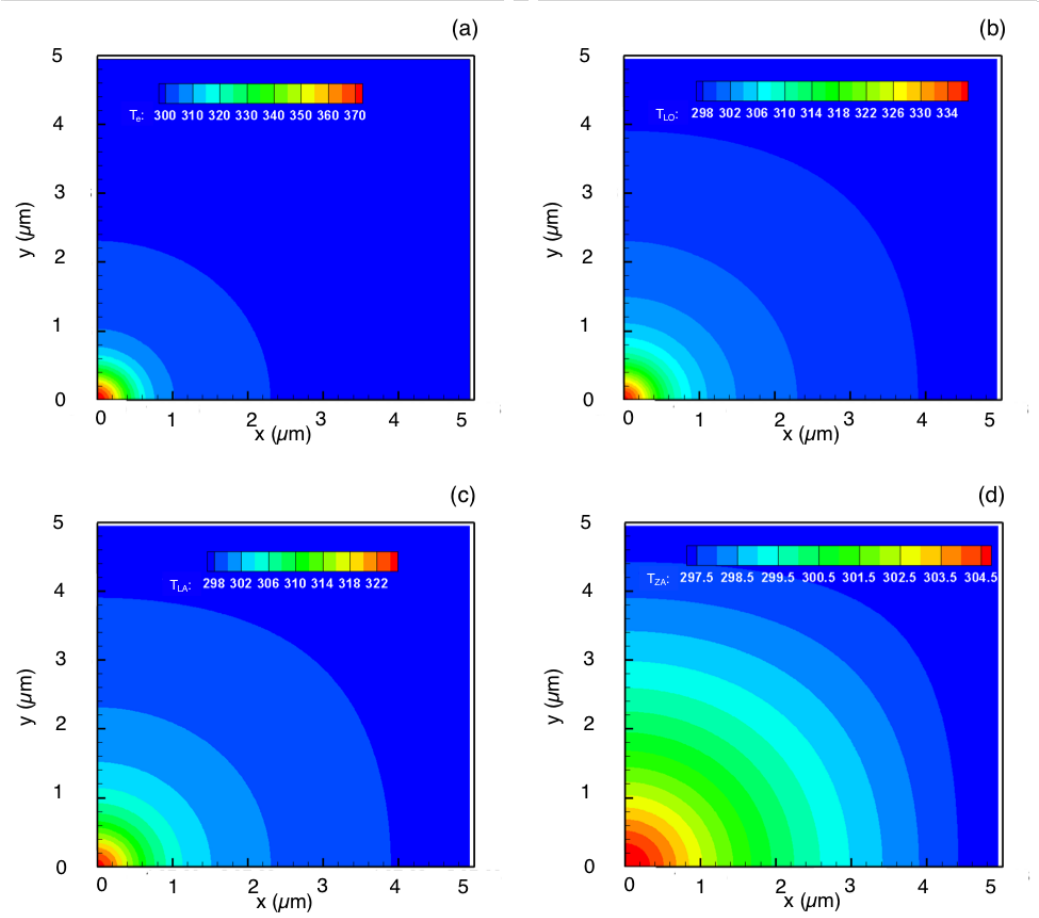

Figure 2.9: Multitemperature model calculations for graphene suspended over a 10 μm $\times$ 10 μm hole under an incident laser power of 0.77 mW, T_{stage} = 297 K, beam radius of 360 nm, and laser absorptivity of 3.1%. The color plots correspond to temperature distributions for (a) electrons, (b) in-plane transverse optical (iTO) phonons, (c) longitudinal optical (LO) phonons, and (d) flexural acoustic (ZA) phonons. The electronic thermal conductivity was assumed to follow the relation $\kappa_e = (20\mathrm{Wm}^{-1}\mathrm{K}^{-1})T_e/(300$ K). Results provided by Ajit Vallabhaneni and Xiulin Ruan.

Meanwhile, one-dimensional temperature profiles along the x-axis for the electrons and all six phonon polarizations are indicated in Fig. 2.10, which shows the sharp drop off outside the Gaussian laser spot.

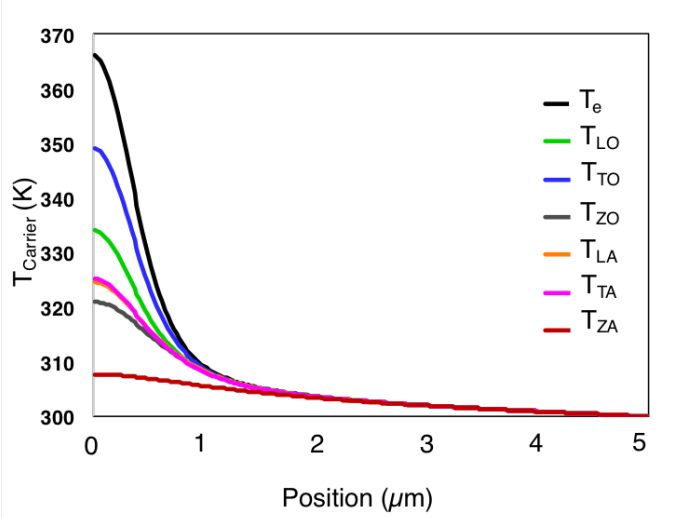

Figure 2.10: Calculated temperature profiles along the x-axis based on the multi-temperature model for T_{stage} = 297 K, 0.77 mW incident laser power, and $\kappa_e = (50\mathrm{Wm^{-1}K^{-1}})T_e/(300\ \mathrm{K})$. Calculations provided by Ajit Vallabhaneni and Xiulin Ruan.

The effect of changing κ_e in the calculations was found to have only a small effect on the nonequilibrium between energy carriers, as summarized in Table 2.2, which lists the average temperatures inside the laser spot for the different carriers. The reason for the small sensitivity lies in the fact that the contribution to thermal conductivity by hot electrons is rather small in comparison with the contribution from phonons. As a result, despite the relatively elevated electron temperatures within the Gaussian laser spot, the electron heat current drops appreciably beyond the Gaussian beam radius, while the relative contribution to the heat current from the ZA phonons increases dramatically, as shown in Fig. 2.11. The ZA phonons are found to contribute the greatest to the overall heat spreading, despite having a lower temperature rise. This results from the the ZA phonons' large specific heat and thermal conductivity contribution. In addition, Appendix B summarizes the temperature profiles and time-resolved pseudo-atomic heat currents obtained by a molecular dynamics (MD) simulation of pointlike heating in a freestanding graphene

sheet using a modified Tersoff potential.

Table 2.2: Calculated Average Energy Carrier Temperatures in the Laser Spot at Different Laser Powers, Stage Temperatures, and Electronic Thermal Conductivities

$\boldsymbol{\kappa_e}$ ($\mathbf{Wm^{-1}K^{-1}}$)	**Power (mW)**	$\boldsymbol{T_{stage}}$ **(K)**	T_e (K)	T_{LO} (K)	T_{TO} (K)	T_{ZO} (K)	T_{LA} (K)	T_{TA} (K)	T_{ZA} (K)
$20T_e/300$	0.77	297	358.1	329.6	343.2	318.1	321.2	321.7	304.7
$50T_e/300$	0.77	297	358.1	326.2	338.5	316.3	319.0	319.3	304.4
$20T_e/300$	0.77	448	492.4	481.9	486.2	477.1	480.9	480.8	468.5
$50T_e/300$	0.77	448	488.3	479.1	482.8	474.9	478.2	478.0	467.3
$20T_e/300$	0.77	523	567.3	560.4	563.3	556.6	559.8	559.7	549.5
$50T_e/300$	0.77	523	563.1	557.0	559.5	553.8	556.5	556.4	547.6
$20T_e/300$	0.77	598	643.7	638.9	641.1	635.8	638.5	638.4	630.2
$50T_e/300$	0.77	598	639.2	635.0	636.9	632.4	634.6	634.5	627.5
$20T_e/300$	3.5	297	484.1	434.1	454.4	402.2	423.8	423.3	339.2
$50T_e/300$	3.5	297	470.3	422.9	442.1	393.8	412.3	411.9	337.3
$20T_e/300$	4.71	297	530.0	478.0	499.4	442.8	470.4	469.6	359.2
$50T_e/300$	4.71	297	513.1	463.5	483.6	431.3	455.4	454.7	356.2

The effects of the heating condition − laser power and stage temperature − on the calculated local nonequilibrium are also summarized in Table 2.2. The largest predicted local nonequilibrium occurs between the electronic temperature and the ZA phonon temperature. Even at the lowest laser powers of 0.77 mW, the ZA phonons are still predicted to be relatively underpopulated compared with the other energy carriers. The underpopulation of the ZA phonons can be more easily seen by taking the ratio of the average ZA temperature rise relative to the temperature rise of the other carriers, as indicated in Table 2.3. In this table, a smaller ratio reflects larger nonequilibrium. The prior calculation by Vallabhaneni et al.,[135] indicates that these ratios remain small and that nonequilibrium persists even down to laser powers as low as 10 μW. In fact, based on these and previous calculations, the $\Delta T_{ZA}/\Delta T_x$ ratio decreases as the laser power or ambient temperature is reduced, meaning nonequilibrium is more prevalent. As the temperature of the graphene is lowered, the relaxation length for the hot charge carriers to exchange their energy with optical and acoustic phonons is increased, so that the nonequilibrium is increased. This trend, of course, would not be expected to persist to zero laser power where there should be complete equilibrium. Thus, the dependence of the local non equilibrium on the laser power is

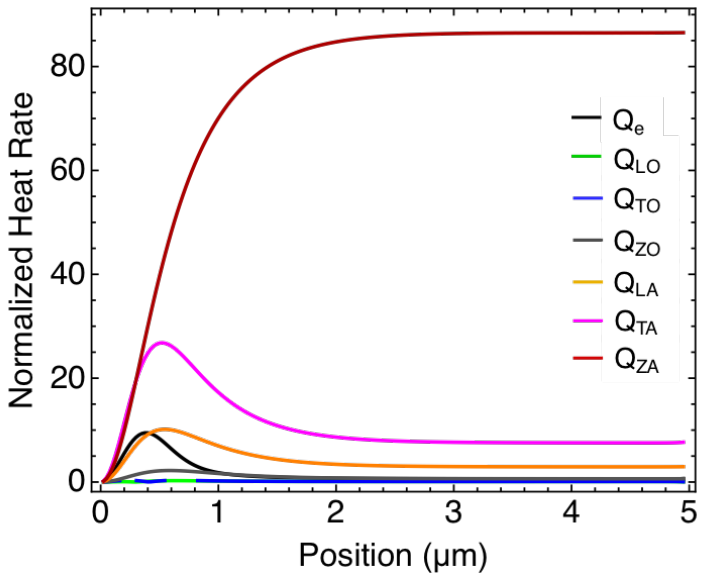

Figure 2.11: Calculated heat transfer rate contribution along the x-axis from the different energy carriers across a square domain concentric with the laser spot. The heat transfer rate is normalized by the total input heating rate from the laser. Incident laser power is 0.77 mW, $T_{stage} = 297$ K, and $\kappa_e = (20\text{Wm}^{-1}\text{K}^{-1})T_e/(300\text{ K})$. Calculations provided by Ajit Vallabhaneni and Xiulin Ruan.

expected to be nonmonotonic.

To make clear the comparison between the experiment and simulation, the apparent and predicted temperatures for the two highest laser powers at the lowest stage temperature ($T_{stage} = 297$ K) are plotted in Fig. 2.12. The obtained T^{eq} from the Raman peak shifts are all significantly lower than the T_O values extracted from the anti-Stokes/Stokes intensity ratio, and the T^{eq} values decrease in magnitude and away from T_O as one moves from the G-band, 2D-band, 2D'-band, (D+D")-band, to the D" frequency. At the largest incident laser power used, 4.71 ± 0.08 mW, temperatures are $T_O = 536\pm19$ K, $T_G^{eq} = 498\pm13$ K, $T_{2D}^{eq} = 460\pm10$ K, $T_{D''}^{eq} = 397\pm10$ K. In comparison, the results from the multitemperature model are plotted as black horizontal bars overlaid with the experimental data. Under the simulated experimental conditions using $\kappa_e = (20\text{Wm}^{-1}\text{K}^{-1})T_e/(300\text{ K})$, the temperatures are $T_e = 530$ K, $T_{LO} = 478$ K, $T_{LA} = 470$ K, and $T_{ZA} = 359$ K. The difference between the calculated T_{LA} and T_{ZA} of 110 K is larger than the 52 K difference between T_e and T_{LO}, and the only 8 K difference between T_{LO} and T_{LA}. The calculations suggest that under these

Table 2.3: Ratios of the Calculated Average ZA Phonon Temperature Rise Relative to Other Energy Carriers in the Laser Spot

$\boldsymbol{\kappa_e}$ $(\mathbf{Wm^{-1}K^{-1}})$	**Power (mW)**	$\boldsymbol{T_{stage}}$ **(K)**	$\frac{\Delta T_{ZA}}{\Delta T_e}$	$\frac{\Delta T_{ZA}}{\Delta T_{LO}}$	$\frac{\Delta T_{ZA}}{\Delta T_{TO}}$	$\frac{\Delta T_{ZA}}{\Delta T_{ZO}}$	$\frac{\Delta T_{ZA}}{\Delta T_{LA}}$	$\frac{\Delta T_{ZA}}{\Delta T_{TA}}$
$20T_e/300$	0.77	297	0.13	0.25	0.17	0.38	0.33	0.32
$50T_e/300$	0.77	297	0.14	0.26	0.19	0.39	0.34	0.34
$20T_e/300$	0.77	448	0.42	0.57	0.50	0.67	0.59	0.59
$50T_e/300$	0.77	448	0.44	0.58	0.51	0.68	0.60	0.60
$20T_e/300$	0.77	523	0.57	0.68	0.63	0.77	0.70	0.70
$50T_e/300$	0.77	523	0.58	0.70	0.64	0.78	0.71	0.71
$20T_e/300$	0.77	598	0.68	0.77	0.73	0.84	0.78	0.78
$50T_e/300$	0.77	598	0.69	0.78	0.74	0.84	0.79	0.79
$20T_e/300$	3.5	297	0.18	0.23	0.20	0.30	0.24	0.24
$50T_e/300$	3.5	297	0.19	0.25	0.22	0.33	0.26	0.26
$20T_e/300$	4.71	297	0.23	0.31	0.27	0.40	0.33	0.33
$50T_e/300$	4.71	297	0.23	0.32	0.28	0.42	0.35	0.35

conditions, the greatest nonequilibrium among the energy carriers is actually between the different acoustic phonon polarizations, with the ZA phonons being substantially underpopulated relative to the in-plane polarized TA and LA phonons. The origin is the restricted phase space for scattering of ZA phonons by either electrons or other phonon polarizations − since monolayer graphene has out-of-plane reflection symmetry, scattering processes cannot involve an odd number of ZA phonons.[8,137,152]

In comparison to the experimental measurements, the T_O extracted from the intensity ratio of the G-band, which involves a LO phonon, is slightly higher than the calculated T_{LO}. This disparity may be due to the ignorance of defects in the calculations, as defects could reduce different phonon polarizations' contributions to thermal conductivity. The measured T_G^{eq}, meanwhile, is comparable to T_{LA} and T_{TA} obtained from the calculations. As discussed previously, the G-band arises from an LO phonon near the zone center ($\mathbf{\Gamma}$) and scatters with two intermediate frequency phonons (IFPs) in the LA and TA branches that have equal and opposite wavevectors.[148] As such, one expects T_G^{eq} to be affected by the populations of LA and TA phonons away from $\mathbf{\Gamma}$. In contrast, the 2D-band involves two TO phonons around the **K**-point, which involves intraband transitions that span from one **K**-valley to the next. The

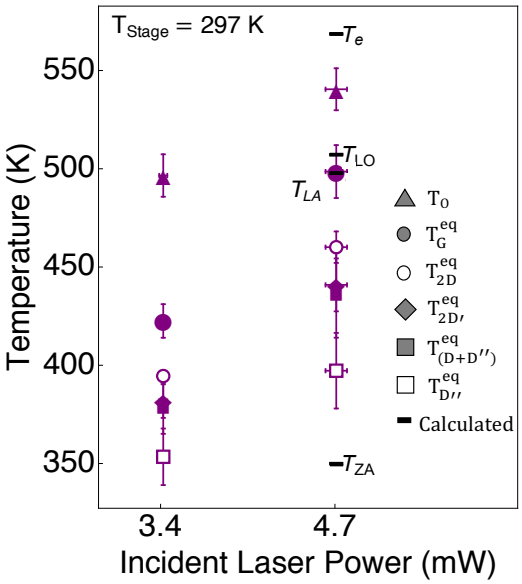

Figure 2.12: Measured temperatures for the two highest incident laser powers and calculated energy carrier temperatures at the highest laser power (black bars) for $T_{stage} = 297$ K. $\kappa_e = (20\text{Wm}^{-1}\text{K}^{-1})T_e/(300\text{ K})$.

TO phonon can not only scatter with IFPs, but also can decay into another optical phonon and a low frequency acoustic phonon near $\mathbf{\Gamma}$.[139,148,151,153] Thus, T_{2D}^{eq} is more affected by the temperatures of lower frequency phonons than T_G^{eq}. The measured $T_{2D}^{eq} < T_G^{eq}$ therefore indicates a lower temperature of low-frequency acoustic phonons near $\mathbf{\Gamma}$ as compared with the IFPs in the TA and LA branches away from the zone-center. Also an overtone peak, the 2D'-band results from scattering of photoexcited carriers by two LO phonons with equal and opposite wavevectors near $\mathbf{\Gamma}$. In contrast to the 2D-band, the LO phonons involved here occur within a single $\mathbf{K}$-valley before scattering with IFPs that decay into TA and LA phonons.[139] However, the decay processes for both 2D and 2D' bands ultimately involve similar types of acoustic phonons, and so the resulting T_{2D}^{eq} is similar to $T_{2D'}^{eq}$. Finally, the (D+D")-band arises from scattering with one TO phonon (D) and one LA phonon (D") around $\mathbf{K}$. Because the LA phonon that contributes to D" can scatter with a pair of ZA phonons, $T_{D''}^{eq}$ is expected to have the greatest sensitivity to the ZA phonon population. Compared with the other measured temperatures, the lower $T_{D''}^{eq}$ is in qualitative agreement with

the calculation results that predict underpopulated ZA phonons within the laser spot. For such nonequilibrium to be present and sustained in the measurement, the length scale over which the ZA phonons exchange energy with other carriers − the so-called thermalization length − must be larger than the submicron laser spot size.

Sustained nonequilibrium behavior among the energy carriers in graphene, especially the ZA phonon polarizations, can have implications in photoexcited and electrically biased graphene devices. In addition, previous opto-thermal Raman measurements of graphene have assumed energy carrier equilibrium in their heat diffusion analysis to extract thermal conductivity. The measured thermal conductivity based on the multimodal temperature results helps to illustrate the effects of this assumption.

2.4.2 Apparent Thermal Conductivity of the Suspended Graphene

Based on the knowledge of the spatial profile of the Gaussian laser beam, the laser absorption, and the measured temperature, one can calculate the thermal conductivity of the suspended graphene provided that the transport is in the diffusive regime. The procedure follows from Cai et al.[104], in which the heat diffusion equation is solved analytically in the cylindrical coordinate while the temperature rise and power dissipated in the graphene is understood to follow the same Gaussian profile as that of the focused laser spot. In this model, the peak temperature rise is at the very center, and the temperature at the edge of the hole very close to the temperature of the ambient. The temperature probed by the Raman measurement is the average of this temperature profile weighted by the Gaussian beam. Specifically, for a hole with radius R and a Gaussian beam radius of r_0, the temperature measured by Raman is

$$T_m \approx \frac{\int_0^R T(r) e^{\frac{-r^2}{r_0^2}} r dr}{\int_0^R e^{\frac{-r^2}{r_0^2}} r dr} \tag{2.6}$$

where the temperature profile $T(r)$ is found to be

$$T(r) = T_1 + \frac{Q}{2\pi\kappa t} \ln \frac{R}{r} \beta(r), \text{ for } r \leq R \tag{2.7}$$

in which T_1 is the temperature at $r = R$, Q is the laser power absorbed in the graphene, κ is the apparent thermal conductivity, $t \approxeq 0.335$ nm is the thickness of the graphene, and $\beta(r) = \left[1 + \frac{\mathrm{Ei}\,(-r^2/r_0^2) - \mathrm{Ei}\,(-R^2/r_0^2)}{2 \ln R/r_0}\right]$ with Ei being the exponential integral. When the laser is focused on the center of the suspended graphene, the thermal resistance measured by Raman is

$$\mathcal{R}_m = \mathcal{R}_g + \mathcal{R}_c \tag{2.8}$$

where $\mathcal{R}_g = (T_m - T_1)/Q$ is the equivalent thermal resistance of the suspended graphene and $\mathcal{R}_c = (T_1 - T_a)/Q$ is the equivalent contact thermal resistance between the nitride membrane and the supported graphene at the edge of the hole and T_a is the ambient substrate temperature. Since $T_1 = T(R)$ is not explicitly known, but instead depends on the contact resistance between the membrane and the supported graphene, the derived expression for the contact thermal resistance from Cai et al.

$$\mathcal{R}_c = \frac{1}{2\pi R\sqrt{gt\kappa_s}} \frac{K_0(z_R)}{K_1(z_R)} \tag{2.9}$$

is used to estimate the thermal contact resistance in these measurements, where K_0 and K_1 are the zeroth- and first-order modified Bessel functions of the second kind, respectively, and $z_R = (g/\kappa_s t)^{1/2} R$. Using the values from Cai et al. for the thermal interface conductance per unit area, $g = 28{+}16/{-}9.2$ MW m^{-2} K^{-1}, and the supported graphene thermal conductivity, $\kappa_s = 370{+}650/{-}320$ W m^{-1} K^{-1}, a contact thermal resistance of $\mathcal{R}_c \approx (1.6 + 1.5/{-}0.75) \times 10^4$ K/W is obtained. With the value for $\mathcal{R}_c$ known, T_1 and $\mathcal{R}_g$ can be obtained, and the graphene thermal conductivity can be calculated as

$$\kappa = \frac{\ln\,(R/r_0)}{2\pi t \mathcal{R}_g} \alpha \tag{2.10}$$

where the parameter $\alpha = \frac{T_m - T_1}{T_0 - T_1} \beta(r_0)$ accounts for the Gaussian distribution of the heater/sensor and T_0 is the temperature at $r = r_0$. As discussed in §2.4, $\mathcal{R}_c$ is small in comparison with the total measured thermal resistance, $\mathcal{R}_m \approx (1.6 \pm 0.74) \times 10^6$ K/W, which is calculated as the measured graphene temperature rise by either peak shift or the intensity ratio divided by the absorbed laser power.

Uncertainty Analysis

The uncertainties in the thermal conductivity values were propagated from the initial measurements of Raman peak position and intensity measured under different heating conditions. Between 6 and 27 Raman acquisitions ranging from 30 seconds to one minute were taken at each condition. The random uncertainties of the peak position, $P_{\bar{\omega}}$, and of the intensity ratio, $P_{\bar{\rho}}$, were taken using Student's t-distribution with double-sided 95% confidence. For n measurements, the random uncertainty of quantity X is

$$P_{\bar{X}} = \frac{t_{n-1,95} s_X}{\sqrt{n}} \tag{2.11}$$

where the value $t_{n-1,95}$ is the t-distribution value for 95% confidence and $n-1$ degrees of freedom, and s_X is the standard deviation of the n measured values of X. The total uncertainty in X is then

$$U_{\bar{X}} = \sqrt{(P_{\bar{X}})^2 + (B_{\bar{X}})^2} = \delta X, \tag{2.12}$$

implying that the Studentized random uncertainty $P_{\bar{X}}$ and the bias uncertainty $B_{\bar{X}}$ are added in quadrature, if a bias uncertainty can be attributed. For functions such as thermal conductivity that depend upon multiple measured variables, each with their own uncertainty, the total error must be propagated. Given a function $f(X, Y)$, the error in f due to uncertainties in independent variables X and Y are summed in quadrature:[154]

$$\delta f = \sqrt{(\frac{\partial f}{\partial X}\delta X)^2 + (\frac{\partial f}{\partial Y}\delta Y)^2} \tag{2.13}$$

The uncertainty in the thermal conductivity values calculated by Eqn. (2.10) is propagated from random uncertainties in the measurements, systematic uncertainties in the laser power absorption, laser spot size, and hole size, and uncertainties in the supported graphene thermal conductivity and interfacial thermal conductance taken from Cai et al. as summarized in Fig 2.13.

Apparent Thermal Conductivity of Suspended Graphene

Figure 2.14 shows the apparent thermal conductivity of the suspended graphene extracted via Eqn. (2.10) for an incident laser power of 4.71 mW, utilizing the different

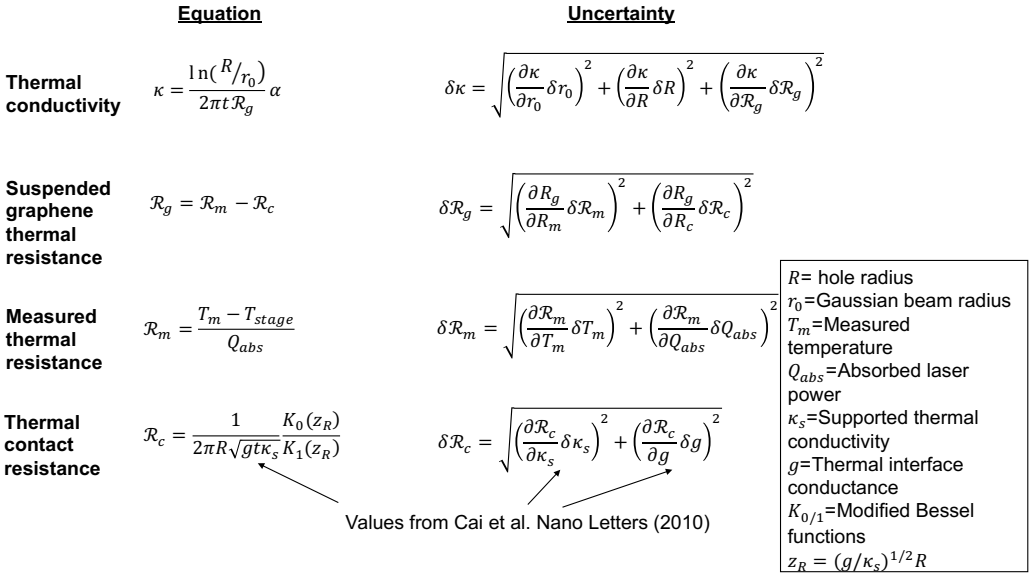

Figure 2.13: Uncertainty propagation for the thermal conductivity calculation.

apparent temperatures from the Raman measurement. For a given stage temperature, the extracted thermal conductivity values can vary widely depending on if a particular peak shift or the anti-Stokes/Stokes intensity ratio was used to measure the temperature. Apparent temperatures measured from the peak shift of Raman bands that involve low frequency phonons, like the (D+D")-band (filled squares), are especially lower than the temperatures measured directly from the population of the zone-center LO phonon population taken from the intensity ratio (triangles). The measured higher temperatures result in the extraction of proportionally lower thermal conductivities. This effect can potentially explain the relatively lower thermal conductivity values obtained in a Raman measurement of suspended SLG based on the intensity ratio,[129] as compared with the higher values obtained from measurements based on peak shift.[103,104,131,155] The values shown in Fig. 2.14 are comparable to the thermal conductivities measured for similar CVD graphene samples utilizing peak shift as a temperature sensor.[104,131]

Thermal conductivity is a diffusive property that is only meaningful if local equilibrium is established among the propagating energy carriers. Recalling Eqn. (1.17), the steady-state Boltzmann transport equation for phonons with group velocity v_g can be written as

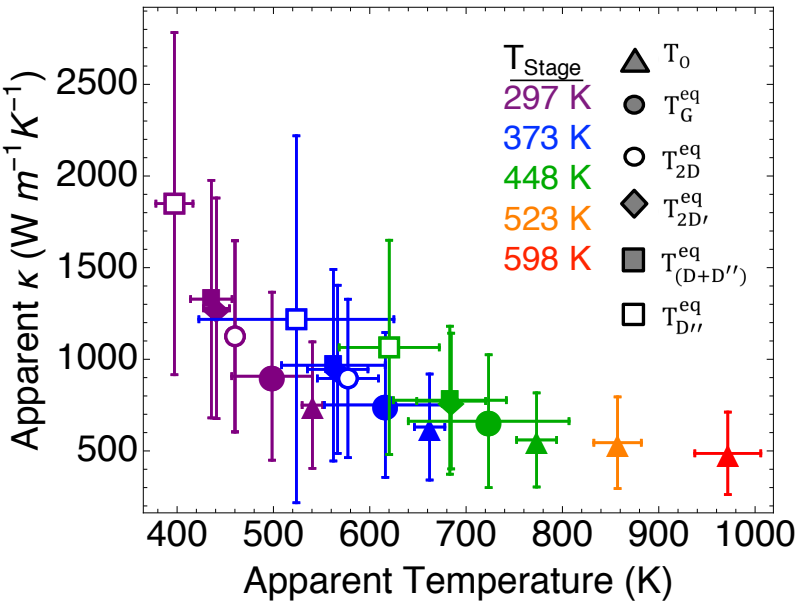

Figure 2.14: Apparent thermal conductivity of suspended graphene at extracted using different phonon temperatures obtained from the Raman spectra. All values were measured at an incident laser power of 4.71 mW.

$$v_g \cdot \nabla_r f_0 = -\frac{f - f_0}{\tau} \tag{2.14}$$

where $f_0 = \frac{1}{\exp(\hbar\omega/k_B T)-1}$ is the equilibrium Bose-Einstein distribution at temperature T. Since f_0 depends on T, Eqn. (2.14) can be rewritten as

$$f(\boldsymbol{r}, \boldsymbol{q}) = f_0 - \tau \frac{df_0}{dT} v_g \cdot \nabla T \tag{2.15}$$

The phonon heat flux within volume V along direction r can be determined by summing over all polarizations p and all wavevectors $\boldsymbol{q}$

$$Q_{qr}(r) = \frac{1}{V} \sum_p \sum_{\boldsymbol{q}} \hbar\omega(\boldsymbol{q}, p) \left[f_0(T) - \tau \frac{df_0}{dT} \frac{dT}{dr} v_{g,r} \right] \tag{2.16}$$

If a local equilibrium distribution $f_0(T)$ can be defined, the total heat flux contribution can be summed over all polarizations p, and the Fourier law is recovered as $Q_{qr} = -\kappa_r \frac{dT}{dr}$ from Eqn. (2.16). On the other hand, if no local equilibrium distribution at

temperature T can be defined, then the inherently diffusive description of κ described by the Fourier law is not meaningful.

2.5 Summary

Single layer graphene was grown by LPCVD and suspended over 10 μm-scale holes. Heating in the suspended graphene caused by a tightly focused laser heater/probe was investigated by opto-thermal micro-Raman measurements. In these measurements, the temperature and power-dependence of the G-band anti-Stokes/Stokes intensity ratio, along with the peak shifts of four Raman peaks were calibrated as temperature sensors. Depending on which Raman spectral feature was used as a sensor, the measured temperature of the graphene varied significantly, even under the same heating conditions.

In addition, a first-principles-based multitemperature simulation was used to show that the focused laser heating heats different energy carriers by different amounts, driving a local thermal nonequilibrium between the energy carriers. In particular, the greatest nonequilibrium was predicted between the out-of-plane acoustic (ZA) phonons and the in-plane polarized acoustic (TA and LA) phonons, rather than between the hot charge carriers and optical phonons or between the optical phonons and acoustic phonons. An analysis of the scattering pathways for the different Raman-active phonons, along with the simulation results, showed that the different Raman peaks are sensitive to different phonon populations in the graphene and that the observed nonequilibrium behavior should be sustained only when the thermalization length scales are larger than the size of the laser probe.

To illustrate the effects of the nonequilibrium, the apparent thermal conductivity of the suspended graphene was extracted from the various measured temperatures and was found to vary considerably based on which apparent temperature was used. The reason for the variability lies in the necessity to be able to define a single local temperature for all the energy carriers that contribute to the thermal conductivity inside the laser spot. Under equilibrium conditions, the ZA phonons ordinarily make the dominant contribution to thermal conductivity; however, given that they are relatively underpopulated compared to the other carriers, they cannot achieve their full heat spreading potential. The experimental and simulation results have

implications for the graphene opto-electronic devices operating far from equilibrium, where the driven nonequilibrium among the acoustic phonons could drastically reduce heat spreading performance and the nonequilibrium between the high-energy carriers and acoustic phonons can affect electronic transport. In addition, the results call into question the meaningfulness of ascribing a thermal conductivity based on opto-thermal Raman measurements when the heater/probe spot size is smaller than the energy carrier relaxation lengths in the material under investigation.

Chapter 3

Unusual Ultrahigh Thermal Conductivity in Boron Arsenide[1]

3.1 Predicted High-κ Criteria-Breaking Boron Arsenide

In the early 1970s, Glenn Slack outlined the criteria necessary for achieving a high thermal conductivity via phonon transport in materials.[7] Namely, a high-κ material should consist of light atoms with a low abundance of isotopic impurities that form strong interatomic bonding and are arrayed in a simple crystal structure. These

[1]The content in §3.3 in this chapter was published in F. Tian, B. Song, X. Chen, N.K. Ravichandran, Y. Lv, K. Chen, S. Sullivan, J. Kim, Y. Zhou, T.H. Liu, M. Goni, Z. Ding, J. Sun, G.A.G. Udalamatta Gamage, H. Sun, H. Ziyaee, S. Huyan, L. Deng, J. Zhou, A.J. Schmidt, S. Chen, C.W. Chu, P.Y. Huang, D. Broido, L. Shi, G. Chen, and Z. Ren, Science (80-.). 361, 582 (2018). F.T., B.S., and X.C. contributed equally. F.T. and Z.R. designed the crystal growth process. F.T. grew the crystal samples. B.S., K.C., M.G., T.-H.L., Z.D., A.J.S., and G.C. performed the thermal conductivity measurements and analyses by microprobe. X.C., S.S., J.K., Y.Z., J.Z., and L.S. performed the thermal conductivity measurements by steady-state and Raman methods and the electrical transport property measurements. N.K.R. and D.B. performed the thermal conductivity calculations. Y.L. and P.Y.H. performed electron microscopy characterization in the Fredrick-Seitz Material Research Laboratory Central Facilities. J.S., G.A.G.U.G., H.S., H.Z., L.D., S.H., S.C., and C.-W.C. performed structural characterizations. F.T., B.S., X.C., D.B., L.S., G.C., and Z.R. wrote the paper. All authors contributed to the discussion of the results and writing of the manuscript. The project was directed and supervised by Z.R., G.C., L.S., and D.B.

criteria neatly explain the large thermal conductivity found in the carbon allotropes diamond and basal plane graphite: C is a light element that forms very strong covalent bonds, and the diamond and hexagonal crystal structures are relatively simple. However, in 2013, Lindsay, Broido, and Reinecke proposed a new potential route to high κ through a phonon band engineering approach.[31] Using first principles calculations, they predicted that an extraordinarily high thermal conductivity could be achieved in binary compounds in which the two constituent elements have drastically different masses, due to the resulting unique phonon bandstructure. In Chapter 1, it was shown that changing the ratio of the constituent atomic masses in a diatomic solid farther from unity resulted in an increased gap between the optical and acoustic phonon branches (recall Fig. 1.2). Lindsay, Broido, and Reinecke predicted that the semiconductor boron arsenide (BAs) would have a large phonon band gap due to its light boron and heavy arsenic atoms. Additionally, the trio predicted that the acoustic phonon branches in BAs would be relatively bunched together even at wavevectors far away from the Brillouin zone center. They expected the combination of acoustic phonon bunching and large optical-acoustic phonon bandgap to reduce the phase space for phonon-phonon scattering, leading the way for BAs to have a theoretical room temperature (RT) thermal conductivity value comparable to diamond at around 2000 W m^{-1} K^{-1} when considering up to three-phonon scattering. Since then, however, experimental verification of ultrahigh κ in BAs was stymied by the difficulty of growing sufficiently large, high-quality BAs single crystals. In 2017, calculations that included phonon-phonon scattering up to the fourth order revised the original 2000 W m^{-1} K^{-1} RT value down to 1400 W m^{-1} K^{-1},[32] which is still quite high, yet unusual because four-phonon scattering was previously considered to make a negligible contribution to the thermal resistance in most materials. Additionally, even if specimens with high thermal conductivity could be produced, there are many challenges to accurately measuring their κ that arise from the necessarily small temperature gradients in high conductance samples and the issue of contact resistance between temperature probes and the sample. As a result, there is a need to develop sensitive contact-free methods for probing thermal transport in materials with larger κ.

3.2 Non-Contact Measurements for High-κ Materials

Materials with high thermal conductivity will develop proportionally small temperature gradients in response to a relatively modest heat flux that would generate large gradients in a low-κ material. As a result, it is necessary to use temperature sensors that can sensitively distinguish the small temperature drops across the material. The need for high sensitivity is especially important for small, mm- or μm-scale samples. Many of the most sensitive temperature sensing approaches are often actuated by electrical detection, including resistance thermometry and thermocouples, and require physical contact with the sample. However, there is always a resistance associated with imperfect thermal contact between the temperature probe and the sample, resulting in a temperature drop between the sample and sensor.[54] Furthermore, if the thermal contact is good, and the sensors and leads themselves have non-negligible thermal conductance and radiation, there can be heat loss from the sample material through the sensor contacts.

To address some of these issues, several non-contact microprobe techniques have been developed to probe thermal transport in materials, including time and frequency domain thermoreflectance (TDTR and FDTR, respectively). These methods often utilize a metal transducer layer that is deposited on top of the polished smooth sample in order to improve the reflectivity signal. Typically, a pulsed or modulated pump laser will heat the sample while a probe laser will then interrogate the change in reflectivity after some time or phase delay. By measuring the reflectivity change for various delays, the data can be fit to a model that includes the thermal conductivity of the sample and the thermal interface conductance between the transducer film and the sample.[156] While long time and phase delays provide information on how the heat is spreading far from the probe region, there are experimental limitations to both the maximum length of the delay and the fidelity of the measured reflectance signal for large delay times. These limitations make it difficult for microprobe measurements to adequately probe thermal transport processes far away from the probed region and throughout the bulk of a sample, thereby relegating them to quasi-local measurements of thermal conductivity.

As discussed in Chapter 2, Raman spectroscopy can be calibrated as a local

temperature sensor. Other inelastic light scattering spectroscopies (ILS), including Brillouin light scattering (BLS), have also been demonstrated as non-contact temperature sensors.[95–97] However, the precision of Raman and other ILS thermometry techniques has traditionally been relatively poor, with a temperature sensitivity on the order of 10 K.[104,131,135,157] The poor sensitivity of traditional Raman thermometry limits its utility for detection of the small temperature gradients in materials with high thermal conductivity. To circumvent these sensitivity limitations, modulation techniques can be employed, as will be discussed later. Further complications in Raman thermometry measurements can arise if the mean free paths of the predominate heat carriers in the sample are sufficiently long and the thermalization length between the Raman-active optical phonons and the heat carrying excitations is larger than the laser probe's spot size. When the thermalization length exceeds the probe spot size, significant nonequilibrium of the optical phonons can be sustained and the thermal transport becomes non-Fourier, as discussed in detail in Chapter 2. Finally, a major limitation of ILS thermometry is the typical ignorance of the laser power absorbed by the sample, which, under standard analysis, is a critical quantity for obtaining the thermal conductivity.

Laser flash analysis (LFA) is another non-contact optical technique that is used to probe thermal transport in materials. LFA measurements are time-resolved measurements in which a material's thermal diffusivity (α) can be obtained from the heat equation $\frac{\partial T}{\partial t} = \alpha \nabla^2 T$. In LFA measurements, a strong heat pulse, usually in the form of a bright light, is incident on one side of a sample. Over the course of time, the thermal emission on the opposite side of the sample is monitored by an infrared (IR) sensor. Once the heat pulse traverses the sample to reach the monitored side, the surface temperature rise is detected by the IR sensor and the delay time is recorded. In one dimension with adiabatic boundaries and a short heating pulse, the thermal diffusivity is obtained as[158]

$$\alpha \approx -\frac{L^2 \ln \frac{1}{4}}{\pi^2 t_{1/2}} \tag{3.1}$$

in which L is the distance between the heated and probed surface and $t_{1/2}$ is the time to half maximum temperature rise. The measured thermal diffusivity can be coupled with the specific heat (C_p) measured by calorimetry to obtain the thermal conductivity: $\kappa = \alpha \rho C_p$ where ρ is the density. However, there are key limitations relating

to the size and geometry of allowed samples in LFA measurements. Specifically, the typical sample geometry requires mm-scale rectangles, which limits its use for small samples or those samples with varying aspect ratios. Additionally, different samples may have different emissivities at their surfaces, and so samples are typically coated with graphite to homogenize sample-to-sample emissivity variation.

Finally, a technique that represents a synthesis of the two above is laser flash Raman.[159] In this measurement, a high aspect ratio sample is cantilevered from or suspended between two heat sinks while a laser probe is focused to either the end of the cantilevered sample or the center of the suspended sample. In this configuration, two types of Raman measurements are performed: a traditional measurement with a continuous wave (CW) laser and a measurement with short laser pulses separated by long delay times. These two configurations represent two separate heating configurations, with the CW laser providing completely steady-state heating and the pulsed laser providing completely transient heating. In short, two separate solutions to the heat equation can be obtained for these two cases, and by normalizing them, the optical absorptivity can be canceled while the thermal diffusivity can still be obtained. Key limitations in laser flash Raman are the requirement of additional optics to provide the laser pulses, a more cumbersome analysis, and necessary pre-knowledge of the material's specific heat in order to obtain its thermal conductivity.

3.3 Measurement of BAs Crystals with Ultrahigh Bulk κ

Large BAs crystals on the scale of several mm have recently been grown at the University of Houston (UH) and UT Dallas via a seeded chemical vapor transport (CVT) technique.[35,36,160] In Tian et al.,[35] the thermal conductivity of various samples cut from the crystals grown at UH was investigated by several techniques performed by different groups, including TDTR and FDTR performed in Gang Chen's group at MIT, and steady-state bulk thermal conductivity measurement by a comparative method performed at UT. Meanwhile, samples cut from these crystals were investigated for defects by transmission electron microscopy (TEM) at the University of Illinois Champaign-Urbana in Pinshane Huang's group, while theoretical calculations

of the BAs thermal conductivity were performed in David Broido's group at Boston College. Additionally, electrical resistance, mobility, and Seebeck measurements were carried out at UT Austin.

3.3.1 Bulk Steady-State Measurements

In the steady-state comparative method, because the reference and sample are placed thermally in series, the thermal conductivity of the sample can be obtained as follows.

$$\begin{aligned} Q_h &= -\kappa_r \nabla T_r A_r = -\kappa_s \nabla T_s A_s \\ \therefore \kappa_s &= \frac{\kappa_r \nabla T_r A_r}{\nabla T_s A_s} = \frac{\kappa_r \Delta T_r A_r l_s}{\Delta T_s A_s l_r} \end{aligned} \tag{3.2}$$

where Q_h is the heater power, ΔT is the temperature drop, A is the cross-sectional area, l is the distance over which ΔT is measured, and the subscripts s and r refer to the sample and reference, respectively. In this approach, pre-knowledge of reference thermal conductivity κ_r at a particular ambient temperature can yield the sample thermal conductivity without measurement of the heater power Q_h. The thermal conductivity of three BAs samples were evaluated in the temperature range of 150 K to 300 K using this method.

Several crystals obtained from UH were diced into large aspect ratio bars (samples numbered 3, 4, and 5) with lengths on the order of 2 mm and lateral dimensions of approximately 100 μm $\times$ 200 μm using a wafer dicing saw (DAD 321) and a diamond-coated blade with with a thickness of 100 μm. Shown in the schematic in the inset of Fig. 3.1(a), the long, thin BAs bars were adhered by silver epoxy end-to-end with a 0.4 mm $\times$ 0.4 mm $\times$ 4 mm Si bar. Two sets of differential thermocouples each consisting of two copper/constantan ($Ni_{0.45}Cu_{0.55}$) junctions in series were fabricated with $D = 12.7$ μm wire and attached to the BAs sample and the Si reference with superglue. A heater was attached to the far end of the Si reference, while the opposite end of the BAs was adhered to a Cu heat sink with silver epoxy. The temperature drops across the Si reference and the BAs sample were measured by the voltage signal from the differential thermocouples. The thermal conductivity of the Si reference bar was measured using the thermal transport measurement option in a Quantum Design Physical Properties Measurement System (PPMS) and by the comparative method using another Si bar as a reference, and was found to be consistent with literature

values,[161,162] as shown in Fig. 3.1(b).

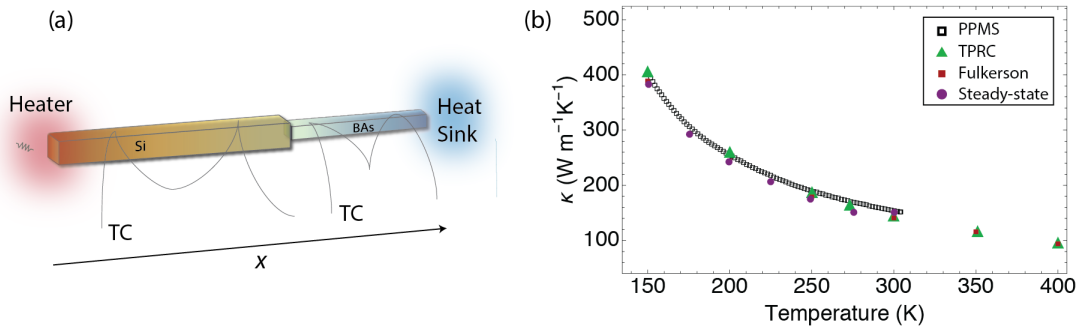

Figure 3.1: (a) Illustration of the steady state comparative method used to measure the BAs bulk thermal conductivity by both Raman and differential thermocouples (TC). (b) Thermal conductivity of Si measured by PPMS and a steady state comparative method with another Si bar, as compared to two literature values.[161,162]

At each ambient temperature, the temperature drops ΔT_r along the Si reference and ΔT_s along the sample were measured by the voltage signal from the differential thermocouples at different heater powers, Q_h. Using a current source, four different heating currents (I_h) were applied to the heater with a resistance of $R_h \approx 350\ \Omega$, and the heating power was approximated as $Q_h \approx I_h^2 R_h$. The slopes based on linear fits to ΔT versus Q_h were then used to calculate the ratio between the reference and the sample temperature gradients in order to obtain the sample thermal conductivity. As previously mentioned, this approach was verified on a Si sample (Fig. 3.1(b)).

Using the thermocouples, the room temperature thermal conductivity ranged from about 570 $\mathrm{Wm^{-1}K^{-1}}$ for sample #4 to about 900 $\mathrm{Wm^{-1}K^{-1}}$ for sample #5, as shown in Fig. 3.2. If the BAs samples do indeed have such high thermal conductivities, the thermal contact resistance at the thermocouple junctions could play a significant role and add error to the measurement. To investigate the role of thermal contact resistance and to validate the high thermal conductivity of the thermocouple measurement, a form of contact-free Raman thermometry with improved temperature sensitivity was developed.

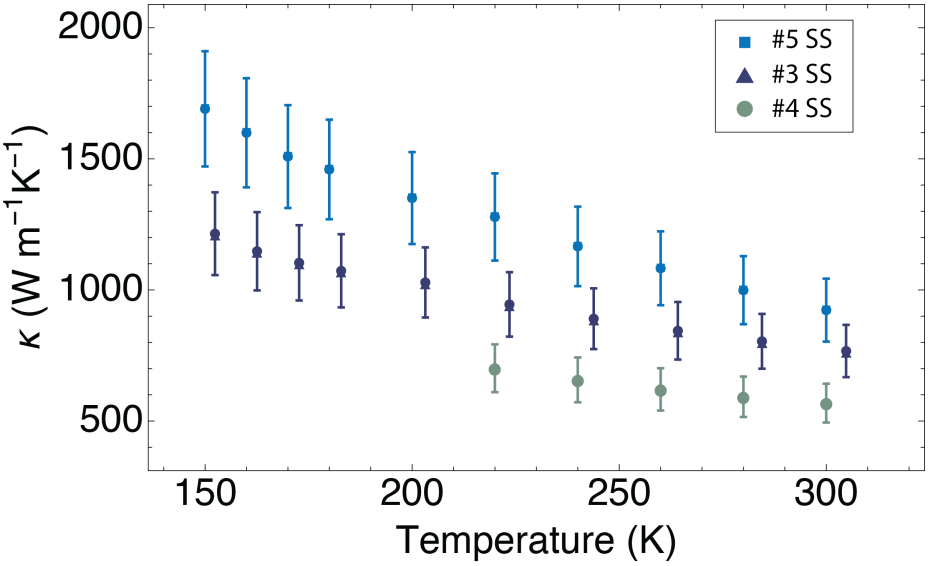

Figure 3.2: Temperature-dependent bulk thermal conductivity of BAs samples #3-5 obtained by the steady state comparative method using Si as a reference. Based on measurements performed by Xi Chen.

3.3.2 Probing Intrinsic Thermal Conductivity by Lock-in Raman Thermometry (LIRT)

In a typical Raman thermometry measurement, the Raman shift as a function of ambient temperature is used to calibrate the peak shift as a temperature sensor. At a given heating condition, many measurements of the peak shift are taken and the average shift can be converted into a temperature rise. However, as discussed previously, this approach has poor sensitivity and is inadequate for detecting the small temperature gradients in high conductivity materials. To improve the sensitivity of Raman thermometry and to investigate the role of contact resistance in thermal transport measurements, a numerical lock-in approach has been developed.[35]

In these measurements, a DC current supplied to the heater was modulated to follow a sinusoid of the form $I(j) = I_0 \sin \frac{2j\pi}{N}$ where $I_0 = 15$ mA is the maximum current supplied to the heater, $N = 12$ is the number of discrete points per complete cycle, and the integer j increases from 0 to $25N$. At roughly 1000 seconds, the period of each measurement cycle was kept rather long in order to ensure steady state had been reached. The position of the 520 cm^{-1} Raman band was used as a local

temperature sensor for Si and the 698 cm^{-1} band was used for BAs, and the probe spot was scanned along x, choosing locations close to the thermocouple junctions, in order to quantify the temperature drops. Figure 3.3(a) shows the measured temperature rise measured by LIRT at two locations on the Si and the BAs at room temperature. Fig. 3.3(b) shows the amplitude spectrum for the Raman shift at the two locations, points 1 and 2, along the BAs bar. The spectrum for point 2 is shifted by 0.2 along the x-axis for clarity. The amplitude of the second harmonic peak shift was converted into a temperature rise using the Raman temperature coefficients, $\chi_{Si} = -0.0176$ cm^{-1}/K and $\chi_{BAs} = -0.02094$ cm^{-1}/K. The Raman temperature coefficients were calibrated by placing both the Si and BAs directly in contact with a hot plate and measuring the Raman shift at various hot plate temperatures, as shown in Fig. 3.3(c,d).

The ability for LIRT to improve upon the sensitivity of ordinary Raman measurements is demonstrated in the following comparison. Figure 3.4 shows the Raman-measured temperature rise at two locations on the Si and the BAs bars as a function of heater current (a) and heater power (b) when all 25 of the measurements at the same heating current were averaged together. The temperature gradients obtained from the average of these measurements were 4.0 ± 2.1 K/mm for the Si and 2.4 ± 1.7 K/mm for the BAs for a heater power of 81 mW. The random uncertainties are large because averaging the measurements also includes the broad spectrum of noise.

In comparison, the temperature gradients measured by the LIRT approach are 2.6 ± 0.6 K/mm on the Si and 2.2 ± 0.4 K/mm along the BAs bar. The numerical lock-in approach and Fourier component analysis substantially reduces the uncertainty by eliminating noise at other frequency components by isolating only the heating signal at the Joule heating frequency. In analyzing frequency spectra, there are two distinct types of noise: frequency-dependent or "$1/f$" noise, and "white" noise or random noise. In order to maximize the signal-to-noise ratio, it is important to choose a modulation frequency that ensures that the measured signal is in the frequency-independent white noise regime. As shown in Fig. 3.5, the signal at the second harmonic is outside of the $1/f$ noise region.

In addition, drift in the ambient temperature was eliminated by subtracting the Raman peak shift measured at the first point in each cycle when no current was applied, $I(0) = I_0 \sin 0 = 0$, from the other 11 points in the cycle. The FFT of the data obtained with this zero-point offset approach has a smaller noise floor than the

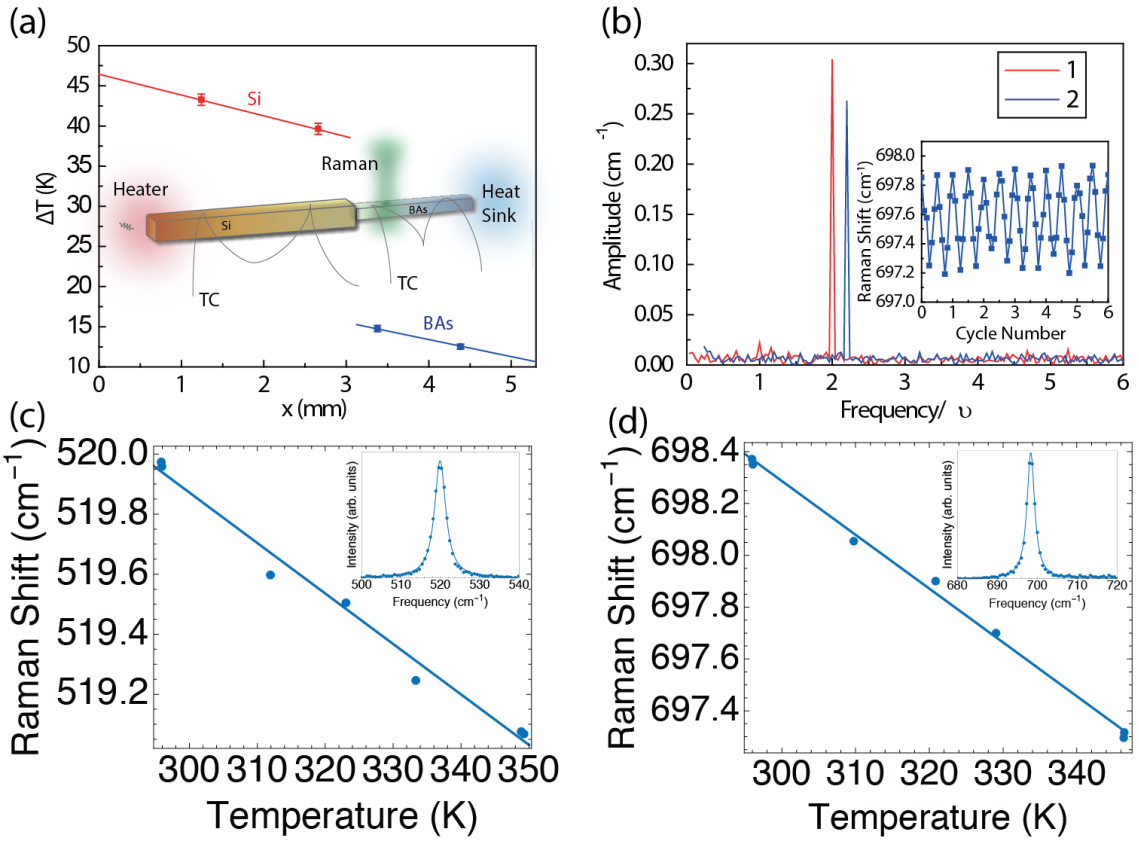

Figure 3.3: (a) Measured temperature drop as a function of x along the Si bar and BAs bar (circles). Lines are linear fits. The inset schematically shows the comparative method. (b) Amplitude spectrum of the Raman shift taken at $x = 3.38$ mm (location 1) and $x = 4.39$ mm (location 2) along the BAs bar. They are offset by 0.2 along the x-axis so that the two can be distinguished. The inset shows the raw Raman peak position modulation caused by the heating. Peak shift as a function of hot plate temperature for (c) Si and (d) BAs. The lines are linear fits, obtaining $\chi_{Si} = -0.0176$ cm^{-1}/K and $\chi_{BAs} = -0.02094$ cm^{-1}/K, and the insets show prototypical Raman peaks.

amplitude spectrum of the peak shift alone. The signal-to-noise ratio (SNR) of the second harmonic peak in the zero-point offset amplitude spectrum was as large as 140, meaning the ratio of the noise floor to the signal was only about 0.7%. This represents the relative uncertainty in the Raman peak shift measurement. In comparison, the difference in the peak amplitudes shown in Fig. 3.3(b) was 15%, indicating that this measurement approach is sufficiently sensitive to resolve the temperature drop along

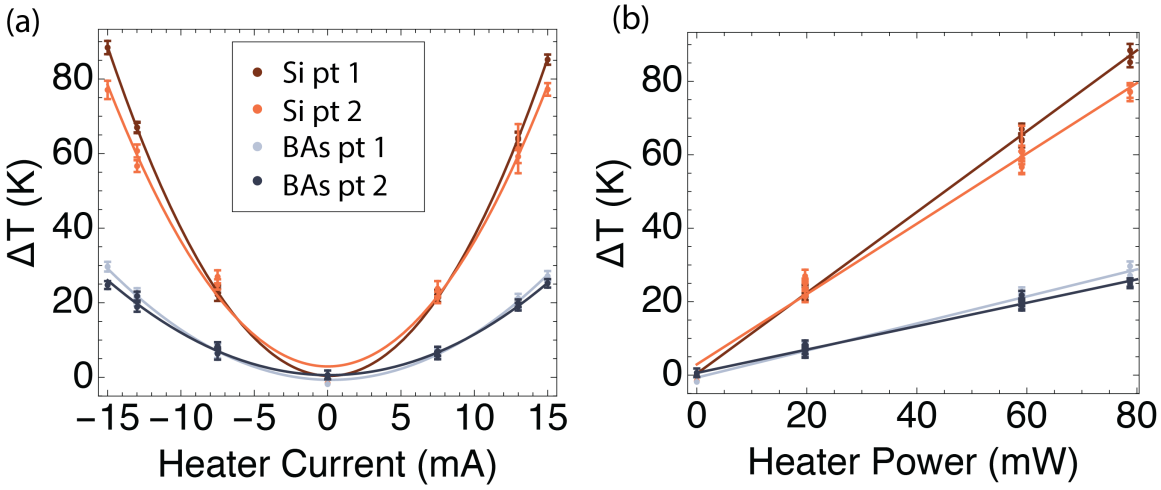

Figure 3.4: Measured temperature rise at two locations along the Si reference and BAs sample as a function of heater current (a) and heater power (b). Dashed lines are fits to the data, quadratic in (a) and linear in (b).

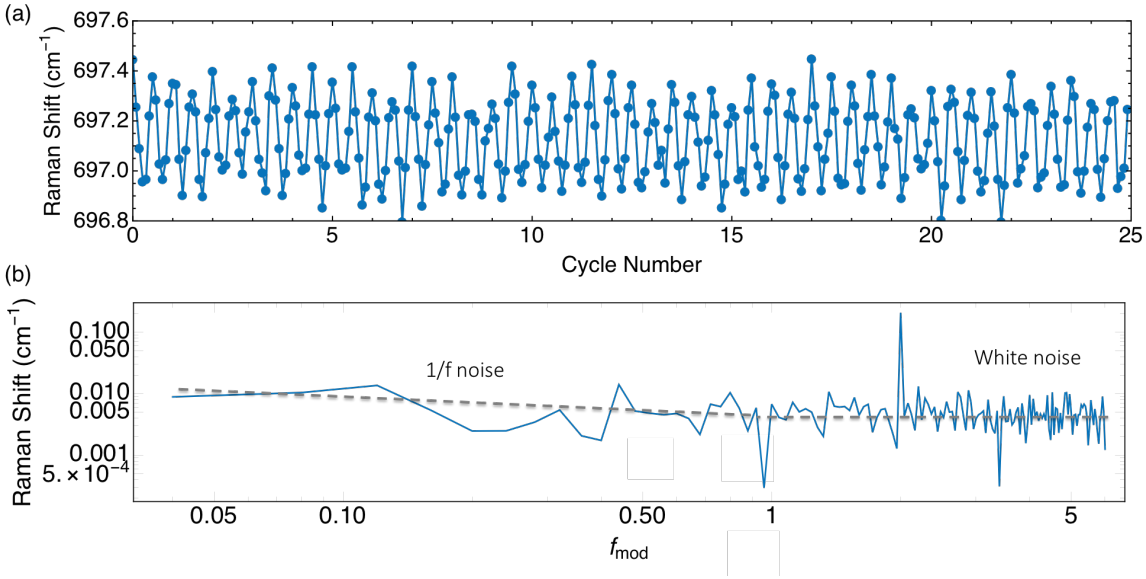

Figure 3.5: (a) Measured Raman shift over 25 heating cycles. (b) The FFT of (a) with the $1/f$ and white noise regions indicated.

the sample. Further details about the uncertainty analysis in the measurements will be discussed below.

Uncertainty Analysis for the Steady-State Comparative Measurements and LIRT

As derived in Eqn. (3.2), the thermal conductivity of a sample in the comparative method is obtained as

$$\kappa_s = \frac{\kappa_r \nabla T_r A_r}{\nabla T_s A_s} \tag{3.3}$$

in which temperature gradient is given as $\nabla T = \Delta T/\Delta x$, and the temperature drop ΔT across length $\Delta x = x_2 - x_1$ is measured by either the differential thermocouples or by scanning the Raman probe laser. As such, in the LIRT measurement, the temperature drop is $\Delta T = \Delta T_2 - \Delta T_1$, where ΔT_i is the temperature rise measured at location i. As before, the uncertainty in κ_s is calculated by the quadrature sum:

$$\delta\kappa_s = \left[\left(\frac{\partial\kappa_s}{\partial\kappa_r}\delta\kappa_r\right)^2 + \left(\frac{\partial\kappa_s}{\partial\nabla T_r}\delta\nabla T_r\right)^2 + \left(\frac{\partial\kappa_s}{\partial A_r}\delta A_r\right)^2 + \left(\frac{\partial\kappa_s}{\partial\nabla T_s}\delta\nabla T_s\right)^2 + \left(\frac{\partial\kappa_s}{\partial A_s}\delta A_s\right)^2\right]^{1/2} \tag{3.4}$$

In the Raman measurements in particular, the uncertainty in the temperature drop is obtained from the quadrature sum of the uncertainties in ΔT_i as

$$\delta\Delta T = \left[\left(\frac{\partial\Delta T}{\Delta T_1}\delta\Delta T_1\right)^2 + \left(\frac{\partial\Delta T}{\Delta T_2}\delta\Delta T_2\right)^2\right]^{1/2} \tag{3.5}$$

The uncertainty in each Raman-measured temperature rise ΔT_i arises from two sources − the uncertainty in the measured Raman shift $\Delta\omega$ and uncertainty in the calibrated Raman temperature coefficient χ. The uncertainty in $\Delta\omega$ is quantified by the SNR of the second harmonic peak amplitude in the FFT of the zero-point offset Raman shift data. As discussed previously, the relative uncertainty in the peak shift is on the order of 0.7%, which is appreciably smaller than the random uncertainty obtained by simply averaging the data together. Once the Raman shift $\Delta\omega$ is measured, it is then converted into a temperature rise based on the Raman temperature coefficient $\chi = d\omega/dT$, which is the second source of random uncertainty. The temperature rise measured by Raman at point i is $\Delta T_i = \frac{\Delta\omega}{\chi}$ and its uncertainty is

$$\delta\Delta T_i = \left[\left(\frac{\partial\Delta T_i}{\Delta\omega_i}\delta\Delta\omega_i\right)^2 + \left(\frac{\partial\Delta T_i}{\partial\chi}\delta\chi\right)^2\right]^{1/2} \tag{3.6}$$

The coefficient χ is obtained by a least-squares fit to a set of N data point pairs (T_p, ω_p). The least-squares fit algorithm obtains the slope as

$$\chi = \frac{N\sum_{p=1}^{N} T_p\omega_p - \sum_{p=1}^{N} T_p \sum_{p=1}^{N} \omega_p}{N\sum_{p=1}^{N}(T_p)^2 - \left(\sum_{p=1}^{N} T_p\right)^2} \tag{3.7}$$

Therefore the random uncertainty in χ propagated through the least-squares fit is

$$\delta\chi = \left[\sum_{p=1}^{N}\left(\frac{\partial\chi}{\partial\omega_p}\right)^2 \delta\omega_p^2 + \sum_{p=1}^{N}\left(\frac{\partial\chi}{\partial T_p}\right)^2 \delta T_p^2\right]^{1/2} \tag{3.8}$$

in which $\delta\omega_p$ is the random uncertainty in n measurements of the Raman shift taken at each temperature point T_p. This uncertainty is given by

$$\delta\omega_p = \frac{t_{n-1,95}\sigma_{\omega_p}}{\sqrt{n}} \tag{3.9}$$

where $t_{n-1,95}$ is the t-distribution value for 95% confidence and $n-1$ degrees of freedom, and σ_{ω_p} is the standard deviation in the n measured ω_p values.

With the uncertainties in the Raman measurements propagated, the temperature gradients along the Si and the BAs can be quantified with reasonable precision in a contact-free measurement. As shown in the comparison in Fig. 3.6(a), temperature gradients measured by the differential thermocouples and by LIRT are the same within uncertainty. Figure 3.6(b) shows the thermal conductivity of the three BAs samples measured by the thermocouples in addition to that measured by LIRT (open triangle). The temperature in the LIRT measurement was taken as the cryostat ambient temperature plus the average temperature rise in the BAs because a larger heating power was used in LIRT as compared with the thermocouple-based measurements. The non-contact measurements by LIRT validate BAs as the only semiconductor with ultrahigh thermal conductivity.

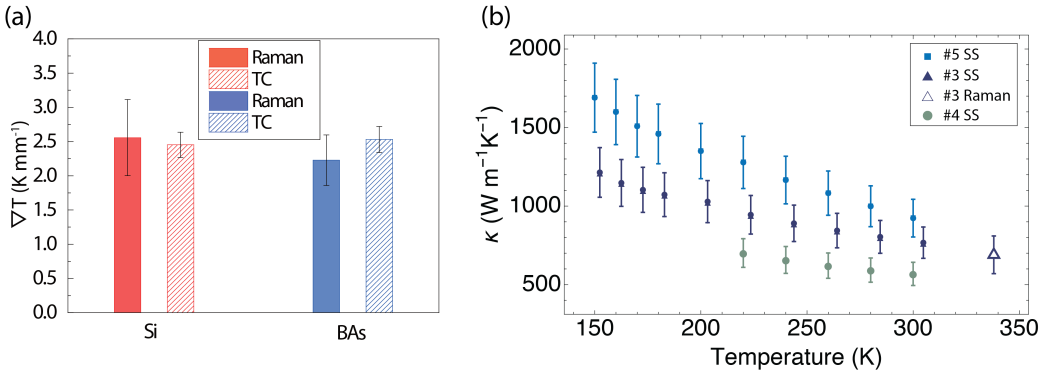

Figure 3.6: (a) Comparison of the temperature gradients (∇T) measured on the Si and BAs #3 by thermocouples (TC) and LIRT at an ambient temperature of 308.9 K and a heater power of 81 mW. (b) Temperature-dependent bulk thermal conductivity of BAs samples #3-5 obtained by the steady state comparative method and lock-in Raman for BAs #3 (open triangle).

3.4 Measurement of Thermal Transport in a BAs Microrod

As shown in prior work from UT Austin, BAs microstructures can be obtained during the chemical vapor transport (CVT) growth process when using boron particles as a source/seed.[163–165] These structures nucleate on the surface of the boron particles and grow outward into high aspect ratio needles or microrods. Figure 3.7 shows one such microrod that was transferred to a microfabricated device, with one end of the rod resting on a suspended metal serpentine heater patterned on a silicon nitride membrane and the other end resting on the surface of a silicon nitride/silicon wafer. The adjacent suspended heating membrane is left blank. The side-view scanning electron micrograph in Fig. 3.7(b) shows the roughly conical cross-section of the microrod. After transfer, $\sim$1.5 μm of aluminum was deposited on the two ends of the rod by electron beam evaporation through a shadow mask in order to enhance thermal contact between the suspended heater and the supported heat sink. The device was then loaded into an optical cryostat (Montana Instruments) and evacuated to high vacuum by a turbomolecular pump.

Measurement of the thermal conductance of the microrod was carried out using the suspended serpentine metal line as a heater with quantifiable heating power and

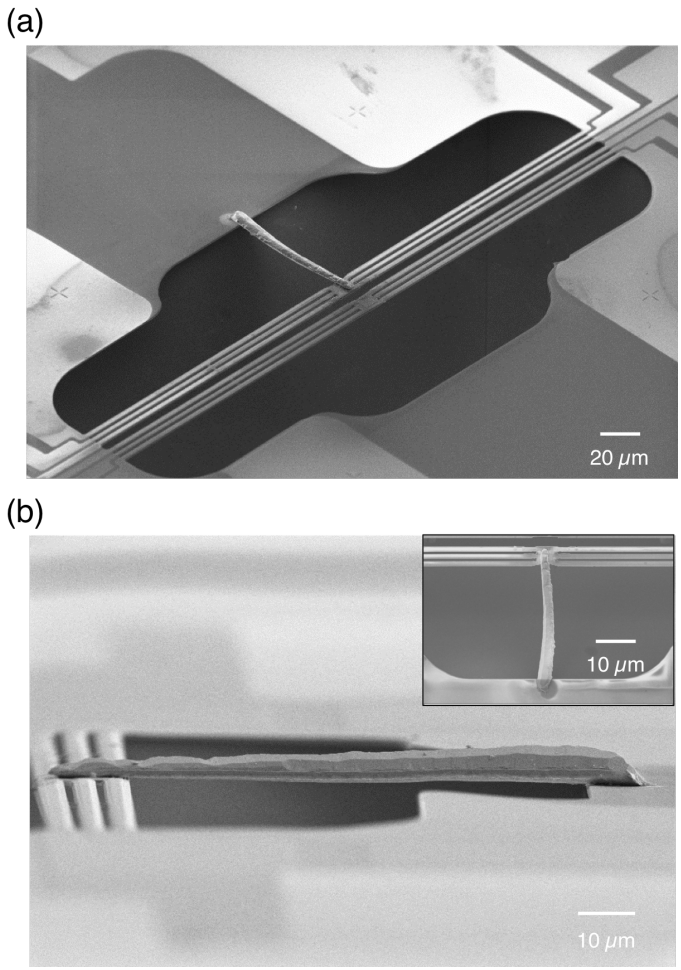

Figure 3.7: Scanning electron micrographs of the BAs microrod with one end resting on a suspended heater/thermometer device and the other end supported on the substrate (a) in perspective and (b) up-close side view. The inset in (b) is a top-down view.

using micro-Raman thermometry to probe the temperature rise at various locations along the sample's length. A $\lambda = 532$ nm laser with a power of approximately 115 μW was focused through a 50$\times$ long working distance objective lens onto the microrod while a direct heating current, I was provided to the serpentine on the heating membrane to generate a Joule heating power of $Q_h = I^2 R_h$. The Raman-active zone-center T_2 phonons in the cubic BAs produce inelastically scattered light with a Raman shift of approximately 698 cm^{-1}. This Stokes-shifted light was sent to a Raman spectrometer with a 320 mm focal length and a diffraction grating with

2400 grooves per mm to achieve a spectral resolution of around 1.1 cm^{-1}.

3.4.1 LIRT Measurements of a BAs Microrod

Lock-in Raman thermometry was again employed to investigate the intrinsic thermal conductivity of BAs. In this approach, the DC heating current was stepped in discrete intervals to follow a sinusoidal pattern of the form $I(j) = I_0 \sin \frac{2j\pi}{N}$ where $I_0 \approx 350\mu$A, $N = 12$, and the integer j increases from 0 to $40N$, i.e. 40 full periods of 12 discrete points were used. At each of the discrete values of the heating current, the Raman spectrum at a particular point along the BAs was collected over 6 seconds, meaning each cycle took approximately 72 seconds. This is shown schematically in Fig. 3.8(a), which shows a false-color scanning electron micrograph of the suspended microrod and the three measured locations at 11.9, 36.9, and 70 μm away from the heater edge indicated by green circles. During the measurement, the voltage and the current though the heating line are measured. Each applied DC heating current $I(j)$ generates a Joule heating power of $Q_h(j) = I(j)^2 R_h$ in the serpentine heater and $Q_L(j) = I(j)^2 R_L$ in the current-carrying leads with resistance R_L. Because the power depends quadratically on the supplied current, Q_h and Q_L, and thus the temperature rise ΔT will vary at twice the frequency of the applied current, or $2\nu_J$. The measured heating current over the first 10 cycles of a measurement is shown in Fig. 3.8(b), while the corresponding measured Raman shift at a point in the BAs microrod is shown to oscillate at twice the frequency of the applied heater current (Fig. 3.8(c)).

Fourier frequency component analysis was used to isolate the Raman shift at various points in the BAs microrod due to heating in the suspended membrane. The fast Fourier transform (FFT) algorithm as implemented by Matlab was used to convert the Raman shift time-series data, e.g. that shown partially in Fig. 3.8(c), into the frequency domain. Fig. 3.9(a) displays the amplitude spectra obtained by the FFT of the Raman shift time-series data obtained at each of the three points along the microrod at $T = 298$ K. The only evident peak in the amplitude spectra occurs at the second harmonic, $2\nu_J$, which is the same frequency as the Joule heating in the suspended heater. Compared to traditional Raman thermometry measurements, this numerical lock-in approach improves the sensitivity by removing the broad spectrum of noise at other frequency components through the isolation of only the Joule heating

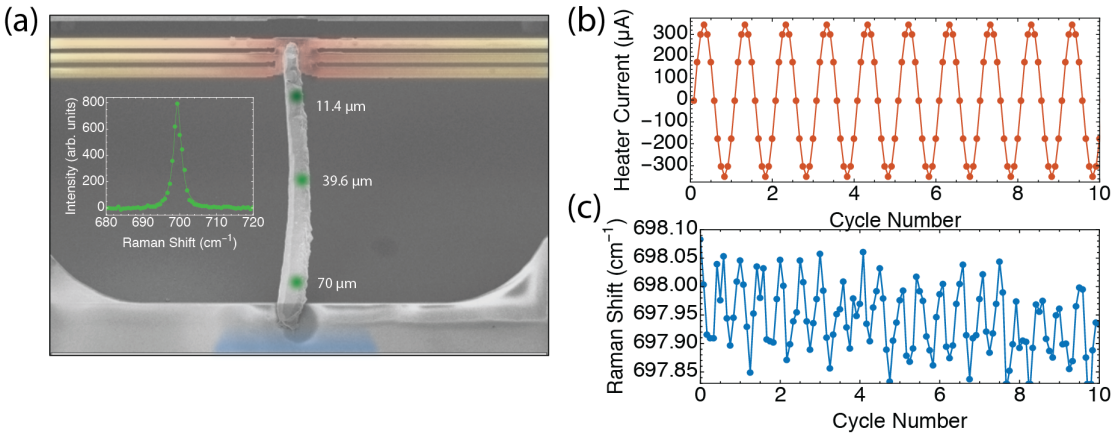

Figure 3.8: (a) False-color scanning electron micrograph of the suspended BAs microrod with the locations of the Raman-measured temperature rise indicated schematically by the green circles. (Inset) Raman spectrum collected at $T = 233.5$ K. (b) Measured heater current over the 10 first cycles. The 12 discrete points per cycle approximate a sine with frequency ν_J. (c) Corresponding Raman shift over the first 10 cycles.

component at the second harmonic. The Raman spectra taken when there is no heating applied to the device ($Q_h = Q_L = 0$) were used to calibrate the peak shift versus ambient temperature slope, shown in Fig. 3.9(b). By using the slope $\chi = \frac{df_R}{dT}$, the second harmonic amplitude $\langle \delta f_R \rangle_{2\nu_J}$ can be converted into an equivalent temperature rise at the point x probed by the laser as

$$\Delta T(x) = \frac{\langle \delta f_R \rangle_{2\nu_J}(x)}{\chi(x)} \tag{3.10}$$

The procedure of obtaining the ΔT versus position (x) was performed for multiple ambient temperatures between 233.5 K and 320 K. During the Raman measurements, the heater current, two-probe voltage, and four-probe voltage across the suspended heater was simultaneously measured. In addition, the two-probe and four-prove I-V characteristics of the adjacent blank suspended heating device were measured under the same ambient conditions.

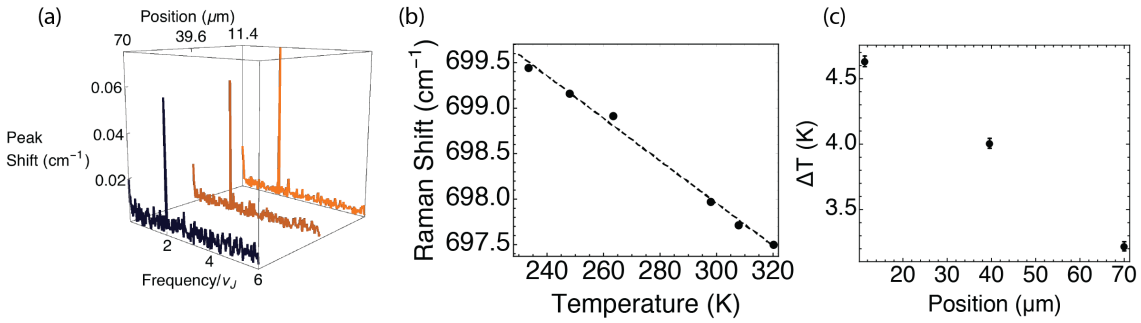

Figure 3.9: (a) Amplitude spectra of the measured Raman shift data at the three different points probed along the length of the microrod. The large peak at the second harmonic of the current excitation frequency decreases as function of distance from the heating membrane. (b) Measured Raman shift as a function of ambient cryostat temperature when there is no heating applied to the device. (c) Equivalent temperature rise as a function of position using the amplitude of the second harmonic peaks in (a) and the slope of (b) to convert to ΔT.

Differential Measurement to Isolate BAs Heat Flux

To obtain the thermal conductance of the sample, it is necessary to know the heat flow though it. As shown schematically in Fig. 3.10(a), both heater islands are connected to the ambient environment at temperature T_0 by six silicon nitride beams. The excitation current is delivered to the heating membrane through leads on beams $i = 1, 2$ for the blank device and $i = 7, 8$ for the device with the BAs sample, thereby generating heating power Q_L on each of the leads. Q_L generates a parabolic temperature distribution along the length of the beams that is symmetric about the halfway point, causing half of the heat flow $Q_L/2$ to go toward the heating membrane and half to go to the ambient. Meanwhile, current flow through the serpentine heaters on the membranes generates a heating power $Q_{h,B}$ and temperature rise $\Delta T_{h,B} = T_{h,B} - T_0$ on the blank heater island, and similarly a heating power $Q_{h,S}$ on the heater island with the sample generates a temperature rise $\Delta T_{h,S} = T_S - T_0$. The generated heat is transferred to the environment through the beams, each with nominal thermal conductance g_B and through the BAs sample with conductance G_{BAs}. For the blank heater, the heat flow through the beams into the substrate can be written as

$$\begin{aligned} Q_{1-2} &= 2\left(g_b \Delta T_{h,B} + Q_{L,B}/2\right) \\ Q_{3-6} &= 4 g_b \Delta T_{h,B} \end{aligned} \tag{3.11}$$

and for the heater with the sample:

$$\begin{aligned} Q_{7-8} &= 2\left(g_b \Delta T_{h,S} + Q_{L,S}/2\right) \\ Q_{9-12} &= 4 g_b \Delta T_{h,S} \\ Q_{BAs} &= G_{BAs} \Delta T_{h,S} \end{aligned} \tag{3.12}$$

Figure 3.10(b) shows the equivalent thermal circuit for this configuration, with the total beam resistance $\mathcal{R}_b = 1/(6g_b)$. This makes the assumption that the beam conductances g_b are nominally the same for both the blank and non-blank heater islands, which is typically true to within 5%.[166] In addition, the heat generated in each of the heater islands must be balanced exactly by the heat dissipation in the substrate due to the conservation of energy:

$$\begin{aligned} Q_{h,B} + 2Q_{L,B} &= Q_{1-2} + Q_{3-6} \\ &= 2\left(g_b \Delta T_{h,B} + Q_{L,B}/2\right) + 4 g_b \Delta T_{h,B} \\ &= G_b \Delta T_{h,B} + Q_{L,B} \end{aligned} \tag{3.13}$$

for the blank device, and

$$\begin{aligned} Q_{h,S} + 2Q_{L,S} &= Q_{7-8} + Q_{9-12} + Q_{BAs} \\ &= 2\left(g_b \Delta T_{h,S} + Q_{L,S}/2\right) + 4 g_b \Delta T_{h,S} + Q_{BAs} \\ &= \Delta T_{h,S} G_b + Q_{BAs} + Q_{L,S} \end{aligned} \tag{3.14}$$

for the heater with the sample, with $G_b = 6g_b$. Eqns. (3.13) and (3.14) simplify to

$$\begin{aligned} Q_{total,B} &= Q_{h,B} + Q_{L,B} = G_b \Delta T_{h,B} \\ Q_{total,S} &= Q_{h,S} + Q_{L,S} = \Delta T_{h,S} G_b + Q_{BAs} \end{aligned} \tag{3.15}$$

Therefore, a measurement of $Q_{total,B}$ versus $\Delta T_{h,B}$ in the blank device can obtain the total beam conductance G_b, and the heat flux through the BAs, Q_{BAs}, can be isolated.

The voltage drop between two points where current-carrying lines meet the substrate, V_{2p} yields the heating power $Q_h + 2Q_L = I_h V_{2p}$. Meanwhile, the power in the serpentine heater is obtained from the four-probe voltage configuration as $Q_h = I_h V_{4p}$. Therefore, the power dissipated in the current-carrying leads is $Q_L = I_h \left(V_{2p} - V_{4p}\right)/2$,

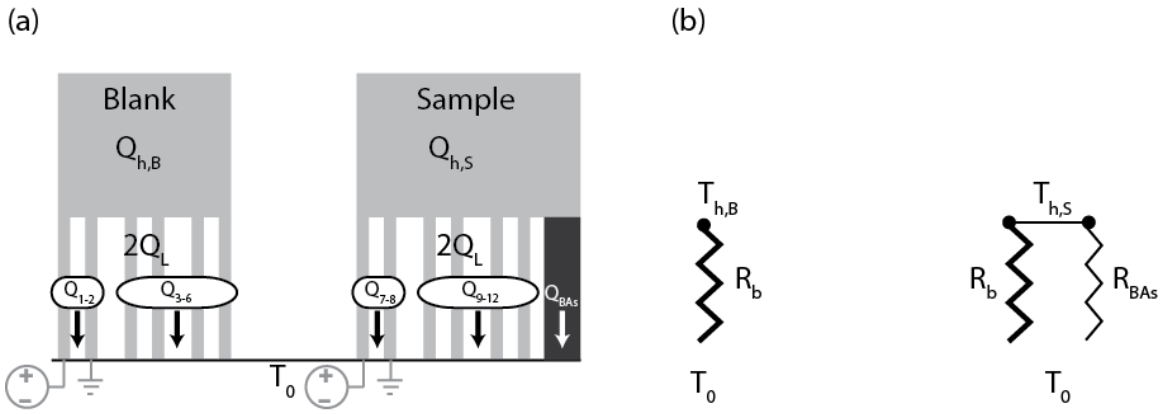

Figure 3.10: (a) Schematic of the two suspended micro-heaters that comprise the measurement device and the heat conduction pathways to the environment. (b) The equivalent thermal circuit.

and the beam conductance can be obtained from the blank device and Eqn. 3.15 as $G_b = (Q_{h,B} + Q_{L,B})/\Delta T_{h,B}$. The temperature rise in the heaters is measured by resistance thermometry − measuring the change in resistance in the blank and sample-contacting heaters $\Delta R_{h,B}$ and $\Delta R_{h,S}$. At each of the environment temperatures, T_0, the resistance of the heater is measured at zero heating power $R_h(I_h = 0)$, which yields the temperature coefficient of the blank and sample-contacting resistance thermometers $dR_{h,B}/dT$ and $dR_{h,S}/dT$, respectively. The temperature rises are thus $\Delta T_{h,B} = \Delta R_{h,B}/(dR_{h,B}/dT)$ and $\Delta T_{h,S} = \Delta R_{h,S}/(dR_{h,S}/dT)$. Fig. 3.11(b) shows the blank heater plus lead power, $Q_{h,B} + Q_{L,B}$, versus the heater temperature rise $\Delta T_{h,B}$ for $T_0 = 298$ K. From Eqn. 3.15, the slope yields the total beam conductance of $G_b \approx 130$ nW/K. With the extracted beam conductance, the heat flow through the sample is then

$$Q_{BAs} = Q_{h,S} + Q_{L,S} - G_b \Delta T_{h,S} \tag{3.16}$$

where $Q_{L,S}$ is again obtained from the difference between the two-probe and four-probe voltage measurements.

Assuming one dimensional heat conduction, the heat flux through the sample is related to its thermal conductivity as

$$Q_{BAs} = Q_x = -\kappa_{BAs} A_c \frac{dT}{dx} \tag{3.17}$$

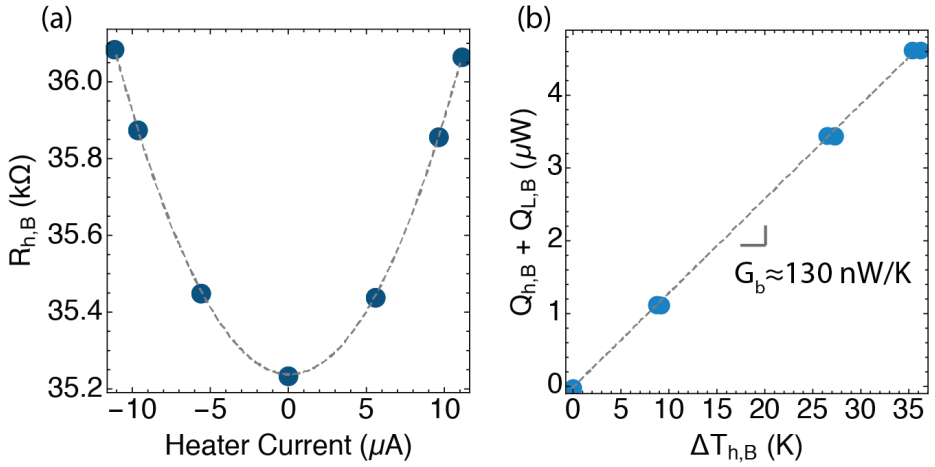

Figure 3.11: (a) Blank serpentine heater resistance as a function of applied heating current at $T_0 = 298$ K. Gray, dashed line is a quadratic fit. (b) Serpentine heater + lead power versus temperature rise in the blank heater. The line is a linear fit whose slope yields the beam conductance, G_b.

where A_c is the cross-sectional area of the microrod and varies along the length of the conically-shaped sample. The thermal conductivity can be obtained by numerically integrating Fourier's law and solving for the temperature in terms of the varying cross-sectional area:

$$\begin{aligned} dT &= Q_x \frac{dx}{\kappa A_c(x)} \\ \int_0^{\Delta T(x)} dT &= \int_0^x Q_x \frac{dx}{\kappa A_c(x)} \\ \Delta T(x) &= \Delta T(0) + \frac{Q_x}{\kappa} \int_0^x \frac{1}{A_c(x)} dx \end{aligned} \tag{3.18}$$

The cone-shaped microrod had an elliptical cross-section with a semi-major axis half-length of $a_1 = 4.6$ μm and semi-minor axis half-length of $b_1 = 3.3$ μm on the large end of the cone and $a_2 = 3.1$ μm and $b_2 = 2.0$ μm on the small end of the cone as measured by SEM. The cross-sectional area is assumed to vary along x according

to

$$A_c(x) = \pi r_1(x) r_2(x)$$

where

$$r_1(x) = \frac{(a_2 - a_1)x}{L} + a_1 \qquad (3.19)$$

$$r_2(x) = \frac{(b_2 - b_1)x}{L} + b_1$$

The last equation in (3.18) is fit to the experimentally measured temperatures at the three different positions along x and the thermal conductivity κ can be obtained based on the fit. The uncertainty is then estimated based on the difference between the numerically calculated temperature and the experimentally measured temperatures. The thermal conductivity of the microrod as a function of temperature is shown in Fig. 3.12.

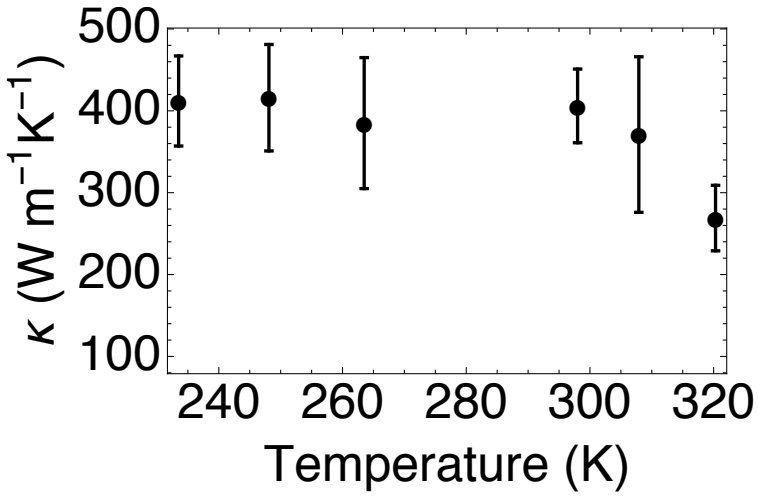

Figure 3.12: Thermal conductivity of the BAs microrod as a function of average temperature as measured by lock-in Raman.

3.5 Origin of Reduced Thermal Conductivity in BAs

Previous measurements of BAs have obtained thermal conductivity values only as high as a couple hundred $\mathrm{Wm^{-1}K^{-1}}$ in relatively small crystals or microstructures.

[160,165,167], and recently in large crystals.[168] The relatively low thermal conductivities were attributed to elemental impurities from the source materials, crystal grain boundaries, charge carrier-phonon scattering due to unintentional doping, point defects including isotopic disorder, and vacancies resulting from arsenic deficiency. The latter, for example, was thought to be especially plausible due to the disparate melting temperatures and thus vapor pressures between elemental boron and arsenic in the growth process and the As deficiency was found to be as high as 2.8%.[167] However, Fig. 3.13 shows representative X-ray photoelectron spectroscopy (XPS) signals for the As 3d and B 1s peaks for a BAs particle grown by CVT. Based on the XPS spectra, the atomic ratio of As:B is calculated to be 49.98:50.02, indicating an As deficiency of only about 0.04% in this sample. However, other impurities may be the cause of the reduced thermal conductivity, which is presently being investigated by time of flight secondary ion mass spectrometry (TOF-SIMS) analysis.

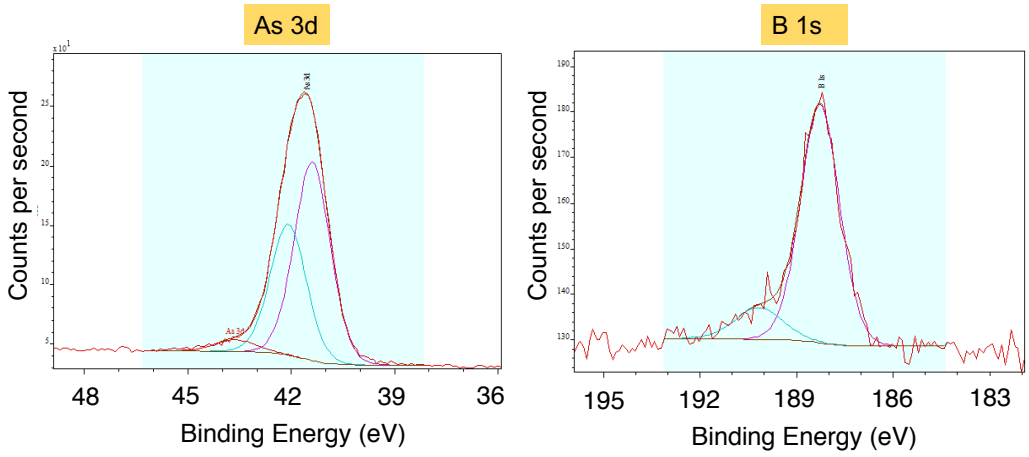

Figure 3.13: XPS spectrum for a CVT-grown BAs particle after 15 seconds of sputtering with argon ions. The calculated As:B ratio of the particle is 49.98:50.02.

Figure 3.14 shows the measured thermal conductivity of the three bulk BAs samples grown at UH measured by the steady-state comparative method and LIRT along with the results for the microrod grown at UT. The red solid line is the intrinsic thermal conductivity calculated from first principles by David Broido's group. Specifically, density functional perturbation theory (DFPT) was used to obtain the interatomic force constants (IFCs) up to the fourth order. A full solution of the Boltzmann transport equation (BTE) for phonons including three-phonon, four-phonon,

and Tamura-type isotope impurity scattering using the natural abundance of $^{10}B/^{11}B$ was implemented to obtain the intrinsic thermal conductivity. While the bulk thermal conductivity values obtained for BAs are quite high, it is clear that they are still below the theoretical limit. In addition to three-phonon, four-phonon, and isotope impurity scattering, the experimental measurements were fit with the additional phonon-point defect scattering rates and grain boundary scattering. A mass variance parameter, g, was used to characterize the strength of the scattering by point defects. Meanwhile, the grain boundary scattering rate was taken as $1/\tau_\lambda^{gb} = L/v_\lambda$, where L is the characteristic grain size and v_λ is the group velocity of mode λ. As indicated in the legend, sample BAs #4 is found to have the smallest characteristic grain size and largest mass variance parameter, while #5 has the largest grain size and lowest g. In addition, it was found that the experimental data could not be adequately fit by considering three-phonon scattering alone. In particular, the full BTE considering three-phonon scattering alone predicts a considerably weaker temperature dependence of the thermal conductivity.[35]

Furthermore, cross-sectional TEM analysis was performed on BAs crystals grown at UH. While no point defects or vacancies were clearly visible, planar defects including mirror twin boundaries were observed. In addition, TDTR and FDTR measurements found variation in the thermal conductivity at different locations on the same sample. For sample #1, the lowest measured room temperature value was 640 ± 70 $Wm^{-1}K^{-1}$, while the largest was 1160 ± 130 $Wm^{-1}K^{-1}$. The fitting of the experimental data to the calculations, the cross-sectional TEM results, and the spatially varying thermal conductivity indicate that planar defects such as grain boundaries and point defects, including vacancies or impurity atoms, play an important role and may be the cause for reduced bulk κ in the measured crystals. These results motivate the very sensitive dependence of BAs thermal conductivity on any defects in the crystal.

3.6 Summary

Millimeter-scale boron arsenide (BAs) crystals grown at UH were measured to have high thermal conductivities by a variety of techniques. To investigate the bulk thermal conductivity (κ) of these crystals, a steady-state comparative method us-

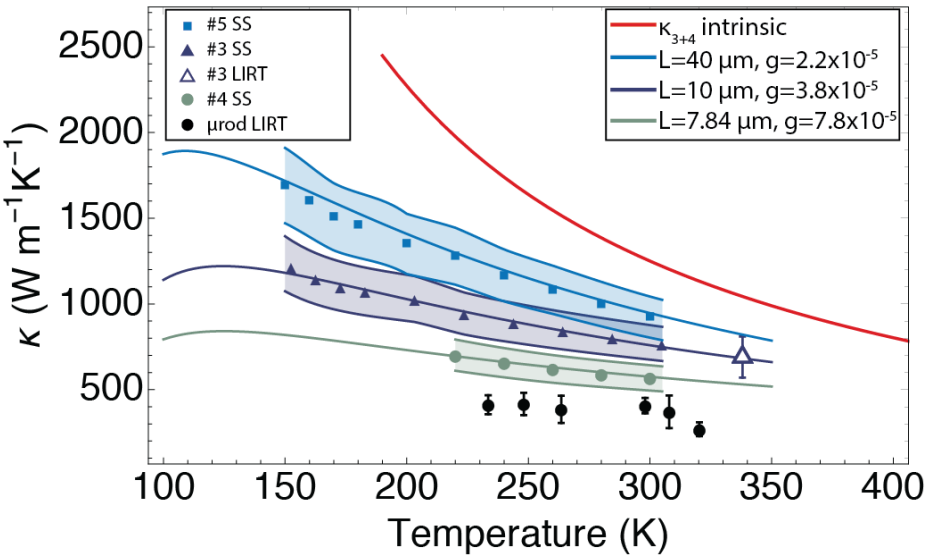

Figure 3.14: Temperature-dependent bulk thermal conductivity of BAs samples #3-5 obtained by the steady state comparative method and lock-in Raman (open triangle) and for a BAs microrod obtained by lock-in Raman (black circles). The lines are theoretical calculations that include three- and four-phonon scattering, as well as scattering by isotopic disorder and point defects and grain boundaries. Boundary scattering mean free path L and point scattering strength parameter g are specified in the legend. The shaded bands demarcate the uncertainties in the experimentally-measured data.

ing silicon (Si) as a reference material and differential thermocouples as temperature sensors was employed. These measurements obtained room temperature thermal conductivity values up to almost 1000 $\mathrm{Wm^{-1}K^{-1}}$. However, measurements of high thermal conductivity materials are prone to errors due to thermal resistance at contacts made with the high-κ sample. To investigate the role of thermal contact resistance and to validate the ultrahigh κ of BAs, a contact-free lock-in Raman technique was developed.

The lock-in Raman thermometry (LIRT) utilized a modulated heating profile that followed a discrete sinusoid. Steady-state was reached at each heating condition, and the peak shift in the Raman spectrum of either the Si or the BAs was used as a temperature sensor. Fourier component analysis of the results was used to isolate the second harmonic component of the Raman shift caused by the modulated Joule heating in the heater placed on the Si. This approach was found to help

eliminate the broad spectrum of noise that is ordinarily averaged into traditional Raman thermometry measurements, and improves the sensitivity to be better than 1 K. The measured temperature gradients, and thus thermal conductivity of the BAs was found to match that obtained by the differential thermocouples, thereby showing a minimal effect of contact resistance in the measurements and validating BAs as the only semiconductor with ultrahigh thermal conductivity.

In addition, the thermal conductivity of a BAs microstructure grown at UT Austin was measured by LIRT. In lieu of a comparative method, the heat flux through the sample was quantified by using a suspended microfabricated heater/sensor device in a differential configuration. By performing thermal circuit analysis of the blank and sample-contacting heaters, the heat flux through the sample was able to be isolated and the thermal conductivity was obtained.

Finally, BAs has been predicted to have a bulk thermal conductivity somewhat higher than the crystals measured here at around 1300 $\mathrm{Wm^{-1}K^{-1}}$. While previously predicted to have even larger thermal conductivity (> 2000 $\mathrm{Wm^{-1}K^{-1}}$) based on calculations including up to three-phonon scattering, new first-principles calculations have indicated an appreciable effect of four-phonon scattering in BAs. The temperature-dependence of the experimental results was only able to be fit by including three- and four-phonon scattering. In addition, the inclusion of phonon-grain boundary scattering and phonon-point defect scattering to fit the experimental results, along with cross-sectional transmission electron microscopy of crystals indicates the importance of planar defects (e.g. mirror twin boundaries) and point defects on boron arsenide's thermal transport characteristics. While these results finally validate BAs as an ultrahigh-κ semiconductor, there is still much to be understood about its synthesis-processing-thermal properties relationships, as well as improving the scalability of BAs growth.

Chapter 4

Spin-Mediated Energy Transport In Magnetic Insulator-Heavy Metal Heterostructures

4.1 Background

The generation, control, and detection of pure spin currents is central to any spintronic device. Past and present iterations of such devices have relied heavily on ferromagnetic metals to generate polarized spin currents or to modulate the magnetotransport behavior of charge currents through their magnetization-dependent resistance, or magnetoresistance (MR). A panoply of MR effects have been uncovered in metallic ferromagnets, including anisotropic magnetoresistance (AMR),[66] giant magnetoresistance (GMR),[68,169] and tunnel magnetoresistance (TMR),[67,170–172] and play a critical role in modern data storage technologies.[173] In addition, MR effects have been uncovered in normal metals that are in close proximity to ferromagnets and are enabled by the spin Hall effect (SHE).[63,69,70] Predicted by D'yakonov in the 1970s and first referred to as such by Hirsch in the late 1990s, the SHE in a normal metal can convert some portion of an ordinary charge current into a pure spin current (i.e. net zero charge, yet finite angular momentum) that flows transverse to the charge current; meanwhile, the inverse effect can generate a transverse electric potential from a pure spin current.[51,52,174]

Because the generated pure spin current does not have to be collinear with the ordinary charge current, the SHE has opened up the possibility for launching and detecting spin currents in magnetic insulators (MIs). In such a configuration, a normal metal film in which the SHE is appreciable is deposited on top of the MI. When a charge current is passed through the metal film, a pure spin current is generated across the film thickness and results in a so-called "spin accumulation" at the metal/MI interface. The polarized spins of the itinerant electrons in the metal are then free to exchange angular momentum with magnons in the MI via a torque, and can generate spin diffusion in the MI that is mediated by magnons. Similarly, a spin current in the MI can polarize a spin current in the metal at the interface, generating a pure spin current across the film thickness that the inverse spin Hall effect (ISHE) can convert into a detectable voltage. The SHE and ISHE have become essential ingredients in driving and detecting spin currents in magnetic insulators, which have potential applications in the field of magnonics. The generation and control of magnon-based spin currents has recently enabled magnonic spin valves and transistors in NM/MI structures.[13–15] In addition, the SHE/ISHE are central to a variety of spin caloritronic phenomena, including the spin Seebeck effect (SSE), which is the generation of a spin current driven by a temperature gradient and its reciprocal, the spin Peltier effect (SPE).

Spin Peltier Effect

As shown in Fig. 4.1, a charge current J_c in a normal metal (NM) flowing along x generates a pure spin current J_s along y with spin polarization along z due to the spin Hall effect. When the magnetization $\boldsymbol{M}$ is perpendicular to spin polarization vectors $s^{\pm 1/2}$ of the electrons in the NM, spin-flip scattering at the interface enables the injection of a spin current that generates a spin transfer torque (STT) on the magnetic order parameter in the MI. The torque attempts to rotate the magnetization, but this does not result in a change in the magnitude of the magnetization or the magnon population. However, when $\boldsymbol{M}$ of the underlying MI is parallel or antiparallel to $s^{\pm 1/2}$, the transfer of angular momentum can annihilate or create a magnon in the YIG, altering the magnon population, equivalent to a heat current $J_q \propto J_s \propto J_c \times \boldsymbol{M}$. The concomitant transfer of energy between the NM electrons and the MI magnons that goes along with the spin current is the spin Peltier effect (SPE).

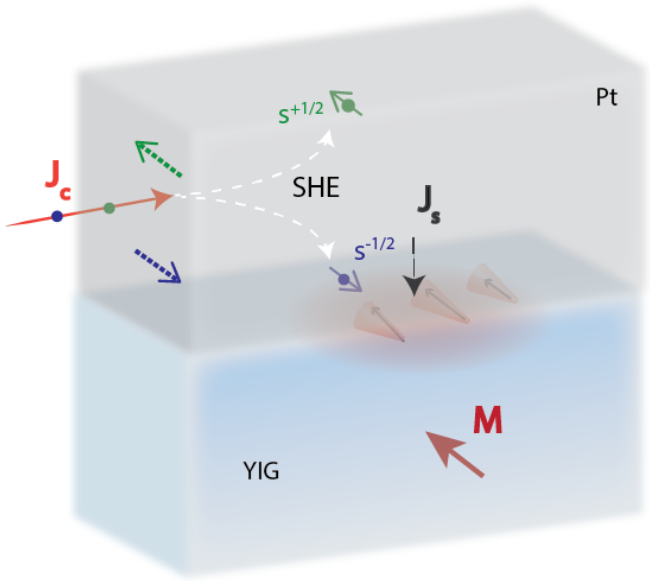

Figure 4.1: Illustration of the spin Hall effect injection of spin current from a normal metal (NM) to a magnetic insulator (MI).

In addition to spin caloritronic effects that modulate temperature by spin-dependent phenomena, there are variety of competing thermoelectric and thermomagnetic effects that can cause spurious temperature and voltage modulations. For example, in a conductor, the ordinary Peltier effect can generate a heat current proportional to the charge current times the Peltier coefficient Π. In the presence of a magnetic field $\boldsymbol{H}$, the ordinary Ettingshausen effect (OEE), which is the reciprocal of the Nernst effect, generates a transverse heat current $Q_E = NT\boldsymbol{B} \times \boldsymbol{J_C}$, where N is the Nernst coefficient, T is the temperature, and $\boldsymbol{B}$ is the magnetic induction and is proportional to the applied magnetic field $\boldsymbol{H}$.[175] If the metal conductor in proximity to the MI is magnetic or is subject to proximity-induced magnetization, furthermore, this opens the door to a variety of magnetotransport and spin-dependent thermoelectric effects, including the anomalous Hall effect (AHE) and the anomalous Ettingshausen effect (AEE). These many commingling phenomena can make detection and interpretation of the SPE challenging.

YIG

Yttrium iron garnet (YIG) is an insulating ferrimagnet with chemical composition $Y_3Fe_5O_{12}$. With its relatively complex garnet crystal structure having 80 atoms (four formula units) per unit cell,[176,177], its thermal conductivity is rather low at around 10 to 11 $Wm^{-1}K^{-1}$ at room temperature.[98,178] Eight of its 20 magnetic Fe^{3+} ions sit on octahedral sites, while the remaining 12 occupy tetrahedral coordinations with the neighboring O^{2-} ions, giving its magnon spectrum 20 distinct branches.[176,179] Despite the complex magnon structure, YIG is unsurpassed in terms of its efficient long-range transport spin currents borne by magnons owing to its low damping parameter, α_G.[64,65] YIG can be grown in high-quality bulk single crystals using the traveling solvent floating zone technique.[98,180] In addition, excellent lattice matching with gadolinium gallium garnet (GGG) allows for the growth of high-quality YIG thin films via liquid phase epitaxy,[181] molecular beam epitaxy,[79] and pulsed laser deposition.[77]

This chapter presents a measurement of coupled charge, spin, and heat transport in Pt/YIG structures. Using lock-in electrothermal measurements, the Pt resistance is found to modulate at the second harmonic. An analytical multitemperature model for the heterostructure is developed and the spin-mediated heat flux and the resulting temperature profiles are derived in the Pt and YIG. In addition, amplitude modulated micro-Brillouin light scattering (BLS) measurements are used to directly probe the magnon population in the YIG at the interface with the Pt, estimating the change in the magnon number density. Meanwhile, spatially-resolved BLS measurements coupled with a 2D magnon diffusion model estimate the magnon spin-flip diffusion length λ_m in the YIG.

4.2 Coupled Heat and Spin Transport at the Pt/YIG Interface and in the YIG

4.2.1 Model for Spin-Mediated Heat Transfer in Pt/YIG/GGG

We first consider a prototypical heterostructure consisting of Pt/YIG/GGG that is common in SPE/SSE measurements. To better describe the coupled spin

and heat transfer resulting from the SPE, an analytical multitemperature model that includes the Pt electrons and phonons, the YIG phonons and magnons, and the GGG phonons is developed. In this model, it is assumed that the temperature of the phonons in the Pt line can be probed using resistance thermometry, resulting from the electron-phonon interaction in the Pt. By solving the coupled differential equations, we can relate the Pt phonon temperature to the equivalent temperature of the magnons in the YIG, and the rate of spin-dependent heat transfer between the Pt and YIG.

Recalling §1.1.1, two- and four-magnon scattering relax energy but not spin and therefore, the magnon-phonon energy relaxation length ℓ_{mp} is considerably shorter than the micron-scale spin-flip diffusion length λ_m.[37,182] If the width of the Pt line to be measured is much larger than the Pt film thickness l and ℓ_{mp}, transport directly beneath the Pt line can be considered as one-dimensional (1D) and it is possible to analytically obtain the spatial distributions of the different temperatures of magnons, phonons, and electrons in the heterostructure. To summarize the derivations outlined in Appendix E, the coupled heat equations considering a two-temperature model for electrons and phonons in the Pt were solved in tandem with coupled equations for phonons and magnons in the YIG and phonons in the GGG. The coupled equations are

$$
\begin{aligned}
&\text{in Pt:}\\
&\nabla\cdot(\kappa_{Pt}\nabla\theta_{p,Pt}+\kappa_{e,Pt}\nabla\theta_{e-p,Pt})+q=0\\
&\nabla^2\theta_{e-p,Pt}-\frac{\theta_{e-p,Pt}}{\ell_{ep}^2}+\frac{q}{\kappa_{e,Pt}}=0\\
&\text{in YIG:}\\
&\nabla\cdot(\kappa_{YIG}\nabla\theta_{p,YIG}+\kappa_{m,YIG}\nabla\theta_{m-p,YIG})=0\\
&\nabla^2\theta_{m-p,YIG}-\frac{\theta_{m-p,YIG}}{\ell_{mp}^2}=0\\
&\text{in GGG:}\\
&\nabla\cdot(\kappa_{p,GGG}\nabla\theta_{p,GGG})=0
\end{aligned}
\tag{4.1}
$$

Here, subscripts m, p, and e refer to magnons, phonons, and electrons, respectively. θ_{m-p} and θ_{e-p} are the difference between the temperature rises for magnons and phonons in the YIG and between electrons and phonons in the Pt, and ℓ_{mp} and ℓ_{ep}

are the energy carrier thermalization lengths for the YIG and Pt, respectively. The source term in the Pt, q, is the heat generation. From these equations, the spin-mediated heat flux $Q^i_{s,}$ across the Pt/YIG interface can be calculated in terms of the Pt phonon temperature rise, $\theta_{p,Pt}$. If the SPE is appreciable, a component of the Pt electron temperature change results from the direct exchange of energy and spin angular momentum between the Pt electrons and the YIG magnons. The Pt phonon temperature change is then affected by the Pt electron temperature through electron-phonon coupling.[19] Resistance thermometry would provide information on the Pt phonon temperature averaged over the thickness of the Pt line as $\langle\theta_{p,Pt}\rangle = \frac{1}{l}\int_0^l \theta_{p,Pt}(y)dy$. In the absence of other sources of heating, the measured average Pt phonon temperature $\langle\theta_{p,Pt}\rangle$ would depend on the spin-mediated heat flux as

$$\langle\theta_{p,Pt}\rangle \approx \left\{ \frac{1}{G_P} + \frac{\ell_{ep}}{\kappa_{Pt}}\left[\coth\left(\frac{l}{\ell_{ep}}\right) - \frac{\ell_{ep}}{l}\right] + \frac{\ell_{mp}}{\kappa_{YIG}}\frac{\cosh\left(\frac{d}{\ell_{mp}}\right)-1}{\sinh\left(\frac{d}{\ell_{mp}}\right)} \right\} Q^i_s \qquad (4.2)$$

In the model, $d = 10$ μm is the YIG film thickness, $l = 7$ nm is the thickness of the Pt, and G_p is the phonon-mediated thermal conductance per unit area of the Pt/YIG interface ($1/G_p$ is the Kapitza resistance). Our collaborators in the Cahill group (UIUC) have measured $G_p \approx (170 \pm 50)$ MW m^{-2}K^{-1} for Pt/YIG interfaces, which equates to a Kaptiza length of $\ell_K \equiv \kappa_{YIG}/G_p \approx 60 \pm 20$ nm. The thermal conductivity of YIG is approximately 10 W m^{-1} K^{-1} based on several measurements,[98,183,184] (§4.2.3) and the electron-phonon coupling length in Pt can be calculated as $\ell_{ep} \approx \sqrt{\kappa_{e,Pt}/g} = 9.4$ nm, where $\kappa_{e,Pt} = 22$ W m^{-1} K^{-1} is obtained from the Wiedemann-Franz relation and the measured electrical resistivity (ρ) of the Pt line (assuming a resistance of 1000 Ω, $w = 20$ μm, $L = 400$ μm), and $g = 2.5 \times 10^{17}$ W m^{-3} K^{-1} is the reported electron-phonon coupling constant for Pt.[185,186]

The calculated $Q^i_s/\langle\theta_{p,Pt}\rangle$ ratio is shown in Fig. 4.2, and is in the range of $(2 - 21) \times 10^3$ W cm^{-2} K^{-1} for the above G_p range and ℓ_{mp} in the reported range between 1 nm and 250 nm.[37,182] The second term in Eqn. (4.2) is the thermal resistance in the Pt and is small in comparison with the Kapitza resistance given by the first term. The third term, meanwhile, is the thermal resistance in the the YIG within a distance ℓ_{mp} of the interface.

In addition, we can calculate the temperature profiles in the vicinity of the

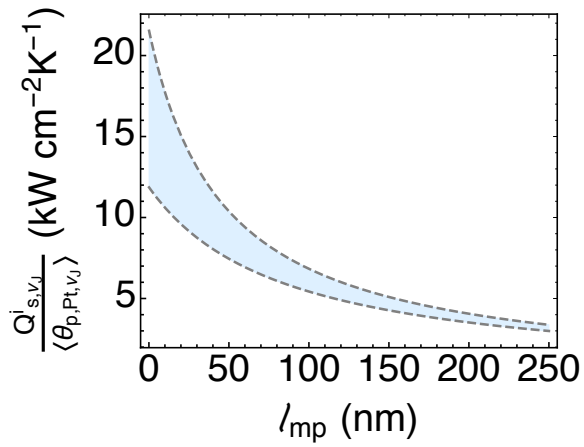

Figure 4.2: The ratio of spin-mediated interfacial heat flux to Pt phonon temperature rise for a range of ℓ_{mp} of 1 to 250 nm and $G_P \approx (170 \pm 50) \times 10^6$ W m^{-2} K^{-1} calculated from Eqn. 4.2. The upper dashed line corresponds to $G_P = 220 \times 10^6$ W m^{-2} K^{-1}, while the lower line corresponds to $G_P = 120 \times 10^6$ W m^{-2}K^{-1}.

Pt/YIG interface. The coupled equations in Eqn. (4.1) have analytical solutions

$$
\begin{aligned}
&\text{in Pt:} \\
&\theta_{e,Pt}(y) = \frac{\kappa_{p,Pt}}{\kappa_{Pt}}\left[b_1 \sinh\left(\frac{y}{\ell_{ep}}\right) + b_2 \cosh\left(\frac{y}{lep}\right)\right] + b_3 y + b_4 \\
&\theta_{p,Pt}(y) = -\frac{\kappa_{e,Pt}}{\kappa_{Pt}}\left[b_1 \sinh\left(\frac{y}{\ell_{ep}}\right) + b_2 \cosh\left(\frac{y}{lep}\right)\right] + b_3 y + b_4 \\
&\text{in YIG:} \\
&\theta_{m,YIG}(y) = \frac{\kappa_{p,YIG}}{\kappa_{YIG}}\left[a_1 \sinh\left(\frac{y}{\ell_{mp}}\right) + a_2 \cosh\left(\frac{y}{\ell_{mp}}\right)\right] + a_3 y + a_4 \\
&\theta_{p,YIG}(y) = -\frac{\kappa_{m,YIG}}{\kappa_{YIG}}\left[a_1 \sinh\left(\frac{y}{\ell_{mp}}\right) + a_2 \cosh\left(\frac{y}{\ell_{mp}}\right)\right] + a_3 y + a_4
\end{aligned}
\tag{4.3}
$$

where a_i and b_i are coefficients described in Appendix E.

Figure 4.3 shows the calculated temperature profiles in the Pt and YIG under spin Peltier cooling assuming a magnon-phonon thermalization length scale of $\ell_{mp} =$ 250 nm in the YIG.[182] The spin Hall injection of magnons in the YIG drives a the magnon and phonon temperatures out of local thermal equilibrium, which is sustained over a distance ℓ_{mp} away from the interface. In the Pt, the electron temperature and

thus the phonon temperature is reduced while the equivalent magnon temperature in the YIG is greatly increased. Within a distance of ℓ_{mp} from the interface, meanwhile, the phonon temperature is dragged down by the phonon-mediated heat flux from the Pt.

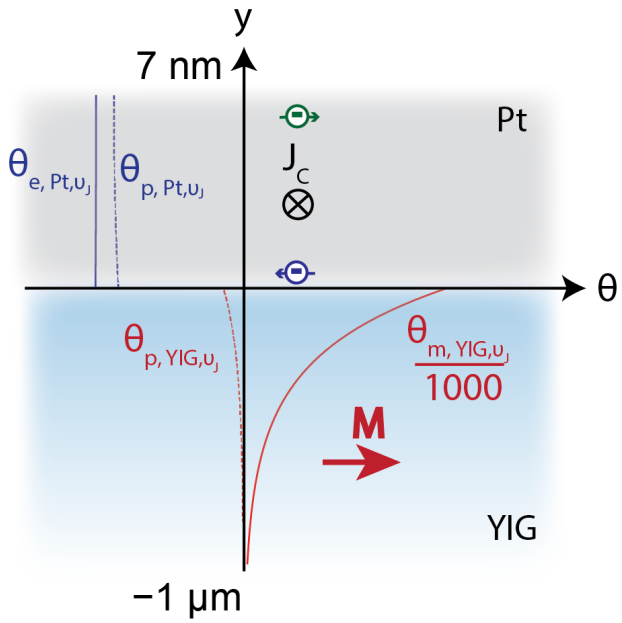

Figure 4.3: Analytically calculated Pt electron (solid blue) and phonon (dashed blue) temperature profiles and, and YIG phonon (dashed red) and equivalent magnon (solid red) temperature profiles during spin Peltier cooling at the Pt/YIG interface, assuming $\ell_{mp} = 250$ nm. The equivalent magnon temperature is divided by a factor of 1000 for clarity.

Temperature rises in the Pt can expected to be small – in the mK range – based on prior SPE measurements.[10,71] In addition, there are several other thermoelectric and magnetotransport effects that could interfere with the detection of the Pt phonon temperature change by resistance thermometry. It is important to consider these effects in order to design an experiment to mitigate them.

4.2.2 Phenomenological Spin and Charge Transport in the Pt

This section outlines some of the various effects that are important to consider for the experimental detection of the SPE/SSE in a device that consists of a thin Pt line deposited on a YIG film grown on GGG with coordinates described in Fig. 4.4. Specifically, there are several commingling effects that can cause either resistivity or voltage modulations in electrical measurements of the Pt line. These are derived here phenomenologically.

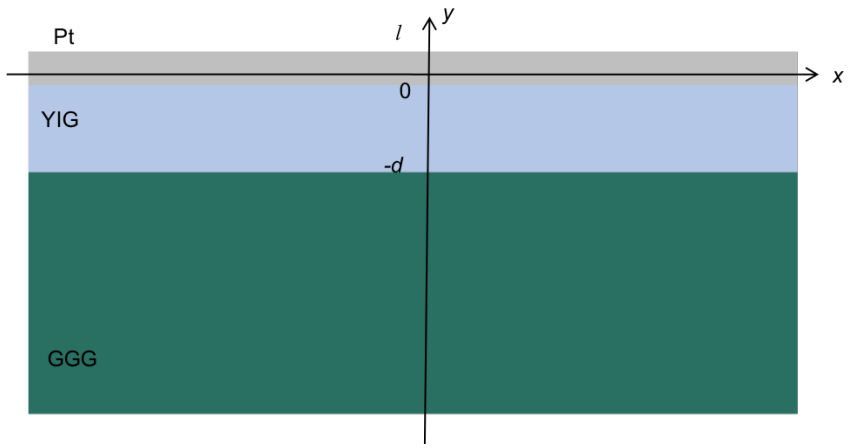

Figure 4.4: Coordinate system for the Pt/YIG/GGG structure.

Consider the electrical transport in the Pt line phenomenologically with electron particle current density vector $\boldsymbol{q}$ and charge current density vector $\boldsymbol{J}$. When the spin Hall effect (SHE) is negligible, the charge current is

$$\begin{aligned} J^0 \equiv -e\boldsymbol{q}^0 &= -\sigma\nabla\Phi - \sigma\alpha\nabla T \\ \nabla\Phi &= -\rho\boldsymbol{J}^0 - \alpha\nabla T \end{aligned} \tag{4.4}$$

where the Φ is the electrochemical potential, the superscript 0 refers to the case where the spin Hall angle $\Theta_{SH} = 0$, e is the elementary charge, $\rho = \sigma^{-1}$ is the electrical resistivity tensor, and α is the Seebeck coefficient tensor. In addition, each electron may carry some spin polarization. The flow of spin polarization carried by each particle, q_{ij} can be defined for flow direction along i and spin polarization along j.

Based on this definition, the SHE can be written as[174]

$$q_{ij} = q^0_{ij} - \Theta_{SH}\epsilon_{ijk}q^0_k \tag{4.5}$$

where Θ_{SH} is the spin Hall angle and $\epsilon_{xyz} = -\epsilon_{yxz} = \epsilon_{yzx} = -\epsilon_{zyx} = \epsilon_{zxy} = -\epsilon_{xzy} = 1$ is the Levi-Civita symbol. Similarly, the inverse spin Hall effect (ISHE) can be written as

$$\begin{aligned} q_i \equiv \frac{J_i}{-e} &= q^0_i + \Theta_{SH}\epsilon_{ijk}q^0_{jk} \\ J_i &= J^0_i - e\Theta_{SH}\epsilon_{ijk}q^0_{jk} \end{aligned} \tag{4.6}$$

And similarly for a current in the j direction

$$\begin{aligned} q_j \equiv \frac{J_j}{-e} &= q^0_j + \Theta_{SH}\epsilon_{jkl}q^0_{kl} \\ J_j &= J^0_j - e\Theta_{SH}\epsilon_{jkl}q^0_{kl} \end{aligned} \tag{4.7}$$

Based on Eqn. (4.4), the potential gradient along direction i would be

$$\frac{\partial\Phi}{\partial i} = -\rho_{ij}J^0_j - \alpha_{ij}\frac{\partial T}{\partial j} \tag{4.8}$$

Rearranging Eqn. (4.7) and inserting into Eqn. (4.8) yields

$$\frac{\partial\Phi}{\partial i} = -\rho_{ij}J_j - e\rho_{ij}\Theta_{SH}\epsilon_{jkl}q^0_{kl} - \alpha_{ij}\frac{\partial T}{\partial j} \tag{4.9}$$

Based on the coordinate system shown in Fig. 4.4, when the current is flowing in the Pt line along x and the longitudinal voltage (the integral of the potential gradient) is also measured along x, one has

$$\frac{\partial\Phi}{\partial x} = -\rho_{xx}J_x - e\rho_{xj}\Theta_{SH}\epsilon_{jkl}q^0_{kl} - \alpha_{xj}\frac{\partial T}{\partial j} \tag{4.10}$$

Magnetic Field Perpendicular to the Current

If there is a temperature gradient along y into the YIG driven by self-heating in the Pt and a magnetic field perpendicular to the Pt along z, then the second term

becomes

$$e\rho_{xx}\Theta_{SH}q_{yz}^{0} \tag{4.11}$$

where the spin polarization density current along y, q_{yz}^{0} could be non-zero due to the spin Seebeck effect (SSE) and would be proportional to the temperature gradient dT/dy, which is proportional to J_x^2 due to Joule heating. The voltage modulation from this term is due to the inverse spin Hall effect (ISHE) and can also arise from reflected spin current at the Pt/YIG interface. This coexistence of the SHE and the ISHE underpins the spin Hall magnetoresistance (SMR). In addition, the resistivity components can be written in terms of the ordinary Hall coefficient R_H based on the relation

$$\begin{aligned} -\epsilon_{ijk}R_H &\equiv \frac{1}{B_k}\left(\frac{\partial E_i}{\partial J_j}\right)_{\nabla T=0} \\ \rho_{ij} &= \rho_0\delta_{ij} - \epsilon_{ijk}B_kR_H(1-\delta_{ij}) \end{aligned} \tag{4.12}$$

Thus the resistivity for $B_x = B_y = 0$ is

$$\begin{aligned} \rho_{xx} &= \rho_0 \\ \rho_{xy} &= -B_zR_H \\ \rho_{xz} &= 0 \end{aligned} \tag{4.13}$$

Furthermore, an appreciable temperature gradient along y would yield the third term $\alpha_{xy}\frac{\partial T}{\partial y}$, where α_{xy} represents contributions from both the ordinary Nernst effect and the anomalous Nernst effect. Both the ISHE and Nernst contributions would be proportional to the temperature gradient along y that is proportional to J_x^2.

The ordinary Nernst effect is the generation of an electric field E_i in response to an orthogonal temperature gradient $\partial T/\partial j$ and magnetic field B_k. The Nernst coefficient is given as

$$N \equiv -\epsilon_{ijk}\left[\frac{1}{\mu_0 B_k}\frac{\partial E_i}{\partial\frac{\partial T}{\partial j}}\right]_{\boldsymbol{J}=0,\boldsymbol{M}=0} \tag{4.14}$$

In a ferromagnetic conductor, a local magnetization $\boldsymbol{M}$ can give rise to the anomalous Nernst effect (ANE):

$$N_A \equiv -\epsilon_{ijk}\left[\frac{1}{\mu_0 M_k}\frac{\partial E_i}{\partial\frac{\partial T}{\partial j}}\right]_{\boldsymbol{J}=0,\boldsymbol{B}=0} \tag{4.15}$$

where μ_0 is the vacuum permeability.

To relate these Nernst coefficients and their field dependence to the coefficient α_{xy}, consider the definition of the Seebeck coefficient

$$\alpha_{jk} = \frac{\partial E_j}{\partial \frac{\partial T}{\partial k}} \tag{4.16}$$

and so the term α_{xy} is

$$\alpha_{xy} = -\epsilon_{ijk} B_k N - \epsilon_{ijk} \mu_0 M_k N_A \tag{4.17}$$

For $B_x = B_y = 0$ and $M_x = M_y = 0$, one has

$$\alpha_{xy} = -N B_z - \mu_0 M_z N_A \tag{4.18}$$

And so the total contribution to the electric potential gradient along x is

$$\frac{\partial \Phi}{\partial x} = \underbrace{-\rho_{xx} J_x}_{\text{Peltier/SPE}} - \underbrace{e \rho_{xx} \Theta_{SH} q^0_{yz}}_{\text{SSE+ISHE; SMR}} - \underbrace{\alpha_{xy} \frac{\partial T}{\partial y}}_{\text{Nernst}} - \underbrace{\alpha_{xx} \frac{\partial T}{\partial x}}_{\text{Seebeck}} \tag{4.19}$$

All four contributions can yield a change in the resistance measured along x either by causing a modulation in the resistivity ρ_{xx}, or by producing a voltage. In a lock-in measurement utilizing an AC current, those phenomena that are linearly proportional to the current, including the ordinary Peltier and spin Peltier effect, will modulate the Pt temperature at the same frequency as the applied current, ν_J. Furthermore, these temperature modulations at ν_J will also modulate the Pt resistivity at ν_J. The voltage signal that the lock-in amplifier detects is related to the resistivity modulation by Ohm's law as $V_{2\nu_J} = I_{\nu_J} R_{\nu_J}$, where $R_{\nu_J} = \rho_{\nu_J} \frac{L}{A}$ and L and A are the Pt length and cross-section, respectively. The product of the two sines yields a voltage modulation at twice the measurement frequency, $2\nu_J$. The temperature modulation occurs out-of-phase with the sine at ν_J, and thus has a phase of $\pi/2$ at the second harmonic.[187] Because the second, third, and fourth term in Eqn. (4.19) are also temperature-dependent, they would also appear at the second harmonic with phase of $\pi/2$, with a slight distinction for the SMR contribution to the second term. The SMR is independent of the applied current and would thus

only modulate the longitudinal voltage at the first harmonic.[63,69] Meanwhile, Joule heating causes temperature modulations at the frequency of the Joule heating power $Q_{2\nu_J} = I_{\nu_J} V_{\nu_J}$, and thus its voltage signal arises at the third harmonic, $3\nu_J$.[188]

Magnetic Field Parallel to the Current

For a magnetic field applied parallel to the current direction and zero components along other directions, $B_z = B_y = 0$,

$$\rho_{zj} = \rho_0 \delta_{zj} - \epsilon_{zjx} B_x R_H (1 - \delta_{zj}) \tag{4.20}$$

and so the resistivities are

$$\begin{aligned} \rho_{zx} &= 0 \\ \rho_{zy} &= B_x R_H \\ \rho_{zz} &= \rho_0 \end{aligned} \tag{4.21}$$

In addition, the Nernst coefficient is

$$\alpha_{zy} = N B_x + \mu_0 M_x N_A \tag{4.22}$$

Consider the case of a transverse (Hall) measurement of the voltage along z. The gradient in the electrical potential along z is given as

$$\frac{\partial \Phi}{\partial z} = \underbrace{e \rho_{zz} \Theta_{SH} q^0_{yx}}_{\text{SSE+ISHE; SMR}} - \underbrace{\alpha_{zy} \frac{\partial T}{\partial y}}_{\text{Nernst/Ettingshausen}} \tag{4.23}$$

in which q^0_{yx} is again driven by the SSE and Joule heating that is proportional to J_x^2. This SSE+ISHE/SMR term would contribute to a transverse voltage measured along z and has an opposite sign from the SSE+ISHE/SMR term from the longitudinal measurement.

4.2.3 Lock-in Electrothermal Measurements

Lock-in electrothermal measurements of the Pt resistance were employed to study the effects of coupled spin-heat transfer at the Pt/YIG interface, utilizing a device design intended to reduce some of the spurious signals in the longitudinal

resistance measurements. The samples were fabricated on 10 μm-thick, [111] YIG films grown on a gadolinium gallium garnet (GGG) substrate via liquid phase epitaxy in Miguel Levy's group (Michigan Tech).[181] Two parallel 7 nm-thick Pt lines with lateral dimensions 20 μm x 500 μm were patterned onto the YIG with a spacing of 420 μm, as shown in Fig. 4.5. For the fabrication of the Pt transducers, the YIG surface was cleaned in a piranha solution for 10 minutes, followed by deposition of an 80 nm-thick Ti film. The Ti film under two 20 μm x 500 μm open windows of a photoresist mask was etched to expose YIG, which was cleaned with oxygen plasma for 3 minutes at a RF power of 20 W and inductively coupled plasma (ICP) power of 500 W prior to the deposition of 7 nm thick Pt by radio-frequency (RF) sputtering. The Pt deposited on Ti was removed by etching the underlying Ti in 10% HF solution, leaving only the two Pt lines on the YIG surface. Subsequently, 6 nm of Cr and 60 nm-thick Au were deposited through a photoresist mask via an electron beam deposition and subsequent liftoff process to form the bonding pads and leads. Similar devices were also patterned on [111] GGG crystals purchased from MTI Crystal.

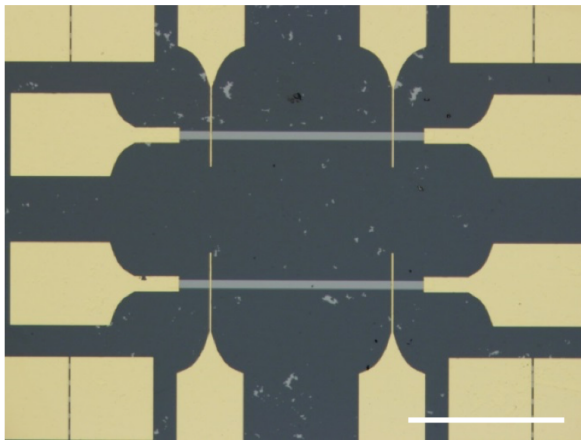

Figure 4.5: Optical image of the parallel-line Pt/YIG device. The scale bar is 400 μm. The dark background is the YIG film, the gray lines are the Pt, and the yellow regions are gold electrodes.

The resulting parallel Pt lines had almost the same resistance of close to 1 kΩ. When a charge current is driven through the Pt lines on top of the YIG, there are various thermoelectric, magnetoelectric, and magnetothermal effects that can give rise to longitudinal voltages measured along the length of the Pt lines, as discussed

in the previous section. These can include ordinary Joule heating, Peltier/Seebeck effects at the junctions of the Pt with the Cr/Au probes, inductive coupling in the measurement circuit, ordinary and anomalous Nernst/Ettingshausen effects, as well as the spin Peltier effect (SPE), the spin Seebeck effect (SSE), and the spin Hall magnetoresistance (SMR). In order to minimize the first three and to isolate the magnetothermal effects, lock-in measurements were performed on the two parallel Pt lines using a differential double Wheatstone bridge configuration.

A sinusoidal charge current with frequency $\nu = \nu_J \approx 5$ Hz was applied to the Pt lines from the voltage output of a lock-in amplifier (SRS 830). Because both the ordinary Peltier/Seebeck effect and the magnetothermal effects can be detected from the second harmonic, out-of-phase (quadrature) voltage signal from the lock-in, it was necessary to devise an experimental setup to minimize the ordinary Peltier effect and maximize the SPE. This was accomplished by taking advantage of the magnetic-field dependence of these two effects. When the applied magnetic field, and thus the YIG magnetization direction $\boldsymbol{M}$, is perpendicular to the direction of the current flow in the Pt lines, the SPE/SSE is expected to be maximized. Meanwhile, the ordinary Peltier effect has no such dependence on the magnetic field or YIG magnetization. In the measurement configuration shown in Fig. 4.6, the AC current in the two Pt lines flows antiparallel and the voltage difference between two different segments of each circuit is measured by two lock-in amplifiers, represented by V_A and V_B. In the presence of a perpendicular magnetic field, the two counter-propagating currents produce opposite signs of the SPE in each of the Pt lines, thereby maximizing the difference signal measured between the two lines. On the other hand, the ordinary Peltier effect and Joule heating in each of the lines should be approximately the same and does not depend on the magnetic field orientation, defined by α in Fig. 4.6(a), and so these contributions are minimized in this configuration.

The measured voltage for this device is $V_{2\nu_J} = V_{2\nu_J,A} - V_{2\nu_J,B}$. Despite measuring at the second harmonic of the excitation frequency, the large first harmonic signal can overwhelm the detection circuit of the lock-in amplifiers unless a sufficiently high dynamic reserve is chosen. To maximize sensitivity, a double Wheatstone bridge circuit is employed to reduce the first harmonic component, allowing the lock-ins to operate with a sufficiently high sensitivity to detect the small signals arising from the SPE and eliminating the SMR, which occurs at the first harmonic. To accomplish

this, variable resistance potentiometers were included in the circuit (shown by boxes with arrows in Fig. 4.6. The resistance of the various legs of the circuit were then adjusted by tuning the potentiometers in order to nullify the first harmonic in-phase (V_X) signal measured by lock-in A, lock-in B, and the difference between the two: $V_{\nu_J,X} \rightarrow 0$ at the highest output voltage amplitude used, 5 V_{rms}. After balancing the bridge, the second harmonic in-phase and quadrature components were measured as a function of the output voltage amplitude using a time constant (τ) of 10 seconds. The output voltage was stepped as 1, 3, 5, 4, 2, 0.004 V_{rms}, taking five measurements at each voltage condition separated by 7τ.

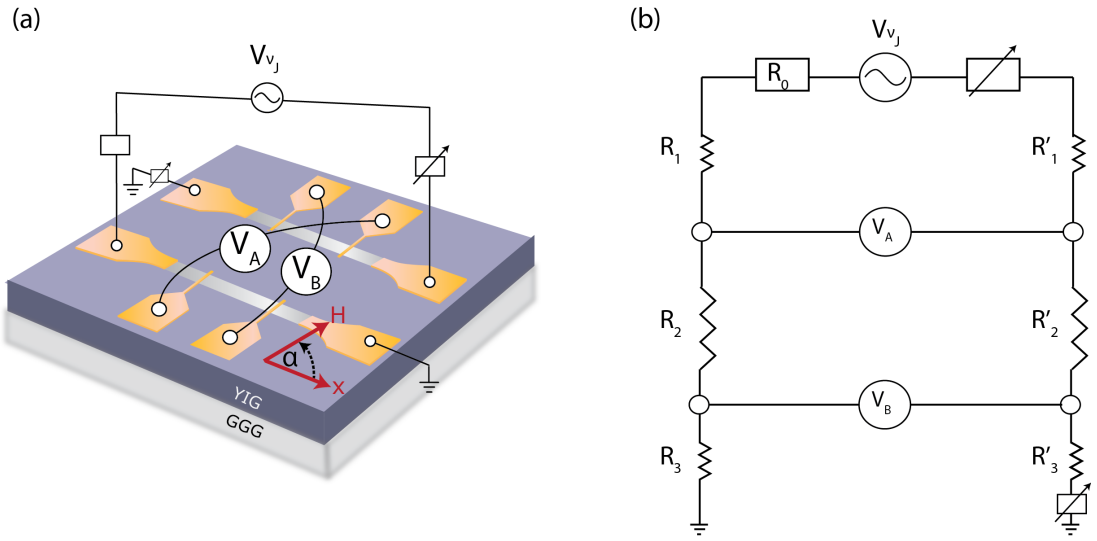

Figure 4.6: (a) Schematic of the double-Wheatstone bridge detection circuit used for the lock-in electrothermal measurements. (b) Equivalent circuit diagram.

The results of the lock-in electrothermal measurements for an applied field of $\boldsymbol{H} = 350$ Oe are summarized in Fig. 4.7. The golden circles and upright triangles represent measurements taken for $\alpha = 90°$ and $\alpha = 0°$, respectively, while the dark blue circles and upside-down triangles represent measurements taken for $\alpha = -90°$ and $\alpha = 180°$, respectively. In addition to measurements on the Pt/YIG/GGG device, another device was fabricated on Pt/GGG as a reference. GGG is not magnetically ordered at room temperature and so no SPE or anomalous Nernst/Ettingshausen effects are expected to be present. Magnetic-field dependent effects in the Pt like the ordinary Nernst effect, however, should still be present. Measurements from the

Pt/GGG device are shown as open symbols.

While the SPE/SSE signal is expected to show up in the quadrature second harmonic signal, the in-phase components were also measured for reference. Figure 4.7(a) shows that there is no apparent trend in the in-phase components of the double-Wheatstone voltage as the output voltage amplitude is increased. The quadrature voltage components, on the other hand, (Fig. 4.7(b)) show a clear trend with increasing output voltage amplitude, the Pt/GGG device included. The field-dependence of these measurements is more clearly visualized when the voltage measured for fields (anti)parallel to the current flow is subtracted from those measured at perpendicular fields. This field-offset voltage is defined as $\Delta V_{2\nu_J}(\pm 90°) = V_{2\nu_J}(\pm 90°) - V_{2\nu_J}(0° \text{ or } 180°)$, and is shown in Fig. 4.7(c) for the in-phase components and Fig. 4.7(d) for the quadrature. While the offset in-phase voltages show neither field dependence nor output voltage dependence, the quadrature components for the Pt/YIG/GGG sample show a pronounced quadratic dependence on the output voltage that flips sign when the magnetic field orientation is changed from $+90°$ to $-90°$. The quadrature results for the Pt/GGG sample, however, show no apparent trend, indicating that the Nernst effect is not apparent in these measurements. Furthermore, recent electrical and lock-in infrared thermography (LIT) measurements of Pt/YIG, FePt/Si and other heterostructures have revealed that the spin Peltier effect dominates anomalous Ettingshausen/Nernst effects based on the difference in the magnetic field-dependence of the two effects.[71,72,189] Thus, the contributions to the longitudinal voltage signal can be written as

$$\frac{\partial \Phi}{\partial x} = \underbrace{-\rho_{xx} J_x}_{\text{SPE}} - \underbrace{e \rho_{xx} \Theta_{SH} q^0_{yz}}_{\text{SSE+ISHE}} \tag{4.24}$$

However, further measurements are necessary to adequately separate resistivity modulations arising from the SPE from the SSE/ISHE voltage.

To investigate the origin of the observed signals, additional measurements were performed on modified Wheatstone circuits. A test bridge circuit consisting entirely of precision resistors and potentiometers with similar resistances to the Pt lines was constructed outside the magnetic cryostat and the same measurement procedure was carried out. The in-phase and quadrature signals for the test bridge are shown in Fig. 4.8. Despite not being inside the cryostat, the quadrature components show a

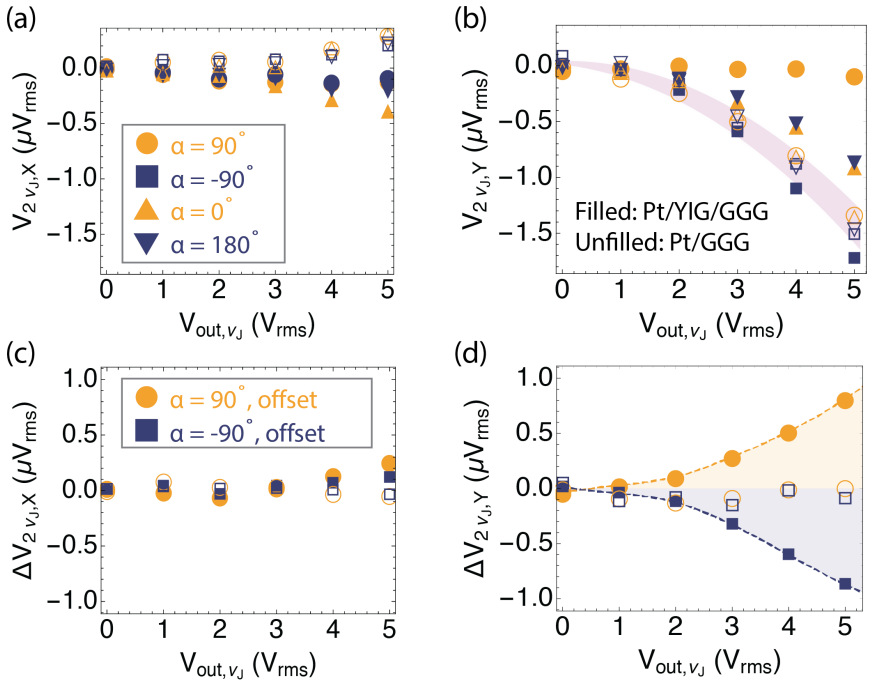

Figure 4.7: (a) In-phase and (b) quadrature second harmonic voltages, $V_{2\nu_J} = V_{2\nu_J,A} - V_{2\nu_J,B}$, obtained from the double-Wheatstone device as a function of magnetic field orientation α for a Pt/YIG/GGG device (filled symbols) and at Pt/GGG device (unfilled symbols). The purple shading in (b) highlights the trend of the Pt/GGG results. The difference in perpendicular and parallel field-measured (c) in-phase and (d) quadrature voltages, $\Delta V_{2\nu_J}(\pm 90°) = V_{2\nu_J}(\pm 90°) - V_{2\nu_J}(0° \text{ or } 180°)$.

slight downward trend with increasing output voltage, similar to the results shown in Fig. 4.7(b). This indicates some level of voltage-dependent noise or coupling present in the measurement circuit that lies outside the cryostat.

It is also conceivable that there could be a source of crosstalk between the two Pt lines mediated by spin currents in the YIG. If this were the case, a spin Hall-driven spin current injected into the YIG by Pt line 1 would diffuse the distance between the two lines and drive a spin current into Pt line 2, thereby generating a longitudinal voltage from the ISHE that could be detected in the bridge measurement. To rule out this possibility, a double-Wheatstone bridge circuit was constructed in which one of the Pt lines was replaced by a set of precision resistors and potentiometers, as shown in the circuit diagram in Fig. 4.9, and the results for this bridge configuration are summarized in Fig. 4.10. The trends in the in-phase and quadrature raw voltages are

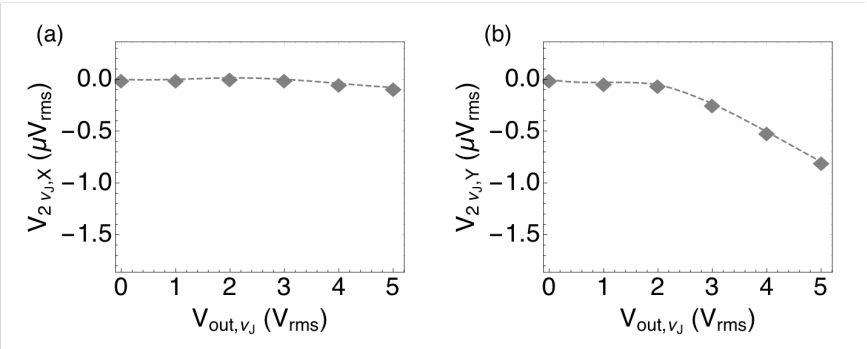

Figure 4.8: Second harmonic (a) in-phase and (b) quadrature voltages measured in a test Wheatstone bridge circuit consisting of precision resistors and potentiometers outside of the magnetic cryostat.

similar to the bridge measurement between two Pt lines; however, as apparent in Fig. 4.10(b), the overall background signal is larger. In addition, the quadrature voltages obtained by subtracting the voltages measured at (anti)parallel fields show a similar quadratic dependence, but are only half in magnitude of the signals collected for the two Pt line case. The measured signal indicates that the magnetic-field dependent effect is present in one Pt line and is not a result of crosstalk between the two lines.

Equivalent Temperature Rise in the Pt

If the origin of the second harmonic quadrature voltage signals to the SPE rather than the SSE+ISHE, they can be converted into an equivalent temperature rise occurring at the first harmonic, θ_{ν_J}, with knowledge of the first harmonic Pt resistance change and the temperature coefficient of the Pt resistance, dR_2/dT. Referring to Fig. 4.9, one arm consists of a precision resistor (R_0) and a Pt line, where R_2 is the four-probe resistance and R_1 and R_3 are the small and approximately equal resistances of the lead wires. The other arm consists of two precision resistors (R_0' and R_2') and two potentiometers (R_1' and R_3'), all with small temperature coefficients. Voltages V_A and V_B are measured between the two arms, and the potentiometers are tuned until V_A, V_B, and $V_A - V_B$ are nullified at the first harmonic when a sinusoidal voltage V_{ν_J} is applied. The in-phase component of the first harmonic resistance change for the one Pt line in the bridge circuit can be obtained as follows. Referring to Fig. 4.9, the measured voltages V_A and V_B are

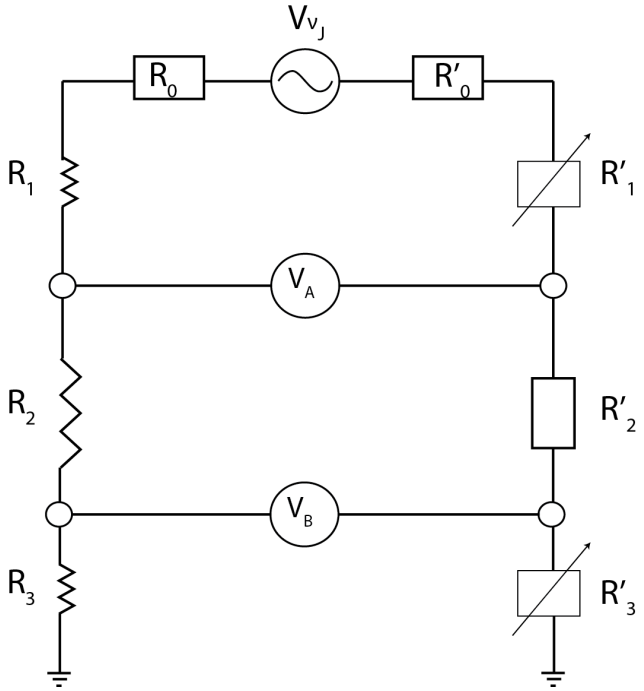

Figure 4.9: Double-Wheatstone bridge with one Pt line replaced by precision resistors.

$$\begin{aligned} V_A &= V\left(\frac{R_2+R_3}{R_t}-\frac{R'_2+R'_3}{R'_t}\right) \\ V_B &= V\left(\frac{R_3}{R_t}-\frac{R'_3}{R'_t}\right) \end{aligned} \tag{4.25}$$

These can be expanded as

$$\begin{aligned} V_A &= V\left(\frac{R^0_2+\Delta R_2+R^0_3+\Delta R_3}{R^0_t+\Delta R_t}-\frac{R'_2+R'_3}{R'_t}\right) \\ V_B &= V\left(\frac{R^0_3+\Delta R_3}{R^0_t+\Delta R_t}-\frac{R'_3}{R'_t}\right) \end{aligned} \tag{4.26}$$

where R^0_1, R^0_2, R^0_3, and R^0_t are the unmodulated (zero-current) resistances and $R_t = R_0 + R_1 + R_2 + R_3$, and ΔR_i are the changes in resistances. Under the balancing

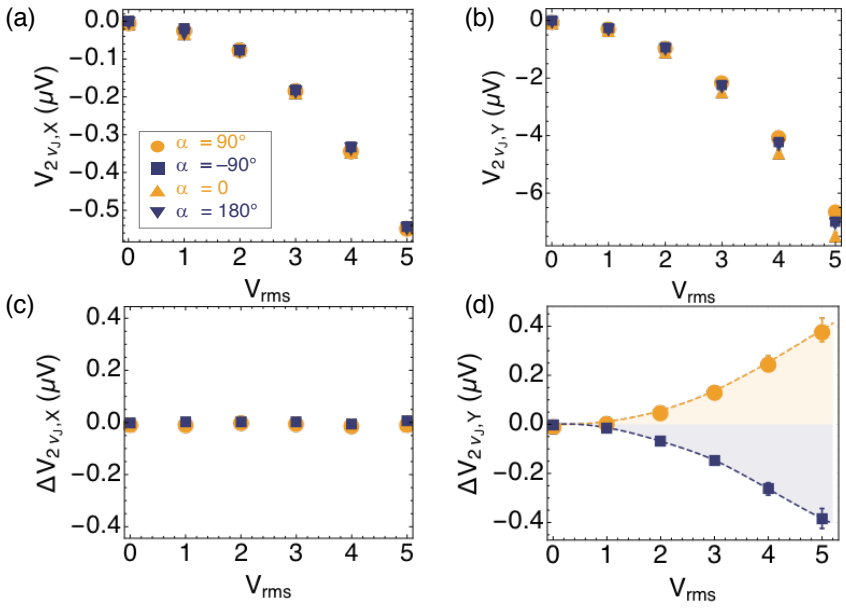

Figure 4.10: (a) In-phase and (b) quadrature second harmonic voltages, $V_{2\nu_J} = V_{2\nu_J,A} - V_{2\nu_J,B}$, obtained from the double-Wheatstone device as a function of magnetic field orientation α for one of the Pt lines on YIG/GGG balanced with a set of precision resistors. The difference in perpendicular and parallel field-measured (c) in-phase and (d) quadrature voltages, $\Delta V_{2\nu_J}(\pm 90°) = V_{2\nu_J}(\pm 90°) - V_{2\nu_J}(0° \text{ or } 180°)$.

conditions, $V_A \to 0$ and $V_B \to 0$, therefore

$$\begin{aligned} V_A &= V\left(\frac{\Delta R_2 + \Delta R_3}{R_t^0} - \frac{R_2^0 + R_3^0}{R_t^{0\,2}}(\Delta R_2 + \Delta R_3)\right) \\ V_B &= V\left(\frac{\Delta R_3}{R_t^0} - \frac{R_3^0}{R_t^{0\,2}\Delta R_3}\right) \end{aligned} \tag{4.27}$$

Solving for ΔR_2 under the reasonable assumption $R_1 \approx R_3$ and $\Delta R_1 \approx \Delta R_3$ yields

$$\Delta R_{\nu_J,X} = -2R_t^{0\,2}\frac{(R_0 + R_2^0)\Delta V_{A,2\nu_J,Y} - (R_0 - R_2^0)\Delta V_{B,2\nu_J,Y}}{V_{\nu_J}\left(R_0^2 + 2R_0R_3^0 + R_2^0R_0\right)} \tag{4.28}$$

Here, R_0 can be made equal to R_2^0 in order to minimize the voltage drop across the relatively small lead wire resistance. Similarly, for the bridge circuit consisting of Pt

lines in both arms (Fig. 4.6(b)), the resistance modulation of the Pt is

$$\Delta R_{\nu_J,X} = -R_t^{0\,2} \frac{(R_0 + R_2^0)\Delta V_{A,2\nu_J,Y} - (R_0 - R_2^0)\Delta V_{B,2\nu_J,Y}}{V_{\nu_J}\left(R_0^2 + 2R_0R_3^0 + R_2^0R_0\right)} \tag{4.29}$$

The above resistance modulation can then be converted into an equivalent average phonon temperature rise in the Pt at the first harmonic as

$$\langle \theta_{\nu_J} \rangle = \Delta R_{\nu_J,X} \frac{dT}{dR_2} \tag{4.30}$$

where $\frac{dT}{dR_2}$ is obtained from temperature-dependent measurements. Figure 4.11 shows the temperature-dependent resistance and the four-probe voltage-current characteristics of the Pt/YIG/GGG device. The temperature measurements Fig. 4.11(a) were carried out by placing the device in an oven and yields a slope of $dR_2/dT = 1.01\ \Omega/\mathrm{K}$. In addition, the voltage-current characteristics of the device indicate approximately 40 K average temperature rise in the Pt due to Joule heating when 6 mA of DC current is passed through the line (Fig. 4.11(c,d)).

Based on Eqn. (4.30) and the calibrated dT/dR_2 (Fig. 4.11(a)), the second harmonic quadrature signals can be converted into an average temperature rise. Shown as a function of the equivalent current amplitude, Fig. 4.12 indicates the Pt resistance modulation for the circuit consisting of two Pt lines (a) and the circuit consisting of one Pt line (b). While the measured voltage from the single Pt line bridge circuit is half of that from the two-line circuit, the resulting resistance modulation and temperature rise obtained from the two measurement configurations is almost the same. This indicates that each Pt line in the device contributes to one-half of the signal shown in Fig. 4.7(a) and Fig. 4.12(a).

If the measured resistance modulation in Fig. 4.12 is attributable to the SPE, this spin Peltier magnetoresistance (SPMR) implies that each additional milliampere of charge current in the Pt lines generates 0.25 mK of heating or cooling, i.e. $\langle \theta_{\nu_J,Pt} \rangle / I_{\nu_J} \approx \pm 0.25$ mK/mA. This is comparable to several recent measurements of the spin Peltier effect in Pt/YIG structures.[10,59,60]

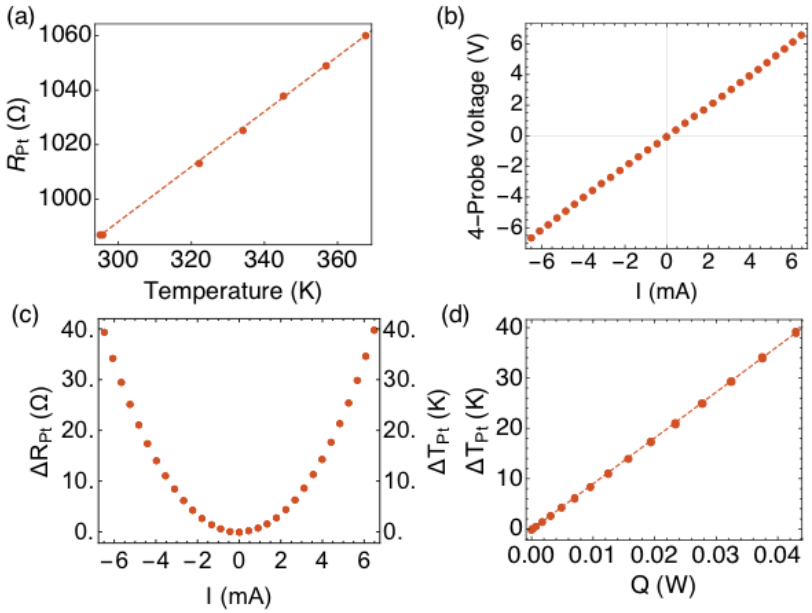

Figure 4.11: (a) The resistance of the Pt transducer line measured at a low bias current as a function of the sample stage temperature. The dashed line is a linear fit to the data and yields the temperature coefficient of resistance. (b) Measured four-probe voltage versus current for one of the Pt lines on YIG/GGG. (c) Change in the Pt resistance (left axis) and temperature (right axis) as a function of the heating current. (d) Temperature rise in the Pt line as a function of the heating power, $Q = IV$.

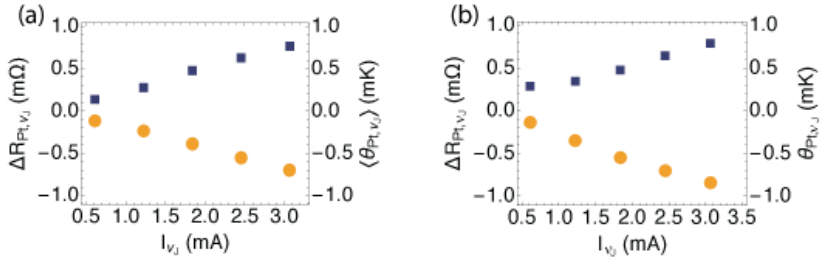

Figure 4.12: Equivalent first harmonic resistance modulation (left axis) and equivalent temperature rise (right axis) as a function of excitation current, as obtained from the second harmonic Wheatstone voltage signals for (a) two Pt lines and (b) one Pt line and one set of precision resistors.

Frequency Dependence

It is known that Joule self-heating in metal films on substrates is very sensitive to the frequency of the measurement. This forms the basis for the 3ω measurement, which investigates the frequency dependence of the third harmonic voltage signals that arise from the Joule heating at the second harmonic.[188] These signals can then be converted into a temperature rise and the frequency dependence can be used to extract the thermal conductivity of the substrate. To investigate whether there was any significant frequency dependence in the measurement of the first harmonic voltage signals, the bridge measurement of the second harmonic voltages was carried out at a higher frequency. Fig. 4.13 shows no appreciable difference in the second harmonic voltage signals for the case $V_{out} = 5\ \mathrm{V}_{rms}$ at the original $\nu_J = 5.066$ Hz and at $\nu_J = 10.132$ Hz. This indicates that whatever effect that would be modulating the Pt phonon temperature at the first harmonic is weakly dependent on frequency in this range, and has a thermal length scale shorter than $\sim \sqrt{\alpha/(4\pi\nu_J)} \approx 160\ \mu$m, where $\alpha \approx 3.2 \times 10^{-6}\ \mathrm{m^2 s^{-1}}$ is the thermal diffusivity of YIG or GGG, which have similar thermal properties.

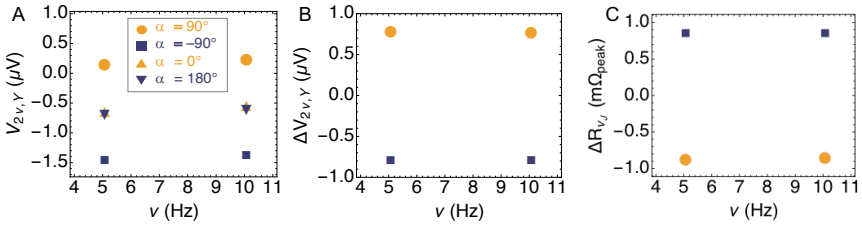

Figure 4.13: (a) Raw and (b) offset second harmonic voltage signals measured for a double Wheatstone bridge between two Pt lines on YIG/GGG at two different frequencies using $V_{\nu_J} = 5\ \mathrm{V}_{rms}$. (c) Equivalent first harmonic resistance modulation.

On the other hand, 3ω measurements of a double bridge consisting of one Pt line and a set of precision resistors show a pronounced frequency dependence. Based on the bridge circuit in Fig. 4.9, the second harmonic temperature rise (Joule heating) measured from the third harmonic voltage signal is given by

$$\langle \theta_{2\nu_J} \rangle = \Delta R_{2\nu_J,Y} \frac{dT}{dR_2} = -2R_t^{0\,2} \frac{dT}{dR_2} \frac{(R_0 + R_2^0)\Delta V_{A,3\nu_J,X} - (R_0 - R_2^0)\Delta V_{B,3\nu_J,X}}{V_{\nu_J}\,(R_0^2 + 2R_0R_3^0 + R_2^0R_0)} \tag{4.31}$$

The resistance modulation $\Delta R_{2\nu_J}$ and the equivalent temperature rise $\theta_{2\nu_J}$ obtained from the 3ω measurements is shown in Fig. 4.14 in a frequency range from about 1 to 200 Hz.

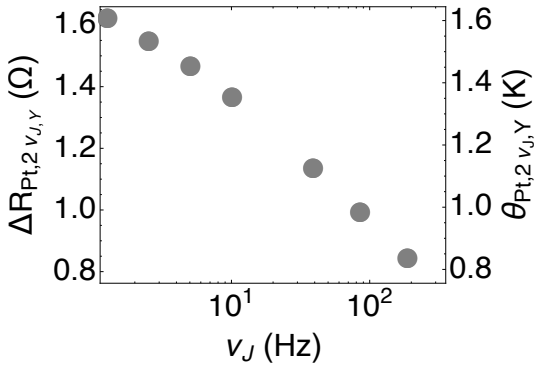

Figure 4.14: Second harmonic resistance modulation (left axis) and equivalent temperature rise (right axis) obtained from 3ω measurements of a double bridge consisting of one Pt line on YIG/GGG and a set of precision resistors as a function of excitation frequency.

The thermal conductivity of the substrate can be obtained as

$$\kappa = \frac{V_{\nu_J}^3 R_2^0 \ln(f_1/f_2)}{(4\pi L R_t^{04})} \frac{dR_2}{dT} \frac{(R_0^2 + 2R_0 R_3^0 + R_2^0 R_0)}{(R_0 + R_2^0)\Delta V_{A,3\nu_J,X} - (R_0 - R_2^0)\Delta V_{B,3\nu_J,X}} \tag{4.32}$$

where f_1 and f_2 are two different measurement frequencies, L is the length of the Pt line segment representing R_2, and $\Delta V = V(f_2) - V(f_1)$. Based on the measurements in Fig. 4.14, the thermal conductivity of the YIG/GGG is measured to be 10 $\mathrm{Wm^{-1}K^{-1}}$, which is consistent with prior measurements.[98,183,184]

This difference in frequency dependence between these two measurements can potentially provide insight into the origins of the resistance modulation. The lack of a frequency dependence in the second harmonic measurements is consistent with the SPE, which results from the direct exchange of energy between Pt electrons and YIG magnons, and only has a very short thermal length scale of ℓ_{mp}. Due to the small thermal length scale, the SPE should remain frequency independent until very

high frequencies. However, the frequency dependence may also be consistent with the SSE if the thermally generated spin flux is proportional to the phonon temperature gradient rather than simply the phonon temperature rise in the YIG. This is because the length scale of the temperature drop would also scale with the change in frequency due to the changing thermal penetration depth. As a result, the temperature gradient could be roughly frequency independent.

Separation of the SPE from the SSE+ISHE

Based on the above analysis ,the measured longitudinal voltage signal is either due to resistivity modulations from the SPE or due to voltage modulations from self-heating-driven SSE coupled with the ISHE. It is unknown whether these two effects would have different frequency dependencies. However, some insight into the origins of the voltage signal may be obtained by transverse Hall measurements. As discussed in §4.2.2, the longitudinal voltage in the bridge measurements is proportional to

$$\frac{\partial \Phi}{\partial x} = \underbrace{-\rho_{xx} J_x}_{\text{SPE}} - \underbrace{e\rho_{xx}\Theta_{SH} q^0_{yz}}_{\text{SSE+ISHE}} \tag{4.33}$$

whereas a transverse voltage measured at the second harmonic would be proportional to

$$\frac{\partial \Phi}{\partial z} = \underbrace{e\rho_{zz}\Theta_{SH} q^0_{yx}}_{\text{SSE+ISHE}} \tag{4.34}$$

By adding Hall probes onto the Pt lines, the transverse voltage can be measured along z when a magnetic field and current flow is applied along x. The measured voltage signal would be proportional to the length of Pt between the voltage probes, and so the transverse voltage could be compared with the longitudinal voltage by a geometric scaling factor. Since the transverse signal should only contain components due to the SSE+ISHE, this comparison can be used to determine if the longitudinal signal is primarily due to the SPE or the SSE+ISHE or if some combination of the two either enhances or reduces the overall measured signal. In addition, the lack of frequency dependence observed in the second harmonic measurements is consistent with the SPE, which should occur over a very small length scale. However, this effect could also be consistent with the SSE+ISHE if the SSE-generated spin flux is

proportional to the temperature gradient rather than simply the temperature rise.

Spin Peltier Heat Flux

If the resistance modulation at the second harmonic is ascribed to the SPE, the interfacial heat flux can be obtained using the previously derived model in Eqn. (4.2). Based on the measured first harmonic Pt phonon temperature rises and the range of values for G_p and ℓ_{mp}, and the ratio $\langle \theta_{p,Pt,\nu_J} \rangle / I_{\nu_J} = 0.25$ K/A, each additional mA of charge current in the Pt line results in spin-mediated heat flux across the interface of (1.9 ± 1.1) W cm^{-2}, which is appreciable in comparison to the ~ 10 W cm^{-2} of Joule heating at 1 mA of current. As shown in Fig. 4.15, the interfacial heat transfer due to the SPE would begin to dominate that caused by Joule heating for currents below ~ 0.2 mA.

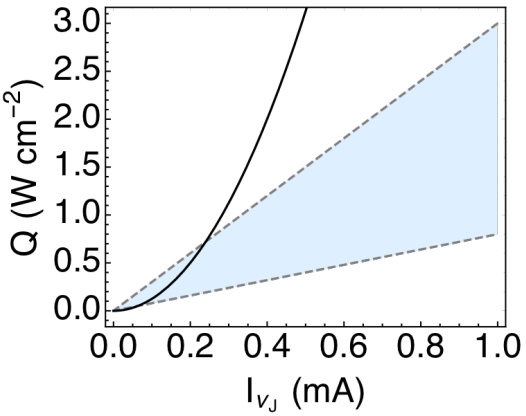

Figure 4.15: Calculated interfacial heat flux due to Joule heating (black line) and due to spin-mediated transfer (shaded blue region) based on the measured $\langle \theta_{p,Pt,\nu_J} \rangle / I_{\nu_J}$, a range of values for G_p, and $\ell_{mp} = 250$ nm.

Even though the calculated SPE heat flux is appreciable compared with heat flux due to Joule heating, the temperature rise caused by the SPE is roughly three orders of magnitude smaller than that caused by the Joule heating. This is because only the thin layer of YIG within roughly ℓ_{mp} of the interface is available to provide thermal resistance to sustain the temperature difference. The nonequilibrium magnon distribution would also be expected to maintain a non-zero chemical potential over distance λ_m from the interface.[85,190] The population of magnons in the YIG at the interface with the Pt can be investigated directly with BLS.

4.3 Direct Characterization of the Magnons in Pt/YIG by Brillouin Light Scattering

In addition to the lock-in electrothermal characterization of the Pt/YIG/GGG heterostructures, spin-dependent transport across the Pt/YIG interface was investigated using micro-Brillouin light scattering spectroscopy (BLS). Similar to the numerical lock-in based Raman measurements discussed in Chapter 3, by modulating the electrical excitation in discrete intervals, BLS can be adapted to provide information about the thermal magnon population in the YIG that depends on the harmonic frequency of the measurement. This frequency dependence can be utilized isolate the different contributions to the changing magnon population, including Joule heating and spin caloritronic phenomena.

The magnon frequency in YIG probed by BLS follows from the dispersion relation for dipolar-exchange magnons,[98]

$$f_m(\boldsymbol{q}, M, H) = \frac{\gamma}{2\pi}\sqrt{(H + H_a - 4\pi NM + A\boldsymbol{q}^2)(H + H_a - 4\pi NM + A\boldsymbol{q}^2 + 4\pi M)} \tag{4.35}$$

in which $\gamma = 17.6$ GHz kOe^{-1} is the gyromagnetic ratio, M is the YIG magnetization, H is the applied external field, H_a is the anisotropy field of about 10 Oe,[191] $N = 0.08$ is the demagnetization factor along the applied field direction, and A is the exchange stiffness constant of $(5.4 \pm 0.1) \times 10^{-9}$ Oe cm^2.[98] The peak frequency f_m measured by BLS corresponds to the magnon mode measured with wavevector $\boldsymbol{q}$, which is set by the wavevector of the light in the measurement.

Brillouin Light Scattering Experiments

In the experiments here, a 100× objective lens was used to focus a $\lambda = 532$ nm single-mode laser (Spectra-Physics Excelsior) through the semi-transparent Pt lines onto the underlying YIG surface. The laser power prior to the objective lens was controlled by neutral density (ND) filters to a level of 18.5 mW. Whereas light-matter interactions with phonons do not change the polarization of light, light inelastically scattered by magnons has its polarization rotated by 90° relative to the incident light. Detection of the light scattered by magnons in the YIG was realized experimentally in the following way. Vertically polarized light from the laser was transmitted through

a Glan-laser calcite polarizer oriented to maximize vertically polarized light transmission, which was then focused onto the sample with the long working distance lens (Mitutoyo Plan Apo SL infinity corrected). Inelastic scattering by magnons resulted in light with shifted frequencies and horizontal polarization, which was collected by the objective lens. This horizontally polarized light was then rejected by the Glan-laser polarizer and sent to the tandem scanning Fabry-Pérot interferometer (TFP-1, JRS Scientific Instruments, now TableStable Ltd.).

The first mirror cavity in the tandem Fabry-Pérot interferometer was set to an equilibrium mirror spacing of $L_1 = 9$ mm, giving a free spectral range (FSR) of $\Delta\lambda = c/(2L_1) = 16.7$ GHz. In the 10 μm-thick YIG film, the frequency of the thermal magnons at an applied field of $\boldsymbol{H} = 350$ Oe was found to be roughly 9.5 GHz. Using the BrilliaNT LabVIEW code, a region of interest (ROI) was defined around the anti-Stokes magnon peak appearing on the right side of the spectrum. The settings for the ROI control the distance and speed over which the mirror cavity spacing is scanned, and the operation of the shutter that blocks elastically scattered light from the sample. For this particular measurement, the right-side of the spectrum was obtained by sweeping the mirrors 0.64 FSR. The right-side ROI was set to begin at 0.49 FSR and ended at 0.64 FSR. A slowness factor of 7 or 8 was applied, meaning that the mirror cavities spent a factor of 7 or 8 longer in this region (0.49 to 0.64 FSR $\approx$ 8 to 10.7 GHz). The number of channels was set to 800 channels/FSR, which sets the number of discrete points during the mirror cavity scan at which the detector is gated to count the photons. Therefore a higher number of channels implies a higher number of points along the x-axis of the BLS spectra. Increasing the slowness factor and the number of channels also increases the time for the mirrors to make one full scan. It is necessary to balance the different parameters in order that the sweep time does not greatly exceed one second/scan; otherwise, the auto-alignment of the mirror cavities will not work effectively and the alignment will drift over time. Further details about the BLS interferometer and operating procedure can be found in Appendix C.

Frequency-Domain BLS Measurements

While the scanning monochromator approach of the BLS interferometer allows for improved spectral resolution and the ability to measure small shifts into the GHz range, the mechanism of operation is incompatible with standard optical

lock-in homodyne detection schemes that ordinarily require very fast response times. [192] As in Chapter 3, an amplitude-modulated approach using discrete DC currents was employed to provide frequency-domain analysis of the BLS measurements. These measurements for the Pt/YIG/GGG structures are summarized schematically in Fig. 4.16. In these measurements, the a discrete DC current was stepped to follow the form $I(j) = I_0 \sin \frac{2j\pi}{N}$, with $N = 16$ and the integer j ramping from 0 to $200N$. At each j, the device was allowed to equilibrate for 0.5 seconds, the current and four-probe voltage were measured, and then a BLS spectrum was taken, integrating over 60 scans of the mirror cavities and using the parameters listed above. A representative magnon peak is shown in Fig. 4.16(b). One full cycle had a period of about 1100 seconds, and so each measurement of 200 cycles took approximately 60 hours. Each BLS spectrum was saved in its own distinct file, while the current and voltage measurements were collected into two files at the end of the measurement. By fitting each collected magnon peak with an asymmetric Lorentzian function, the magnon frequency f_m (Fig. 4.16(c)), intensity, and full width at half-maximum (FWHM) were obtained as a function of $I(j)$ (Fig. 4.16(e)). The FFT algorithm was used to take the discrete Fourier transform of the $f_m(j)$ data to obtain the amplitude spectrum of the magnon measurements. As shown in Fig. 4.16(d), the amplitude spectrum shows that the magnon frequency was modulated at the first, second, fourth, and sixth harmonics of the applied current frequency ν_J.

These measurements were carried out under several different magnetic field orientations at angle α to the Pt lines. In addition, the amplitude of the current I_0 was varied from 5 to 8 mA. When the applied in-plane magnetic field H, and thus the YIG magnetization $\boldsymbol{M}$ were made perpendicular to the direction of the current flow in the Pt lines ($\alpha = \pm 90°$), the spin-mediated energy transfer between the spin Hall-generated spin current in the Pt and the magnons in the YIG is expected to be maximized. [10,59,60] The measured magnon peak position is sensitive to changes in the local magnetization $\boldsymbol{M}$. [98,193,194] Based on Eqn. (1.19), since each magnon carries a magnetic moment of $-g\mu_B$, the measured magnon frequency shift (Δf_m) is sensitive to the number density of magnons.

In general, the BLS-measured magnon peak down shifts in frequency and broadens as the excitation charge current is increased in the Pt. This behavior is predominately due to the Joule heating in the Pt line that causes a reduction in

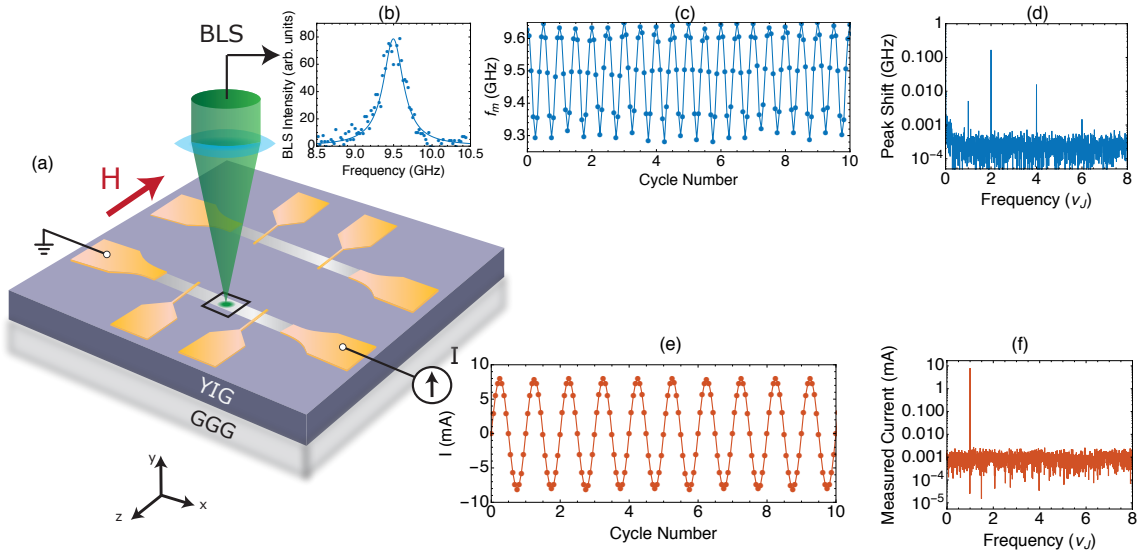

Figure 4.16: (a) Schematic illustration of the measurements of the magnon population in YIG directly beneath the center of the Pt line. (b) A representative measured magnon peak. (c) Measured magnon peak frequency modulation and (d) the amplitude spectrum when a discretized sinusoidal electrical current flows in the Pt line, as shown in (e) the measured current modulation and (f) the corresponding amplitude spectrum.

the YIG magnetization and can be visualized by plotting the BLS intensity at each frequency measured by the interferometer as a function of the excitation current, as shown in Fig. 4.17.

To separate the effects of Joule heating from those due to spin Hall injection or other phenomena, frequency-domain spectral analysis was once again employed. The results of the amplitude-modulated BLS measurements can be analyzed by examining the current amplitude (I_0) and angle (α) dependence of the amplitudes $\langle f_{m,\nu} \rangle$ and phase lag (ϕ_ν) of the various peaks that appear in the f_m amplitude spectra, e.g. that shown in Fig. 4.16(d). Figure 4.18(a-c) shows the dependence of the peak amplitude (b) and the phase (c) obtained from the FFT of the modulated magnon peak data. The even-harmonic components show no sensitivity or dependence on the applied magnetic field: both the amplitude, $\langle f_{m,2n\nu} \rangle$, and phase $\phi_{2n\nu}$ for the even harmonic components do not change appreciably with α. Therefore the $\langle f_{m,2n\nu} \rangle$ components are attributed mainly to modulation of $\boldsymbol{M}$ by Joule heating that is proportional to J_c^2. On the other hand, the first harmonic peak is sensitive to the magnetic field

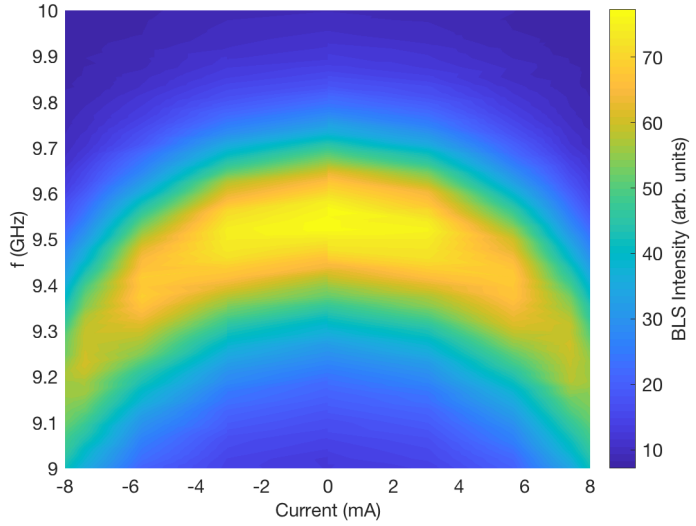

Figure 4.17: Averaged BLS intensity (colorbar) for different measured frequencies (y-axis) at different excitation currents in the Pt (x-axis) when $\boldsymbol{H}$ is perpendicular to the Pt line ($\alpha = 90°$).

angle. When the field is perpendicular, the amplitude of this first harmonic peak remains roughly constant if the field is flipped from $+90°$ to $-90°$. However, when the field is made to be collinear with the Pt line, the first harmonic amplitude drops to the noise floor. Furthermore, $\langle f_{m,\nu_J} \rangle$ shows an approximately linear dependence on I_0 when $\alpha = 90°$ (Fig. 4.18(d)), revealing its origin in a mechanism that is linear with I_0.

The phase angle from the FFT is obtained as atan2(Y, X), where atan2 is the four-quadrant inverse tangent, and Y and X are the quadrature and in-phase components of the FFT signal, respectively. The excitation current is output to follow a sine wave with zero phase. In the exponential form, the phase of the sine is $\pi/2$; therefore, frequency components computed from the FFT with phase angles of $\pm\pi/2$ are in-phase with the applied current. The phase lag ϕ_ν shown in Fig. 4.18(c) is obtained as the difference between the phase angle from the FFT and the phase angle of the applied sinusoidal current. The $\pm\pi/2$ phase lags of the even-harmonic components imply that they are always out-of-phase with the applied current, regardless of field orientation. Meanwhile, the first harmonic components observed when the magnetic field is perpendicular to the line are in-phase. Furthermore, the phase lag of $\langle f_{m,\nu_J} \rangle$

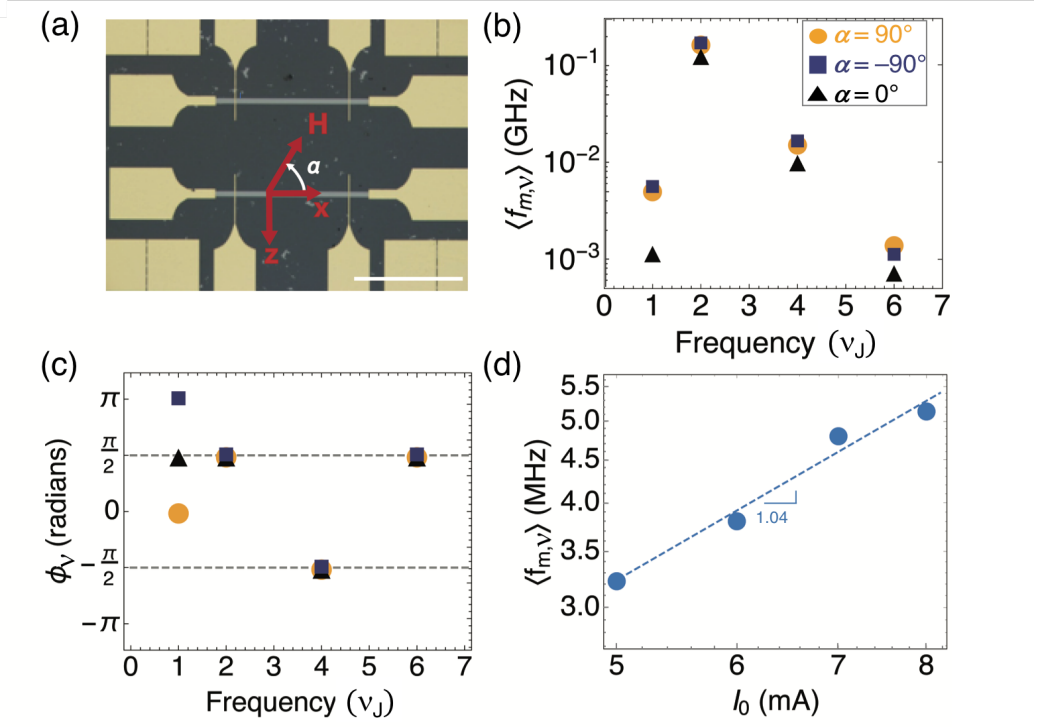

Figure 4.18: (a) Optical micrograph of the Pt/YIG sample with the definition of angle α. The scale bar is 400 μm. (b) The amplitudes and (c) the phase lag (ϕ_ν) of the measured f_m modulation frequency components at $I_0 = 8$ mA and different α values as indicted in (b). (d) The first-harmonic f_m amplitude as a function of I_0 for $\alpha = 90°$. Both axes are in the logarithmic scale and the slope of the linear fit is 1.04.

flips from 0 to π when the magnetic field is flipped from $+90°$ to $-90°$. This behavior indicates that whatever phenomenon is causing the magnetization modulation at the first harmonic frequency flips its sign when the magnetic field is reversed.

Origin of the First Harmonic Peak Shift

Based on the dependence of the amplitude and phase on the magnetic field orientation and applied current, the phenomenon that causes magnetization modulation at the first harmonic should be (1) linearly proportional to the charge current, (2) disappear when the magnetic field is parallel to the Pt line, and (3) flip signs when the perpendicular magnetic field polarity is flipped. While linearly proportional to I_0, the ordinary Peltier effect, which is independent of α, cannot yield the observed

change in ϕ_{ν_J} and $\langle f_{m,\nu_J} \rangle$. The aforementioned ordinary Ettingshausen effect (OEE) can, under a magnetic field, generate a heat current that travels transverse to an applied charge current. The lock-in electrothermal measurements of Pt/GGG provided evidence that the OEE is was insignificant in those measurements. To be doubly-sure, further modulated BLS measurements were carried out at different magnetic field intensities. The OEE heat current is proportional to the the magnetic field induction $\boldsymbol{B}$, which is proportional to the applied field $\boldsymbol{H}$. If the OEE effect were dominating the first harmonic magnetization modulation, then the signal should increase with increasing applied field. Figure 4.19 shows a variation of less than 2% in the first harmonic magnon frequency modulation when the magnetic field is increased from 350 Oe to 1 kOe, indicating that the OEE plays a negligible role in the measurement results.

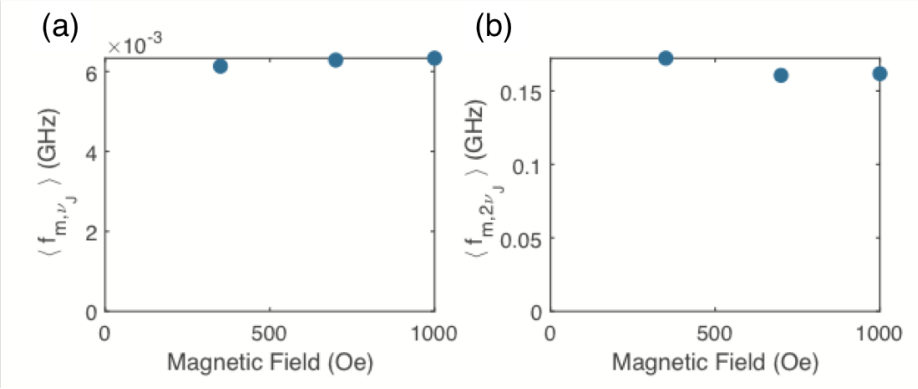

Figure 4.19: (a) The first harmonic and (b) the second harmonic magnon frequency modulation as a function of applied perpendicular magnetic field.

In addition, platinum is close to the Stoner ferromagnetic instability, and it was hypothesized that Pt could become magnetized in close proximity to a magnetic insulator like YIG.[195,196] In such a case, the Pt film would be subject to magneto-transport phenomena such as the anomalous Hall effect (AHE) and the anomalous Nernst/Ettingshausen effect (ANE/AEE) that could modulate the Pt temperature in the presence of a magnetic field and a charge current. However, subsequent electrical measurements have found these effects to be negligible in comparison with spin Seebeck and Peltier effects in Pt/YIG structures[189] and LIT measurements have revealed the dominance of the SPE over the anomalous Ettingshausen effect.[71,72] For

these reasons, the AHE and AEE are not expected to play an important role in these measurements.

Oersted Field

The dispersion relation for dipolar-exchange spin waves in YIG is given by Eqn. (4.36):

$$f_m(\boldsymbol{q}, M, H) = \frac{\gamma}{2\pi}\sqrt{(H + H_a - 4\pi NM + D\boldsymbol{q}^2)(H + H_a - 4\pi NM + D\boldsymbol{q}^2 + 4\pi M)} \tag{4.36}$$

in addition to changes in magnetization M, the BLS-probed magnon frequency is sensitive to changes in the external field H. As shown in Fig. 4.20, a changing external field modulates the zero-wavevector magnon gap, effectively shifting the dispersion up or down in frequency.

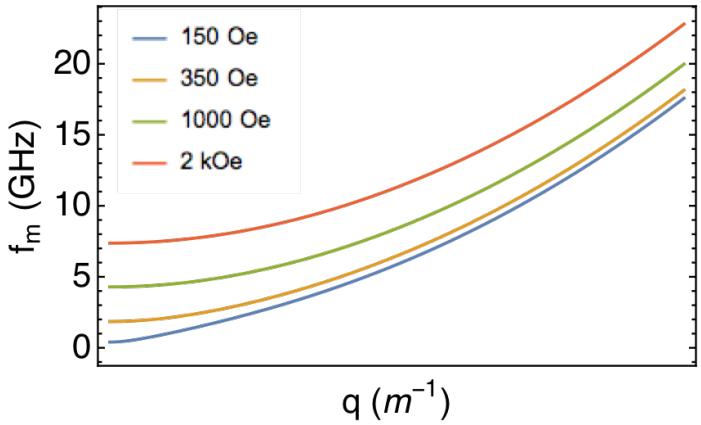

Figure 4.20: Calculated dipolar-exchange magnon dispersion based on Eqn. (4.36) for a range of wavevectors $\boldsymbol{q}$ near the Γ point for four different applied fields

A current-carrying conductor will generate a magnetic field according to the law of Biot-Savart. Often referred to as the Oersted field,[85,190,197] this magnetic field would wrap around the rectangular Pt line given by the left-hand rule for electrons. This effect would be linearly proportional to the charge current in the Pt, would be maximized when the YIG magnetization was made perpendicular to the Pt (and thus (anti)parallel to the Oersted field), and would flip phase when the the perpendicular magnetic field is reversed. In Appendix D, the magnitude of the Oersted field is derived analytically and the equilibrium magnon frequency at different magnetic fields

is used to show that the Oersted field could result in appreciable first harmonic modulation. In an attempt to separate the effect of the Oersted field from spin transfer phenomena at the Pt/YIG interface, a set of modulated BLS measurements is underway on two new devices patterned on 3 μm-thick YIG films: one consisting of Pt/YIG/GGG as before, and one with a 10 nm layer of Al_2O_3 grown by atomic layer deposition (ALD) between the Pt and the YIG. In principle, the Al_2O_3 should allow the effects of the Oersted field to be felt by the YIG, yet block any direct spin transfer. Figure 4.21 shows the measured first harmonic peak shift amplitudes as a function of current amplitude for these two new devices when a magnetic field of 350 Oe is applied perpendicular to the Pt lines.

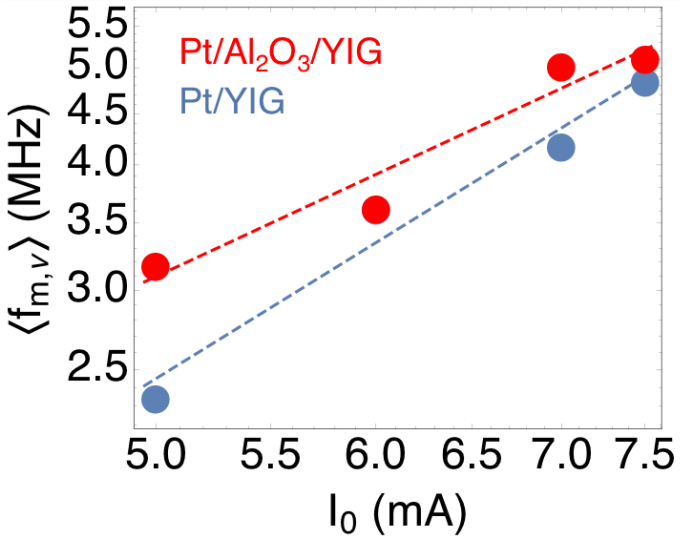

Figure 4.21: Comparison of the first harmonic amplitude of the magnon frequency modulation for the $Pt/Al_2O_3/YIG$ device (red) and the Pt/YIG device (blue) as a function of applied charge current amplitude I_0 when a field of 350 Oe is applied perpendicular to the Pt line. Note that both axes are on a log scale, and the dashed lines are linear fits to the data with a slope of about 1.3 and 1.7 for the red and blue, respectively.

However, these two different devices have resistances that differ by about 50% and so a direct comparison is difficult. The difference in resistance could be attributed to nonuniform Pt film thickness during sputtering or different Pt wetting behavior on Al_2O_3 as compared to YIG. To provide a direct comparison, further device fabrication is underway in attempt to produce Pt films deposited on either Al_2O_3/YIG or directly

on YIG that have measured sheet resistances within 10% of one another. Once this is obtained, the Pt will be patterned into lines and gold electrical contacts will be deposited.

Spatially-Resolved Modulated BLS Measurements

To characterize the lateral length scales of magnon diffusion in the 10 μm-thick YIG, amplitude-modulated micro-BLS measurements were carried out as a function of position away from the edge of the current-carrying Pt line (along the z-axis in Fig. 4.22(a)). The amplitudes of all the harmonics of the frequency shift were found to fall off as the laser was scanned a distance Δz away from the Pt edge. As shown in Fig. 4.22(b), the first harmonic component in particular drops off precipitously, while the second harmonic amplitude falls off over a longer length scale. If the first harmonic signal is driven primarily by magnon diffusion in the YIG and not from the Oersted field, it is possible to extract a magnon spin-flip diffusion length (λ_m) from these measurements. Directly beneath the Pt line, transport can be considered to be one-dimensional (1D) because the laser spot size is small compared to the 20 μm width of the Pt. The 1D magnon diffusion equation is (see Appendix E.1.2 for further derivation)

$$\nabla^2 n_m = \frac{n_m - n_0}{\lambda_m^2} = \frac{\delta_n}{\lambda_m^2} \tag{4.37}$$

where δ_n is the deviation in the magnon number density n_m, from the equilibrium number density n_0 at a local phonon temperature T_p. This can be related to the gradient in the phonon temperature and the first harmonic magnon frequency change δ_{f_m} as

$$\nabla^2 \theta_{p,YIG} + \nabla^2 \epsilon_{m,\nu} = \frac{1}{\lambda_m^2} \epsilon_{m,\nu} \tag{4.38}$$

where $\theta \equiv T - T_\infty$, T_∞ is the ambient temperature, and

$$\epsilon_{m,\nu} \equiv \frac{\delta_n}{\frac{dn_0}{dT_p}} = \frac{\delta_{f_m}}{\frac{\partial f_m}{\partial T_p}} \tag{4.39}$$

(Appendix E.1.2). As the laser is scanned away from the Pt, the 1D approximation is no longer valid, and so we are then tasked with solving Eqn. (4.38) in two dimensions. This task is additionally complicated by the Gaussian nature of the laser beam,

which implies that those quantities probed by the laser represent an average over the Gaussian distribution of the beam in 2D. The calculation was accomplished by a 2D finite element approach outlined in Appendix E.2. In brief, Eqn. (4.38) was solved in 2D for a variety of λ_m values and compared with experimental results. Specifically, the ratio between two of the experimentally-measured first harmonic frequency shifts (at points Δz_2 and Δz_1 away from the Pt line) were compared with the equivalent cases in the simulation for a range of λ_m. When the ratio from the simulation $\langle \epsilon \rangle_{\Delta z_2} / \langle \epsilon \rangle_{\Delta z_1}$ (solid line in Fig. 4.22(c)) was found to equal the ratio from experiment $\langle f_{m,\nu_J} \rangle_{\Delta z_2} / \langle f_{m,\nu_J} \rangle_{\Delta z_1}$ (dashed line in Fig. 4.22(c)), that represented the best-fit value for λ_m and was found to be ~ 0.95 μm. This value was then plugged back into the diffusion equation and used to solve for $\langle f_{m,\nu_J} \rangle$. This solution is plotted as the solid blue line in Fig. 4.22(b).

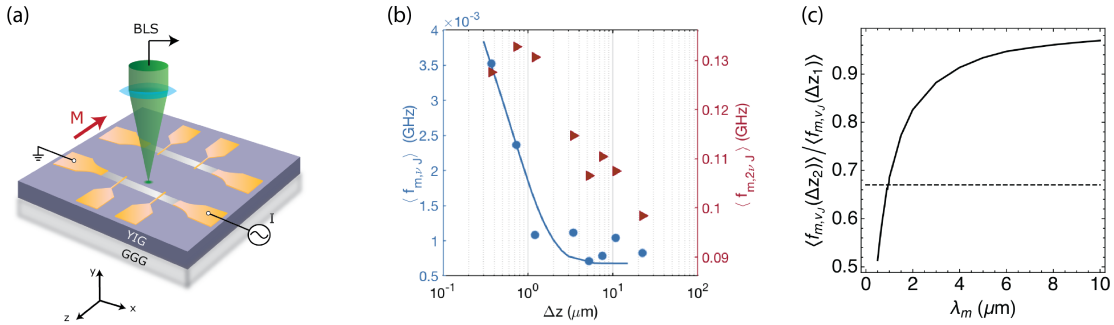

Figure 4.22: (a) Schematic of the nonlocal BLS measurements. (b) Measured first harmonic (blue circles) and second harmonic (red triangles) magnon frequency shift as a function of distance Δz away from the edge of the Pt. The blue line is a best-fit to the two-dimensional magnon diffusion equation and represents $\lambda_m \approx 0.95$ μm. (c) Solution to the non-dimensionalized magnon diffusion equation in 2D for a range of λ_m (solid line) in comparison with experimental results (dashed line).

Given that the Oersted field is appreciable, the precipitous drop in the first harmonic signal away from the Pt line is likely due to the decaying Oersted field rather than magnon diffusion in the YIG. In this case, the actual value of λ_m may be longer than 0.95 μm, but can simply not be detected by BLS. However, previous works have obtained magnon spin flip diffusion lengths on the order of several microns in YIG that is still much smaller than the 420 μm spacing between the two parallel Pt lines, indicating again that magnon diffusion between the two should be negligible

at room temperature.[64,71,98]

4.3.1 Measurement of Magnon Number Density at the Interface

From the BLS measurements, the magnon frequency shift is related to the change (Δn_m) in the magnon population (n_m) according to

$$\Delta n_m = -(g\mu_B \frac{\partial f_m}{\partial \boldsymbol{M}})^{-1} \Delta f_m \tag{4.40}$$

for a small Δf_m,[98] where the measured temperature-dependent $\boldsymbol{M}$ and f_m yield $\frac{\partial f_m}{\partial M} = \frac{\partial f_m}{\partial T} / \frac{\partial \boldsymbol{M}}{\partial T}$. For these YIG/GGG/YIG crystals, $\frac{\partial f_m}{\partial T}$ was obtained by temperature-dependent BLS measurements, as shown in Fig. 4.23(a). Meanwhile, $M(H)$ measurements (Fig. 4.23(b)) and $M(T)$ measurements (Fig. 4.23(c)) using vibrating sample magnetometry (VSM), were used to obtain $\frac{\partial \boldsymbol{M}}{\partial T}$.

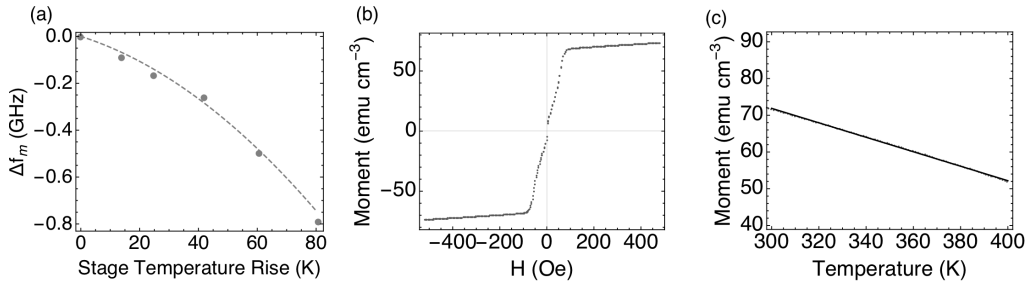

Figure 4.23: (a) BLS-measured magnon frequency change Δf_m as function of ambient temperature rise. The dashed line is a second-order polynomial fit. (b) Magnetic moment as a function of the applied magnetic field for the YIG/GGG/YIG (10 μm/500 μm/10 μm) sample in emu per cubic centimeter of YIG measured by a vibrating sample magnetometer at 300 K. The result indicates approximately 3.5×10^{21} cm^{-3} Bohr magnetons at the saturation magnetization in the YIG film. (c) Magnetic moment per cubic centimeter of YIG in the temperature range between 300 K to 400 K at an applied field of 350 Oe. The line is a linear fit to the data. The slope indicates $\frac{\partial \boldsymbol{M}}{\partial T} = -197$ JT^{-1}m^{-3}K^{-1}.

Based on this calibration, if the first harmonic frequency modulation measured by BLS is due to the SHE injection of spin, the measured $\langle f_{m,\nu_J} \rangle$ beneath the center of the Pt line can be used to obtain the number density of magnons that are injected

across the interface. The derivation of the analytical solution is in Appendix E leading up to Eqn. (E.66). In brief, the first harmonic modulation of the BLS frequency is expected to occur from two sources: the transfer of pure spin flux J_{s,ν_J} and from the spin-mediated heat flux Q^i_{s,ν_J} across the interface. For simplicity, the terms relating the magnon frequency shift to the pure spin flux are lumped into a coefficient α_1 and those terms relating the frequency shift to heat flux are lumped into a coefficient α_2:

$$f_{m,\nu_J} = \alpha_1 \frac{J_{s,\nu_J}}{eD_m \hat{M}_z} + \alpha_2 Q^i_{s,\nu_J} \tag{4.41}$$

where e is the elementary charge, D_m is the magnon diffusivity in the YIG, and $\hat{M}_z$ is the unit vector magnetization perpendicular to the Pt line and α_1 and α_2 are defined in Appendix E.1.2. Inside the laser spot, these quantities are weighted by the radial Gaussian beam distribution that also decays vertically into the YIG:

$$\langle f_{m,\nu_J} \rangle = \langle \alpha_1 \rangle \frac{J_{s,\nu_J}}{eD_m \hat{M}_z} + \langle \alpha_2 \rangle Q^i_{s,\nu_J} \tag{4.42}$$

In addition, the pure spin flux by magnons at the Pt/YIG interface (with units of A m^{-2}) can be related to the gradient in the magnon number density as

$$J_s = eD_m \left(\frac{\partial n_m}{\partial y} \right)_{y=0} \hat{M}_z \tag{4.43}$$

Therefore, even with an ignorance of the magnon diffusivity D_m or the magnitude of J_s, the gradient in the magnon number density can be found as

$$\left(\frac{\partial n_m}{\partial y} \right)_{y=0} = \frac{1}{\langle \alpha_1 \rangle} \left[\langle f_{m,\nu_J} \rangle - \langle \alpha_2 \rangle Q^i_{s,\nu_J} \right] \tag{4.44}$$

For the range of ℓ_{mp} up to 250 nm and $\lambda_m \approx 0.95$ μm, the term containing the spin mediated heat flux Q^i_{s,ν_J} is much smaller than the term containing $\langle f_{m,\nu_J} \rangle$. Based on this approximation and with a knowledge of the beam profile and the YIG absorptivity, the magnon number density at the interface is obtained as

$$n_{m,\nu_J,y=0} \approx -\frac{\cosh \frac{d}{\lambda_m}}{g\mu_B \frac{\partial f_m}{\partial M} \langle \cosh \left(\frac{d+y}{\lambda_m} \right) \rangle} \langle f_{m,\nu_J} \rangle \tag{4.45}$$

Figure 4.3.1 shows the extracted magnon number density using Eqn. (4.45) as a function of the applied charge current amplitude I_0 in the Pt. Based on this analysis, the magnon number density increases linearly with the applied I_0 at a rate of 1.9×10^{19} cm^{-3} for every additional mA of current in the Pt line. In comparison, the $M(H)$ measurements in Fig. 4.23(b) indicate approximately 3.5×10^{21} cm^{-3} Bohr magnetons at saturation at room temperature in the YIG film. The Landé g-factor is ~ 2 for YIG − almost the same as for a free electron spin − meaning each magnon reduces the YIG's magnetization by roughly two Bohr magnetons. Assuming the relationship continues linearly, this means a charge current of around 92 mA would inject enough magnons across the interface to desaturate the YIG magnetization.

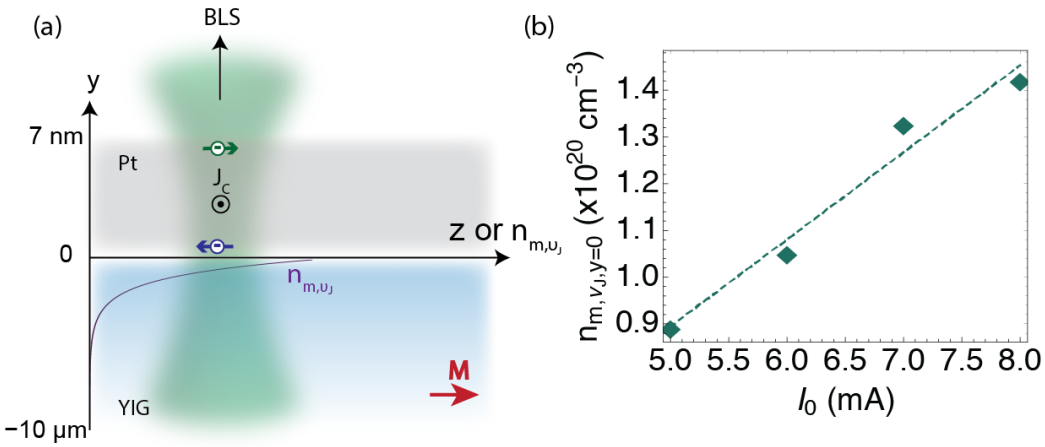

Figure 4.24: (a) Calculated magnon number density as a function of vertical position y (purple line) within the YIG generated by the SHE. (b) Magnon number density at the Pt/YIG interface as a function of the applied charge current.

4.4 Summary

Coupled spin-heat transport was studied at the interface of Pt and yttrium iron garnet (YIG) films using lock-in electrothermal and Brillouin light scattering experiments. A multitemperature model describing the coupled spin-heat transport in the heterostructure was solved analytically in one dimension, yielding the temperature profiles for the energy carriers in the Pt and YIG and estimating the spin-mediated

heat flux. In addition, an analysis of the various thermoelectric, magnetothermal, and spin caloritronic effects identified those effects that could would yield a signal during lock-in measurements. The lock-in electrical measurements were carried out at the second harmonic frequency of the charge current modulation in the Pt line, where the spin Peltier effect would be expected to cause resistivity modulation due to modulations in the Pt phonon temperature and the spin Seebeck effect (SSE) + inverse spin Hall effect (ISHE) would produce a voltage. Utilizing a double-Pt line device in a Wheatstone bridge configuration, effects such as the ordinary Peltier effect, Joule heating, and inductive coupling were minimized in the electrical measurements. Furthermore, the second harmonic measurements of Pt/YIG/GGG showed a dependence on the magnetic field orientation, whereas those performed on Pt/GGG did not, showing that the ordinary Nernst effect is not detectable in the measurements. In addition, frequency-dependent measurements of the third harmonic voltage signal due to Joule heating, coupled with circuit analysis of the double Wheatstone circuit extract the thermal conductivity of the YIG/GGG to be 10 $\mathrm{Wm^{-1}K^{-1}}$. While it is difficult to separate out the contribution from the SPE and that from the SSE+ISHE, if the resistance modulations at the second harmonic are ascribed to a changing Pt phonon temperature at the first harmonic, then the spin Peltier effect causes 0.25 mK temperature change for each mA of current in the Pt line. Based on the model, a spin-mediated heat flux across the interface was found to be 1.9 ± 1.1 W $\mathrm{cm^{-2}}$ for each additional mA of current in the Pt. This heat flux is appreciable compared to Joule heating and would dominate the Joule heating for currents below about 0.2 mA.

In addition, micro-Brillouin light scattering (BLS) measurements were used to characterize the changing magnon population directly at the Pt/YIG interface when current was passed through the Pt line. Using an amplitude modulated approach and frequency domain analysis, the change in magnetization in the YIG due to Joule heating could be separated from other effects. In particular, the first harmonic of the magnon frequency shift was found to depend on the direction of the magnetic field applied to the YIG. The first harmonic component was maximized when the field was perpendicular to the flow of the charge current, and flipped its phase by 180° when the magnetic field polarity was flipped. Additionally, the first harmonic component disappeared when the magnetic field was made parallel to the current flow in the Pt

line. This angle dependence is consistent with both spin Hall injection of spin current from the Pt to the magnon population in the YIG, as well as Oersted fields around the Pt line. Additionally, spatially resolved modulated BLS measurements were performed as the laser was scanned away from the edge of the Pt. In conjunction with a 2D numerical solution to the magnon diffusion equation, we found the first harmonic signal in the BLS frequency shift decayed over a characteristic length scale of $\sim 0.95\ \mu$m, which may likely be due to the decaying Oersted field rather than magnon diffusion in the YIG. Finally, using temperature-dependent magnetometry measurements of the YIG crystals, BLS was calibrated as a sensitive local magnetometer. In particular, an analytical model was used to shown that if the measured change in magnetization by BLS is due to the SHE injection of magnons, then magnon number density increases by 1.9×10^{19} cm^{-3} for for each additional mA of current flowing in the Pt line.

Chapter 5

Conclusion

The purpose of this work has been to investigate the mechanisms and transport characteristics of energy and spin carriers and in materials systems that offer minimal resistance to the carrier transport, as well as to develop measurement techniques with sufficient sensitivity to better characterize this transport. In particular, this work examined local nonequilibrium among different phonon polarizations in suspended graphene, validated the ultrahigh thermal conductivity of boron arsenide, and investigated spin-heat coupling in Pt/yttrium iron garnet (YIG) heterostructures.

Probing the carrier transport processes in materials with high thermal conductivity or low spin wave damping requires sensitive experimental techniques that can adequately drive and resolve the small signals that arise without inadvertently interfering with the intrinsic transport properties or introducing artifacts into the measured signal. Here, inelastic light scattering (ILS) spectroscopy was used as a noncontact technique to probe heat and spin transport in graphene, BAs, and YIG. In addition, microfabricated electrical measurement devices were used to probe the thermal transport in a suspended BAs microstructure and to measure the spin-mediated heat transport driven by the spin Hall effect at Pt/YIG interfaces.

Using a tightly-focused laser to heat suspended graphene, it was found that the different phonon polarizations in the graphene sheet could be driven out of local thermal equilibrium with one another. By performing Raman measurements at different laser intensities and ambient temperatures, the intensity ratio and peak shift of the graphene G-band and the shift of several higher-order bands were used as temperature sensors. The laser heating-induced temperature rise obtained from each of

these temperature sensors was found to be different. In tandem, a first principles-based multitemperature simulation of the experimental conditions predicted that the tightly-focused heater would preferentially heat electrons and optical phonons in the graphene, which then cool over some time and length scale by thermalizing with the acoustic phonons. Because the focused heating laser is also the probe, within the small region probed by the beam, the energy carriers have not come to thermal equilibrium. The experimental results coupled with the multitemperature model and an analysis of the scattering pathways in graphene suggest that the long mean free path flexural acoustic (ZA) phonons are appreciably underpopulated in the measurement. The nonequilibrium among the energy carriers, in particular the acoustic phonon polarizations, implies that an extraction of thermal conductivity from the measurements is not meaningful. These results can partially explain the very different values of thermal conductivity obtained by micro-Raman measurements of suspended graphene and advise checking for equilibrium in future Raman measurements of two-dimensional (2D) materials. In addition, the results are expected to motivate the future study of other 2D materials that can have long mean free path energy carriers. The results additionally motivate the future study of the effects of nonequilibirum on the performance graphene devices when small regions of the material are subject to electrical or optical excitation.

Raman measurements were additionally employed to validate the high thermal conductivity (κ) in bulk BAs crystals. While BAs had been predicted to achieve an ultrahigh κ at room temperature due to its unique phonon band structure, prior measurements of as-synthesized crystals yielded conductivities only as high as a few hundred $\mathrm{Wm^{-1}K^{-1}}$. However, large high-quality crystals recently grown by collaborators at the University of Houston have indicated that they may indeed have excellent thermal transport properties: steady-state comparative measurements indicated that their room temperature thermal conductivity was as high as around 900 $\mathrm{Wm^{-1}K^{-1}}$, while microprobe measurements indicated κ of > 1000 $\mathrm{Wm^{-1}K^{-1}}$ in some places. However, the bulk steady-state comparative measurements relied on thermocouples that make contact with the sample and are thus subject to heat loss and thermal contact resistance. In addition, the spatial inhomogeneity evident in the microprobe measurements made the extraction of a bulk thermal conductivity value for the samples difficult. In order to validate the high bulk thermal conductivity in BAs, Raman

thermometry was utilized as a non-contact temperature probe in the comparative steady-state measurements. In order to improve the temperature sensitivity of Raman, however, a modulated heating approach was developed. In this approach, the current supplied to the heater was stepped in discrete intervals to follow a sine and the Raman peak shift of either the Si reference or the BAs sample was used as a temperature sensor. Frequency domain analysis of the modulated Raman shift isolated the shift caused only by the heating at the second harmonic, improving the sensitivity by removing the broad spectrum of noise at other harmonics. These measurements yielded a similarly high κ, validating BAs as the only semiconductor with ultrahigh thermal conductivity. In addition, modulated Raman measurements were carried out on a suspended BAs microrod using a microfabricated heater/thermometer and a differential method to isolate the heat flux. The microrod also had relatively high κ. While these results do show that BAs can indeed achieve high thermal conductivity, however, there is much to be understood regarding the mechanisms that reduce thermal conductivity and where these fit into the synthesis-processing-thermal properties paradigm for BAs.

Lastly, a combination of lock-in magnetotransport measurements and modulated signal Brillouin light scattering (BLS) measurements were used to evaluate coupled-spin and heat transfer at Pt/YIG interfaces. We developed an analytical one-dimensional multitemperature model for the heterostructure that considered electron and phonon temperatures in the Pt, magnon and phonon temperatures in the YIG, and phonon temperature in the GGG. Utilizing a double-Wheatstone bridge configuration to remove spurious signals and maximize sensitivity, lock-in electrical measurements showed a quadrature voltage signal that was modulated at the second harmonic frequency and was dependent on the orientation of the magnetic field. Such a signal is consistent with resistivity modulation due to the spin Peltier effect (SPE), or a longitudinal electric field resulting from the spin Seebeck effect (SSE) and the inverse spin Hall effect (ISHE). If the second harmonic signal can be ascribed to the SPE, the developed model yields the spin-mediated heat flux at the interface driven by the spin Hall effect (SHE) in the Pt to be about 1.9 ± 1.1 W cm^{-1}. In addition, modulated micro-BLS measurements were used to directly probe the changing magnetization at the Pt/YIG interface based on the spectrum of thermal magnons in the YIG. Frequency domain analysis was able to separate the contributions to re-

duced magnetization by Joule heating in the Pt at the even harmonics. Meanwhile, a change in magnetization that was linearly proportional to the applied charge current was observed and its magnetic field dependence is consistent with either direct spin injection into the YIG driven by the SHE or a magnetization change caused by Oersted fields in proximity to the Pt conductor. An analytical model for the magnon number density at the interface was developed and related to the BLS results. Sensitive detection and isolation of individual spincaloritronic effects in such structures is challenging. Further work is underway to separate the effects of the Oersted fields in the BLS measurements. Meanwhile, this work demonstrates that the sensitivity of BLS can be improved using a modulated technique, enhancing its utility as a sensitive scanning magnetometer. These results will likely stimulate optothermal and electrothermal investigations into additional SHE-driven and SSE/SPE-driven phenomena in new heterostructures.

Appendix A

Theory of Inelastic Light Scattering in Crystals

The exchange of energy and momentum between material excitations (quasi-particles) and light follows from the microscopic theory of light-matter interaction. The origins of light-matter interaction from a classical perspective can be described in the following way.

1. The oscillating electric field of incident light causes the electrons to redistribute about their ionic nuclei, thus creating an oscillating local polarization in the material.

2. Material excitations such as phonons or magnons slightly affect the local complex susceptibility and make spatially periodic changes to the material's optical properties like the refractive index. Specifically they affect the oscillating dipoles that result from the incident light.

3. An oscillating dipole emits radiation. The oscillating dipoles that are affected by phonons/magnons emit photons at a different frequency than the incident light.

The changing electric field of scattered light $\boldsymbol{E}_s$ can be expressed in terms of the dipoles that are polarized by the incident light with polarization $\boldsymbol{p}$ as[198,199]

$$d\boldsymbol{E}_s = -\frac{k_s^2}{4\pi\epsilon_0 r} \exp\left[ik_s \cdot r\right] \hat{r} \times \hat{r} \times \boldsymbol{p} \tag{A.1}$$

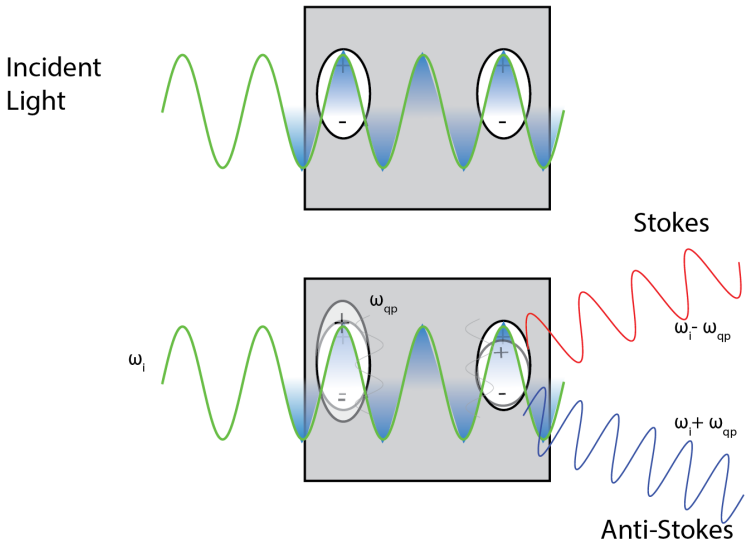

Figure A.1: Schematic of the inelastic light scattering mechanism by quasiparticles. (Top) incoming light polarizes a material. (Bottom) quasiparticle excitations such as magnons or phonons in the material affect the dielectric susceptibility, which alters the frequency of the oscillating dipoles and light is emitted at a shifted frequency from.

where r is the distance from the viewpoint to the dipole and ϵ_0 is the permittivity of free space. Furthermore, the dipole induced by the incident light, $\boldsymbol{p}$, can be written in the terms of the polarization per unit volume $\boldsymbol{P}$ times the differential volume element dV. $\boldsymbol{P}$ arises from the volumetric effect of the incident electric field $\boldsymbol{E}_i$ on the dielectric susceptibility tensor $\overleftrightarrow{\chi}$:

$$\boldsymbol{p} = \epsilon_0 \overleftrightarrow{\chi} \cdot \boldsymbol{E}_i \exp\left[-ik_i \cdot r\right] dV \tag{A.2}$$

Quasiparticle excitations in the material can modulate the susceptibility as $\delta\overleftrightarrow{\chi} \exp\left[\pm i\boldsymbol{q} \cdot r\right]$, where $\boldsymbol{q}$ is the wavevector of the quasiparticle. The scattered light is thus

$$d\boldsymbol{E}_s = -\frac{k_s^2}{4\pi\epsilon_0 r} \exp\left[i(k_i \pm \boldsymbol{q} - k_s) \cdot r\right] \hat{r} \times \hat{r} \times \overleftrightarrow{\chi} \cdot \boldsymbol{E}_i dV \tag{A.3}$$

More commonly, scattering processes are represented in terms of their differential scattering cross-section (scattered power per solid angle) as

$$\frac{d\sigma}{d\Omega} = \frac{r^2 \mid e_s \cdot \boldsymbol{E}_s \mid^2}{e_i \cdot \boldsymbol{E}_i} = \frac{k_s^4}{(4\pi\epsilon_0 \boldsymbol{E}_i)^2} \mid e_s \cdot \delta\overleftrightarrow{\chi} \cdot e_i \mid^2 \exp\left[i(k_i \pm \boldsymbol{q} - k_s) \cdot r\right] dV \tag{A.4}$$

where e_i and e_s are the polarization vectors of the incident and scattered light, respectively. Integrating over volume yields the momentum conservation requirement $k_s = k_i \pm \boldsymbol{q}$. This requirement causes the exponential term to $\to 1$. Utilizing the dispersion relation for light $\omega = ck$, one obtains

$$\frac{d\sigma}{d\Omega} = \frac{\omega_s^4 V^2}{(4\pi\epsilon_0)^2 c^4} \mid e_s \cdot \delta\overleftrightarrow{\chi} \cdot e_i \mid^2 \tag{A.5}$$

where c is the speed of light and V is the volume of the material. The differential scattering cross-section determines the scattering intensity, and thus affects the intensity of signals measured by inelastic light scattering spectroscopy. The expression derived above explains why the expression for the Raman intensity ratio has the ω^4 dependence.

Optical Phonons

Optical phonons result from those normal modes that involve relative atomic motion between the distinct atoms within a unit cell. Intuitively, the frequencies would be large due to the strong bonding interaction within a unit cell. Optical phonons modulate the susceptibility tensor by directly changing the crystal or molecules polarizability, resulting in Raman scattering. The differential scattering cross-section for Raman scattering by optical phonons is

$$\frac{d\sigma}{d\Omega} = \frac{\hbar\omega_s^4 V^2}{32(\pi\epsilon_0)^2 c^4 \omega(\boldsymbol{q})} \mid e_s \cdot \frac{d\overleftrightarrow{\chi}'}{d\xi} \cdot e_i \mid^2 \times \begin{cases} n(\boldsymbol{q}) + 1(\text{Stokes}) \\ n(\boldsymbol{q})(\text{anti-Stokes}) \end{cases} \tag{A.6}$$

where ξ is the normal mode coordinate.

Acoustic Phonons

Light scattering by acoustic phonons, or Brillouin scattering, is effectuated by the perturbations in a material's dielectric tensor due to strain waves caused by the coherent displacement of atoms. The strain wave for a displacement u_0 with polarization e_k is[138] $\varepsilon_{jk}(\boldsymbol{q}) = u_0 e_k q_j \exp\left[i(\boldsymbol{qr} - \omega(\boldsymbol{q})t)\right]$, where $\omega(\boldsymbol{q})$ is acoustic phonon frequency. The differential scattering cross-section for Brillouin scattering by acoustic phonons is

$$\frac{d\sigma}{d\Omega} = \frac{\epsilon^4 \omega_s^4 V^2 \omega(\boldsymbol{q})}{(4\pi)^2 \epsilon_0^4 c^4 \rho v_g^2} \mid e_s \cdot \overleftrightarrow{P} \cdot e_i \mid^2 \times \begin{cases} n(\boldsymbol{q}) + 1(\text{Stokes}) \\ n(\boldsymbol{q})(\text{anti-Stokes}) \end{cases} \tag{A.7}$$

where ρ is the material density, v_g is the phonon group velocity, and the strain wave modifies the components of the elasto-optic tensor $\overleftrightarrow{P}$.[86]

Magnons

Magnons produce time- and spatially distributed variations in the local magnetization, which can modulate the susceptibility. The differential scattering cross-

section for scattering by magnons is given by

$$\frac{d\sigma}{d\Omega} = \frac{\hbar M_s \omega_s^4 \bar{n}}{2\pi c^4} \begin{cases} \mid A^- \mid^2 n_m(\boldsymbol{q}) + 1(\text{Stokes}) \\ \mid A^+ \mid^2 n_m(\boldsymbol{q})(\text{anti-Stokes}) \end{cases} \tag{A.8}$$

where $\bar{n}$ is the refractive index, M_s is the saturation magnetization, and the coefficients $A^{\mp}$ are dependent on the incident and scattered light polarization and the magneto-optic tensors $\overleftrightarrow{G}$ and $\overleftrightarrow{K}$.[200] For the case that the applied field and saturation magnetization are along $\hat{z}$, [001],

$$\begin{aligned} A^- &= 2M_s G_{44}(e_i^z e_s^+ + e_i^+ e_s^z) + iK(e_i^z e_s^+ - e_i^+ e_s^z) \\ A^+ &= 2M_s G_{44}(e_i^z e_s^- + e_i^- e_s^z) - iK(e_i^z e_s^- - e_i^- e_s^z) \end{aligned} \tag{A.9}$$

Here, $\overleftrightarrow{G}$ and $\overleftrightarrow{K}$ are magneto-optic tensors that, for a cubic crystal like YIG have many zero components, and e_i and e_s are the usual incident and scattered light polarizations. The superscripts indicate transverse polarization components $e^{\pm} = e^x \pm ie^y$. Thus the polarization selection rules shown in the $A^{\pm}$ coefficients indicate that the scattering cross-section is maximized when the incident and scattered light have orthogonal polarizations.

Appendix B

Molecular Dynamics Simulation of Point-Like Heating in Freestanding Graphene

B.1 Simulation Parameters

Using the molecular dynamics package LAMMPS[201], several different experiments were carried out on graphene *in silico* using the Stampede cluster maintained by TACC. Throughout all simulations, the Tersoff potential optimized by Lindsay and Broido[202] for studying thermal transport in graphene was used, along with a constant timestep of 1 fs. The pairwise Tersoff empirical interatomic potential (EIP) consists of repulsive and attractive terms, the latter of which includes a coordination-dependent bond angle coefficient that seeks to optimize the angles between neighboring atoms to match those found in strong covalently bonded systems like graphene. The generic Tersoff potential is written as

$$U_{ij} = f_C(r_{ij}) \left[f_R(r_{ij}) + b_{ij} f_A(r_{ij}) \right] \tag{B.1}$$

where r_{ij} is the separation betweens atoms i and j and $f_R(r) = Ae^{-\lambda_1 r}$ and $f_A(r) = -Be^{-\lambda_2 r}$ are attractive and repulsive pairwise functions, respectively. f_C is a cutoff

function

$$f_C(r) = \begin{cases} 1, & r < R - D \\ \frac{1}{2} - \frac{1}{2}\sin\left[\frac{\pi}{2}(r-R)/D\right], & R - D < r < R + D \\ 0, & r > R + D \end{cases} \tag{B.2}$$

where R and D are parameters with units of distance. The b_{ij} term modulates the bond strength as a function of coordination number:

$$\begin{aligned} b_{ij} &= \left(1 + \beta^n \zeta_{ij}^n\right)^{-\frac{1}{2n}} \\ \zeta_{ij} &= \sum_{k \neq i,j} f_C(r_{ij}) g(\theta_{ijk}) e^{\left[\lambda_3^3 (r_{ij} - r_{ik})^3\right]} \\ g(\theta) &= 1 + \frac{c^2}{d^2} - \frac{c^2}{\left[d^2 + (h - \cos\theta)^2\right]} \end{aligned} \tag{B.3}$$

in which θ_{ijk} is the angle between atoms i and k subtended at atom j and β, n, c, d, h, and λ_x are fitting parameters. The Tersoff parameters optimized by Lindsay and Broido to closely reproduce the acoustic phonon dispersion were used in this study. Specifically, the B and h parameters have been modified from the original Tersoff potential parameters for carbon.[202]

The structures that were studied all consisted of pristine, single layer graphene ranging in size from 340 to 68,000 atoms. These structures were generated to have the Tersoff-optimized lattice parameter $a = 2.492$ Å; however, following structure initialization, energy minimization was performed on the structures to ensure an optimal configuration prior to thermalization. The graphene was then thermalized by initiating a Gaussian distribution of velocities and equilibrated at the desired temperature and zero in-plane pressure under the isobaric-isothermal (NPT) ensemble, using a Nosé-Hoover thermostat/barostat. After thermalization, the structure was allowed to relax in the microcanonical (NVE) ensemble. Total thermalization and relaxation times ranged from 600 ps to 1 ns.

To examine the effects on phonon dispersion and density of states as described by the Lindsay-Broido-Tersoff potential, graphene structures 17 x 10 unit cells (340 atoms) in size were used. After thermalizing and relaxing at the desired temperature, the LAMMPS command *fix phonon* was used to calculate the dynamical matrix averaged over a 2.5 ns period. The post processing code *Phana*[203] allowed for the cal-

culation of phonon dispersion curves and phonon density of states using a fluctuation-dissipation method. The phonon dispersion curves were numerically calculated with 300 discrete values between high-symmetry $\boldsymbol{q}$-points, and the phonon density of states were calculated on a $34 \times 20 \times 1$ Monkhorst-Pack mesh.

B.2 Phonon Dispersion and Density of States Calculation

Calculations of the graphene phonon dispersion and density of states (DOS) were carried out at three different ambient temperatures: 150 K, 300 K and 1500 K. Figure B.1(a-c) shows the calculated phonon dispersion curves along the $\mathbf{\Gamma}-\mathbf{M}-\mathbf{K}$ path at the three different temperatures. The waviness of (a) and (b) indicate the 2.5 ns sampling time in the fluctuation-dissipation method calculation is insufficient for temperatures far below graphene's Debye temperature. However, the results are similar to those shown by Lindsay and Broido using this potential and are close to the experimentally-derived dispersions for graphene.[202] In all cases, the linear LA and TA branches, the quadratic ZA branch, and the three optical branches can all be seen, with group velocities that appear close to experimental values with $v_{g,LA} \approx 15$ km/s and $v_{g,TA} \approx 22$ km/s.

As the temperature is increased, the first feature of note is a general downshift in the vibrational frequencies. This trend can be explained by the nature of the bonding interactions and the accurate depiction of anharmonicity and bond softening by the potential. While the exact frequency shifts may not be accurately described by this potential, the trend is there. Figure B.1(d) shows the relatively large DOS for the high-frequency optical modes, which is consistent with experimental and other theoretical studies.[204] Lower frequency phonons, like the flexural acoustic (ZA) phonons, are expected to dominate at low temperatures.[8,137] Slight evidence of this trend can be seen in the phonon dispersions and density of states: at all three temperatures, the lower frequency phonon populations are about the same. As temperature is increased, only the density of states of higher frequency optical phonons grows. It is important to note that MD does not take into account quantum phenomena, such as the Uncertainty Principle, and so cannot fully describe phonon behavior far below the

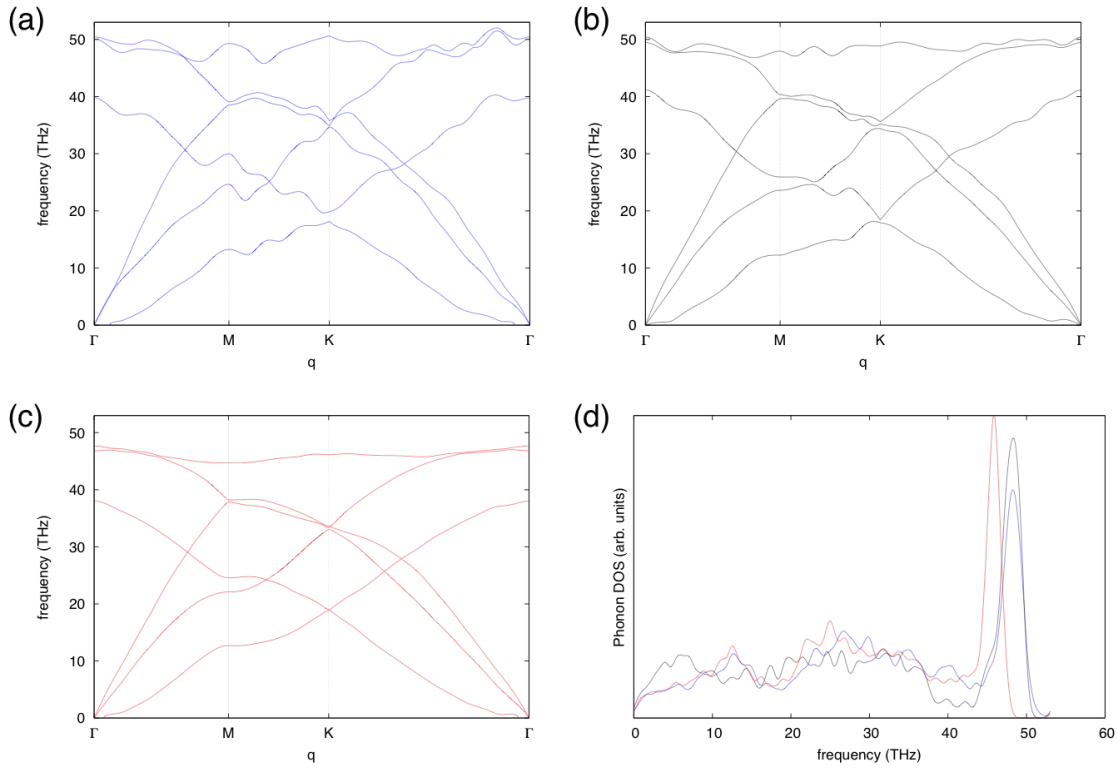

Figure B.1: Graphene phonon dispersions calculated from molecular dynamics using the Lindsay-Broido-Tersoff potential at (a) 150 K, (b) 300 K, and (c) 1500 K. (d) shows the calculated phonon density of states at the three different temperatures.

Debye temperature, which is quite high (∼2100 K[205]) for graphene. The disparities are especially large for optical phonons, which occur at higher frequencies and consist of atomic vibrations that are more highly localized. Additionally, the phonon dispersion curves for temperatures far below T_{Debye} (150 K, 300 K) are less smooth than that for 1500 K. As the temperature increases, the sampling of the Green's function becomes better and the averaged dynamical matrix is better converged. The undulations occurring in the phonon dispersions at low temperatures can be mitigated by choosing a longer (> 2.5 ns) correlation time to compute the dynamical matrix.

B.3 Point-like Heating in a Graphene Sheet

To simulate the effects of laser heating on a graphene membrane, a scaled-down version of an experimental configuration was required due to computational limitations. A 68,000 atom square sheet of graphene with periodic boundary conditions was used with the laser-heated region defined in a cylindrical region with a radius of 10 unit cells (24.92 Å) in the center of the sheet. Several methods were attempted in order to simulate the heat input of the laser, including introducing a constant heat current, as well as introducing an oscillating electric field while using a potential that includes electrostatic interactions, such as reaxFF. However, simply thermostatting the laser-heated region to a higher temperature (2000 K) while thermostatting the periphery atoms to 300 K seemed to perform the best and was far less computationally intensive than using reaxFF. In this heat source/sink geometry, the dynamics of the atoms in between the laser spot region and the periphery atoms − atoms within an annulus of inner radius $10a$ and outer radius $80a$, were described using the microcanonical (NVE) ensemble, while the atoms beyond the outer radius were thermostatted to 300 K (Fig. B.2).After allowing this system to develop over about 2 ns, the individual atomic temperatures and pseudo-heat currents were averaged over 10 ps time intervals (approximately one tenth the thermal time constant for graphene[205,206]) for a total of 1.1 ns.

Using the dual thermostatting method, a radial temperature gradient was generated from the center of the 42 nm x 42 nm graphene sheet. This temperature profile can be seen visually in Fig. B.3(a), which shows the color-coded atomic temperature distribution. These atomic temperatures are calculated based on the per-atom kinetic energies and are averaged every 10 ps. Fig. B.3(b) shows a temperature profile with spatial averaging performed azimuthally, while Fig. B.3(c) shows the Cartesian spatially averaged profile. The profiles are roughly Gaussian.

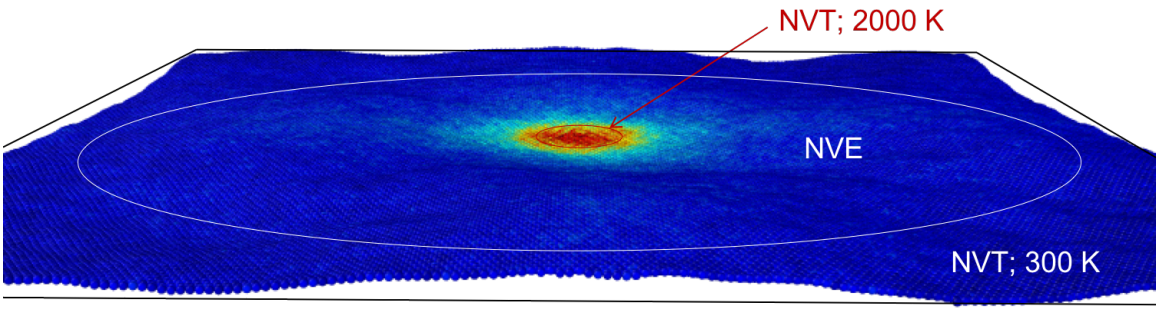

Figure B.2: Atomistic model of the freestanding graphene sheet used for the pointlike heating experiments. The central portion was thermostatted to 2000 K in the NVT ensemble, the central annulus was allowed to evolve under the NVE ensemble, and the outer atoms were thermostatted to 300 K under NVT. The atom coloring correspond to atomic temperatures.

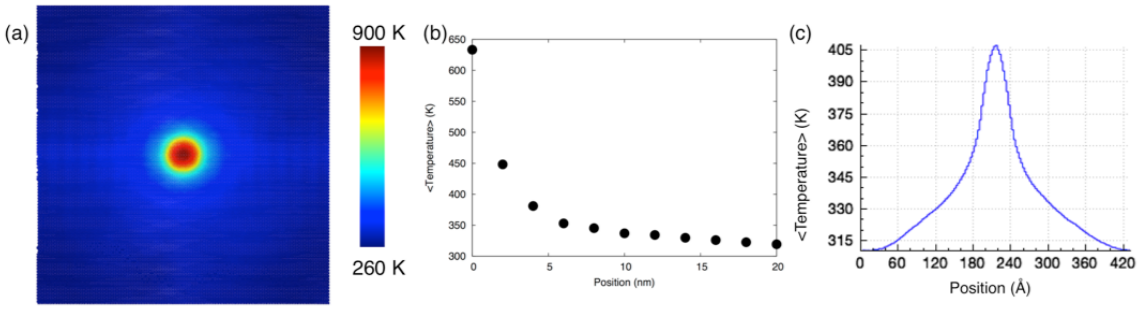

Figure B.3: Temperature profiles under pointlike heating temporally averaged over 1 ns (a) per atom, (b) spatially averaged azimuthally, and (c) spatially averaged on a Cartesian mesh.

B.4 Atomic Heat Current Distribution

In addition to temperature, it is possible to examine the heat flux on an atomic basis via MD. Commonly used in the Green-Kubo equilibrium formalism, heat flux transported by a group of atoms is defined as

$$J_Q = \frac{1}{\Omega}\left[\sum_i T_i U_i v_i - \sum_i \overleftrightarrow{s_i} v_i\right] \tag{B.4}$$

where v_i, T_i and U_i are the velocity, kinetic energy, and potential energy of the i^{th} atom, $\overleftrightarrow{s_i}$ is the six-component virial stress tensor, and Ω is the total volume containing the group of atoms. Computing only the summands will provide the atomic flux vector; however an appropriate volume, Ω, must be chosen to be dimensionally correct. While it is possible to calculate per-atom volumes through Voronoi tessellation in LAMMPS, this is a computationally expensive undertaking. Instead of tessellation and to avoid the arbitrariness of defining an atomic volume, only the summands in brackets are computed to obtain atomic pseudo-heat current vectors that have units of [W m] instead of the typical [W m^{-2}] for heat flux.[23,207] Visualizations of the radial and out-of-plane components of the atomic pseudo-heat current are shown in Fig. 3. Fig. 3 (a) shows a radial heat flux that is similar in profile to the temperature distribution in Fig. B.3(a). The snapshots, each averaged over 10 ps, shown in Fig. B.4(b-d) indicate a wave of relatively high out-of-plane-polarized heat current that propagates radially outward from the heated spot. This real space visualization is similar to the ZA phonon modes in graphene, which have an out-of-plane polarization, but propagate in-plane. This atomic heat current "wave" can be seen at different times over the 1 ns run, and has a relatively slow velocity of 500-700 m/s. ZA phonons have a quadratic dispersion (and $\boldsymbol{q}$-dependent group velocity), but are known for traveling with low group velocities close to or slightly above this range near the $\boldsymbol{\Gamma}$-point.[208,209] However, due to the periodic boundary conditions of the simulation, the heat currents re-enter the simulation domain on the opposite sides.

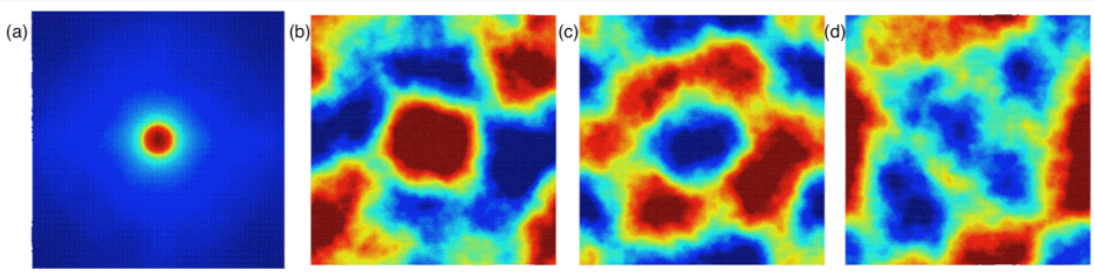

Figure B.4: Per-atom pseudo-heat current vectors in the graphene sheet with pointlike heating with polarization (a) in-plane and (b-d) out-of-plane. Units are on the order of 1 to 5×10^{-19} W m. Snapshots (b-d) show the radial outward propagation of a heat current with out-of-plane polarization at a velocity of 500-700 m/s.

Appendix C

BLS Measurement Procedure

C.1 Description of the Micro-Brillouin Light Scattering (BLS) Experiment

A schematic of a micro-BLS measurement for magnons and the inside of the interferometer are reproduced in Fig. C.1. The Sandercock tandem Fabry-Pérot interferometer[87] consists of two cavities of parallel mirrors with reflective coatings optimized for light near $\lambda = 532$ nm. The first Fabry-Pérot (FP1) cavity has a spacing of L_1 while the second (FP2) has a spacing L_2. In an ideal FP cavity, light of wavelength λ will only be transmitted through the cavity when the constructive interference condition $L = n\lambda/2$ is met, where n is an integer. By scanning the spacing L, different wavelengths of light can be let through. However, in practice, the mirrors do not behave as a perfect filter. Instead, the transmittance has a finite spectral width as described by the Airy function

$$T \approx \frac{1}{1 + \frac{4F^2}{\pi^2} \sin \frac{2\pi L}{\lambda}^2} \tag{C.1}$$

where F is called the finesse and is related to the quality of the mirror's reflectivity. The cavities in the Sandercock interferometer have a finesse of about 100. BLS spectra are acquired by slightly scanning the mirror spacing and measuring the intensity of the transmitted light. The frequency range and resolution of a measurement is related to the equilibrium mirror spacing L. By setting the mirrors to smaller spacing, a

larger frequency range can be observed. This is quantified by the free spectral range (FSR), which describes the frequency spacing between two transmitted peaks of light at wavelength λ as the mirror cavity is scanned. It is given by $\Delta\lambda = c/(2L)$, where c is the speed of light. The spectral resolution of the instrument is related to $\Delta\lambda$ and the finesse by $\delta\lambda = \Delta\lambda/F$. Therefore, the smaller the mirror spacing, the larger the FSR and the poorer the spectral resolution. The Sandercock design utilizes two interferometer cavities to increase the the FSR and improve contrast without sacrificing resolution. Cavities FP1 and FP2 have slightly different mirror spacings, L_1 and L_2 as shown in Fig. C.1. In order for light to be transmitted through both cavities, the constructive interference condition must be met for both, i.e. $L_1 = n\lambda/2$ and $L_2 = m\lambda/2$. This is satisfied only for large multiples of the FSR for the first cavity, and in effect increases the FSR of the whole system. In the design here, light makes six passes through the FP cavities (3 through the first and 3 through the second), which enhances the filtering effect of the cavities and improves the contrast. The transmitted beam is ultimately focused through a pinhole and onto the avalanche photo diode (APD). The APD relies on a photsensitive semiconductor diode that produces a large voltage upon excitation by a photon. An amplification mechanism allows the detector to register single photons. The intensity of the incoming light is measured by counting the number of photons that reach the detector within a very short time-gated increment. This gating is synchronized to the scanning of the mirrors by means of a timing board inside the BLS control unit and allows the intensity to be associated with a particular frequency of light. In order to protect the sensitive APD from overload and damage by the very strong elastic light reflected from the sample, a shutter is placed after the entrance pinhole. This shutter closes every time the mirrors scan to a spacing where 532 nm light would be allowed to be transmitted.

The transmittance of light through the cavities is very sensitive to the spacing and mirror orientation and is only optimized when the internal surfaces of the mirrors are parallel. The mirrors are maintained parallel to one another throughout the measurement by means of a feedback control loop mechanism. A weak ($\sim<$ 1 mW) reference beam of λ = 532 nm light is allowed to enter the beam path. This is accomplished by a beam sampler placed just after the laser, which picks off a weak portion of the beam and directs it to the light diffusing optic on the side of the BLS. A beam splitter then couples this diffuse reference beam into ordinary beam path. When

the shutter is closed to block the elastic light from the sample, the reference beam is still allowed to enter and transmits through the cavities. A set of two piezoelectric transducers (PZTs) on the non-scanning mirror of each of the mirror cavities provides fine adjustment to the mirror angle. Throughout the measurement, the voltages on the PZTs are continuously tuned to maximize the transmission of the reference beam, thereby maintaining mirror alignment. In addition, the scanning stage is mounted on an active vibration damping mechanism. A three-axis accelerometer monitors ambient vibrations and a series of PZTs are used to attenuate these by actuation along the appropriate axis with a frequency and amplitude necessary to deconstructively interfere with the detected vibration.

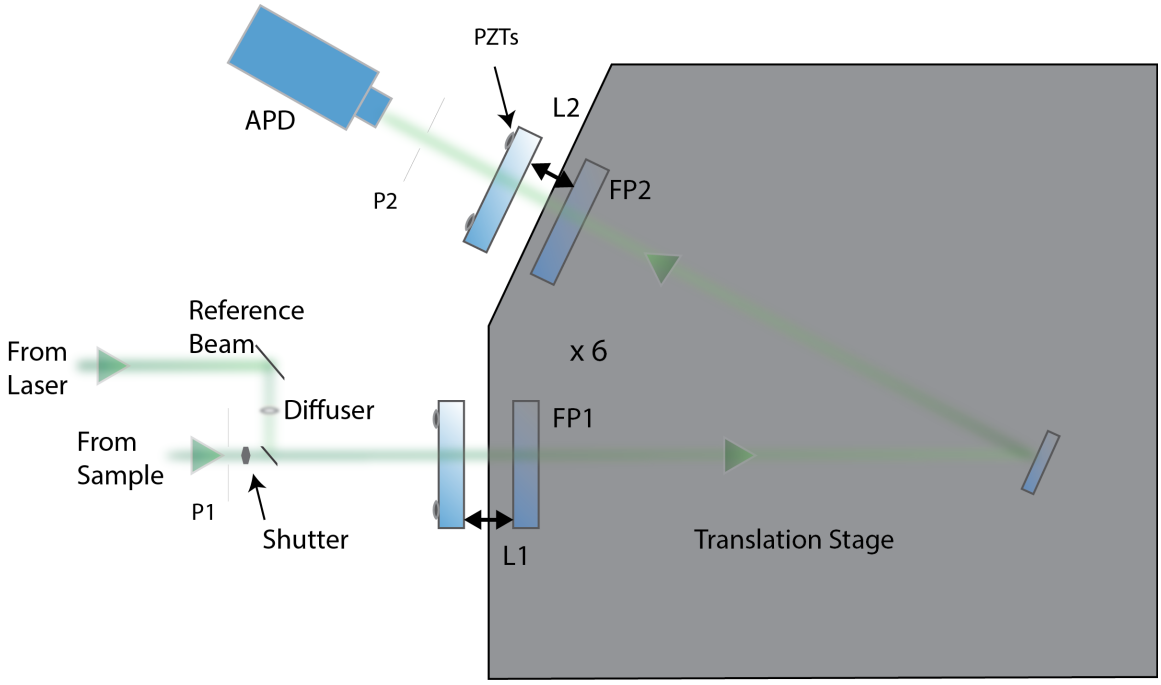

Figure C.1: Key components of the tandem scanning Fabry-Pérot interferometer.

C.2 Standard Operating Procedure for Micro-BLS Measurements

1. **Verify that all potential beam paths to the avalanche photodiode (APD) detector are blocked**

(a) Check that both the entrance pinhole to the BLS and the exit pinhole to the detector are in-between pinhole increments (i.e. blocking the beam)

2. Turn on the laser

   (a) Press the black toggle switch on the 532 nm Excelsior Spectra-Physics laser to begin warm-up

   (b) Once the "Enable" LED is lit (∼3 minutes), you may turn the key to enable emission

   (c) Open the shutter on the laser head

3. Select the appropriate mirror spacing for your measurement

   (a) Current mirror spacing (in mm) is displayed on the dial gauge just inside the circular panel on the front of the interferometer

   (b) Use the knob on the left side of the interferometer to select the Z motors

   (c) Use the +/- switch to set the mirror spacing to the appropriate value

   (d) Note: free spectral range (FSR) of the interferometer is given by $FSR = c/2L$ in which c is the speed of light and L is the mirror spacing.

4. Check the condition of the interferometer

   (a) The scan amplitude LED on the top panel to the right of the interferometer should be amber (in the center)

   (b) If the LED is not in the center and amber, open the top cover and use the small rod tool (in the BLS components drawer) to adjust the capacitor spacing until it is amber again

   (c) The shutter switch should be toggled to"Window"

   (d) The other LEDs should be either amber or green

   (e) If not, the coarse mirror motors may need to be adjusted (see step 6)

5. Start the BrilliaNT software in LabVIEW

   (a) Once it has started, input your mirror spacing on the bottom right or under the "Parameters" tab

(b) Click on the "Reflection" mode button in the upper left to place the interferometer in reflection alignment mode

(c) **Double-check that the beam path to the detector is blocked**

(d) In the software, make sure it is running and that the scale on the spectrum is set to "Auto"

(e) Flip the detector power switch, which is located on the rear of the top panel to the right of the interferometer

(f) The "Detector" LED should light up red

(g) Watch the spectrum in the software and wait for the dark counts to appear (these should be small, ∼1 count, and there should be very few)

(h) With your eyes on the spectrum, open the pinhole to the detector

(i) In reflection mode, **the background signal should be ∼300 cts/channel. If it is larger, close the pinhole immediately**

(j) Click "Auto Align" along the top to begin the mirror alignment procedure

(k) The software will sweep the positions of the two cavity mirrors using piezo actuators in order to find the optimal parallel mirror alignment

(l) It will then switch to tandem mode and look for the transmission peak

(m) If the transmission peak is not visible or any of the piezo LEDs are far from the center of their range, proceed to step 6. Else go on to 7.

6. Manual alignments

(a) If the piezos are far out of range, it may be necessary to use the motors for adjustment

i. Click on "Set PZT" and use the left and right mouse buttons to select the offending piezo

ii. Use the game controller to return the piezo to the center of its range

iii. Watching the peaks in reflection mode, adjust the corresponding motor on the interferometer with the +/- switch until the negative peak for that mirror cavity becomes strongly visible again

iv. Use the "Set PZT" to fine tune the peak

(b) If a strong peak cannot be observed in transmission (tandem) mode, the manual "Set PZT" can be used to optimize the negative peaks in reflection mode

i. Adjust each of the different piezos until there are two distinct, sharp peaks − one for each Fabry-Pérot cavity

ii. Use the dZ piezos to make these peaks exactly overlap

iii. Use the Z piezo (X and A on controller) to center this peak around 0

iv. Switch to Tandem mode

7. Set up your sample

(a) Your sample should be placed underneath the objective lens

(b) The lens height can be coarsely adjusted with the rail system

(c) Turn the two knobs on the side of the rail and support the weight of the objective as you slide it up and down

(d) Fine alignment can be performed with the knob at the bottom of the translation stage to which the objective is mounted (100 ×) or the small knob above the lens (50×)

(e) With the laser on, adjust the height of the objective until the laser light coming out of the Glan-Laser polarizer forms a bright focused spot on a white card of paper, indicating that your sample is in focus

(f) Alternatively, turn on the blue LED light source and observe the image from the optical camera

(g) Adjust the laser power to your desired value using the neutral density filter wheel and verify with the power meter placed under the ?-wave plate

(h) Adjust the 1/4-wave plate to either magnon or phonon mode

8. Begin the measurement

(a) In BrilliaNT, select "Measurement" mode

(b) Block the beam leading from the sample to the interferometer

(c) Select the appropriate input pinhole

(d) Unblock the beam while keeping an eye on the spectrum to make sure the signal is not too large

(e) Adjust your region of interest in BrilliaNT and set desired number of channels and extended measurement time

(f) Make sure each scan of the mirrors is on the order of or less than 1 second

Appendix D

Oersted Field from a Rectangular Conductor in Proximity to YIG

D.1 Oersted field from a Rectangular Conductor

For an infinitesimally thin wire transporting a constant current I, the magnetic field produced at radial position r is given by the Biot-Savart Law as

$$B(r) = \frac{\mu_0}{2\pi}\frac{I}{r} \tag{D.1}$$

To find the field from a rectangular conductor, consider it as a bundle of many infinitesimal wire conductors with cross-sections $dS = dzdy$. We wish to calculate the field at an arbitrary point (z', y') that is distance r from the element dS and at an angle β from the z-axis. To do this, we will perform an integration over all the bundled conductors in the rectangle.
Geometrically, r is defined as $r = \sqrt{(z'-z)^2 + (y'-y)^2}$, and the vector potential at (z', y') can be defined based on the angle β as

$$\begin{aligned} dB_z(z', y') &= \gamma\frac{\sin\beta}{r}dzdy \\ dB_y(z', y') &= -\gamma\frac{\cos\beta}{r}dzdy \\ dB_x(z', y') &= 0 \end{aligned} \tag{D.2}$$

where $\gamma = \frac{\mu_0 J}{2\pi}$ and $J = I/(tw)$ is the current density. Based on the coordinates

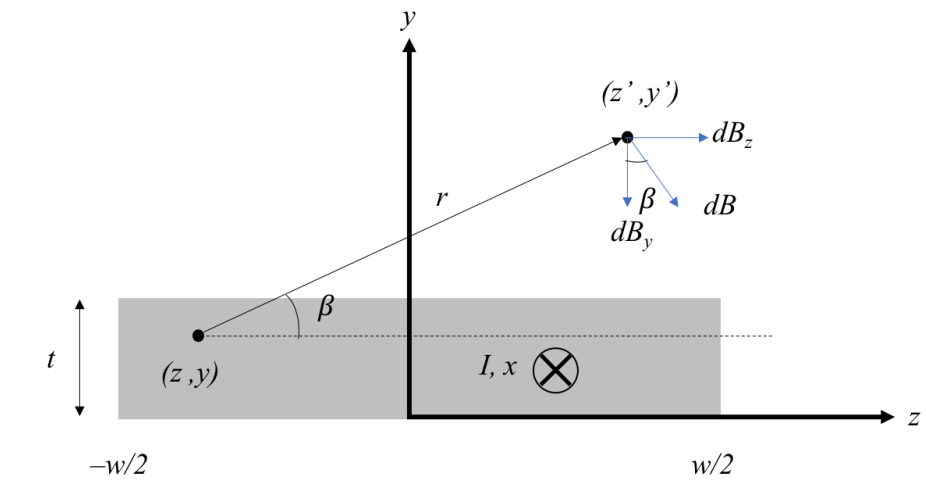

Figure D.1: Schematic of the coordinate system.

shown in Fig. D.1,

$$\begin{aligned} \sin\beta &= \frac{y'-y}{\sqrt{(z'-z)^2+(y'-y)^2}} \\ \cos\beta &= \frac{z'-z}{\sqrt{(z'-z)^2+(y'-y)^2}} \end{aligned} \tag{D.3}$$

The z magnetic field component is

$$\begin{aligned} B_z(z',y') &= \gamma \int_0^t \int_{-w/2}^{w/2} dB_z(z',y')dzdy \\ &= \gamma \int_0^t \int_{-w/2}^{w/2} \frac{y'-y}{(z'-z)^2+(y'-y)^2} dzdy \end{aligned} \tag{D.4}$$

And similarly the y field component is

$$\begin{aligned} B_y(z',y') &= \gamma \int_0^t \int_{-w/2}^{w/2} dB_y(z',y')dzdy \\ &= \gamma \int_0^t \int_{-w/2}^{w/2} \frac{z'-z}{(z'-z)^2+(y'-y)^2} dzdy \end{aligned} \tag{D.5}$$

By using the transformation of variables $u = z' - z$, the field components can be re-written as

$$\begin{aligned} B_z(z', y') &= \gamma \int_0^t \int_{z'-w/2}^{z'+w/2} \frac{y' - y}{u^2 + (y' - y)^2} du dy \\ B_y(z', y') &= \gamma \int_0^t \int_{z'-w/2}^{z'+w/2} \frac{u}{u^2 + (y' - y)^2} du dy \end{aligned} \tag{D.6}$$

which can readily be solved numerically.

Below are plots of the in-plane (B_z) and out-of-plane (B_y) components for a constant current in a Pt line with dimensions $t = 7$ nm and $w = 20$ μm.

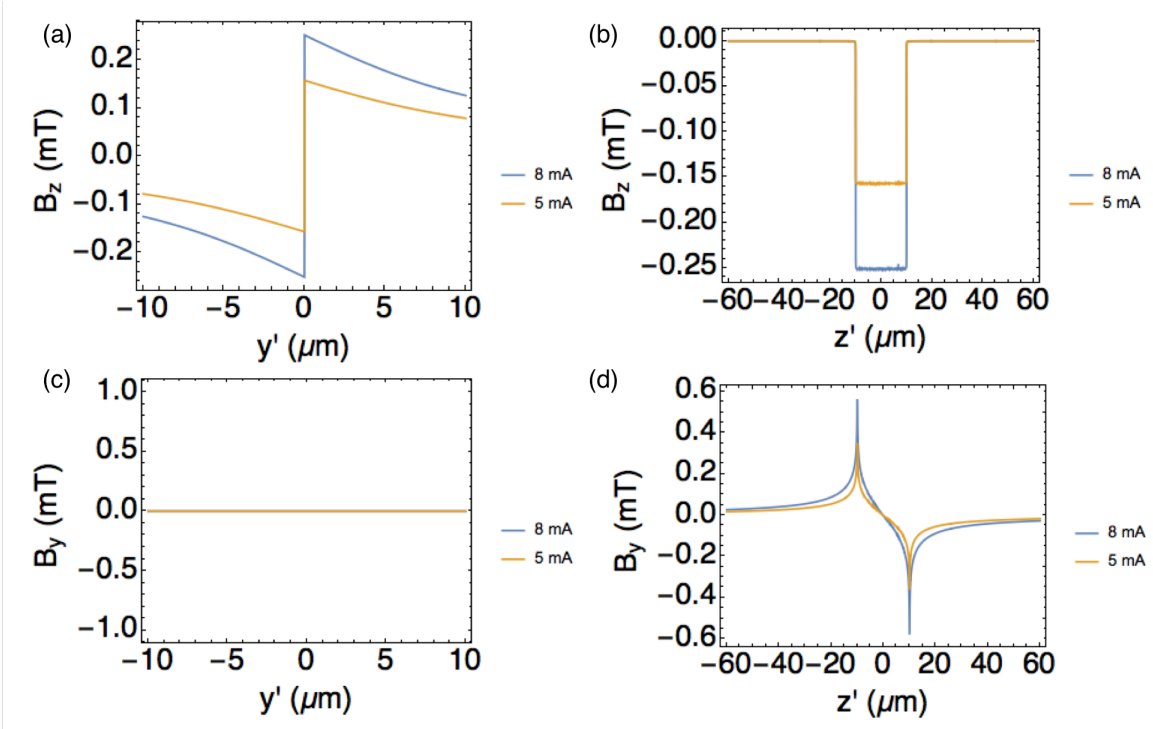

Figure D.2: B_z as a function of depth (a) and lateral distance (b). B_y as a function of depth (c) and lateral distance (d). The blue lines correspond to $I = 8$ mA and the orange lines correspond to $I = 5$ mA. (a) and (c) are evaluated at $z' = 0$ while (b) and (d) are evaluated at $y' = 0$.

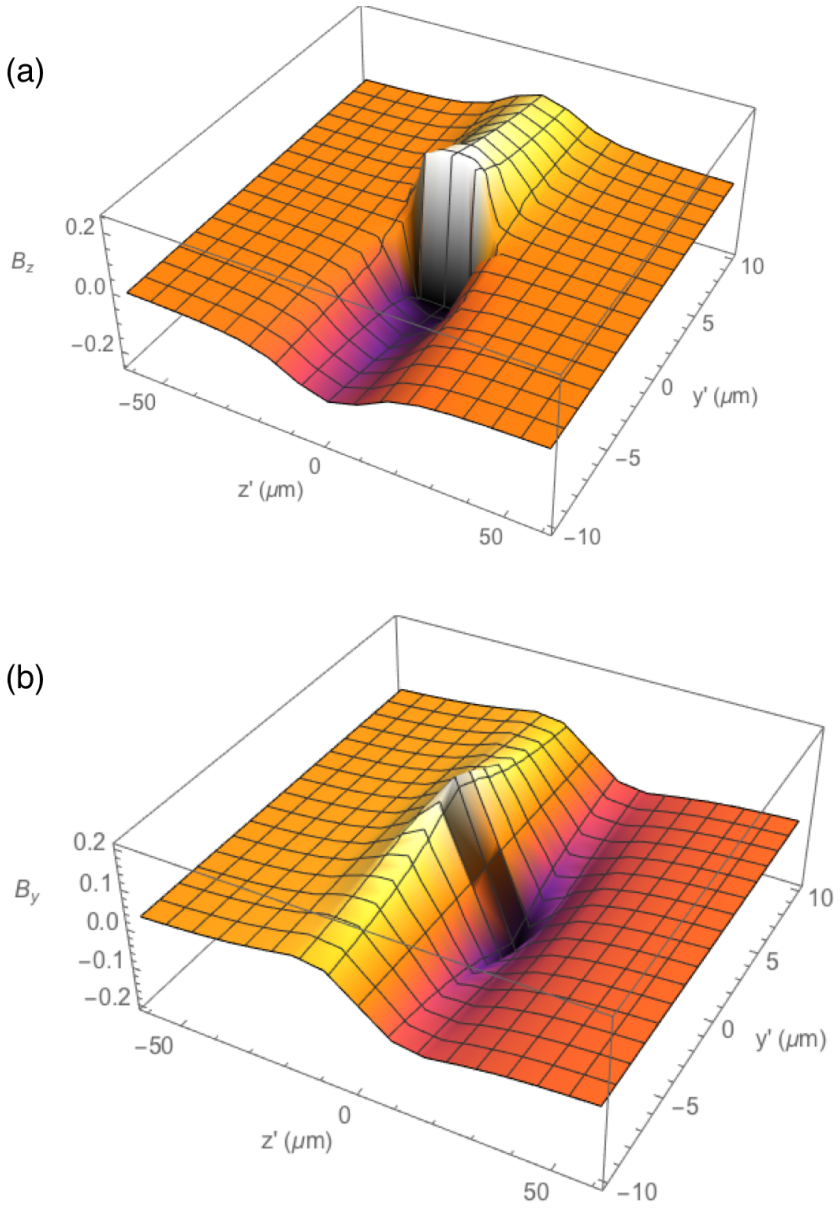

Figure D.3: (a) B_z in both dimensions and (b) B_y in both dimensions for $I = 8$ mA.

The power of the probe beam as a function of y inside the YIG film follows an exponential decay

$$P_{laser}(y') = P_0 e^{-\alpha_{abs} y'} \tag{D.7}$$

where P_0 is the peak laser power right at the Pt/YIG interface ($y' = 0$) and $\alpha_{abs} = 5 \times 10^4$ m^{-1} is the measured absorption of the YIG. The dissipated power density as a function of y' is

$$\dot{P}(y') = -\frac{\partial P_{laser}}{\partial y'} = -\alpha_{abs} P_0 e^{-\alpha_{abs} y'} \tag{D.8}$$

When the laser probe is placed in the center of the Pt line, the magnetic field is constant as a function of lateral position z. The Oersted magnetic field sampled by the BLS probe is given by the weighted average of the beam as it decays into the YIG film of thickness $d = 10$ μm:

$$\langle B_{z,y} \rangle = \frac{\int_0^{y'=-d} B_{z,y}(z'=0, y') \dot{P}(y')\, dy'}{\int_0^{y'=-d} \dot{P}(y')\, dy'} \tag{D.9}$$

Additionally, the magnon frequency f_m in the YIG has been measured as a function of applied magnetic field B_{ext} applied along z, as shown in Fig. D.4. The slope $\frac{df_m}{dB_{ext}}$ indicates that the magnon frequency increases approximately 32 MHz for each additional mT of B_{ext}.

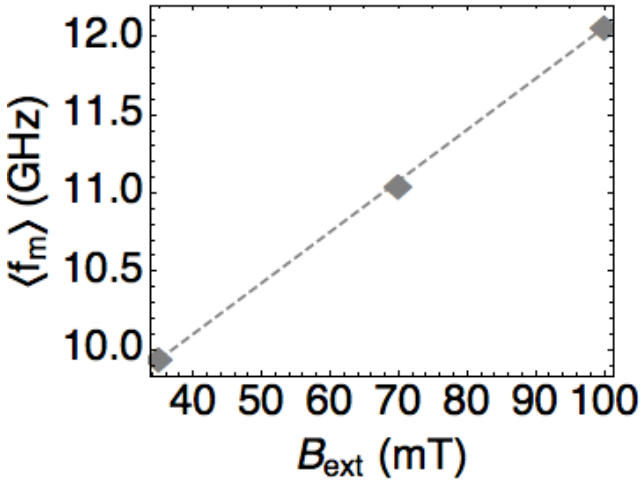

Figure D.4: BLS-measured magnon frequency as a function of applied magnetic field.

When the laser is placed in the center of the Pt, the y components of the Oersted field are negligible, so only $\langle B_z \rangle$ will have an effect on the measured $\langle f_m \rangle$. The calculated field can be related to an estimated shift in the magnon frequency as $\langle B_z \rangle \frac{df_m}{dB_{ext}}$, and is plotted as the thick solid line in comparison with the measured first harmonic $\langle f_{m,\nu_J} \rangle$ in Fig. D.5.

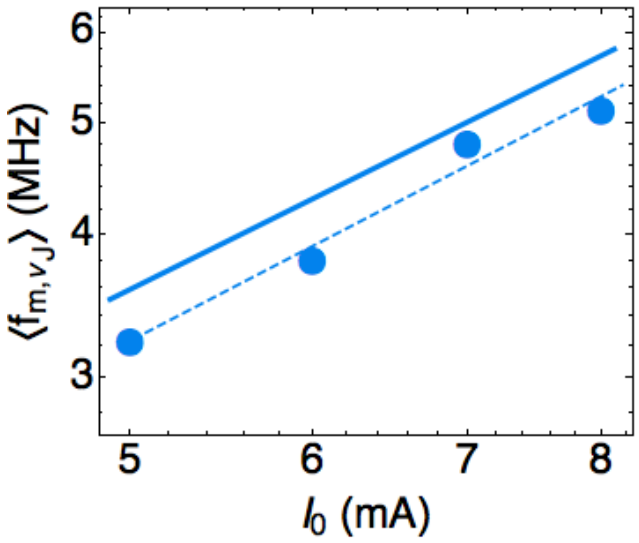

Figure D.5: Measured first harmonic BLS peak shift (circles) and calculated shift due to weighted Oersted field (thick solid line). The dashed line is a fit to the measurement data. Note that both axes are on a log scale.

Appendix E

Analytical Solution of Coupled Spin and Heat Transfer in Pt/YIG/GGG Heterostructures[1]

[1]Much of the heavy lifting for the analytical derivations outlined in this section was done by Prof. Li Shi. They are included here in their complete form for reference pertaining to Chapter 4.

E.1 Analytical solutions of one-dimensional coupled spin and heat diffusion equations

The coordinates used in the following discussion are defined in Fig. E.1.

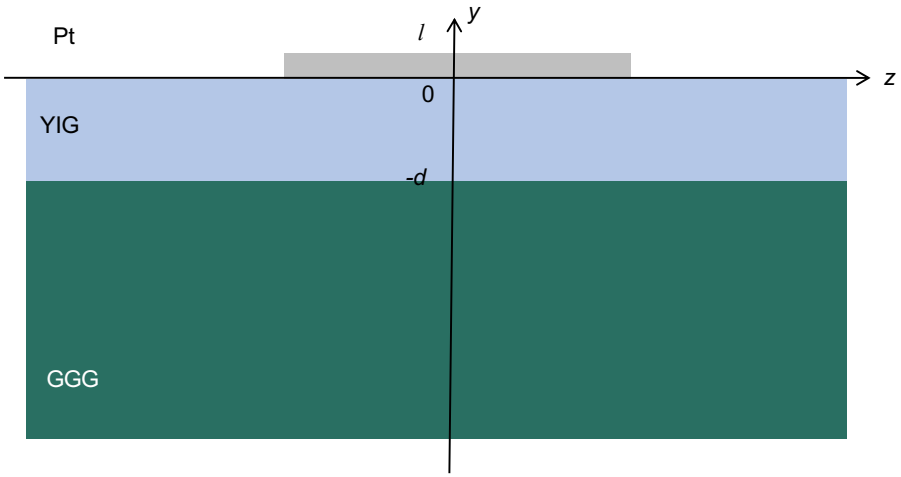

Figure E.1: Schematic illustration of the Pt/YIG/GGG structure.

E.1.1 Temperature distributions

The experiments have been conducted at a modulation frequency much slower than the thermal time constant of the system. Consequently, the time derivative terms are negligible in all the equations, which become essentially the same as the steady state equations. Inside the gadolinium gallium garnet (GGG), the Fourier transform of the heat diffusion equation is used to obtain the frequency (ν) components as

$$\nabla \cdot (\kappa_{p,GGG} \nabla \theta_{p,GGG,\nu}) = 0 \tag{E.1}$$

where $\kappa_{p,GGG}$ is the thermal conductivity of GGG, $\theta \equiv T - T_\infty$, where T is the temperature and T_∞ is the ambient temperature, the subscript p is used to denote phonon, and the subscript ν is used to denote the frequency component.

Inside the YIG,

$$\begin{aligned} \nabla \cdot (\kappa_{p,YIG} \nabla \theta_{p,YIG,\nu}) + g_{mp} (\theta_{m,YIG,\nu} - \theta_{p,YIG,\nu}) = 0 \\ \nabla \cdot (\kappa_{m,YIG} \nabla \theta_{m,YIG,\nu}) + g_{mp} (\theta_{p,YIG,\nu} - \theta_{m,YIG,\nu}) = 0 \end{aligned} \tag{E.2}$$

where $\kappa_{p,YIG}$ and $\kappa_{m,YIG}$ are the phonon and magnon contributions to the thermal conductivity (κ_{YIG}) of YIG, g_{mp} is the magnon-phonon coupling constant, and the subscripts p and m represent phonons and magnons, respectively. These two coupled equations are equivalent to

$$\begin{aligned} \nabla \cdot (\kappa_{YIG} \nabla \theta_{p,YIG,\nu} + \kappa_{m,YIG} \nabla \theta_{m-p,YIG,\nu}) = 0 \\ \nabla^2 \theta_{m-p,YIG,\nu} - \frac{\theta_{m-p,YIG,\nu}}{\ell_{mp}^2} = 0 \end{aligned} \tag{E.3}$$

where $\theta_{m-p} \equiv \theta_m - \theta_p$, $\ell_{mp} \equiv \left[g_{mp} \left(\frac{1}{\kappa_{p,YIG}} + \frac{1}{\kappa_{m,YIG}} \right) \right]^{-1/2}$ is the magnon-phonon thermalization length in YIG, and the spatial variation of $\kappa_{m,YIG}$ and $\kappa_{p,YIG}$ have been ignored.
Inside the Pt,

$$\begin{aligned} \nabla \cdot (\kappa_{p,Pt} \nabla \theta_{p,Pt,\nu}) + g_{ep} (\theta_{e,Pt,\nu} - \theta_{p,Pt,\nu}) = 0 \\ \nabla \cdot (\kappa_{e,Pt} \nabla \theta_{e,Pt,\nu}) + g_{ep} (\theta_{p,Pt,\nu} - \theta_{e,Pt,\nu}) + q_\nu + q_{Th,\nu} = 0 \end{aligned} \tag{E.4}$$

where the subscript e denotes electrons, the Joule heating density (q) and the Thomson heating density (q_{Th}) are $q = \rho \boldsymbol{J_C} \cdot \boldsymbol{J_C}$ and $q_{Th} = \beta \boldsymbol{J_C} \cdot \nabla \theta_{e,Pt}$, respectively, and $\boldsymbol{J_C}$ is the charge current density vector, ρ is the electrical resistivity, $\kappa_{p,Pt}$ and $\kappa_{e,Pt}$ are the phonon and electron contributions to the thermal conductivity (κ_{Pt}) of Pt, g_{ep} is the electron-phonon coupling constant, and β is the Thomson coefficient. For the sample configuration shown in Fig. E.1, the electric current consists of only the x component (J_x) in a Pt thin film of thickness t_{Pt} deposited on YIG and the magnetic field has only the component (B_z) along the z direction. Because $\boldsymbol{J_C}$ and $\nabla \theta_{e,Pt}$ are aligned along the in-plane and cross-plane direction of the Pt film, $q_{Th} = 0$. Thus,

these two coupled equations are equivalent to

$$\begin{aligned} \nabla \cdot (\kappa_{Pt} \nabla \theta_{p,Pt,\nu} + \kappa_{e,Pt} \nabla \theta_{e-p,Pt,\nu}) + q_\nu &= 0 \\ \nabla^2 \theta_{e-p,Pt,\nu} - \frac{\theta_{e-p,Pt,\nu}}{\ell_{ep}^2} + \frac{q_\nu}{\kappa_{e,Pt}} &= 0 \end{aligned} \tag{E.5}$$

where $\theta_{e-p} \equiv \theta_e - \theta_p$, $\ell_{ep} \equiv \left[g_{ep} \left(\frac{1}{\kappa_{e,Pt}} + \frac{1}{\kappa_{p,Pt}} \right) \right]^{-1/2}$ is the electron-phonon thermalization length in Pt, and the spatial variation of $\kappa_{e,Pt}$ and $\kappa_{p,Pt}$ have been ignored. Transport is approximately one-dimensional inside the micron-scale laser spot right beneath the center of the 20 μm-wide Pt line. Hence,

$$\theta_{m-p,\nu} = a_{1,\nu} \sinh\left(\frac{y}{\ell_{mp}}\right) + a_{2,\nu} \cosh\left(\frac{y}{\ell_{mp}}\right) \text{ for } y \leq 0 \tag{E.6}$$

and

$$\theta_{e-p,\nu} = b_{1,\nu} \sinh\left(\frac{y}{\ell_{ep}}\right) + b_{2,\nu} \cosh\left(\frac{y}{\ell_{ep}}\right) + \frac{q_\nu \ell_{ep}^2}{\kappa_{e,Pt}} \text{ for } y \geq 0 \tag{E.7}$$

where the a and b coefficients depend on the frequency ν component. In addition,

$$\nabla \cdot (\kappa_{YIG} \nabla \theta_{p,YIG,\nu}) = -\nabla \cdot (\kappa_{m,YIG} \nabla \theta_{m-p,YIG,\nu}) = -\frac{\kappa_{m,YIG}}{\ell_{mp}^2} \left[a_{1,\nu} \sinh\frac{y}{\ell_{mp}} + a_{2,\nu} \cosh\frac{y}{\ell_{mp}} \right]$$

$$\nabla \cdot (\kappa_{Pt} \nabla \theta_{e,Pt,\nu}) = -\nabla \cdot (\kappa_{m,YIG} \nabla \theta_{m-p,YIG,\nu}) - q_\nu = -\frac{\kappa_{e,Pt}}{\ell_{ep}^2} \left[b_{1,\nu} \sinh\frac{y}{\ell_{ep}} + b_{2,\nu} \cosh\frac{y}{\ell_{ep}} \right] - q_\nu \tag{E.8}$$

Hence,

$$\theta_{p,YIG,\nu} = -\frac{\kappa_{m,YIG}}{\kappa_{YIG}} \left[a_{1,\nu} \sinh\frac{y}{\ell_{mp}} + a_{2,\nu} \cosh\frac{y}{\ell_{mp}} \right] + a_{3,\nu} y + a_{4,\nu}$$

$$\theta_{p,Pt,\nu} = -\frac{\kappa_{e,Pt}}{\kappa_{Pt}} \left[b_{1,\nu} \sinh\frac{y}{\ell_{ep}} + b_{2,\nu} \cosh\frac{y}{\ell_{ep}} \right] - \frac{q_\nu}{2\kappa_{Pt}} y^2 + b_{3,\nu} y + b_{4,\nu} \tag{E.9}$$

and

$$\begin{aligned}\theta_{m,YIG,\nu} &= \theta_{p,YIG,\nu} + \theta_{m-p,YIG,\nu} \\ &= \frac{\kappa_{p,YIG}}{\kappa_{YIG}}\left[a_{1,\nu}\sinh\frac{y}{\ell_{mp}} + a_{2,\nu}\cosh\frac{y}{\ell_{mp}}\right] + a_{3,\nu}y + a_{4,\nu}\end{aligned}$$

$$\begin{aligned}\theta_{e,Pt,\nu} &= \theta_{p,Pt,\nu} + \theta_{e-p,Pt,\nu} \\ &= \frac{\kappa_{p,Pt}}{\kappa_{Pt}}\left[b_{1,\nu}\sinh\frac{y}{\ell_{ep}} + b_{2,\nu}\cosh\frac{y}{\ell_{ep}}\right] + q_\nu\left(\frac{\ell_{ep}^2}{\kappa_{e,Pt}} - \frac{y^2}{2\kappa_{Pt}}\right) + b_{3,\nu}y + b_{4,\nu}\end{aligned} \tag{E.10}$$

The Pt surface ($y = l$) is adiabatic,

$$\left(\frac{\partial\theta_{p,Pt,\nu}}{\partial y}\right)_{y=l} = 0 \tag{E.11}$$

and

$$Q_{E,\nu} - \kappa_{e,Pt}\left(\frac{\partial\theta_{e,Pt,\nu}}{\partial y}\right)_{y=l} = 0 \tag{E.12}$$

where the ordinary Ettingshausen heat current density $Q_{E,\nu} = \kappa_{Pt}\Xi B_z J_{x,\nu}$, and the Ettingshausen coefficient Ξ is related to the Nernst (N) coefficient according to the Bridgman relation, $\kappa_{Pt}\Xi = NT$. Hence,

$$\left(\frac{\partial\theta_{p,Pt,\nu}}{\partial y}\right)_{y=l} = -\frac{\kappa_{e,Pt}}{\kappa_{Pt}\ell_{ep}}\left[b_{1,\nu}\cosh\left(\frac{l}{\ell_{ep}}\right) + b_{2,\nu}\sinh\left(\frac{l}{\ell_{ep}}\right)\right] - \frac{q_\nu l}{\kappa_{Pt}} + b_{3,\nu} = 0$$

$$\left(\frac{\partial\theta_{e-p,Pt,\nu}}{\partial y}\right)_{y=l} = -\frac{b_{1,\nu}}{\ell_{ep}}\cosh\left(\frac{l}{\ell_{ep}}\right) + \frac{b_{2,\nu}}{\ell_{ep}}\sinh\left(\frac{l}{\ell_{ep}}\right) = \frac{Q_{E,\nu}}{\kappa_{e,Pt}} \tag{E.13}$$

Thus

$$b_{3,\nu} = \frac{Q_{E,\nu} + q_\nu l}{\kappa_{Pt}} \tag{E.14}$$

and

$$b_{2,\nu} = -b_{1,\nu}\coth\left(\frac{l}{\ell_{ep}}\right) + \frac{Q_{E,\nu}\ell_{ep}}{\kappa_{e,Pt}\sinh\frac{l}{\ell_{ep}}} \tag{E.15}$$

At the Pt/YIG interface ($y = 0$), the spin mediated heat current density ($Q^i_{s,\nu}$) and phonon mediated heat current density ($Q^i_{p,\nu}$) are

$$\begin{aligned} Q^i_{s,\nu} &= Q_{E,\nu} - \kappa_{e,Pt}\left(\frac{\partial\theta_{e,Pt,\nu}}{\partial y}\right)_{y=0} = -\kappa_{m,YIG}\left(\frac{\theta_{m,YIG,\nu}}{\partial y}\right)_{y=0} \\ Q^i_{p,\nu} &= -\kappa_{p,Pt}\left(\frac{\partial\theta_{p,Pt,\nu}}{\partial y}\right)_{y=0} = -\kappa_{p,YIG}\left(\frac{\theta_{p,YIG,\nu}}{\partial y}\right)_{y=0} \end{aligned} \tag{E.16}$$

These equations satisfy the energy conservation for the Pt film,

$$Q^i_{s,\nu} + Q^i_{p,\nu} + q_\nu l = 0 \tag{E.17}$$

In addition,

$$b_{1,\nu} = \ell_{ep}\left(\frac{\partial\theta_{e-p,Pt,\nu}}{\partial y}\right)_{y=0} = \frac{\ell_{ep}Q_{E,\nu}}{\kappa_{e,Pt}} - \frac{\ell_{ep}q_\nu l}{\kappa_{p,Pt}} - \left(\frac{1}{\kappa_{p,Pt}} + \frac{1}{\kappa_{e,Pt}}\right)\ell_{ep}Q^i_{s,\nu} \tag{E.18}$$

so that

$$b_{2,\nu} = \frac{1-\cosh\frac{l}{\ell_{ep}}}{\kappa_{e,Pt}\sinh\frac{l}{\ell_{ep}}}\ell_{ep}Q_{E,\nu} + \coth\left(\frac{l}{\ell_{ep}}\right)\frac{\ell_{ep}q_\nu l}{\kappa_{p,Pt}} + \coth\left(\frac{l}{\ell_{ep}}\right)\left(\frac{1}{\kappa_{p,Pt}} + \frac{1}{\kappa_{e,Pt}}\right)\ell_{ep}Q^i_{s,\nu} \tag{E.19}$$

Similarly,

$$a_{1,\nu} = \ell_{mp}\left(\frac{\partial\theta_{m-p,YIG,\nu}}{\partial y}\right)_{y=0} = -\frac{\ell_{mp}q_\nu l}{\kappa_{p,YIG}} - \left(\frac{1}{\kappa_{p,YIG}} + \frac{1}{\kappa_{m,YIG}}\right)\ell_{mp}Q^i_{s,\nu} \tag{E.20}$$

In addition,

$$\begin{aligned} q_\nu l &= -Q^i_{s,\nu} - Q^i_{p,\nu} \\ &= \kappa_{m,YIG}\left(\frac{\partial\theta_{m,YIG,\nu}}{\partial y}\right)_{y=0} + \kappa_{p,YIG}\left(\frac{\partial\theta_{p,YIG,\nu}}{\partial y}\right)_{y=0} = \left(\kappa_{m,YIG} + \kappa_{p,YIG}\right)a_{3,\nu} \end{aligned} \tag{E.21}$$

Thus,

$$a_{3,\nu} = \frac{q_\nu l}{\kappa_{YIG}} \tag{E.22}$$

The spin mediated heat flux ($Q_{m,GGG,\nu}$) and phonon mediated heat flux ($Q_{p,GGG,\nu}$) respectively, across the YIG/GGG interface ($y=-d$) are

$$\begin{aligned} Q_{m,GGG,\nu} &= -\kappa_{m,YIG}\left(\frac{\partial\theta_{m,YIG,\nu}}{\partial y}\right)_{y=-d} = 0 \\ Q_{p,GGG,\nu} &= -\kappa_{p,YIG}\left(\frac{\partial\theta_{p,YIG,\nu}}{\partial y}\right)_{y=-d} \end{aligned} \tag{E.23}$$

These equations satisfy the energy conservation for the YIG layer, $-Q^i_{s,\nu} - Q^i_{p,\nu} + Q_{m,GGG,\nu} + Q_{p,GGG,\nu} = 0$, so that $Q_{p,GGG,\nu} = -q_\nu l$. Hence,

$$\left(\frac{\partial\theta_{m-p,YIG,\nu}}{\partial y}\right)_{y=-d} = \frac{a_{1,\nu}}{\ell_{mp}}\cosh\left(\frac{-d}{\ell_{mp}}\right) + \frac{a_{2,\nu}}{\ell_{mp}}\sinh\left(\frac{-d}{\ell_{mp}}\right) = -\frac{q_\nu l}{\kappa_{p,YIG}}, \tag{E.24}$$

which is used to obtain

$$\begin{aligned} a_{2,\nu} &= a_{1,\nu}\coth\left(\frac{d}{\ell_{mp}}\right) + \frac{\ell_{mp}q_\nu l}{\kappa_{p,YIG}\sinh\frac{d}{\ell_{mp}}} \\ &= \frac{1-\cosh\frac{d}{\ell_{mp}}}{\kappa_{p,YIG}\sinh\frac{d}{\ell_{mp}}}\ell_{mp}q_\nu l - \coth\left(\frac{d}{\ell_{mp}}\right)\left(\frac{1}{\kappa_{p,YIG}} + \frac{1}{\kappa_{m,YIG}}\right)\ell_{mp}Q^i_{s,\nu} \end{aligned} \tag{E.25}$$

The heat conduction across the YIG/GGG substrate can be calculated as

$$Q_{GGG,\nu} = -G_{GGG}\theta_{p,YIG,\nu}\,(y=-d) \tag{E.26}$$

where G_{GGG} is the thermal conductance per unit area of the YIG/GGG interface for heat conduction from the YIG through the GGG substrate to the ambient. Thus,

$$Q_{GGG,\nu} = -G_{GGG}\left\{-\frac{\kappa_{m,YIG}}{\kappa_{YIG}}\left[a_{1,\nu}\sinh\left(\frac{-d}{\ell_{mp}}\right) + a_{2,\nu}\cosh\left(\frac{-d}{\ell_{mp}}\right)\right] - a_{3,\nu}d + a_{4,\nu}\right\} = -q_\nu l$$

$$a_{4,\nu} = \left[\frac{1}{G_{GGG}} + \frac{d}{\kappa_{YIG}} - \frac{\kappa_{m,YIG}\ell_{mp}}{\kappa_{YIG}\kappa_{p,YIG}}\frac{1-\cosh\frac{d}{\ell_{mp}}}{\sinh\frac{d}{\ell_{mp}}}\right]q_\nu l - \frac{\kappa_{m,YIG}\ell_{mp}}{\kappa_{YIG}\sinh\frac{d}{\ell_{mp}}}\left(\frac{1}{\kappa_{p,YIG}} + \frac{1}{\kappa_{m,YIG}}\right)Q^i_{s,\nu} \tag{E.27}$$

At the Pt/YIG interface ($y = 0$), the phonon mediated heat flux ($Q^i_{p,\nu}$) can be calculated as

$$Q^i_{p,\nu} = G_p \theta^i_{p-p,\nu} \tag{E.28}$$

where

$$\theta^i_{p-p,\nu} \equiv \left(\theta_{p,YIG,\nu}\right)_{y=0} - \left(\theta_{p,Pt,\nu}\right)_{y=0} = \frac{\kappa_{e,Pt}}{\kappa_{Pt}} b_{2,\nu} - b_{4,\nu} - \frac{\kappa_{m,YIG}}{\kappa_{YIG}} a_{2,\nu} + a_{4,\nu}$$

$$\begin{aligned} b_{4,\nu} = & \frac{1 - \cosh\frac{l}{\ell_{ep}}}{\kappa_{Pt} \sinh\frac{l}{\ell_{ep}}} \ell_{ep} Q_{E,\nu} \\ & + \left[\frac{1}{G_p} + \coth\left(\frac{l}{\ell_{ep}}\right) \left(\frac{1}{\kappa_{p,Pt}} + \frac{1}{\kappa_{e,Pt}} \right) \frac{\kappa_{e,Pt}}{\kappa_{Pt}} \ell_{ep} - \frac{1 - \cosh\frac{d}{\ell_{mp}}}{\sinh\frac{d}{\ell_{mp}}} \left(\frac{1}{\kappa_{p,YIG}} + \frac{1}{\kappa_{m,YIG}} \right) \frac{\kappa_{m,YIG} \ell_{mp}}{\kappa_{YIG}} \right] Q^i_{s,\nu} \\ & + \left[\frac{1}{G_p} + \frac{1}{G_{GGG}} + \frac{d}{\kappa_{YIG}} + \coth\left(\frac{l}{\ell_{ep}}\right) \frac{\kappa_{e,Pt} \ell_{ep}}{\kappa_{Pt} \kappa_{p,Pt}} - 2 \frac{\kappa_{m,YIG} \ell_{mp}}{\kappa_{YIG} \kappa_{p,YIG}} \frac{1 - \cosh\frac{d}{\ell_{mp}}}{\sinh\frac{d}{\ell_{mp}}} \right] q_\nu l. \end{aligned} \tag{E.29}$$

In addition, the spin mediated heat flux ($Q^i_{s,\nu}$) across the Pt/YIG interface can be calculated as

$$Q^i_{s,\nu} = \Pi_s g_s \frac{V_{s,\nu}}{2} + G_s \theta^i_{m-e,\nu} \tag{E.30}$$

where $\Pi_s \equiv \left(\frac{\partial Q^i_{s,\nu}}{\partial J_s}\right)_{\theta^i_{m-e,\nu}=0}$ is the spin Peltier coefficient of the interface spin flux, $J_s = g_s \left(\frac{V_{s,\nu}}{2} - S_s \theta^i_{m-e,\nu}\right)$, and related to the spin Seebeck coefficient, $S_s \equiv \left(\frac{\partial V_{s,\nu}}{2\partial \theta^i_{m-e,\nu}}\right)_{J_s=0}$, via the Onsager relationship $\Pi_s = S_s T$, g_s is the interface spin conductance per unit area, $G_s \equiv \left(\frac{\partial Q^i_{s,\nu}}{\partial \theta^i_{m-e,\nu}}\right)_{V_{s,\nu}=0}$ is the spin-mediated thermal interface conduction measured under vanishing spin accumulation ($V_{s,\nu}$), and $\theta^i_{m-e,\nu}$ is defined as

$$\theta^i_{m-e,\nu} \equiv \left(\theta_{m,YIG,\nu}\right)_{y=0} - \left(\theta_{e,Pt,\nu}\right)_{y=0} = \frac{\kappa_{p,YIG}}{\kappa_{YIG}} a_{2,\nu} + a_{4,\nu} - \frac{\kappa_{p,Pt}}{\kappa_{Pt}} b_{2,\nu} - q_\nu \left(\frac{\ell^2_{ep}}{\kappa_{e,Pt}}\right) - b_{4,\nu}. \tag{E.31}$$

Hence,

$$
\begin{aligned}
&Q^i_{s,\nu} \\
&= \frac{\Pi_s g_s \frac{V_{s,\nu}}{2G_s} - \frac{1-\cosh\frac{l}{\ell_{ep}}}{\kappa_{e,Pt}\sinh\frac{l}{\ell_{ep}}}\ell_{ep}Q_{E,\nu} - \left[\frac{1}{G_p} + \frac{\ell_{ep}^2}{\kappa_{e,Pt}l} + \frac{\ell_{ep}}{\kappa_{p,YIG}}\coth\left(\frac{l}{\ell_{ep}}\right) - \frac{\ell_{mp}}{\kappa_{p,YIG}}\frac{1-\cosh\frac{d}{\ell_{mp}}}{\sinh\frac{d}{\ell_{mp}}}\right] q_\nu l}{\frac{1}{G_p} + \frac{1}{G_s} + \coth\left(\frac{l}{\ell_{ep}}\right)\left(\frac{1}{\kappa_{p,Pt}} + \frac{1}{\kappa_{e,Pt}}\right)\ell_{ep} + \coth\left(\frac{d}{\ell_{mp}}\right)\left(\frac{1}{\kappa_{p,YIG}} + \frac{1}{\kappa_{m,YIG}}\right)\ell_{mp}}
\end{aligned}
\tag{E.32}
$$

First harmonic component ($\nu = \nu_J$) of the Pt temperature

When $J_x = J_0 \sin 2\pi\nu_J t$, q does not contain the first harmonic component: $q_{\nu_J} = 0$.

$$
\theta_{p,Pt,\nu_J}(y) = -\frac{\kappa_{e,Pt}}{\kappa_{Pt}}\left[b_{1,\nu_J}\sinh\left(\frac{y}{\ell_{ep}}\right) + b_{2,\nu_J}\cosh\left(\frac{y}{lep}\right)\right] + b_{3,\nu_J}y + b_{4,\nu_J} \tag{E.33}
$$

where

$$
\begin{aligned}
b_{1,\nu_J} &= \frac{\ell_{ep}Q_{E,\nu_J}}{\kappa_{e.Pt}} - \left(\frac{1}{\kappa_{p,YIG}} + \frac{1}{\kappa_{m,YIG}}\right)\ell_{ep}Q^i_{s,\nu_J} \\
b_{2,\nu_J} &= \frac{1-\cosh\frac{l}{\ell_{ep}}}{\kappa_{e,Pt}\sinh\frac{l}{\ell_{ep}}}\ell_{ep}Q_{E,\nu_J} + \coth\left(\frac{l}{\ell_{ep}}\right)\left(\frac{1}{\kappa_{p,YIG}} + \frac{1}{\kappa_{m,YIG}}\right)\ell_{ep}Q^i_{s,\nu_J} \\
b_{3,\nu_J} &= \frac{Q_{E,\nu_J}}{\kappa_{Pt}} \\
b_{4,\nu_J} &= \frac{1-\cosh\frac{l}{\ell_{ep}}}{\kappa_{e,Pt}\sinh\frac{l}{\ell_{ep}}}\ell_{ep}Q_{E,\nu_J} \\
&+ \left[\frac{1}{G_p} + \coth\left(\frac{l}{\ell_{ep}}\right)\left(\frac{1}{\kappa_{p,Pt}} + \frac{1}{\kappa_{e,Pt}}\right)\frac{\kappa_{e,Pt}}{\kappa_{Pt}}\ell_{ep} - \frac{1-\cosh\frac{d}{\ell_{mp}}}{\sinh\frac{d}{\ell_{mp}}}\left(\frac{1}{\kappa_{p,YIG}} + \frac{1}{\kappa_{m,YIG}}\right)\frac{\kappa_{m,YIG}\ell_{mp}}{\kappa_{YIG}}\right]Q^i_{s,\nu_J}
\end{aligned}
\tag{E.34}
$$

and

$$
\begin{aligned}
&Q^i_{s,\nu_J} \\
&= \frac{\Pi_s g_s \frac{V_{s,\nu_J}}{2G_s} - \frac{1-\cosh\frac{l}{\ell_{ep}}}{\kappa_{e,Pt}\sinh\frac{l}{\ell_{ep}}}\ell_{ep}Q_{E,\nu_J}}{\frac{1}{G_p} + \frac{1}{G_s} + \coth\left(\frac{l}{\ell_{ep}}\right)\left(\frac{1}{\kappa_{p,Pt}} + \frac{1}{\kappa_{e,Pt}}\right)\ell_{ep} + \coth\left(\frac{d}{\ell_{mp}}\right)\left(\frac{1}{\kappa_{p,YIG}} + \frac{1}{\kappa_{m,YIG}}\right)\ell_{mp}}
\end{aligned}
\tag{E.35}
$$

The first harmonic component of the average phonon temperature rise across the Pt film thickness is

$$\begin{aligned}\langle\theta_{p,Pt,\nu_J}\rangle &= \frac{1}{l}\int_0^l \theta_{p,Pt,\nu_J}(y)dy \\ &= -\frac{\kappa_{e,Pt}\ell_{ep}}{\kappa_{Pt}l}\left\{b_{1,\nu_J}\left[\cosh\left(\frac{l}{\ell_{ep}}\right)-1\right]+b_{2,\nu_J}\sinh\left(\frac{l}{\ell_{ep}}\right)\right\}+b_{3,\nu_J}\frac{l}{2}+b_{4,\nu_J}\end{aligned} \tag{E.36}$$

Thus,

$$\langle\theta_{p,Pt,\nu_J}\rangle = \langle\theta_{p,Pt,\nu_J}\rangle_{Q^i_{s,\nu_J}} + \langle\theta_{p,Pt,\nu_J}\rangle_{Q_{E,\nu_J}} \tag{E.37}$$

where the two components are

$$\begin{aligned}\langle\theta_{p,Pt,\nu_J}\rangle_{Q^i_{s,\nu_J}} = \Bigg\{&\frac{1}{G_p}+\frac{\kappa_{e,Pt}}{\kappa_{Pt}}\left(\frac{1}{\kappa_{p,Pt}}+\frac{1}{\kappa_{e,Pt}}\right)\ell_{ep}\left[\coth\left(\frac{l}{\ell_{ep}}\right)-\frac{\ell_{ep}}{l}\right] \\ &+\frac{\kappa_{m,YIG}\ell_{mp}}{\kappa_{YIG}}\left(\frac{1}{\kappa_{p,YIG}}+\frac{1}{\kappa_{m,YIG}}\right)\frac{\cosh\frac{d}{\ell_{mp}}-1}{\sinh\frac{d}{\ell_{mp}}}\Bigg\}Q^i_{s,\nu_J}\end{aligned} \tag{E.38}$$

and

$$\langle\theta_{p,Pt,\nu_J}\rangle_{Q_{E,\nu_J}} = \left[\frac{1}{2\ell_{ep}}+\frac{1-\cosh\frac{l}{\ell_{ep}}}{\sinh\frac{l}{\ell_{ep}}}\right]\frac{\ell_{ep}}{\kappa_{Pt}}Q^i_{E,\nu_J} \tag{E.39}$$

Comparison between the Pt phonon measurement results obtained on the Pt/YIG and Pt/YIG/GGG structures suggests that $\langle\theta_{p,Pt,\nu_J}\rangle_{Q_{E,\nu_J}} \ll \langle\theta_{p,Pt,\nu_J}\rangle_{Q^i_{s,\nu_J}}$, so that

$$\langle\theta_{p,Pt,\nu_J}\rangle \approx \langle\theta_{p,Pt,\nu_J}\rangle_{Q^i_{s,\nu_J}} \tag{E.40}$$

In addition, because $\kappa_{e,Pt} \gg \kappa_{p,Pt}$ and $\kappa_{p,YIG} \gg \kappa_{m,YIG}$,

$$\langle\theta_{p,Pt,\nu_J}\rangle \approx \left\{\frac{1}{G_P}+\frac{\ell_{ep}}{\kappa_{Pt}}\left[\coth\left(\frac{l}{\ell_{ep}}\right)-\frac{\ell_{ep}}{l}\right]+\frac{\ell_{mp}}{\kappa_{YIG}}\frac{\cosh\left(\frac{d}{\ell_{mp}}\right)-1}{\sinh\left(\frac{d}{\ell_{mp}}\right)}\right\}Q^i_{s,\nu_J} \tag{E.41}$$

which can be used to evaluate Q^i_{s,ν_J} from the measured $\langle\theta_{p,Pt,\nu_J}\rangle$. For $G_P \approx (170 \pm 50)$ $\times 10^6$ W m^{-2}K$\hat{}-1$, the Kaptiza length $\ell_K \equiv \kappa_{YIG}/G_p \approx 60 \pm 20$ nm. The thermal conductivity of YIG is approximately 10 W m^{-1} K^{-1} based on several measurements, [98,183,184] (§4.2.3) and the electron-phonon coupling length in Pt can be calculated

as $\ell_{ep} \approx \sqrt{\kappa_{e,Pt}/g} = 9.4$ nm, where $\kappa_{e,Pt} = 22$ W m^{-1} K^{-1} is obtained from the Wiedemann-Franz relation and the measured electrical resistivity (ρ) of the Pt line, and $g = 2.5 \times 10^{17}$ W m^{-3} K^{-1} is the reported electron-phonon coupling constant for Pt.[185,186] The calculated $Q^i_{s,\nu_J}/\langle\theta_{p,Pt,\nu_J}\rangle$ ratio is shown in Fig. E.2, and is in the range of $(2-21) \times 10^3$ W cm^{-2} K^{-1} for the above G_p range and ℓ_{mp} in the reported range between 1 nm and 250 nm.[37,182]

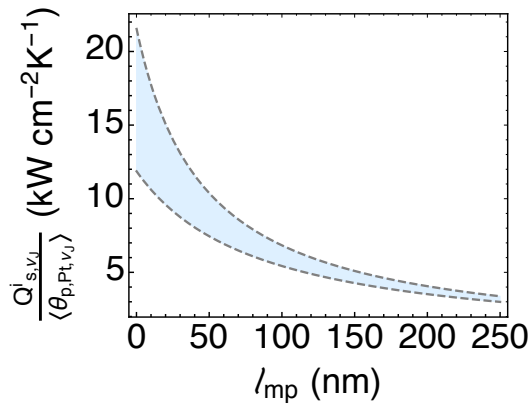

Figure E.2: The ratio of spin-mediated interfacial heat flux to Pt phonon temperature rise for a range of ℓ_{mp} of 1 to 250 nm and $G_P \approx (170 \pm 50) \times 10^6$ W m^{-2} K^{-1} calculated from Eqn. E.41. The upper dashed line corresponds to $G_P = 220 \times 10^6$ W m^{-2} K^{-1}, while the lower line corresponds to $G_P = 120 \times 10^6$ W m^{-2}K^{-1}.

E.1.2 Interface spin pumping and relaxation in YIG

The magnon diffusion equation in YIG is

$$\nabla^2 n_m = \frac{n_m - n_0}{\lambda_m^2} \tag{E.42}$$

where n_m is the magnon number density, n_0 is the magnon number density given by the equilibrium distribution function at the local phonon temperature (T_p), and λ_m is the magnon spin-flip diffusion length. Based on the definition $\delta_n \equiv n_m - n_0$, the diffusion equation can be expanded as

$$\left(\frac{dn_0}{dT_p}\right)\nabla^2 T_p + \left(\frac{d^2 n_0}{dT_p^2}\right)|\nabla T_p|^2 + \nabla^2 \delta_n = \frac{\delta_n}{\lambda_m^2} \tag{E.43}$$

Because each magnon carries a magnetic moment of $-g\mu_B$, where g is the Landé g factor, and μ_B is the Bohr magneton,

$$\frac{dn_0}{dT_p} = -\frac{1}{g\mu_B}\frac{\partial M}{\partial T_p} \tag{E.44}$$

and

$$\frac{d^2n_0}{dT_p^2} = -\frac{1}{g\mu_B}\frac{\partial^2 M}{\partial T_p^2} \tag{E.45}$$

where M is the magnitude of the local magnetization vector ($\boldsymbol{M}$). Because the measured M shows a highly linear dependence on T_p in the temperature range between 300 and 400 K according to Fig. 4.23(c), the $\frac{d^2n_0}{dT_p^2}$ term vanishes to yield[98]

$$\nabla^2 T_{p,YIG} + \nabla^2 \epsilon_m = \frac{\epsilon_m}{\lambda_m^2} \tag{E.46}$$

where $\epsilon_m \equiv \frac{\delta_n}{\frac{dn_0}{dT_p}}$. The deviation δ_n results in a a change in M as $\delta_M = -g\mu_B\delta_n$. The δ_M further results in a shift δ_{f_m} of the magnon frequency f_m as $\delta_{f_m} \approx \frac{\partial f_m}{\partial M}\delta_M = -\frac{\partial f_m}{\partial M}g\mu_B\delta_n$. Thus, $\epsilon_m = \frac{\delta_{f_m}}{\frac{\partial f_m}{\partial T_p}}$.
The Fourier transform is used to obtain the frequency components as

$$\nabla^2 \theta_{p,YIG} + \nabla^2 \epsilon_{m,\nu} = \frac{1}{\lambda_m^2}\epsilon_{m,\nu} \tag{E.47}$$

where $\theta \equiv T - T_\infty$ and T_∞ is the ambient temperature. In addition,

$$\nabla^2 \theta_{p,\nu} = -\frac{\kappa_{m,YIG}}{\kappa_{YIG}\ell_{mp}^2}\left[a_{1,\nu}\sinh\left(\frac{y}{\ell_{mp}}\right) + a_{2,\nu}\cosh\left(\frac{y}{\ell_{mp}}\right)\right] \tag{E.48}$$

Thus

$$\epsilon_{m,\nu} = c_{1,\nu}\sinh\left(\frac{y}{\lambda_m}\right) + c_{2,\nu}\cosh\left(\frac{y}{\lambda_m}\right) + c_{3,\nu}\sinh\left(\frac{y}{\ell_{mp}}\right) + c_{4,\nu}\cosh\left(\frac{y}{\ell_{mp}}\right) \tag{E.49}$$

where

$$\begin{aligned} c_{3,\nu} &= \frac{\kappa_{m,YIG}}{\kappa_{YIG}\left(1-\frac{\ell_{mp}^2}{\lambda_m^2}\right)}a_{1,\nu} \\ c_{4,\nu} &= \frac{\kappa_{m,YIG}}{\kappa_{YIG}\left(1-\frac{\ell_{mp}^2}{\lambda_m^2}\right)}a_{2,\nu} \end{aligned} \tag{E.50}$$

The spin flux across the Pt/YIG interface ($y=0$) is

$$\begin{aligned} J_s &= eD_m\left(\frac{\partial n_m}{\partial y}\right)_{y=0}\frac{M_z}{\sqrt{{M_z}^2}} \\ \frac{\partial n_m}{\partial y} &= \frac{\partial(n_0+\delta_n)}{\partial y} = \frac{dn_0}{dT_p}\left(\frac{\partial \theta_p}{\partial y}+\frac{\partial \epsilon_m}{\partial y}\right) \end{aligned} \tag{E.51}$$

Thus,

$$\begin{aligned} J_{s,\nu} &= -\frac{eD_m}{g\mu_B}\frac{\partial M}{\partial T_p}\frac{M_z}{\sqrt{M_z^2}}\left(\frac{\partial \theta_{p,\nu}}{\partial y}+\frac{\partial \epsilon_{m,\nu}}{\partial y}\right)_{y=0} \\ \left(\frac{\partial \theta_{p,\nu}}{\partial y}\right)_{y=0} &= -\frac{\kappa_{m,YIG}}{\kappa_{YIG}\ell_{mp}}a_{1,\nu}+a_{3,\nu} \\ \left(\frac{\partial \epsilon_{m,\nu}}{\partial y}\right)_{y=0} &= \frac{c_{1,\nu}}{\lambda_m}+\frac{\kappa_{m,YIG}}{\kappa_{YIG}\ell_{mp}\left(1-\frac{\ell_{mp}^2}{\lambda_m^2}\right)}a_{1,\nu} \end{aligned} \tag{E.52}$$

and

$$c_{1,\nu} = -\frac{J_{s,\nu}\lambda_m}{\frac{eD_m}{g\mu_B}\frac{\partial M}{\partial T_p}\frac{M_z}{\sqrt{M_z^2}}}+\frac{\kappa_{m,YIG}\lambda_m}{\kappa_{YIG}\ell_{mp}\left(1-\frac{\lambda_m^2}{\ell_{mp}^2}\right)}a_{1,\nu}-a_{3,\nu}\lambda_m \tag{E.53}$$

The spin flux across the YIG/GGG interface ($y=-d$) vanishes, thus

$$\begin{aligned} &\left(\frac{\partial \theta_{p,\nu}}{\partial y}+\frac{\partial \epsilon_{m,\nu}}{\partial y}\right)_{y=-d} = 0 \\ c_{2,\nu} &= \frac{\kappa_{m,YIG}\lambda_m}{\ell_{mp}\kappa_{YIG}\left(1-\frac{\lambda_m^2}{\ell_{mp}^2}\right)}a_{2,\nu}+\frac{1-\cosh\frac{d}{\lambda_m}}{\sinh\frac{d}{\lambda_m}}\lambda_m a_{3,\nu}-\frac{\lambda_m\coth\frac{d}{\lambda_m}}{\frac{eD_m}{g\mu_B}\frac{\partial M}{\partial T_p}\frac{M_z}{\sqrt{M_z^2}}}J_{s,\nu} \end{aligned} \tag{E.54}$$

First harmonic component ($\nu = \nu_J$) of the YIG temperature and magnon frequency

The first harmonic component of the YIG phonon temperature is

$$\theta_{p,YIG,v_J} = -\frac{\kappa_{m,YIG}}{\kappa_{YIG}}\left[a_{1,v_J}\sinh\left(\frac{y}{\ell_{mp}}\right) + a_{2,v_J}\cosh\left(\frac{y}{\ell_{mp}}\right)\right] + a_{3,v_J}y + a_{4,v_J} \quad \text{(E.55)}$$

where

$$\begin{aligned}
a_{1,\nu_J} &= -\left(\frac{1}{\kappa_{p,YIG}} + \frac{1}{\kappa_{m,YIG}}\right)\ell_{mp}Q^i_{s,\nu_J} \\
a_{2,\nu_J} &= -\left(\frac{1}{\kappa_{p,YIG}} + \frac{1}{\kappa_{m,YIG}}\right)\coth\left(\frac{d}{\ell_{mp}}\right)\ell_{mp}Q^i_{s,\nu_J} \\
a_{3,\nu_J} &= 0 \\
a_{4,\nu_J} &= -\frac{\ell_{mp}}{\kappa_{p,YIG}\sinh\frac{d}{\ell_{mp}}}Q^i_{s,\nu_J}
\end{aligned} \quad \text{(E.56)}$$

Thus,

$$\theta_{p,YIG,\nu_J} = \left[\cosh\left(\frac{y+d}{\ell_{mp}}\right) - 1\right]\operatorname{csch}\left(\frac{d}{\ell_{mp}}\right)\frac{\ell_{mp}}{\kappa_{p,YIG}}Q^i_{s,\nu_J} \quad \text{(E.57)}$$

In addition,

$$\begin{aligned}
c_{1,\nu_J} &= -\frac{\lambda_m}{\frac{eD_m}{g\mu_B}\frac{\partial M}{\partial T_p}\frac{M_z}{\sqrt{M_z}}}J_{z,\nu_J} - \frac{\lambda_m}{\kappa_{p,YIG}\left(1-\frac{\lambda_m^2}{\ell_{mp}^2}\right)}Q^i_{s,\nu_J} \\
c_{2,\nu_J} &= -\frac{\lambda_m\coth\frac{d}{\lambda_m}}{\frac{eD_m}{g\mu_B}\frac{\partial M}{\partial T_p}\frac{M_z}{\sqrt{M_z}}}J_{z,\nu_J} - \frac{\lambda_m}{\kappa_{p,YIG}\left(1-\frac{\lambda_m^2}{\ell_{mp}^2}\right)}\coth\left(\frac{d}{\ell_{mp}}\right)Q^i_{s,\nu_J} \\
c_{3,\nu_J} &= -\frac{1}{\kappa_{p,YIG}\left(1-\frac{\ell_{mp}^2}{\lambda_m^2}\right)}\ell_{mp}Q^i_{s,\nu_J} \\
c_{4,\nu_J} &= -\frac{1}{\kappa_{p,YIG}\left(1-\frac{\ell_{mp}^2}{\lambda_m^2}\right)}\ell_{mp}\coth\left(\frac{d}{\ell_{mp}}\right)Q^i_{s,\nu_J}
\end{aligned} \quad \text{(E.58)}$$

Hence,

$$\begin{aligned}
&\theta_{p,YIG,v_J} + \epsilon_{m,v_J} \\
&= -\frac{\lambda_m}{\frac{eD_m}{g\mu_B}\frac{\partial M}{\partial T_p}\frac{M_z}{\sqrt{M_z^2}}} \operatorname{csch}\frac{d}{\lambda_m}\cosh\frac{y+d}{\lambda_{mp}} J_{s,v_J} - \operatorname{csch}\frac{d}{\ell_{mp}}\frac{\ell_{mp}}{\kappa_{p,YIG}} Q^i_{s,v_J} \\
&- \frac{\lambda_m}{\kappa_{p,YIG}\left(1-\frac{\lambda_m^2}{\ell_{mp}^2}\right)} \operatorname{csch}\frac{d}{\ell_{mp}}\cosh\frac{y}{\lambda_m} + \frac{d}{\ell_{mp}} Q^i_{s,v_J} \\
&+ \frac{1}{1-\frac{\lambda_m^2}{\ell_{mp}^2}} \cosh\frac{y+d}{\ell_{mp}} \cosh^{-1}\frac{d}{\ell_{mp}}\frac{\ell_{mp}}{\kappa_{p,YIG}} Q^i_{s,v_J}
\end{aligned} \tag{E.59}$$

First Harmonic BLS Peak Shift

The first harmonic frequency components of the BLS peak shift is

$$f_{m,v_J} = f_{m,T_p,v_J}(y) + \delta_{f_m,v_J}(y) = (\theta_{p,YIG,v_J} + \epsilon_{m,v_J})\frac{\partial f_m}{\partial T_p} = \alpha_1 \frac{J_{s,v_J}}{eD_m\frac{M_z}{\sqrt{M_z^2}}} + \alpha_2 Q^i_{s,v_J} \tag{E.60}$$

where

$$\alpha_1 = \frac{\lambda_m \frac{\partial f_m}{\partial T_p}}{\frac{eD_m}{g\mu_B}\frac{\partial M}{\partial T_p}\frac{M_z}{\sqrt{M_z^2}}} \operatorname{csch}\left(\frac{d}{\lambda_m}\right)\cosh\left(\frac{d+y}{\lambda_m}\right) \tag{E.61}$$

$$\alpha_2 = \left[\frac{\ell_{mp}}{\left(1-\frac{\lambda_m^2}{\ell_{mp}^2}\right)}\cosh\left(\frac{d+y}{\ell_{mp}}\right) - \frac{\lambda_m}{\left(1-\frac{\lambda_m^2}{\ell_{mp}^2}\right)}\cosh\left(\frac{d}{\ell_{mp}}+\frac{y}{\lambda_m}\right) - \ell_{mp}\right]\frac{\operatorname{csch}\left(\frac{d}{\ell_{mp}}\right)}{\kappa_{p,YIG}}\frac{\partial f_m}{\partial T_p} \tag{E.62}$$

Thus, the first harmonic magnon frequency shift in the laser spot is

$$\langle f_{m,v_J}\rangle = \langle\theta_{p,YIG,\nu_J}\frac{\partial f_m}{\partial T_p}\rangle + \langle\epsilon_{m,\nu_J}\frac{\partial f_m}{\partial T_p}\rangle = \langle\alpha_1\rangle\frac{J_{s,v_J}}{eD_m\frac{M_z}{\sqrt{M_z^2}}} + \langle\alpha_2\rangle Q^i_{s,v_J} \tag{E.63}$$

where $\langle\xi\rangle$ is the weighted average of a function ξ inside the Gaussian laser spot. Since the interfacial thermal conductance, G_p, is relatively high, the θ_{p,YIG,ν_J} in Eqn. E.56 is expected to be close in magnitude to the the measured $\langle\theta_{p,Pt,\nu_J}\rangle = 0.76$ mK, so that the quantity $\langle\theta_{p,YIG,\nu_J}\frac{\partial f_m}{\partial T_p}\rangle$ would be three orders of magnitude smaller than the

measured $\langle f_{m,\nu_J}\rangle$ and $\langle \epsilon_{m,\nu_J}\frac{\partial f_m}{\partial T_p}\rangle$. In addition,

$$\left(\frac{\partial n_{m,\nu_J}}{\partial y}\right)_{y=0} = \frac{J_{s,\nu_J}}{eD_m\frac{M_z}{\sqrt{M_z^2}}} = -\frac{\frac{\partial M}{\partial T_p}}{g\mu_B\lambda_m\frac{\partial f_m}{\partial T_p}\,\mathrm{csch}\left(\frac{d}{\lambda_m}\right)\langle\cosh\frac{d+y}{\lambda_m}\rangle}\left[\langle f_{m,\nu_J}\rangle - \langle\alpha_2\rangle Q^i_{s,\nu_J}\right] \tag{E.64}$$

Hence, the first harmonic component of the magnon density at the YIG/Pt interface is

$$\begin{aligned} n_{m,\nu_J,y=0} &= \frac{dn_0}{dT_p}\left(\theta_{p,YIG,\nu_J} + \epsilon_{m,\nu_J}\right)_{y=0} \\ &= -\frac{1}{g\mu_B}\frac{\partial M}{\partial T_p}\Bigg\{\frac{\cosh\left(\frac{d}{\lambda_m}\right)}{\frac{\partial f_m}{\partial T_p}\langle\cosh\left(\frac{d+y}{\lambda_m}\right)\rangle}\langle f_{m,\nu_J}\rangle \\ &+ \Bigg[\frac{\langle\cosh\left(\frac{d}{\ell_{mp}}+\frac{y}{\lambda_m}\right)\rangle - \langle\cosh\left(\frac{d+y}{\lambda_m}\right)\rangle}{\langle\cosh\left(\frac{d+y}{\lambda_m}\right)\rangle}\cosh\left(\frac{d}{\lambda_m}\right)\frac{\lambda_m}{\left(1-\frac{\lambda_m^2}{\ell_{mp}}\right)} \\ &+ \frac{\cosh\left(\frac{d}{\lambda_m}\right) - \langle\cosh\left(\frac{d+y}{\lambda_m}\right)\rangle}{\langle\cosh\left(\frac{d+y}{\lambda_m}\right)\rangle}\ell_{mp}\Bigg]\frac{\mathrm{csch}\left(\frac{d}{\ell_{mp}}\right)}{\kappa_{p,YIG}}Q^i_{s,\nu_J}\Bigg\} \end{aligned} \tag{E.65}$$

For ℓ_{mp} in the range between 1 and 250 nm and $\lambda_m \approx 0.95$ μm, the term containing Q^i_{s,ν_J} is much smaller than the term containing $\langle f_{m,\nu_J}\rangle$. Hence,

$$\begin{aligned} n_{m,\nu_J}(y) &\approx n_{m,\nu_J,y=0}\frac{\cosh\left(\frac{y+d}{\lambda_m}\right)}{\cosh\left(\frac{d}{\lambda_m}\right)} \\ &\approx -\frac{\frac{\partial M}{\partial T_p}\cosh\frac{d}{\lambda_m}}{g\mu_B\frac{\partial f_m}{\partial T_p}\langle\cosh\left(\frac{d+y}{\lambda_m}\right)\rangle}\langle f_{m,\nu_J}\rangle \end{aligned} \tag{E.66}$$

This equation is used to calculate the density of magnons injected to the YIG interface based on the measured $\langle f_{m,\nu_J}\rangle$ at different currents in Pt, as shown in Fig. E.3.

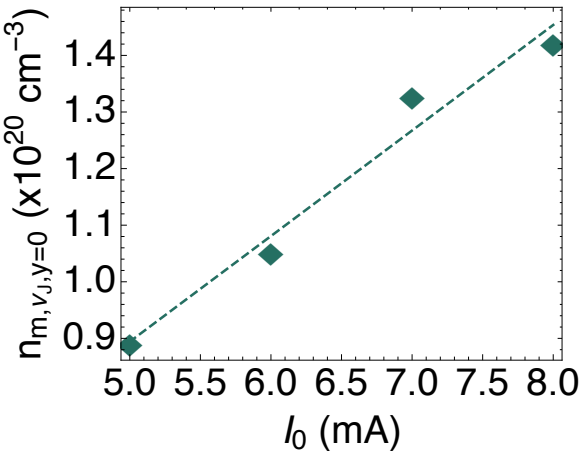

Figure E.3: Magnon population generated by the SHE at the Pt/YIG interface as a function of the applied charge current.

As a comparison, the M-H curve shown in Fig. 4.23(b) indicates approximately 3.5×10^{21} cm^{-3} Bohr magnetons at the saturation magnetization in the YIG film.

E.1.3 Gaussian convolution and weighting

The laser intensity inside the Gaussian spot is

$$I(r,y) = \frac{I_0}{1+(y/y_0)^2}\exp\left[-\frac{2r^2}{w_0^2}\frac{1}{1+(y/y_0)^2} - \alpha_{abs}y\right] \tag{E.67}$$

where $y_0 = \pi w_0^2 n/\lambda_0$, w_0 is the Gaussian beam radius, and I_0 is the peak intensity right beneath the Pt/YIG interface, n is the index of refraction of YIG, λ_0 is the laser wavelength in vacuum, and $\alpha_{abs} = 5\times10^4$ m^{-1} is the measured absorption coefficient for YIG. Thus the spatially varying power density of the green probe laser is

$$\begin{aligned} Q(r,y) &= -\frac{\partial I(r,y)}{\partial y} \\ &= \left[\frac{2y}{[1+(y/y_0)^2]\,y_0^2} - \frac{4r^2y}{w_0y_0^2\,[1+(y/y_0)^2]^2} + \alpha_{abs}\right]\frac{I_0}{1+(y/y_0)^2}e^{-\frac{2r^2}{w_0^2[1+(y/y_0)^2]}-\alpha_{abs}y} \end{aligned} \tag{E.68}$$

Thus, the weighted average is calculated as

$$\langle \xi \rangle = \frac{\int_0^\infty dy \int_0^\infty \xi(r,y) Q(r,y) r\, dr}{\int_0^\infty dy \int_0^\infty Q(r,y) r\, dr}$$
$$= \frac{\int_0^\infty dy \int_0^\infty r\, dr \xi(r,y) \left[\left(\frac{2y}{[1+(y/y_0)^2]^2 y_0^2} - \frac{2r^2}{w_0} \frac{2y}{y_0^2[1+(y/y_0)^2]^3} + \frac{\alpha_{abs}}{1+(y/y_0)^2} \right) e^{-\frac{2r^2}{w_0^2[1+(y/y_0)^2]} - \alpha_{abs} y} \right]}{\int_0^\infty dy \int_0^\infty r\, dr \left[\left(\frac{2y}{[1+(y/y_0)^2]^2 y_0^2} - \frac{2r^2}{w_0} \frac{2y}{y_0^2[1+(y/y_0)^2]^3} + \frac{\alpha_{abs}}{1+(y/y_0)^2} \right) e^{-\frac{2r^2}{w_0^2[1+(y/y_0)^2]} - \alpha_{abs} y} \right]} \tag{E.69}$$

The weighted average $\langle \xi \rangle$ is what is truly being measured by the BLS laser probe. For example, the weighted average of lumped coefficient α_1 used in the analysis of spin current transfer at the Pt/YIG interface is

$$\langle \alpha_1 \rangle = \frac{\int_0^\infty dy \int_0^\infty -\frac{\lambda_m \frac{\partial f_m}{\partial T_p}}{\frac{eD_m}{g\mu_B} \frac{\partial M}{\partial T_p} \frac{M_z}{\sqrt{M_z}}} \operatorname{csch} \frac{d}{\lambda_m} \cosh \frac{d+y}{\lambda_m} \left[\left(\frac{2y}{(1+(y/y_0)^2) y_0^2} - \frac{2r^2}{w_0} \frac{2y}{y_0^2(1+(y/y_0)^2)^3} + \frac{\alpha_{abs}}{1+(y/y_0)^2} \right) e^{-\frac{2r^2}{w_0^2(1+(y/y_0)^2)} - \alpha_{abs} y} \right] r\, dr}{\int_0^\infty dy \int_0^\infty \left[\left(\frac{2y}{(1+(y/y_0)^2) y_0^2} - \frac{2r^2}{w_0} \frac{2y}{y_0^2(1+(y/y_0)^2)^3} + \frac{\alpha_{abs}}{1+(y/y_0)^2} \right) e^{-\frac{2r^2}{w_0^2(1+(y/y_0)^2)} - \alpha_{abs} y} \right] r\, dr} \tag{E.70}$$

which is equivalent to

$$\langle \alpha_1 \rangle = -\frac{\frac{\partial f_m}{\partial T_p} g \mu_B \lambda_m^2 \operatorname{csch} \frac{d}{\lambda_m} \left(\alpha_{abs} \lambda_m \cosh \frac{d}{\lambda_m} + \sinh \frac{d}{\lambda_m} \right)}{e D_m \frac{\partial M}{\partial T_p} \left(\alpha_{abs}^2 \lambda_m^2 - 1 \right)} \tag{E.71}$$

Following the same procedure,

$$\langle \alpha_2 \rangle = \frac{\frac{\partial f_m}{\partial T_p} \ell_{mp} \alpha_{abs} \left[\frac{\lambda_m^2 - \ell_{mp}^2}{\alpha_{abs}} + \frac{\ell_{mp}}{2} e^{\frac{-d}{\ell_{mp}}} \left(\ell_{mp} \left(\frac{1}{\frac{1}{\ell_{mp}} + \alpha_{abs}} + \frac{\ell_{mp} e^{\frac{2d}{\ell_{mp}}}}{\ell_{mp} \alpha_{abs} - 1} \right) - \lambda_m \left(\frac{1}{\frac{1}{\lambda_m} + \alpha_{abs}} + \frac{\lambda_m e^{\frac{2d}{\ell_{mp}}}}{\lambda_m \alpha_{abs} - 1} \right) \right) \right] \operatorname{csch} \frac{d}{\ell_{mp}}}{\kappa_{p,YIG} \left(\ell_{mp}^2 - \lambda_m^2 \right)} \tag{E.72}$$

E.2 2D finite element calculation of magnon diffusion

As the BLS laser probe is scanned away from the edge of the Pt line, the one-dimensional approximation for transport directly beneath the Pt is no longer valid, and so we are tasked with solving Eqn. E.47 in two dimensions using a finite element method.

Because $\langle \theta_{p,YIG,\nu_J} \rangle$ is three orders of magnitude smaller than $\langle \epsilon_{m,\nu_J} \rangle$, as discussed above, the dimensionless magnon spin diffusion equation can be reduced to

$$\nabla^2 \epsilon_{m,\nu} = \frac{1}{\lambda_m^2} \epsilon_{m,\nu}, \tag{E.73}$$

A numerical solution of this equation was obtained in a two-dimensional domain using the commercial software package COMSOL. The domain was set up to simulate a cross-section of the YIG underneath the 20 μm-wide Pt, and had dimensions of 10 μm in the vertical direction (y) and 50 μm in z, with the $z = 0$ boundary bisecting the Pt line lengthwise. With λ_m as a variable parameter, $\epsilon(z, y)$ was calculated on a rectangular mesh with the following boundary conditions in Cartesian coordinates

$$\begin{cases} \frac{\partial \epsilon(z=0\mu m, y)}{\partial y} = 0 \\ \frac{\partial \epsilon(z=50\mu m, 0)}{\partial y} = 0 \\ \frac{\partial \epsilon(z<10\mu m, y=0\mu m)}{\partial y} = C \\ \epsilon(z = 50\mu m, y) = 0, \end{cases}$$

with the third boundary condition indicating the injection of spin into the YIG under the Pt and the constant C is taken as unity in the simulation for convenience.

Following each calculation, the result was interpolated, and the Gaussian-weighted average of the normalized magnon frequency change (ϵ(z,y)) was computed as a function of the distance (Δz) between the edge of the Pt and the center of the laser spot in the physical measurement. The Gaussian weighting was carried out over the

interpolated result within the simulation domain at each Δz value.

The calculation result is shown in Fig. E.4. The normalized value of $\frac{\langle\epsilon\rangle_{\Delta z_2}}{\langle\epsilon\rangle_{\Delta z_1}}$ is plotted in Fig. 4.22(c) for different values of λ_m. The optimum value of λ_m is selected when the calculation result intersects with the experimental data such that $\frac{\langle\epsilon\rangle_{\Delta z_2}}{\langle\epsilon\rangle_{\Delta z_1}} = \frac{\langle f_{m,\Delta z_2}\rangle}{\langle f_{m,\Delta z_1}\rangle}$, and is found to be 0.95 μm.

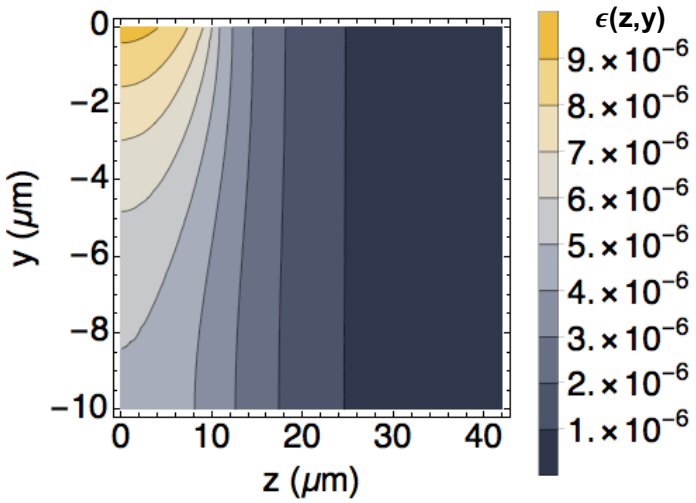

Figure E.4: Two-dimensional solution to the magnon diffusion equation (Eqn. E.73) for a λ_m value of 10 μm.

Bibliography

[1] S. V. Garimella, *et al.*, *IEEE Transactions on Components and Packaging Technologies* **31**, 801 (2008).

[2] P. Ball, *Nature* **492**, 174 (2012).

[3] LLNL, Energy Flow Charts (2016).

[4] T. D. Ladd, *et al.*, *Nature* **464**, 45 (2010).

[5] A. I. Hochbaum, *et al.*, *Nature* **451**, 163 (2008).

[6] G. J. Snyder, E. S. Toberer, *Nature Materials* **7**, 105 (2008).

[7] G. Slack, *Journal of Physics and Chemistry of Solids* **34**, 321 (1973).

[8] J. H. Seol, *et al.*, *Science* **328**, 213 (2010).

[9] K. I. Uchida, *et al.*, *Applied Physics Letters* **97**, 172505 (2010).

[10] J. Flipse, *et al.*, *Physical Review Letters* **113**, 027601 (2014).

[11] H. Yu, S. Granville, D. P. Yu, J. P. Ansermet, *Physical Review Letters* **104**, 146601 (2010).

[12] G. M. Choi, C. H. Moon, B. C. Min, K. J. Lee, D. G. Cahill, *Nature Physics* **11**, 576 (2015).

[13] A. V. Chumak, A. A. Serga, B. Hillebrands, *Nature Communications* **5**, 4700 (2014).

[14] L. Cornelissen, J. Liu, B. van Wees, R. Duine, *Physical Review Letters* **120**, 097702 (2018).

[15] H. Wu, *et al.*, *Physical Review Letters* **120**, 097205 (2018).

[16] A. Kirihara, *et al.*, *Nature Materials* **11**, 686 (2012).

[17] A. B. Cahaya, O. A. Tretiakov, G. E. Bauer, *Applied Physics Letters* **104**, 042402 (2014).

[18] S. R. Boona, S. J. Watzman, J. P. Heremans, *APL Materials* **4**, 104502 (2016).

[19] J. M. J. M. Ziman, *Electrons and phonons : the theory of transport phenomena*

in solids (Clarendon Press, 2001).

[20] C. Kittel, *Introduction to solid state physics* (Wiley, 2005).

[21] N. W. Ashcroft, N. D. Mermin, *Solid state physics* (Holt, Rinehart and Winston, 1976).

[22] M. T. Dove, *Introduction to Lattice Dynamics* (Cambridge University Press, Cambridge, 1993).

[23] S. Sullivan, Thermal transport in nanoengineered silicon nanowires via molecular dynamics simulation, Master's thesis, Purdue University (2013).

[24] L. Verlet, *Physical Review* **159**, 98 (1967).

[25] J. Barker, G. E. Bauer, *Physical Review Letters* **117**, 217201 (2016).

[26] T. L. Gilbert, *IEEE Transactions on Magnetics* **40**, 3443 (2004).

[27] G. P. Chen, *Nanoscale energy transport and conversion : a parallel treatment of electrons, molecules, phonons, and photons* (Oxford University Press, 2005).

[28] A. G. Gurevich, G. A. Melkov, *Magnetization oscillations and waves* (CRC Press, 1996).

[29] B. Flebus, S. A. Bender, Y. Tserkovnyak, R. A. Duine, *Physical Review Letters* **116**, 117201 (2016).

[30] J. Holanda, D. S. Maior, A. Azevedo, S. M. Rezende, *Nature Physics* **14**, 500 (2018).

[31] L. Lindsay, D. A. Broido, T. L. Reinecke, *Physical Review Letters* **111**, 025901 (2013).

[32] T. Feng, L. Lindsay, X. Ruan, *Physical Review B* **96**, 161201 (2017).

[33] C. Dames, *Science* **364**, 549 (2018).

[34] J. S. Kang, M. Li, H. Wu, H. Nguyen, Y. Hu, *Science* **361**, 575 (2018).

[35] F. Tian, *et al.*, *Science* **361**, 582 (2018).

[36] S. Li, *et al.*, *Science* **361**, 579 (2018).

[37] M. Schreier, *et al.*, *Physical Review B - Condensed Matter and Materials Physics* **88**, 094410 (2013).

[38] A. V. Sologubenko, K. Giannó, H. R. Ott, U. Ammerahl, A. Revcolevschi, *Physical Review Letters* **84**, 2714 (2000).

[39] C. Hess, *et al.*, *Physical Review B* **64**, 184305 (2001).

[40] X. Chen, *et al.*, *Physical Review B* **94**, 134309 (2016).

[41] V. Zlatić, R. Monnier, *Modern Theory of Thermoelectricity* (Oxford University

Press, 2014).
[42] L. Onsager, *Physical Review* **38**, 2265 (1931).
[43] L. Onsager, *Physical Review* **37**, 405 (1931).
[44] C. A. Domenicali, *Reviews of Modern Physics* **26**, 237 (1954).
[45] R. Karplus, J. M. Luttinger, *Physical Review* **95**, 1154 (1954).
[46] N. Nagaosa, J. Sinova, S. Onoda, A. H. MacDonald, N. P. Ong, *Reviews of Modern Physics* **82**, 1539 (2010).
[47] L. Berger, *Physical Review B* **2**, 4559 (1970).
[48] J. Smit, *Physica* **24**, 39 (1958).
[49] T. Jungwirth, Q. Niu, A. H. MacDonald, *Physical Review Letters* **88**, 4 (2002).
[50] G. Y. Guo, S. Murakami, T. W. Chen, N. Nagaosa, *Physical Review Letters* **100**, 096401 (2008).
[51] M. I. D'yakonov, V. I. Perel', Possibility of orienting electron spins with current (1971).
[52] J. E. Hirsch, *Physical Review Letters* **83**, 1834 (1999).
[53] A. Hoffmann, *IEEE Transactions on Magnetics* **49**, 5172 (2013).
[54] G. L. Pollack, *Reviews of Modern Physics* **41**, 48 (1969).
[55] T. Zeng, G. Chen, *Journal of Heat Transfer* **123**, 340 (2001).
[56] A. Majumdar, P. Reddy, *Applied Physics Letters* **84**, 4768 (2004).
[57] Y. Tserkovnyak, A. Brataas, G. E. Bauer, B. I. Halperin, *Reviews of Modern Physics* **77**, 1375 (2005).
[58] J. Slonczewski, *Journal of Magnetism and Magnetic Materials* **159**, L1 (1996).
[59] S. Daimon, R. Iguchi, T. Hioki, E. Saitoh, K.-i. Uchida, *Nature Communications* **7**, 13754 (2016).
[60] K. Uchida, *et al.*, *Physical Review B* **95**, 184437 (2017).
[61] K. Uchida, *et al.*, *Nature* **455**, 778 (2008).
[62] E. Saitoh, M. Ueda, H. Miyajima, G. Tatara, *Applied Physics Letters* **88**, 182509 (2006).
[63] N. Vlietstra, *et al.*, *Physical Review B* **90**, 174436 (2014).
[64] L. J. Cornelissen, J. Liu, R. A. Duine, J. B. Youssef, B. J. Van Wees, *Nature Physics* **11**, 1022 (2015).
[65] B. L. Giles, Z. Yang, J. S. Jamison, R. C. Myers, *Physical Review B - Condensed Matter and Materials Physics* **92**, 1 (2015).

[66] T. McGuire, R. Potter, *IEEE Transactions on Magnetics* **11**, 1018 (1975).
[67] M. Julliere, *Physics Letters A* **54**, 225 (1975).
[68] M. N. Baibich, *et al.*, *Physical Review Letters* **61**, 2472 (1988).
[69] H. Nakayama, *et al.*, *Physical Review Letters* **110**, 206601 (2013).
[70] M. Althammer, *et al.*, *Physical Review B* **87**, 224401 (2013).
[71] S. Daimon, K. I. Uchida, R. Iguchi, T. Hioki, E. Saitoh, *Physical Review B* **96**, 024424 (2017).
[72] T. Seki, R. Iguchi, K. Takanashi, K. Uchida, *Applied Physics Letters* **112**, 152403 (2018).
[73] K.-i. Uchida, S. Daimon, R. Iguchi, E. Saitoh, *Nature* **558**, 95 (2018).
[74] C. Kittel, *Physical Review* **73**, 155 (1948).
[75] S. S. Kalarickal, *et al.*, *Journal of Applied Physics* **99**, 093909 (2006).
[76] R. LeCraw, *Phys. Rev.; Physical Review* **110**, 1311 (1958).
[77] C. Hauser, *et al.*, *Scientific Reports* **6**, 20827 (2016).
[78] J. C. Rojas-Sánchez, *et al.*, *Physical Review Letters* **112**, 106602 (2014).
[79] B. Heinrich, *et al.*, *Physical Review Letters* **107**, 066604 (2011).
[80] M. W. Doherty, *et al.*, *Physics Reports* **528**, 1 (2013).
[81] A. Gruber, *Science* **276**, 2012 (1997).
[82] J. R. Maze, *et al.*, *Nature* **455**, 644 (2008).
[83] P. Neumann, *et al.*, *Nano Letters* **13**, 2738 (2013).
[84] P. Andrich, *et al.*, *npj Quantum Information* **3**, 28 (2017).
[85] C. Du, *et al.*, *Science* **357**, 195 (2017).
[86] W. Hayes, R. Loudon, *Scattering of light by crystals / William Hayes, Rodney Loudon.* (Dover Publications, 2004).
[87] R. Mock, B. Hillebrands, R. Sandercock, *Journal of Physics E* **20**, 656 (2000).
[88] A. A. Serga, *et al.*, *Physical Review B* **86**, 134403 (2012).
[89] K. An, Control of Spin Waves using Charge and Heat Flows, Ph.D. thesis, University of Texas at Austin (2016).
[90] C. W. Sandweg, *et al.*, *Review of Scientific Instruments* **81**, 073902 (2010).
[91] P. Clausen, *et al.*, *Applied Physics Letters* **99**, 162505 (2011).
[92] K. Vogt, *et al.*, *Applied Physics Letters* **101**, 042410 (2012).
[93] A. A. Serga, S. O. Demokritov, B. Hillebrands, A. N. Slavin, *Physical Review Letters* **92**, 117203 (2004).

[94] S. O. Demokritov, *et al.*, *Nature* **443**, 430 (2006).
[95] D. R. Birt, *et al.*, *Applied Physics Letters* **102**, 082401 (2013).
[96] K. S. Olsson, *et al.*, *Applied Physics Letters* **106**, 051906 (2015).
[97] K. S. Olsson, *et al.*, *Physical Review B* **96**, 024448 (2017).
[98] K. An, *et al.*, *Physical Review Letters* **117**, 1 (2016).
[99] L. D. Hicks, M. S. Dresselhaus, *Physical Review B* **47**, 12727 (1993).
[100] J. H. Davies, *The Physics of Low-Dimensional Semiconductors* (Cambridge University Press, Cambridge, 1997).
[101] K. Bolotin, *et al.*, *Solid State Communications* **146**, 351 (2008).
[102] A. H. Castro Neto, F. Guinea, N. M. R. Peres, K. S. Novoselov, A. K. Geim, *Reviews of Modern Physics* **81**, 109 (2009).
[103] A. A. Balandin, *et al.*, *Nano letters* **8**, 902 (2008).
[104] W. Cai, *et al.*, *Nano letters* **10**, 1645 (2010).
[105] X. Xu, *et al.*, *Nature Communications* **5**, 1 (2014).
[106] J. Crossno, *et al.*, *Science* **351**, 1058 (2016).
[107] S. Lee, D. Broido, K. Esfarjani, G. Chen, *Nature Communications* **6**, 6290 (2015).
[108] A. Cepellotti, *et al.*, *Nature Communications* **6**, 6400 (2015).
[109] E. H. Hwang, B. Y.-K. Hu, S. Das Sarma, *Physical Review B* **76**, 115434 (2007).
[110] T. Winzer, A. Knorr, E. Malic, *Nano Letters* **10**, 4839 (2010).
[111] M. Breusing, *et al.*, *Physical Review B* **83**, 153410 (2011).
[112] K. J. Tielrooij, *et al.*, *Nature Physics* **9**, 248 (2013).
[113] R. Bistritzer, A. H. MacDonald, *Physical Review Letters* **102**, 13 (2009).
[114] A. C. Betz, *et al.*, *Physical Review Letters* **109**, 056805 (2012).
[115] A. C. Betz, *et al.*, *Nature Physics* **9**, 109 (2013).
[116] J. C. W. Song, M. S. Rudner, C. M. Marcus, L. S. Levitov, *Nano Letters* **11**, 4688 (2011).
[117] M. Freitag, T. Low, P. Avouris, *Nano Letters* **13**, 1644 (2013).
[118] D. K. Efetov, P. Kim, *Physical Review Letters* **105**, 2 (2010).
[119] Q. Ma, *et al.*, *Physical Review Letters* **112**, 1 (2014).
[120] A. Laitinen, *et al.*, *Nano Letters* **14**, 3009 (2014).
[121] J.-H. Chen, *et al.*, *Nature Physics* **4**, 377 (2008).
[122] J. M. Dawlaty, S. Shivaraman, M. Chandrashekhar, F. Rana, M. G. Spencer,

Applied Physics Letters **92**, 042116 (2008).

[123] K. Kang, D. Abdula, D. G. Cahill, M. Shim, *Physical Review B - Condensed Matter and Materials Physics* **81**, 1 (2010).

[124] P. J. Hale, S. M. Hornett, J. Moger, D. W. Horsell, E. Hendry, *Physical Review B* **83**, 121404 (2011).

[125] S. Tani, F. Blanchard, K. Tanaka, *Physical Review Letters* **109**, 166603 (2012).

[126] S. Berciaud, *et al.*, *Physical Review Letters* **104**, 2 (2010).

[127] D.-H. Chae, B. Krauss, K. von Klitzing, J. H. Smet, *Nano Letters* **10**, 466 (2010).

[128] I. Jo, *et al.*, *Nano Letters* **11**, 85 (2011).

[129] C. Faugeras, *et al.*, *ACS Nano* **4**, 1889 (2010).

[130] S. Ghosh, *et al.*, *Nature Materials* **9**, 555 (2010).

[131] S. Chen, *et al.*, *ACS Nano* **5**, 321 (2011).

[132] S. Chen, *et al.*, *Nature Materials* **11**, 203 (2012).

[133] S. Sahoo, A. P. S. Gaur, M. Ahmadi, M. J.-F. Guinel, R. S. Katiyar, *The Journal of Physical Chemistry C* **117**, 9042 (2013).

[134] Z. Luo, *et al.*, *Nature Communications* **6**, 8572 (2015).

[135] A. K. Vallabhaneni, D. Singh, H. Bao, J. Murthy, X. Ruan, *Physical Review B* **93**, 125432 (2016).

[136] P. G. Klemens, *International Journal of Thermophysics* **22**, 265 (2001).

[137] L. Lindsay, D. A. Broido, N. Mingo, *Physical Review B* **82**, 115427 (2010).

[138] M. Cardona, *et al.* (Springer Berlin, 1982), p. 254.

[139] A. C. Ferrari, D. M. Basko, *Nature Publishing Group* **8**, 235 (2013).

[140] I. Pócsik, M. Hundhausen, M. Koós, L. Ley, *Journal of Non-Crystalline Solids* **227-230**, 1083 (1998).

[141] S. Piscanec, M. Lazzeri, F. Mauri, A. C. Ferrari, J. Robertson, *Physical Review Letters* **93**, 185503 (2004).

[142] P. May, *et al.*, *Physical Review B - Condensed Matter and Materials Physics* **87**, 1 (2013).

[143] X. Li, *et al.*, *Science* **324**, 1312 (2009).

[144] X. Li, *et al.*, *Journal of the American Chemical Society* **133**, 2816 (2011).

[145] L. Malard, M. Pimenta, G. Dresselhaus, M. Dresselhaus, *Physics Reports* **473**, 51 (2009).

[146] A. Jorio, R. Saito, G. Dresselhaus, M. S. Dresselhaus, *Raman Spectroscopy in Graphene Related Systems* (Wiley-VCH Verlag GmbH & Co. KGaA, Weinheim, Germany, 2011).

[147] M. Oron-Carl, R. Krupke, *Physical Review Letters* **100**, 127401 (2008).

[148] N. Bonini, M. Lazzeri, N. Marzari, F. Mauri, *Physical Review Letters* **99**, 1 (2007).

[149] R. A. Cowley, *Reports on Progress in Physics* **31**, 123 (1968).

[150] R. Cuscó, B. Gil, G. Cassabois, L. Artús, *Physical Review B* **94**, 155435 (2016).

[151] M. T. Pettes, *et al.*, *Physical Review B* **91**, 035429 (2015).

[152] E. Mariani, F. von Oppen, *Physical Review Letters* **100**, 076801 (2008).

[153] R. Saito, *et al.*, *Physical Review Letters* **88**, 027401 (2001).

[154] C. Yu, *et al.*, *Journal of Heat Transfer* **128**, 234 (2006).

[155] J.-U. Lee, D. Yoon, H. Kim, S. W. Lee, H. Cheong, *Physical Review B* **83**, 081419 (2011).

[156] D. G. Cahill, *Review of Scientific Instruments* **75**, 5119 (2004).

[157] S. Sullivan, *et al.*, *Nano Letters* **17**, 2049 (2017).

[158] W. J. Parker, R. J. Jenkins, C. P. Butler, G. L. Abbott, *Journal of Applied Physics* **32**, 1679 (1961).

[159] J. Liu, H. Wang, Y. Hu, W. Ma, X. Zhang, *Review of Scientific Instruments* **86**, 014901 (2015).

[160] F. Tian, *et al.*, *Applied Physics Letters* **112**, 031903 (2018).

[161] W. Fulkerson, J. P. Moore, R. K. Williams, R. S. Graves, D. L. McElroy, *Physical Review* **167**, 765 (1968).

[162] Y. S. Touloukian, R. W. Powell, C. Y. Ho, P. G. Klemens, *Thermophysical Properties of Matter - The TPRC Data Series. Volume 2. Thermal Conductivity - Nonmetallic Solids* (1971).

[163] D. Evans, Applications of Bis(imino)acenaphthene and Investigation of Boron Arsenide as a High Thermal Conductivity Material, Dissertation, The University of Texas at Austin (2015).

[164] J. H. Kim, Four-Probe Thermal and Thermoelectric Transport Measurements of Bismuth Antimony Telluride, Silicon, and Boron Arsenide Nanostructures, Ph.D. thesis, University of Texas at Austin (2015).

[165] J. Kim, *et al.*, *Applied Physics Letters* **108**, 201905 (2016).

[166] A. Weathers, Transport and Coupling of Phonons, Electrons, and Magnons in Complex Materials, Ph.D. thesis, University of Texas at Austin (2016).
[167] B. Lv, *et al.*, *Applied Physics Letters* **106**, 074105 (2015).
[168] J. Xing, *et al.*, *Applied Physics Letters* **112**, 261901 (2018).
[169] G. Binasch, P. Grünberg, F. Saurenbach, W. Zinn, *Physical Review B* **39**, 4828 (1989).
[170] J. S. Moodera, L. R. Kinder, T. M. Wong, R. Meservey, *Physical Review Letters* **74**, 3273 (1995).
[171] S. Yuasa, T. Nagahama, A. Fukushima, Y. Suzuki, K. Ando, *Nature Materials* **3**, 868 (2004).
[172] S. S. P. Parkin, *et al.*, *Nature Materials* **3**, 862 (2004).
[173] S. S. P. Parkin, *et al.*, *Journal of Applied Physics* **85**, 5828 (1999).
[174] M. I. Dyakonov, *Physical Review Letters* **99**, 126601 (2007).
[175] H. J. Goldsmid, *Electronic refrigeration* (Pion, 1986).
[176] V. Cherepanov, I. Kolokolov, V. L'vov, *Physics Reports* **229**, 81 (1993).
[177] M. Liu, *et al.*, *AIP Advances* **8**, 085117 (2018).
[178] S. R. Boona, J. P. Heremans, *Physical Review B* **90**, 064421 (2014).
[179] A. J. Princep, *et al.*, *npj Quantum Materials* **2**, 63 (2017).
[180] H. Man, *et al.*, *Physical Review B* **96**, 100406 (2017).
[181] M. Levy, R. M. Osgood, A. Kumar, H. Bakhru, *Applied Physics Letters* **71**, 2617 (1997).
[182] A. Prakash, *et al.*, *Physical Review B* **97**, 020408 (2018).
[183] S. R. Boona, R. C. Myers, J. P. Heremans, *Energy & Environmental Science* **7**, 885 (2014).
[184] K.-i. Uchida, T. Kikkawa, A. Miura, J. Shiomi, E. Saitoh, *Physical Review X* **4**, 041023 (2014).
[185] J. Hohlfeld, *et al.*, *Chemical Physics* **251**, 237 (2000).
[186] Z. Lin, L. V. Zhigilei, V. Celli, *Physical Review B - Condensed Matter and Materials Physics* **77**, 075133 (2008).
[187] C. Dames, G. Chen, *Review of Scientific Instruments* **76**, 1 (2005).
[188] D. G. Cahill, *Review of Scientific Instruments* **61**, 802 (1990).
[189] B. F. Miao, S. Y. Huang, D. Qu, C. L. Chien, *AIP Advances* **6**, 015018 (2016).
[190] V. E. Demidov, *et al.*, *Nature Communications* **8**, 1579 (2017).

[191] J. R. Sandercock, W. Wettling, *Solid State Communications* **13**, 1729 (1973).
[192] E. Jakeman, C. J. Oliver, E. R. Pike, *Advances in Physics* **24**, 349 (1975).
[193] H. Suhl, *Journal of Physics and Chemistry of Solids* **1**, 209 (1957).
[194] M. Agrawal, *et al.*, *Physical Review Letters* **111**, 107204 (2013).
[195] S. Y. Huang, *et al.*, *Physical Review Letters* **109**, 107204 (2012).
[196] Y. M. Lu, *et al.*, *Physical Review Letters* **110**, 147207 (2013).
[197] C. O. Avci, *et al.*, *Nature Physics* **11**, 570 (2015).
[198] J. D. Jackson, *Classical electrodynamics* (Wiley, 1999).
[199] K. S. Olsson, Phonon and Magnon Thermometry using Light Scattering Techniques, Ph.D. thesis, University of Texas at Austin (2018).
[200] W. Wettling, M. G. Cottam, J. R. Sandercock, *Journal of Physics C: Solid State Physics* **8**, 211 (1975).
[201] S. Plimpton, *Journal of Computational Physics* **117**, 1 (1995).
[202] L. Lindsay, D. A. Broido, *Physical Review B* **81**, 205441 (2010).
[203] L. T. Kong, *Computer Physics Communications* **182**, 2201 (2011).
[204] B. Mortazavi, M. Pötschke, G. Cuniberti, *Nanoscale* **6**, 3344 (2014).
[205] E. Pop, V. Varshney, A. K. Roy, *MRS Bulletin* **37**, 1273 (2012).
[206] Z.-Y. Ong, E. Pop, *Journal of Applied Physics* **108**, 103502 (2010).
[207] S. E. Sullivan, K. H. Lin, S. Avdoshenko, A. Strachan, *Applied Physics Letters* **103** (2013).
[208] Z.-Y. Ong, E. Pop, *Physical Review B* **84**, 075471 (2011).
[209] D. L. Nika, A. A. Balandin, *Journal of Physics: Condensed Matter* **24**, 233203 (2012).

Vita

Sean Sullivan received his B.S. in 2012 and M.S. in 2013 from the School of Materials Science and Engineering at Purdue University under the supervision of Professor Alejandro Strachan. He is the recipient of the UT Graduate School Fellowship and Cockrell School of Engineering Thrust Fellowship.

Permanent Address: sewsulliv@gmail.com